Doctoral Theses at NTNU, 2006:28

Christoph Stiller

Design, Operation and Control Modelling of SOFC/GT Hybrid Systems

Doctoral thesis
for the degree of philosophiae doctor

Trondheim, March 2006

Norwegian University of
Science and Technology
Faculty of Engineering Science and Technology
Department of Energy and Process Engineering

NTNU
Innovation and Creativity

Preface

This thesis is submitted in partial fulfillment of the requirements for the degree "PhD" at the Norwegian University of Science and Technology (NTNU).

The work was carried out at the Department of Energy and Process Engineering at the Faculty of Engineering Science and Technology, with Professor Olav Bolland as supervisor and Håvard Karoliussen as co-supervisor.

The research was founded by Shell Technology Norway and the Norwegian Research Council.

Acknowledgements

First of all I want to thank my supervisor, Professor Olav Bolland from the Department of Energy and Process Engineering, for the skilful, reliable and friendly guidance during my PhD project. Even though you are a busy man, you always had time when it was necessary. Your confidence, openness and support of my ideas made it a great pleasure to work with you.

My second advisor, associate professor Håvard Karoliussen from the Department of Materials Science and Engineering, and Professor Gunnar Härkegård from the Department of Engineering Design and Materials are acknowledged for guidance in chemical and mechanical questions.

My colleague and friend Bjørn Thorud I want to thank for the uncomplicated and productive collaboration we were having during the project. Working with you was always fun. Good luck for your career!

Rambabu Kandepu and Lars Imsland from Engineering Cybernetics Department are acknowledged for guiding me through the mighty jungles of control engineering.

Gratitude goes to Shell Technology Norway and Norges Forskningsråd for funding the project. Knut Bakke from Shell is acknowledged for giving valuable inputs to the project.

The colleagues from the SOFC groups in Lund, Lausanne and Genoa are appreciated for the exchange of experiences and ideas. Tack, merci and grazie!

Furthermore, I want to express my gratitude to Steinar Seljebø, Øistein Mathisen, Inge Fosse, Morten Schell and Arata Nakajo for good collaboration and contribution to our research with their diploma theses and projects.

I also want to thank my friends Rehan Naqvi, Michael Drescher and Christian Klose, my virtual office mate, for the relaxing breaks and funny discussions, as well as the 10-kaffe team and all colleagues who make this department a friendly place.

Ilko, Dörthe, Alex, Katja and Viktor, thanks for all the cabin trips we have done – they have been among the best recreational activities.

Furthermore I thank my friends from Germany who visited me, and the others for not forgetting me during the three years abroad.

My family was always standing behind me and supporting me in what I wanted. Dankeschön!

Finally, I want to thank my dear girlfriend Ruth for letting me solve your problems when my own ones appeared too heavy and for your readiness to spend all these snowy Easter and rainy summer vacations in Norway!

Summary

This thesis focuses on modelling-based design, operation and control of solid oxide fuel cell (SOFC) and gas turbine (GT) hybrid systems. Fuel cells are a promising approach to high-efficiency power generation, as they directly convert chemical energy to electric work. High-temperature fuel cells such as the SOFC can be integrated in gas turbine processes, which further increases the electrical efficiency to values up to 70%. However, there are a number of obstacles for safe operation of such a system, such as fuel cell damage through thermal loads or undesired chemical reactions, or gas turbine problems related to high thermal capacity and volume of the pressurised components. Development of suitable plant design as well as operation and control strategies is hence a key task for realisation of the mentioned systems.

The first part of the thesis describes the utilised models. All component models that have been developed and applied for the work are mathematically defined based on a fixed pattern. The thermodynamically most relevant components are tubular SOFC, indirect internal reformer and heat exchangers, and spatially discretised models are used for these. For the turbomachinery, map-based steady-state behaviour is modelled. Gas residence times and pressure drops are accounted for in all components they are relevant.

Based on the component models, three different hybrid cycles are examined. In the first cycle, the SOFC replaces the combustion chamber of a recuperated single-shaft turbine. The SOFC is pressurised and the cycle is called "directly integrated SOFC cycle" (DIC). Further cycle options are a DIC with a two-shaft gas turbine (DIC-2T) and an indirectly integrated SOFC cycle (IIC). In the latter, the compressed gas is heated recuperatively with the exhaust gas and the SOFC is operated at ambient pressure by connecting its air inlet to the turbine exhaust. All cycles incorporate the SOFC system design proposed by Siemens-Westinghouse, including indirect internal reforming, a tubular SOFC bundle and anode recirculation by an ejector. The first cycle (DIC) is regarded as standard cycle.

Objectives for highly efficient, safe system design are formulated and design parameters are associated. A design calculation determines the design parameters for the standard cycle, based on a nominal power output of 220 kW. The design LHV-based electric efficiency is app. 63%. Related to the design point, steady-state part-load ability of the system is analysed and displayed in two-dimensional performance maps where each axis represents one degree of freedom. Degrees of freedom considered are fuel and air flow; fuel utilisation is assumed constant. A result is that a strategy with constant mean fuel cell temperature is most advantageous in terms of safe and gentle operation. Further advantages of this strategy are the ability for low part-load and high efficiency at part-load operation.

A control strategy is derived for dynamical implementation of the found part-load strategy. The system power output is primarily controlled by the SOFC power. The

fuel utilisation is kept within certain bounds and the fuel flow is manipulated to control it to its design value. The fuel cell temperature is controlled by the air flow, which again is controlled by manipulating the GT shaft speed through the generator power. To determine the required air flow, a mixed feedforward and feedback strategy is used, where the feedforward part calculates a prediction based on the net power output and the feedback part provides correction based on the measurement of the SOFC fuel outlet temperature. Additional constraints to the control system are the supervision of the shaft speed and the valid operation regime of the anode recirculation ejector.

The proposed control strategy provides robust control. The mean SOFC temperature, however, shows large transient deviation upon large load steps. The time to reach the setpoint power for large load steps is up to 70 s, while small load steps are followed in typically 1-2 s. A conclusion is that the system is suitable for load following operation as long as small load steps occur, as for example in distributed power generation for residential applications.

Shutdown and startup strategies are introduced where the gas turbine provides air for cooling/heating throughout the procedures. Additional equipment and piping such as an auxiliary burner, a turbine exhaust throttle, a bypass around the recuperative heat exchanger as well as nitrogen and hydrogen supply and mixing units are required. Therewith, smooth cooling/heating of the cell can be accomplished without external electric power, but with a considerable amount of fuel and flushing nitrogen required.

A further analysis investigates fuel flexibility of a system designed for methane: Hydrogen can be utilised without larger system modifications; only the control system characteristics must be adapted. Because no endothermic steam reforming takes place, the power output is, however, reduced to 70% of the original value, and efficiency is reduced to 55%. Applying the additional equipment required for shutdown/startup, the power can be increased to 94% of the original value, although at a further efficiency decrease. In order to use ethanol as fuel in the ejector-driven anode, a recuperative vaporiser must be applied in the fuel channel. Supposed that reliable reforming catalysts for ethanol can be provided, 88% of the original power output can be achieved at a high efficiency of 62%.

The investigation of the other cycle options reveals that a two turbine cycle where the power turbine is rotating at constant speed, mostly differs in terms of controllability. For controlling the air flow, another handle such as variable inlet guide vanes or air bypass around the SOFC system is required. The indirectly integrated SOFC cycle (IIC) has a significantly lower efficiency of only 56%, assuming the SOFC at the same temperature level than in the DIC.

Table of Contents

Nomenclature

Symbols

Note: Only symbols appearing in Chapters 5-7 are described here; symbols only appearing in the model descriptions (Chapter 4) are defined separately for each model.

A	Cross-sectional area (m^2)
c	Pressure loss coefficient
CD	Minimum Gibbs energy for carbon deposition reaction ($J\ mol^{-1}$)
$dTdr$	Local radial temperature gradient ($K\ m^{-1}$)
F	Faraday constant (96485 $C\ mol^{-1}$)
J	Current (A)
j	Current density ($A\ m^{-2}$)
l	Length (m)
m	Mass (kg)
$\dot{m}$	Mass flow rate ($kg\ s^{-1}$)
M	Molar weight ($g\ mol^{-1}$)
n	Model multiplicator
$\dot{n}$	Molar flow rate ($mol\ s^{-1}$)
N	Shaft speed (s^{-1})
P	Power
p	Pressure (bar; Pa)
p_{GT}	Gas turbine contribution to gross power (-)
$\dot{q}$	Heat (W)
r	Radius (m)
R_D	Degradation resistance (Ω)
S	Signal
SM	Surge margin
T	Temperature (K)
u	Flow velocity ($m\ s^{-1}$)
V	Voltage (V)
x	Molar fraction
Δp_{Ej}	Ejector mixing pressure difference
Δp_{rel}	Relative pressure loss
ΔT_{eq}	Difference between actual and equilibrium temperature (K)
ΔT_{LM}	Logartihmic mean temperature difference (K)

Greek Symbols

β	Auxiliary parameter for turbomachinery
γ_{H2}	Molar hydrogen yield per mole fuel

γ_R	Reforming degree
γ_{SC}	Steam to carbon ratio
η	Efficiency
κ	Isentropic coefficient
λ	Stoichiometric air excess ratio
π	Pressure ratio
π_S	Surge pressure ratio
τ	Radiation coefficient

Subscripts

Note: subscripts used for component model variables may relate to ports of the components; see model description.

∞	Ambient conditions
0	Design point
A	Actuating fluid (ejector)
C	Cold
c	Critical cross-section (ejector)
Fu	Fuel
Gr	Gross
H	Hot
I	Induced fluid (ejector)
M	Mixed fluid (ejector)
m	Mixing section (ejector)
man	Manual
max	Maximum local value
MEA	Membrane electrolyte assembly
mean	Arithmetic mean value
min	Minimum local value
n	Nozzle exit (ejector)
Net	Net
o	Outlet (ejector)
rot	Rotating
s	Surge
Scale	Refering to design point on unscaled turbomachinery map
Setp	Setpoint
t	Total

Superscripts

*	Unscaled (turbomachinery)
’	Reduced (turbomachinery)
—	Dimensionless, related to design point

Abbreviations

ADT	Air delivery tube
BFDM	Backward finite difference method
CFDM	Centre finite difference method
DIC	Directly integrated SOFC cycle
DIC-2T	Directly integrated SOFC cycle with two-shaft gas turbine
FFDM	Forward finite difference method
FU	Fuel utilisation
GT	Gas turbine
IIC	Indirectly integrated SOFC cycle
IIR	Indirect internal reformer
LHV	Lower heating value
MEA	Membrane electrolyte assembly
MIMO	Multiple input multiple output
OCV	Open circuit voltage
PR	Pre-reformer
RGA	Relative gain array
SOFC	Solid oxide fuel cell
TIT	Turbine inlet temperature
TOT	Turbine outlet temperature
TPB	Three phase boundary
VIGV	Variable inlet guide vanes

Definitions

Design calculation/mode	Calculation where the design objectives are specified
Design objective	Variable specified during design calculation, i.e. temperature difference in heat exchanger
Design parameter	Variable specified during off-design and dynamic calculation, i.e. length of heat exchanger
Design point	Operation point in where all design objectives are reached and the nominal power is supplied
Design premise	Premise which is not supposed to change during normal operation
Dynamic calculation/mode	Off-design calculation considering time response of the system
Fuel utilisation	Part of the fuel which is utilised in the fuel cell; calculated from current and fuel flow
Gross power	Power produced by SOFC and GT before conversion

Hybrid cycle/system	SOFC and GT system
Ignition (of SOFC)	The instance during startup when fuel is introduced and the SOFC reactions are started
Net efficiency	Net power per lower heating value of the fuel
Net power	Power supplied to the grid
Off-design calculation/mode	Calculation where the system design (i.e. parameters) is specified
Port	Interface for exchange between models
Power turbine	Turbine connected to the generator in the DIC-2T concept
Reforming degree	Reformed methane mole rate per entering methane mole flow rate of one or more reformers
Selector	”Switch” that represents a discontinuity
SOFC system	Components in the SOFC pressure vessel, i.e. SOFC, reformers, ejector, burner, preheat tube
Steam to carbon ratio	Molecules of steam per atom of carbon in the fuel leaving the ejector

1 Introduction

This chapter approaches the topic by giving a short overview over the current situation and challenges of energy economy, followed by a discussion of tasks and trends to cope with these challenges. The role and chances of fuel cells are highlighted. After illumination of the project background, the project is described and structure and guidelines of the report are explained.

1.1 Current Situation and Challenges

The world's primary energy[1] consumption has been increasing steadily since the beginning of the industrial revolution around 1850 (see Figure 1-1). Most of today's energy supply is based on fossil resources. Oil has been the most important source of energy since the 1960s. At present, natural gas is the energy source with strongest growth in use, and it may possibly continue this trend and gradually displace the oil in the current and next decade.

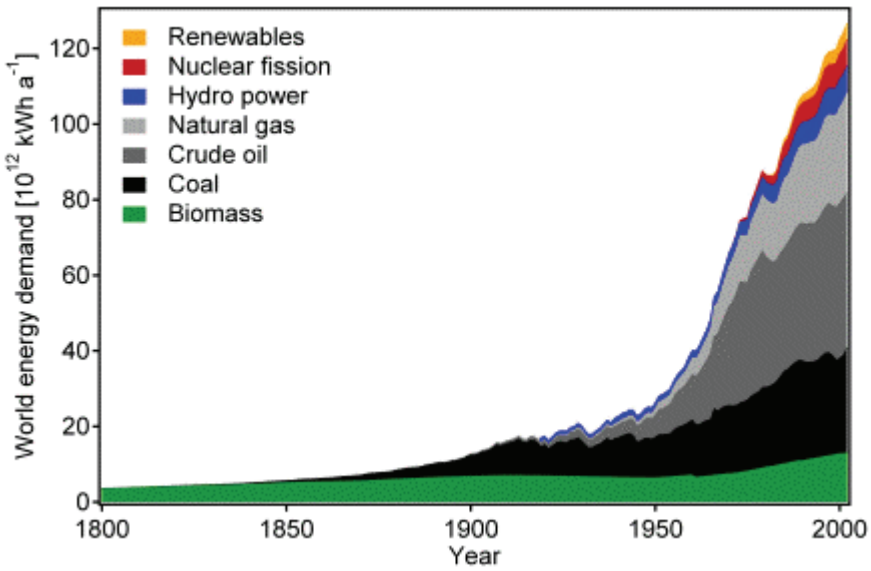

Figure 1-1: World primary energy use [Hydropole 2005]

Fossil energy sources are finite. First of all this means that they will be depleted one day. An even more urgent restriction is, however, that the production effort increases with ever continuing exploitation of a source, because the biggest reservoirs are obviously found and exploited at first. Keeping up or even raising the total production

[1] **Primary energy refers to energy carriers in the shape of their natural appearance; e.g. coal, crude oil, wind**

rates until the last "spill" is impossible [Campbell 2002]. The result is the so-called Hubbert curve[2], which expresses that the production rate of a fossil fuel source is increasing until it reaches a maximum and then decreasing again. Measures that will be taken to stabilise or further increase the production after the peak will only work temporarily and eventually lead to an even steeper decline. This behaviour can be observed for many oil producing countries, as for example the United States, which have reached the production maximum already in the early 1970s [Energiekrise 2005]. Today, many experts and also government representatives are convinced that the global peak in oil production is imminent and will appear during the next five to fifteen years [ASPO 2005]. Already today, the steadily increasing oil price levels indicate that production cannot fully satisfy the world's oil thirst.

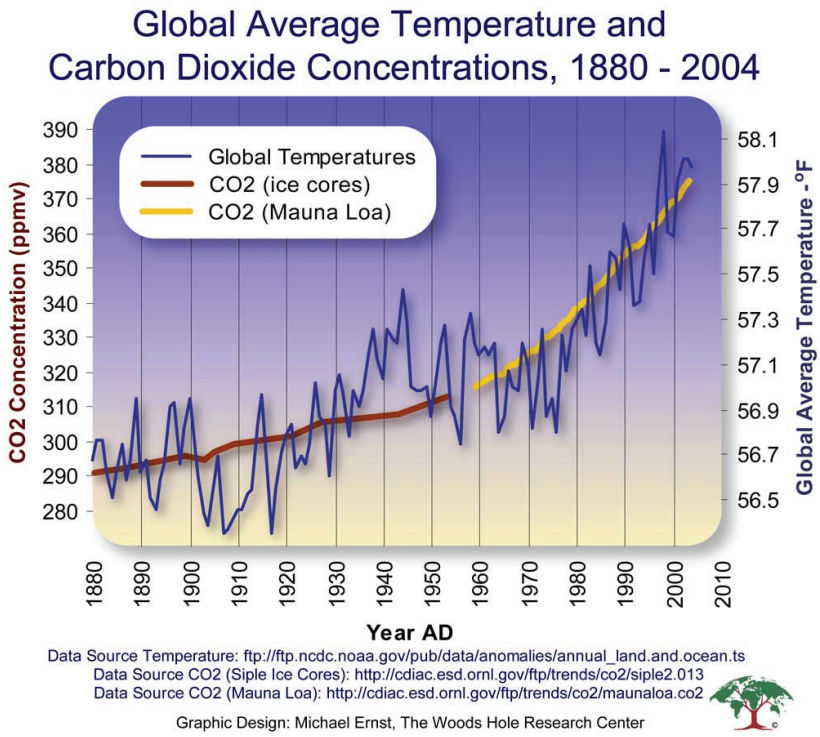

Figure 1-2: CO_2 concentration and global average temperature since 1880 [WHRC 2005]

Yet another problem bound to the use of fossil fuels is the greenhouse effect. Even though not properly provable, most scientists approve that anthropogenic emissions contribute to global warming, and there is high chronological correlation between CO_2 concentration and global average temperature (Figure 1-2). An argument of the opponents of greenhouse theory is that anthropogenic greenhouse gas emissions only make a few percent of the natural emissions. However, this can be enough to displace

[2] **Named after the Dr. M. King Hubbert, Geophysicist [Deffeyes 2005]**

the earth's energy equilibrium. The importance of the magnitude of one percent may become apparent when considering that on a Kelvin temperature scale, one percent temperature increase would already yield app. 3 °C. The direct effect of a higher temperature may be a higher frequency of natural disasters such as floods and storms. Such disasters are already increasing: the reinsurance company Munich Re has recently calculated that following the current trend, the caused damage will exceed the world gross product by 2060 [FÖS 2003].

Concluding, the challenge the energy sector faces today is to move towards more sustainability and security of supply to avoid the worst scenarios. There are many walkable ways towards this goal. Hence there is not yet a reason to despair, but to hit the road!

1.2 Tasks and Trends of the Energy Sector

The means to approximate the goal of a sustainable and secure energy economy may be classified into three groups:

1. Decrease consumer energy demand
2. Increase efficiency of energy conversion
3. Transition to primary energy sources with less carbon content and higher/infinite availability

The first group is generally called "energy saving" and is rather socio-political. The main task is to create a consumer's conscience for rational use of useful energy[3]. This does not necessarily involve a decrease in standard of living, as the possibilities to save energy without even noticing are manifold: Turning off the light and turning down the heating while being away from home is only one example. According to the European Commission's data, total energy end-use consumption in the European Union could be reduced by around 20% without reducing comfort or standards of living [Rothe 2005], and the European Parliament has recently decided a directive for the reduction of consumer energy demand by 11.5% between 2006 and 2015 [EP 2005]. Energy-saving behaviour can be and is being effectuated mainly by educational campaigns. Most governments successfully implement this instrument. However, industry is partially counteracting by promoting for example sports utility vehicles, which consume more fuel than reasonable cars without any measurable benefit for the typical user.

The second group attacks at a higher step in the energy supply chain which is only partially the end user's responsibility, namely the methods of conversion from primary to useful energy. There are several ways for energy conversion; for example electricity from oil can be produced in a gas turbine plant with app. 30% efficiency, or in a combined cycle plant with up to 60%. Furthermore, cogeneration of heat and power

[3] **Useful energy is energy that reaches the consumer; e.g. thermal heat, mechanical work.**

concepts improve the energy efficiency as they allow for utilisation of the waste heat which is inevitable in thermal power cycles. This is especially facilitated by distributed generation plants situated close to heat and power consumers. An example for conversion from secondary[4] to useful energy is electric heating by either a standard electric oven or a heat pump which provides the same heat at app. 50% less power consumption.

The latter conversion step is usually the end user's responsibility and can be influenced through governmental stimulation programmes, as for example grants on the purchase of innovative technology. Conversion from primary to secondary energy is usually performed in industrial scale and can be influenced through economic measures such as regulation of primary energy prices or the newly introduced emission trading system.

The third group is finally the shift of the primary energy carriers. Since the industrial revolution, "decarbonisation" of primary energy has been advancing by the gradual shift from coal to oil and now from oil to gas. Following this trend, future energy carriers would thus involve even less or no fossil carbon at all, which at the same time is mitigating greenhouse gas emissions. Carbon-free primary energy sources at our disposal are renewable[5] and nuclear energy. Even though the latter is CO_2-free, its sustainability is strongly questionable due to nuclear waste and the risk connected to it. For the transition phase, a further possibility can be to make conventional fuels CO_2-neutral by capturing and storing the CO_2. Secondary CO_2-neutral energy carriers are based on electricity, hydrogen and biofuels.

The task to move towards a CO_2-neutral energy economy is a long-term and expensive process, but also the only possible path which leads all the way to the final goal of a sustainable and secure energy economy. Hence, it is necessary today to develop and demonstrate the technology and construct the political and socio-economical road maps towards this goal. At the same time, the previously mentioned methods are required to decrease the total amount of primary energy in need of replacement and therewith the costs.

1.3 Role of Fuel Cells and Fuel Cell Hybrids

Fuel cells are electrochemical energy converters and do not underlie the Carnot efficiency law in practice[6]. They offer high electric efficiency (a typical value is 50%, based on LHV) as well as low noise and emission levels and are arbitrarily scaleable. Disadvantages are the high system costs, low fuel flexibility (premium fuel is hydrogen) and sensitivity to impurities. Power generation sectors where an impact of the

[4] **Secondary energy is primary energy processed for its final use; e.g. electricity, fuel, heating oil.**

[5] **Biomass is not literally carbon-free, but representing a closed carbon loop from growth to use**

[6] **In theory, fuel cells do underlie the Carnot law; however, the upper process temperature is "virtual" and does not occur anywhere in the process [Halseid 2004].**

different types of fuel cells is expected, are portable (electronic devices, small power supplies), mobile (transportation) and stationary (power generation). In the portable sector, fuel cells compete with batteries, and their main benefit is quick refuelling and the potential of achieving high energy density. For mobile applications, they compete with internal combustion engines. The main benefits of fuel cells here are increased efficiency, especially in part-load operation which is predominant in vehicle propulsion, as well as reduction of emissions and noise. In stationary power production, fuel cells have the advantage that they are scaleable and achieve high efficiencies and low emissions even at very small scale. If high temperature fuel cells are applied, carbon containing fuel may be utilised directly or in combination with reformers. Application possibilities of these fuel cells range from heat and power supply for private houses to medium-scale power generation. From a scale of app. 100 kW, they further facilitate the combination with a bottoming thermal power cycle in a so-called hybrid cycle. With up to 70% based on LHV, this method promises higher electric efficiencies than any other electricity generation process at present.

Fuel cells are therewith a promising innovation for achieving an improvement in energy conversion efficiency and flexibility as well as to prepare the transition to carbon-free energy carriers.

1.4 Project Background

Since the beginning of oil production, Norway is focussing on energy related research and especially environmental technologies. A bibliographic analysis of Norwegian hydrogen and fuel cell related research activities was performed by Godø et al. [2003]. It revealed that the solid oxide fuel cell (SOFC) is an especially strongly represented topic in Norwegian research since the early 1990s.

The current PhD project was integrated into a joint demonstration project of the industrial actors Statkraft, Shell Technology Norway and Aker Kværner, called the *Kollsnes* project. The feasibility of a Multi-MW, CO_2-free, SOFC-based demonstration plant at the Kollsnes gas terminal (close to Bergen) should be studied. The plant should use natural gas from the Troll field as a primary energy source [Godø 2003]. Furthermore, a membrane based burner for CO_2 separation and a hybrid cycle should be included in the cycle. The fuel cell system should be provided by Siemens-Westinghouse, who at that time had successfully proven the long term operation of a tubular stack [Bellona 2002]. NTNU should provide research and developmental support for the project.

In 2002, different burner concepts were investigated and technical problems were discovered. Furthermore, the additional costs of CO_2 capture to the already expensive SOFC technology were high, and the highly efficient and natural gas powered plant had comparatively low relative CO_2 emissions already without capture. Gradually, the focus was changed from a zero-emission to a low-emission concept where only 80 to 90% of the CO_2 is captured. When Siemens-Westinghouse turned out to have

problems with their stack development, it was decided to interrupt the ambitious project until these more fundamental problems were solved. A reconsideration of the project is planned for 2006 [Bakke 2004]. The granted PhD scholarships at NTNU were, however, not affected by this project interruption.

1.5 Project Description

1.5.1 Rationale

The project is targeted at the investigation of a SOFC/GT hybrid cycle, a power plant cycle promising very high electric efficiency. Even though first demonstration plants haven proven the general feasibility of such systems, many challenges connected with load change and part-load operation persist. Before such a system can take up normal operation, critical phenomena that can appear such as carbon deposition in the fuel cell or compressor surge must be prevented effectively by a suitable operation and control strategy. The current work shall help to analyse and understand the nature of hybrid systems, improve knowledge on critical incidents and their appearance and give recommendations on optimum process parameters and control design.

1.5.2 Objectives

- Develop a computational model for the simulation of the mentioned system able to predict load characteristics as well as transient behaviour.
- Gain knowledge on part-load performance, load-varying characteristics and startup methods of the mentioned system.
- Optimisation of the mentioned system.
- Gain knowledge on controllability and optimum control designs in order to achieve safe operation.

1.5.3 Practical Relevance

Implications for the Norwegian industry involve:

- Use of the SOFC/GT technology for power and heat production on gas and oil platforms.
- Use of SOFC/GT technology in ship propulsion and/or electricity supply (for example in cruise ships).
- Use of SOFC/GT technology in remote areas where grid maintenance and future upgrading becomes expensive and less feasible in a deregulated market.
- Demonstration plants near or at large gas terminals (Kollsnes, Kårstø, Tjeldbergodden), may be attractive to international companies due to existing

infrastructure and in general public awareness and interest for new energy technologies.

1.6 Thesis Structure and Guidelines

The contents of the thesis are organised in 9 chapters. The subsequent chapters have the following content and purpose:

- Chapter 2 briefly introduces the components of SOFC/GT hybrid systems. Focus is on working principles, design options and operational characteristics and issues connected to the specific components.
- Chapter 3 presents an overview of SOFC and hybrid cycle modelling in open literature. Firstly, requirements on process modelling in general are formulated. Next, purposes for modelling of SOFC hybrids and their requirements to the models are discussed. Then, the main approaches to SOFC modelling found are presented and discussed. Important issues therein are geometry, spatial distribution, reaction kinetics and electric resistance, heat conduction as well as simulation environments and solving methods. Moreover, hybrid cycle models are presented with regard to cycle layout and modelling approaches and currently active groups in hybrid cycle modelling are highlighted.
- Chapter 4 introduces the component models which serve as a "toolbox" for the modelling of SOFC/GT hybrid cycles. First, the common environment and premises for the whole toolbox are introduced. A structure for mathematical model description is introduced for clarity and quick comprehension. Subsequently, all models are explained sequentially in order of decreasing complexity. The chapter shall describe the models in a way to allow reproduction by experienced modellers. However, due to the complexity of the work, only the mathematical elements of the models are described, but no detailed comments on implementation are provided.
- Chapter 5 describes models for different hybrid cycle configurations to be investigated. The hybrid cycle models make use of the model toolbox from Chapter 4 and further provide performance and parameters for the system. Basics for operation are discussed. Requirements for system design are derived with respect to performance and safety. Interactions between design objectives and parameters are detected, and a set of objectives for the directly integrated cycle is developed.
- Chapter 6 is dedicated to design, operation and control of the directly integrated SOFC cycle, which is regarded as the standard hybrid cycle. The subchapters comprise:

  - Chapter 6.1 presents the design case as defined through the chosen set of design parameters and objectives in Chapter 5 together with the key system parameters.
  - Off-design behaviour, i.e. the system at part-load, is investigated in Chapter 6.2. Strategies for part-load operation are discussed and a suitable strategy is chosen. Operation boundaries with respect to safety are given, and part-load performance within the valid boundaries is visualised. A suitable steady-state operation line is chosen.
  - Chapter 6.3 derives a control strategy that is required to implement the steady-state operation line to a dynamic system. The control strategy hence determines the way the system proceeds from one operation point to another. Requirements for a suitable control strategy are defined. Based on a system analysis, a control layout is proposed and the response to various transient processes is investigated.
  - Chapter 6.4 highlights the issues that can occur during shutdown and startup. Extra equipment required to address these issues is introduced. Sequences for shutdown and startup are proposed and the system response to the execution of these is highlighted.
  - Chapter 6.5 is dedicated to the fuel flexibility of a methane-designed DIC system. It discusses necessary modifications depicts the changed design objectives, part-load behaviour and control response when hydrogen or ethanol is used as fuel.

- Chapter 7 discusses two alternatives to the standard directly integrated SOFC cycle, namely the latter with two-shaft gas turbine and a cycle with indirect integration of the SOFC. Adaptations in system design for achieving comparable operation conditions are discussed. Steady-state part-load performance is investigated and compared to the standard cycle, and the differences in controllability are discussed.
- Chapter 8 summarises the conclusions and gives recommendations for further work.

The chapters are mainly based on their preceding ones. Consistency of the model parameters is emphasised; all component model parameters mentioned in later chapters are defined in Chapter 4, while the hybrid system parameters can be found in Chapter 5. Chapters 7 applies the design, part-load and control strategies derived in Chapter 6, and the two chapters follow up on the system safety issues introduced in Chapter 5.

1.7 Papers Published During Thesis Work

1.7.1 Journal Papers

The following journal papers originate from the thesis work and can be found in the appendix:

Paper I

Stiller, C., Thorud, B., Seljebø, S., Mathisen, Ø., Karoliussen, H., Bolland, O., *"Finite-volume modeling and hybrid-cycle performance of planar and tubular solid oxide fuel cells"*, Journal of Power Sources 141 (2005) 227–240.

The paper describes two 2D steady-state models for SOFC with planar and tubular geometries fuelled by methane. The fuel cell models have been written in FORTRAN and implemented into PRO/II for hybrid system simulation. The influences of pressure ratio, air inlet temperature, air flow rate and anode gas recycling are investigated in a parameter study. For both designs air flow rate and pressure ratio are the most important parameters considering the system performance, but for the tubular system these parameters have less impact than for the planar design. Based on the parameter study, a near-optimum case is defined specifically for both systems and the conditions in the fuel cells are investigated. The cycle balance is different in both systems, as the tubular fuel cell requires a lower air inlet temperature. Both fuel cell systems achieve above 65% electric efficiency.

The author contributed to this paper by co-advising the modelling and simulation process, interpreting the results and writing.

Paper II

Stiller, C., Thorud, B., Bolland, O., *"Safe dynamic operation of a simple SOFC/GT hybrid system"*, ASME Turbo Expo 2005, Reno-Tahoe, USA, 6-9 June 2005, Paper 2005-GT-68481. Accepted for publication in ASME Journal of Engineering for Gas Turbines and Power, anticipated April 2006.

This paper shall prove the feasibility and show methods to safely operate a simple SOFC/GT hybrid system under part-load and load change. Dynamic and steady-state studies on a detailed model of a SOFC/GT hybrid system have been performed[7]. A design point is selected. Steady-state part-load behaviour is shown by means of performance maps. An operation line with fairly constant temperatures in the upper part-load regime and an almost constant efficiency down to app. 25% part-load is proposed and the dynamic behaviour of the system on rapid load changes is investigated. Strategies for the dynamic controlling of power by manipulating fuel flow are shown that might enable the system to adapt to a new setpoint power quite quickly.

[7] **Paper II is based on a predecessor of the model presented in this thesis (e.g. different gas turbine characteristics, constant mixing ratio ejector).**

The author elaborated the conception of the paper, performed the simulation work and result interpretation, wrote and presented the paper.

Paper III

Stiller, C., Thorud, B., Bolland, O., Kandepu, R., Imsland, L., *"Control strategy for a solid oxide fuel cell and gas turbine hybrid system"*, Journal of Power Sources, in press (available online).

Paper III presents a multi-loop control strategy for a SOFC/GT hybrid system. A detailed dynamic model of the system is presented and its part-load performance is studied[8]. The control objectives are discussed, with the main issue being a fairly constant fuel cell temperature under all conditions. Based on the system configuration and part-load performance, input and output variables of the control system are detected. Control cycles are introduced and their design is discussed. The responses of the resulting system on load changes, external disturbances as well as malfunction and degradation incidents are investigated. The system is stable under all incidents. An error in fuel flow measurement or assumed fuel quality provokes a steady-state fuel cell temperature offset. For a degraded system, it may be advisable to readjust the control system to the new characteristics. The author elaborated the conception of the paper, performed the simulation work and result interpretation and wrote the paper.

Paper IV

Nakajo, A., Stiller, C., Härkegård, G., Bolland, O., *"Modeling of thermal stresses and probability of survival of tubular solid oxide fuel cells"*, Journal of Power Sources, in press (available online).

In Paper IV, the temperature profile generated by a thermo-electro-chemical model was used to calculate the thermal stress distribution in a tubular SOFC. The solid heat balances were calculated separately for each layer of the MEA (membrane electrode assembly) in order to detect the radial thermal gradients more precisely. It appeared that the electrolyte undergoes high tensile stresses at the ends of the cell in limited areas and that the anode is submitted to moderate tensile stresses. A simplified version of the widely used Weibull analysis was used to calculate the global probability of survival for the assessment of the risks related to both operating points and load changes. The cell at room temperature was considered and revealed as critical. As a general trend, the computed probabilities of survival were too low for the typical requirements for a commercial product. A sensitivity analysis showed a strong influence of the thermal expansion mismatch between the layers of the MEA on the probability of survival. The lack of knowledge on mechanical material properties as well as uncertainties about the phenomena occurring in the cell revealed itself as a limiting parameter for the simulation of thermal stresses.

---

[8] The model Paper III is based on is principally equal to the model in this thesis; however, the thesis contains design adaptations and a refined control strategy.

The author originated and supervised the diploma thesis performed by Arata Nakajo. Furthermore, the author was involved in the result interpretation and compilation as well as in writing the paper.

1.7.2 Conference Papers

Besides the journal papers, the author has contributed to the following papers:

- Stiller, C., Mathisen, Ø., Seljebø, S., Bolland, O., Karoliussen, H., Thorud, B., *"Simulation-based comparison of combined SOFC/GT cycles with flat-plate and tubular fuel cell models"*, Fuel Cell Seminar, Miami, 2003.

The paper represents an extended abstract of the steady-state analyses carried out in Paper I. The author has written and presented it.

- Thorud, B., Stiller, C., Weydahl, T., Bolland, O., Karoliussen, H., *"Part-load and load-change simulation of tubular SOFC systems"*, 6th European Solid Oxide Fuel Cell Forum, Lucerne, Switzerland, 2004

This paper is the first publication of the dynamic SOFC model, but at an early stage where yet no gas turbine is included. The main achievements of the paper are the presentation of novel steady-state performance maps based on the system inputs and the presentation of dynamic results for load changes with the SOFC model. The author contributed with the idea of the performance map display and further with performing simulations and compiling results.

- Kemm, M., Stiller, C., Selimovic, A., Thorud, B., Torisson, T., Bolland, O., *"Transient behaviour of tubular and planar SOFC systems"*, Ninth International Symposium on Solid Oxide Fuel Cells (SOFC-IX), Quebec City, Canada, 2005.

The paper detects particularities of tubular and planar cell geometries at transient operation. This has been achieved by investigating the thermal and electrochemical performance of a planar and a tubular cell at different operation modes, i.e. load change, startup, and shutdown. The comparison of relaxation times and transient temperature gradients within the cell as well as the transients of the power density are presented and discussed. Relaxation times for different processes are shorter for the planar geometry, caused by its compactness. However, due to its longer spatial extension the tubular geometry is more advantageous concerning the level of temperature gradients within the cell. Shutdown and startup relaxation time is similar for both geometries. The author performed the simulations for the tubular SOFC, evaluated and compiled the results in equal collaboration with the main author and furthermore assisted in writing.

- Kandepu, R., Imsland, L., Foss, B.A., Stiller, C., Thorud, B., Bolland, O., *"Control-relevant modelling of a SOFC/GT hybrid system"*, 18th International Conference on Efficiency, Cost, Optimization, Simulation and Environmental Impact of Energy Systems, ECOS, Trondheim, Norway, 2005.

In this paper, a dynamic, lumped SOFC model is described, as a step towards developing control-relevant models for a SOFC integrated in a gas turbine process. Several such lumped models can be aggregated to approximate the distributed nature of important variables of the SOFC. The model is evaluated against a distributed dynamic tubular SOFC model. The simulation results confirm that the simple model is able to capture the important dynamics of the SOFC. It is concluded that the simple model can be used for control and operability studies of the hybrid system.

The author contributed to this paper with supplying a spatially distributed model to compare with the lumped model as well as advising the main authors.

- Kandepu, R., Imsland, L., Stiller, C., Foss, B.A., Kariwala, V., *"Control-relevant modeling and simulation of a SOFC-GT hybrid system"*, Scandinavian Conference on Simulation and Modeling, SIMS, Trondheim, Norway, 2005.

In this paper, control-relevant models of the most important components in a SOFC-GT hybrid system are described. Dynamic simulations are performed on the over all hybrid system. The model is used to develop a simple control structure, but the evaluation shows that more advanced control is needed.

The author contributed to this paper through discussions with the main authors.

1.8 Collaboration and Author's Contribution

A great part of the PhD project was accomplished in collaboration with another PhD student, Bjørn Thorud, who defended his thesis 12 October 2005 [Thorud 2005]. Thorud started to develop a SOFC model app. one year before the author took up his project. When the author had approached the topic, both PhD students were closely collaborating in improving and extending the models. Several papers were produced to publish results with the respective current status of the model. For the dissertations, it was agreed that Thorud should focus on model development, sensitivity analyses and investigation of the dynamic behaviour of the uncontrolled model. The author extended the model by the off-design ejector model and the dynamic indirect internal reformer (see Chapter 4.8 for the author's contribution to modelling), which beside unlike design points are the main difference between the models in the thesis reports. He furthermore developed and evaluated a control strategy without the influence of Thorud. Further main contributions of the author are the performance visualisation maps and the evaluation of shutdown and startup procedures, fuel flexibility and cycle options.

2 Technological Background

The following chapter briefly introduces the components of SOFC/GT hybrid systems. Focus is on working principles, design options and operational characteristics and issues connected to the specific components. The modelling of the latter will be described in Chapter 4.

2.1 Solid Oxide Fuel Cell

The solid oxide fuel cell is the core technology of the investigated system. In the following, its basic working principle is briefly introduced. Furthermore, materials and manufacturing techniques will be described and an overview over current cell and stack design options is provided. For further information it is referred to text books on fuel cells [Larminie 2000; Singhal 2003a]

2.1.1 Fundamentals

The fuel cell effect has first been described by the Christian Friedrich Schönbein in 1839. Some years later, Sir William Grove built the first practical fuel cell. The SOFC technology, however, dates from Walther Nernst, who around 1890 discovered that stabilised zirconia[9] is an isolator at room temperature, but turns into an ionic conductor between 600 and 1000 °C and an electronic and ionic conductor around 1500 °C. The first solid oxide fuel cell based on zirconia was introduced by Baur and Preis in 1937 [Singhal 2003b]. Since then, research on SOFC has been steadily increasing until today. With zirconia remaining the key material, first units have left the lab for prototype and field testing. However, market readiness is still not achieved.

The main characteristics of the solid oxide fuel cell are its solid-phase oxygen-ion conducting electrolyte and its high operation temperature. Due to the latter, it is less vulnerable for carbon and fuel impurities and suitable for combination with bottoming thermodynamic cycles.

Incidents that must be avoided are exposure to sulphur which poisons the anode catalyst and the exposure of the anode towards oxygen which leads to a reoxidation of the catalyst. The latter must be in a reduced state for operation. A further risk is carbon deposition in the fuel channel.

Electrochemistry

Figure 2-1 shows the working principle of the SOFC. Not shown here is the so-called *interconnect* which electrically connects many cells in a serial circuit to increase the voltage and in planar configurations at the same time contains the flow field and separates the flow of adjacent cells.

[9] **Stabilised zirconia (ZrO_2): zirconium oxide doped with calcia, magnesia, yttria, etc.**

The reactions occur at the three phase boundary (TPB) where the gas meets electrode and electrolyte material. The reaction occurring at the cathode TPB is

$$\tfrac{1}{2}O_2 + 2e^- \Rightarrow O^{2-}$$ **Equation 2-1**

while the following reactions may occur at the anode TPB:

$$H_2 + O^{2-} \Rightarrow H_2O + 2e^-$$
$$CO + O^{2-} \Rightarrow CO_2 + 2e^-$$ **Equation 2-2**

The oxygen ions are conducted through the electrolyte, while the electrons are conducted through an external electric circle.

The overall reactions are

$$H_2 + \tfrac{1}{2}O_2 \Rightarrow H_2O$$
$$CO + \tfrac{1}{2}O_2 \Rightarrow CO_2$$ **Equation 2-3**

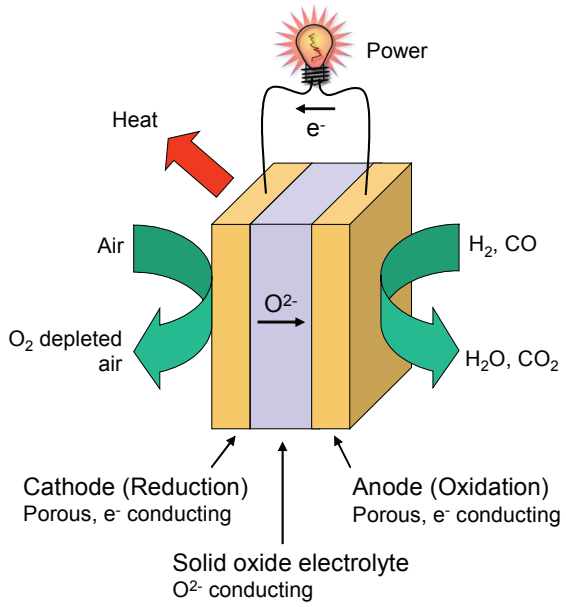

Figure 2-1: Electrochemical principle of the SOFC

In case of the hydrogen reaction (carbon monoxide analogous), the reversible voltage potential that may be supplied by the electrodes is given through the Nernst equation:

$$E^{rev} = E^0 + \frac{RT}{2F}\ln\left(\frac{p_{H_2} \cdot p_{O_2}^{1/2}}{p_{H_2O}}\right)$$ **Equation 2-4**

with the partial pressures p in bar. E^0 is the potential at standard pressure and is determined by

$$E^0 = -\frac{\Delta \bar{g}_f^0}{2F}$$ **Equation 2-5**

where $\Delta \bar{g}_f^0$ is the change in molar Gibbs free energy of formation at standard pressure and at the actual operation temperature for the overall reaction (**Equation 2-3**).

The reversible potential E^{rev} is the maximum voltage that the fuel cell may deliver theoretically at given flow conditions. **Equation 2-4** also indicates that not all the hydrogen can be utilised electrochemically, as E^{rev} approaches negative infinity for zero partial pressure of hydrogen. The fraction of utilised hydrogen divided by hydrogen supplied is called the fuel utilisation (FU). For methane fuel, it may be expressed as

$$FU = 1 - \frac{4 \cdot \dot{n}_{CH_4,out} + \dot{n}_{CO,out} + \dot{n}_{H_2,out}}{4 \cdot \dot{n}_{CH_4,in} + \dot{n}_{CO,in} + \dot{n}_{H_2,in}}$$ **Equation 2-6**

with the inlet and outlet molar flows of the methane, carbon monoxide and hydrogen, assuming no higher hydrocarbons reach the cell. Note that one mole of methane is turned to four moles of hydrogen by complete reforming.

The maximum theoretical electric efficiency of the fuel cell, based on the utilised fuel is hence

$$\eta_{el,max} = \frac{E^{rev} \cdot 2F}{\left|\Delta \bar{h}_f\right|}$$ **Equation 2-7**

where $\Delta \bar{h}_f$ is the change in molar enthalpy of formation for the overall reaction (Equation 2-3). Two values for $\Delta \bar{h}_f$ exist, depending upon whether the products will be in liquid or gaseous state. The former is called the "higher heating value" (HHV) and the latter the "lower heating value" (LHV). It is common to give efficiencies based on LHV.

Losses

If a current is flowing, the voltage supplied at the electrodes will be different from the reversible potential due to losses. The reversible potential is therefore also called "open circuit voltage" (OCV). The dependency of these losses on temperature, current density and species concentrations mainly determine the characteristics of a fuel cell. Three main mechanisms of voltage losses exist:

- **Activation or polarisation losses**: At open circuit, no outer current is flowing. However, reactions are still taking place, but at equal rates in both directions. Just regarding the current which flows into one of the directions, we find the "exchange current density". In order to achieve an outer current higher than this, an extra potential is required to achieve the desired reaction rate, called activation

voltage. The voltage drop is increasing fast at low reaction rates and is from a certain level almost constant. Activation is the dominant source of loss for low-temperature fuel cells, while their influence is smaller for SOFCs.

- **Ohmic losses**: Ohmic losses occur due to the resistance along the flow paths of electric and ionic current. At a given temperature and geometry, the voltage loss is proportional to the current.
- **Diffusion or concentration losses**: Reactants must flow through the porous electrodes to the TPB, and products must flow into the other direction, driven by diffusion. This implies that the concentration of reactants at the TPB is lower and the concentration of products is higher than in the bulk phase. Using TPB instead of the bulk concentrations in **Equation 2-4**, the calculated potential will be lower and the difference is called diffusion or concentration losses. The voltage drop increases with increasing current against an asymptotic maximum current. At this point, the concentration of one of the reactants at the TPB is zero and no further current increase is possible.

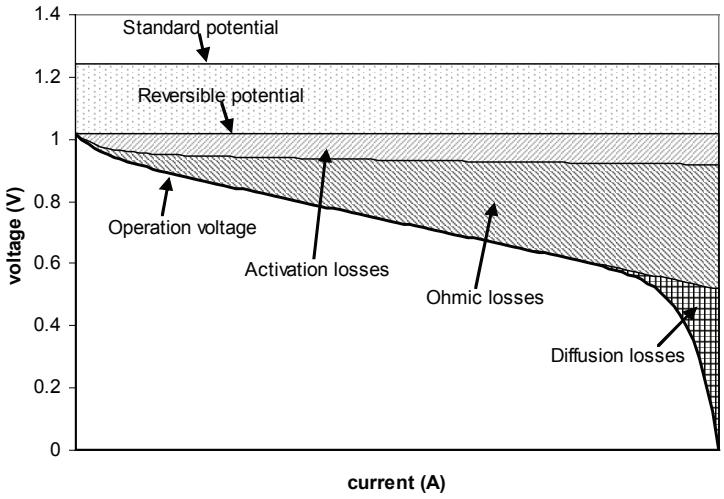

Figure 2-2: Overview of voltage losses

Figure 2-2 shows the qualitative dependency of the losses on the current.

Reforming

A great advantage of the SOFC is its possibility for internal reforming of hydrocarbon fuel. Sulphur-free natural gas (mainly a mixture of the alkanes methane, ethane and propane), which is technically available today, may be used as fuel. Due to the high temperature and the existence of nickel as a catalyst at the anode, the fuel cell reforms

the alkanes to hydrogen and carbon monoxide internally through the steam reforming reaction

$$C_nH_{2n+2} + nH_2O \Leftrightarrow (2n+1)H_2 + nCO\,. \qquad \textbf{Equation 2-8}$$

The equilibrium of this reaction is at the right hand side for elevated temperatures. As the reforming reaction is strongly endothermic, it severely decreases the temperature where it takes place in the fuel cell and therewith the local current density. To mitigate this effect but still provide internal cooling, pre-reformers are often designed to reform only a fraction of the fuel (usually 30% - 50%) before it enters the fuel cell.

The carbon monoxide product is either directly oxidised or converted to hydrogen through the water gas shift reaction

$$CO + H_2O \Leftrightarrow CO_2 + H_2\,. \qquad \textbf{Equation 2-9}$$

The latter is a quick equilibrium reaction. In equilibrium, the both reactions from **Equation 2-3** have the same change in Gibbs free energy and therewith the same reversible potential. As the reaction kinetics and diffusion are faster for hydrogen, it is fair to assume that the latter will dominate the electrochemical reaction.

2.1.2 Materials and Production

Materials and fabrication methods are the key issue of SOFC research. The following section introduces briefly the state of the art and the trends of SOFC materials and fabrication.

The materials must fulfil different requirements:

- **Electric and mechanical performance**: The ionic conductivity of the electrolyte and the electronic conductivity of the electrodes and the interconnect must be high enough to facilitate efficient operation. At the same time, the electrolyte must have a very low electronic conductivity in order to avoid internal short-circuiting. Furthermore, the electrolytes must possess high permeability for the reaction gases while the electrolyte and interconnect must be impermeable.
- **Chemical stability**: All SOFC components must remain chemically stable across the desired lifetime. Critical phenomena are especially reoxidation of the anode and micro-structural changes in the TPB due to interdiffusion.
- **Mechanical stability**: The high temperature operation in combination with dissimilar thermal expansion coefficients imposes high mechanical stresses on the materials. Due to the brittleness, micro-cracks and delamination are likely to appear where the stresses are highest. These incidents lower the electric performance of the fuel cell and must be minimised by choice of materials, production and operation methods.

- **Inexpensive production and processing**: In order to penetrate the market, it is important that the materials and processing methods are inexpensive and reproducible and may be scaled up from lab to industrial scales.

Electrolyte

Because of its high ionic conductivity, chemical stability and economic availability, the "standard" electrolyte material today is zirconia (ZrO_2) doped with about 8-10 mole percent of yttria (Y_2O_3), yielding the so-called *yttria stabilised zirconia* (YSZ) [Singhal 2003b]. Doping is required to stabilise the desired ionic conducting tetragonal lattice structure, which in pure zirconia is exhibited above 1170°C, for temperatures down to ambient level. Other dopants such as bismuth oxide, promise higher ion conductivity, but also problems like higher electron conductivity and costs [Ishihara 2003]. YSZ requires temperatures above 800-900°C for achieving suitable ion conductivity. Electronic conductivity increases with decreasing partial pressure of oxygen, although the values are sufficiently low for technically occurring oxygen partial pressures. YSZ is generally chemically stable, but above 1200°C it reacts with cathode material to form insulating layers at the boundary which decrease the electrical performance [Yokohawa 2003].

Anode

The anode's main tasks are to conduct electrons, to permeate gases to the TPB and to provide the catalyst for fuel oxidisation and possibly hydrocarbon reforming. The most commonly used material is a cermet[10] of nickel (Ni) and YSZ. Nickel is the catalyst for the reforming reaction and at the same time it facilitates electron conductivity, while YSZ is the support material which is introduced to adjust the thermal expansion coefficient to the electrolyte material. Furthermore, its ionic conductivity expands the electrochemical reaction zone. For suitable properties, at least 30 mole percent of nickel is required. In order to achieve the required porosity, anodes are today usually manufactured from nickel oxide (NiO) and YSZ. NiO is then "in situ" reduced to Ni. This decreases the volume and hence creates pores. The latter is called *activation* and this method was first described by Spacil [McEvoy 2003]. Nickel tends to recombine and therewith lower the surface and porosity. A challenge of the production method is therefore to achieve an even distribution of Ni particles.

Cathode

The cathode must mainly provide electrical conductivity, gas permeability, catalytic activity for oxygen reduction as well as chemical and mechanical compatibility with other SOFC components. Beside platinum which is expensive, perovskites[11] are applicable. Today's standard material is lanthanum manganite ($LaMnO_3$) doped with

[10] **Cermet: composite material composed of ceramic and metallic materials**

[11] **Perovskite: Group of crystals with the same structure of $CaTiO_3$, following the pattern ABO_3**

strontium (LSM). The mole ratio of strontium (Sr) and lanthanum (La) decides the catalytic as well as the mechanical properties of the material. Cathodes are prevalently produced by powder processing. As the cathode performance strongly depends on surface area, porosity and microstructure, the processing method is very important. Except the above mentioned high temperature reactions with the electrolyte, LSM is chemically very stable, as long as no chromia forming metallic interconnects are being used [Yokokawa 2003].

Interconnect

The interconnect must maintain its features of high electronic conductivity, low permeability (in planar design) and chemical stability in both oxidising and reducing atmosphere. For the usual operating range of 900-1000°C, these features can be provided by perovskite-type oxide ceramics based on rare earth chromites. For lower temperatures, metallic alloys are suitable. $LaCrO_3$ doped with app. 10 mole percent strontium is the most common configuration today, as it merges high electronic conductivity with a thermal expansion coefficient close to the other components [Anderson 2003].

Seals

Sealing of SOFCs is a very critical task, as the sealing material must be stable in oxidising and reducing atmospheres and be compatible with the SOFC materials. Today, gaskets made of cements, glasses and glass-ceramics are applied. Another type of sealing is to apply mechanical loads to compress the cell components to form a seal, even though at the risk of leakage by uneven surfaces and high mechanical stress [Kendall 2003]. While tubular cells are practically seal-less, sealing is still representing a main problem for planar cells. Seal-less designs are also being investigated [Momma 2005].

Trends in Material Development

The trend in material development is clearly heading towards lower temperature operation. The main task is to achieve an acceptable electric performance at a reduced temperature level of around 700-800°C. This can be achieved either by thinner YSZ electrolytes or new electrolyte materials with lower ionic resistivity. Benefits are the reduced cell degradation due to high-temperature effects, the possibly application of metallic interconnects (hence better heat conduction and reduced thermal stress problems) and the higher efficiency due to higher reversible potential as well as the prospect of lower material and production costs.

Cell Fabrication

The suitable cell fabrication method is strongly depending on the cell design. Generally, fabrication methods are based on the particulate approach or the deposition approach for the electrolyte. The particulate approach comprises

compaction of ceramic powder into cell components and densification at high temperatures. Examples of the particulate approach are tape casting and tape calendering. The deposition approach on the other hand comprises formation of the cell components on a support by a chemical or physical process, such as chemical vapour deposition, plasma spraying or spray pyrolysis [Kendall 2003].

All these processes are applied for planar SOFCs. The tubular SOFC of Siemens-Westinghouse is manufactured by extrusion of the cathode tube and electrochemical vapour deposition of electrolyte and anode [Singhal 2000].

2.1.3 Cell and Stack Design

In SOFC design, many degrees of freedom exist in the three levels of the membrane-electrode assembly (MEA), the single cell design and the stacking. The following section briefly describes and discusses the most common designs.

Membrane Electrolyte Assembly (MEA)

In general, thin layers are required in the MEA in order to reduce the losses through ionic and electric conduction and gas diffusion. Thicknesses in the magnitude of 10 μm are common. In order to achieve a mechanically stable assembly, however, a thicker support is required. In a self-supporting configuration, one of the layers (anode, electrolyte or cathode) acts as the structural support, while in an external supporting configuration, the thin cell layers are supported by the interconnect or a porous substrate. An electrolyte supported configuration (electrolyte thickness >100 μm) requires higher operation temperatures in order to reduce ohmic losses in the electrolyte. On the other hand, if an electrode acts as support, the temperature may be lower, but the electrode mass transport will be slower, leading to higher diffusion losses. Interconnect and porous substrate supports allow for thin cell components, but impose limitations to the flow field design respectively add complexity to the configuration due to addition of new materials [Kendall 2003].

Cell Geometry

Many different cell configurations have been studied for the time being. The most important requirements to a cell design are [Kendall 2003]:

- **Electrical performance**: The ohmic losses should be low. Short current paths as well as sufficient contact areas are means to provide this.
- **Electrochemical performance**: High reversible voltage and low activation losses can be achieved through good separation of the gas flows, avoidance of electrical shortcuts and a uniform gas distribution across the cell.
- **Thermal management**: Sufficient cooling and uniform temperature distribution across cell and stack are required. The design must allow for efficient cooling and appropriate gas flow configuration and withstand the expected thermal stresses.

- **Mechanical strength and compactness**: The design should be strong enough to be easily assembled and handled. Furthermore, it should be compact and stackable to allow for a high power density.

Generally, cell designs can be divided into two groups: planar and tubular. Typically, planar cells have a higher volumetric power density and better electrical performance, while tubular cells have fewer problems with sealing and temperature gradients.

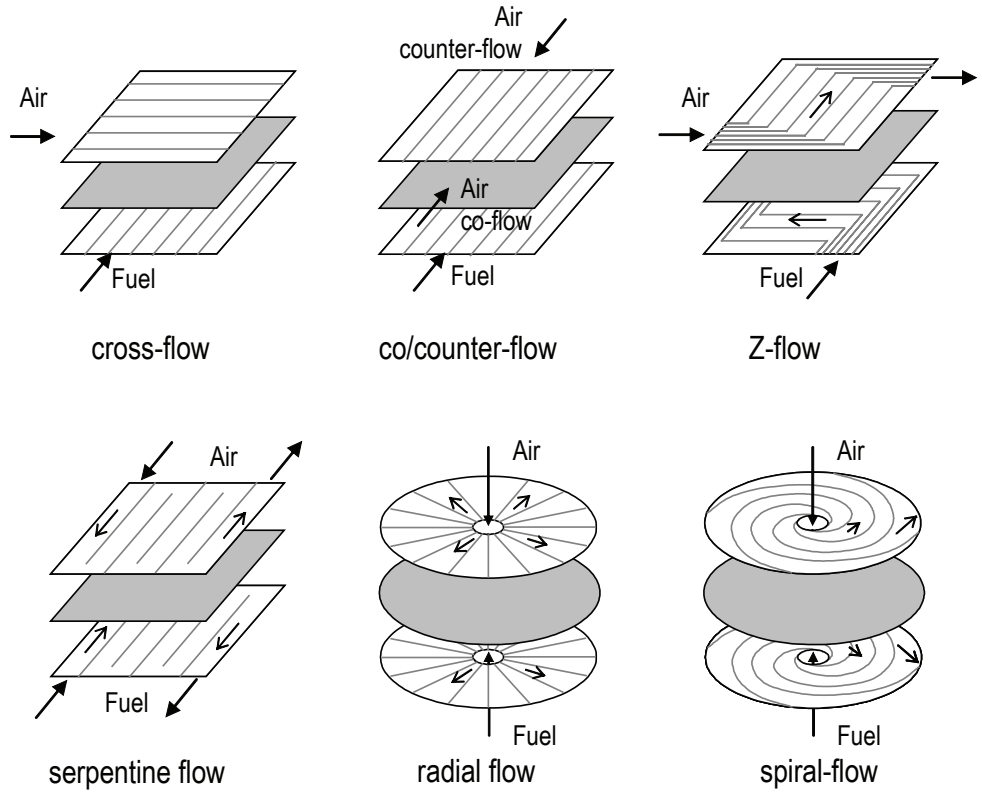

Figure 2-3: Typical flow configurations of planar SOFC

The largest planar cells that can be produced today have a size of e.g. 18 x 40 cm [Christiansen 2004]. Air and fuel flow are directed through gas channels in the interconnect. The flow field configuration greatly determines the temperature and reaction rate distribution within the cell. General possibilities are cross-flow, counter-flow and co-flow. In a rectangular cross-flow configuration, fuel and air inlets and outlets are separated from each other, which allows for a simple manifold system. Therefore it is easy to apply cross-flow in technical systems. Experimental cells are often circular with centre gas inlets and radial co-flow, and also Sulzer Hexis makes use of this configuration. However, counter-flow gives the flattest profiles for temperature and current [Rechenauer 1993]. Mixtures between the flow patterns are for example Z-flow, serpentine flow for rectangular and spiral-flow for circular

configurations. Figure 2-3 shows the most common flow configurations. Modern designs feature manifolding integrated into the cell plates. Planar cells offer principally a high volumetric power density and good electric performance through short current paths. Severe problems are, however, sealing of the cells (see Chapter 2.1.2) and mechanical loads due to high thermal gradients.

Tubular cells on the other hand offer separation of the gas channels without sealing in the cell itself. A well-known configuration is originating from Siemens-Westinghouse. This design is a cathode-supported, 1.5 m long and 22 mm diameter tube which is closed at one end. Air enters an inner (injector or air delivery) tube and is being preheated while flowing towards the closed end of the outer tube. There, it turns and flows along the cathode. Fuel is co-currently fed from the outside of the tube. The interconnect is applied at a small segment of the tube, but across its whole length. Figure 2-4 shows a section of the tube.

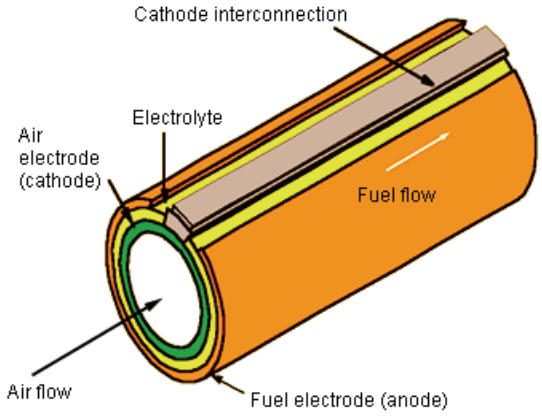

Figure 2-4: The tubular cell [S-W 2005]

The main drawbacks of the tubular cell are the low volumetric power density and the weak electric performance, caused by the long circumferential current paths in the electrodes. In order to increase volumetric power density, Siemens-Westinghouse has recently been focusing on another geometry, which is called the "flattened tubular cell", see Figure 2-5. It comprises several flow channels in one cell and allows for shorter current paths and higher stacking density.

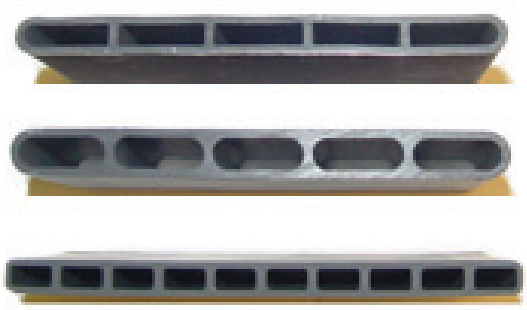

Figure 2-5: The flattened tubular cell [S-W 2005]

Microtubular cells are another approach using shorter tubes with typical diameters of 1-5 mm. The intention is to increase power density and decrease thermal inertia and thermal shock sensitivity in order to allow for quicker startup and shutdown and furthermore to realise small-scale systems. Microtubular cells are usually anode- or electrolyte-supported and open-ended, and the fuel flows inside the tube [Kendall 2003].

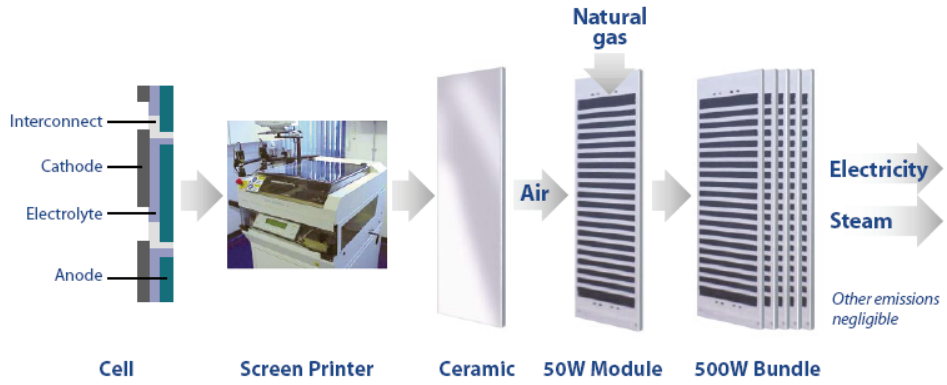

Figure 2-6: Segmented cell in series design [Rolls Royce 2005]

A design that may be applied in a planar and tubular manner is the "segmented cells in series", where several cells are screen-printed on a ceramic plate or tube next to each other and connected serially (see Figure 2-6; left). Rolls Royce applies this design in a planar manner [Agnew 2003], while Mitsubishi Heavy Industries uses tubes as support [Kendall 2003]. Rolls-Royce claims to strongly reduce production costs with this method.

Stacking

The term of stacking is originating from planar cells, which basically are just stacked by connecting electrodes of a cell to the counter-electrode of the adjacent, resulting in

a serial electric connection and increased voltage and power. Figure 2-7 shows a circular planar stack with integrated manifolding.

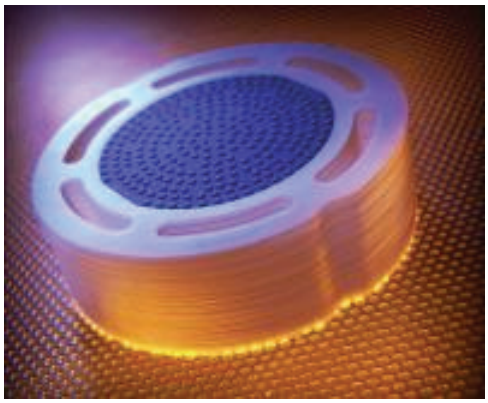

Figure 2-7: Planar SOFC stack with integrated manifolding [CFCL 2005]

It is, however, also common to "stack" tubular cells, even though they are rather bundled. The tubular Siemens-Westinghouse cell is typically arranged vertically in bundles of 3 x 8 tubes. Electrically, three cells each are connected parallel, and eight of these are connected in series, using flexible Nickel felt connectors. A stack contains 48 of these bundles, or 1152 tubes (see Figure 2-8). Indirect internal reformers (IIR; see Chapter 2.3.4) are arranged between the bundles in order to receive heat by radiation and convection. A certain amount of the anode exhaust gas is recycled in order to supply steam for the reforming reaction. Ejectors are applied to drive this recycling (see Chapter 2.3.3).

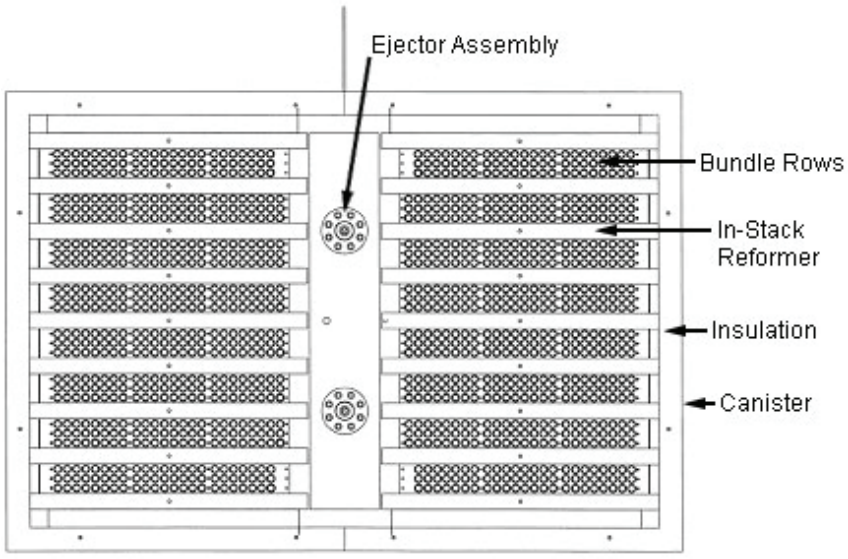

Figure 2-8: Tubular stack, top view [S-W 2005].

Figure 2-9 shows a schematic front view of the tubular stack where the arrangement of the gas flows can be seen. The length of the air injector tube exceeds the fuel cell tube length, and the entering air is being preheated with the exhaust gas before it enters the cell. The fuel is first pre-reformed in order to crack higher hydrocarbons and then fed into the IIR for further reforming. Thereupon it flows along the cell tube and into the recirculation plenum where a part of it is recycled through the ejector. The rest flows into the combustion and recuperation plenum (see Chapter 2.3.5) where the unutilised fuel is combusted together with the air before it recuperatively heats the incoming air.

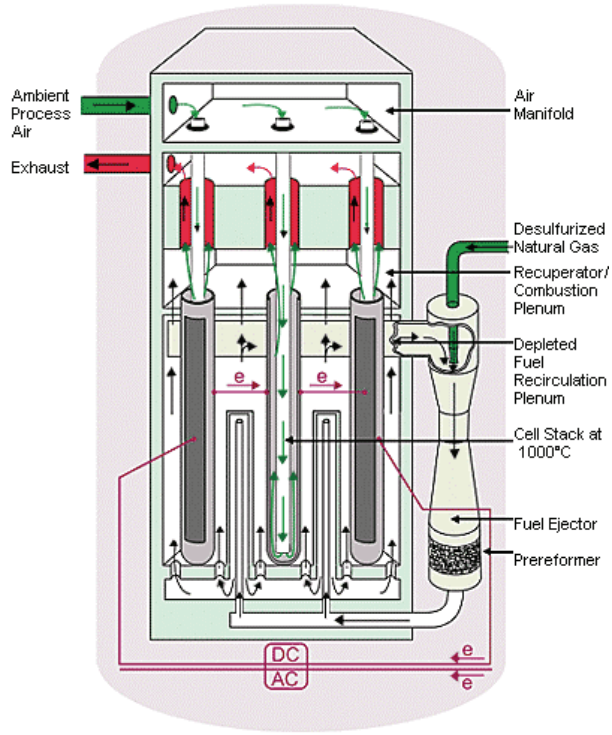

Figure 2-9: Tubular stack, schematic front view [S-W 2005]

2.2 Gas Turbine

Gas turbines are today widely used for power production in a range of 70 kW to 330 MW, mainly because of their high reliability and low investment costs. They are based on the Brayton cycle which ideally comprises two isobaric and two isentropic changes in state (see Figure 2-10). The gas turbine implements this cycle by compression, heating and expansion of a working gas in an open cycle. Heating is usually provided by direct combustion of fuel in a combustion chamber. Recuperative heating upstream the combustion chamber by the exhaust gas is a way to increase efficiency. This is, however, only applied in small systems, as recuperators are

expensive. Large-scale systems rather use higher pressure ratios to increase efficiency. Another means to enhance efficiency is reheating during the expansion in order to increase the turbine work. The following section briefly describes the components of a gas turbine cycle and introduces gas turbine designs and control methods. As the gas turbine combustion chamber will be replaced by the SOFC in a hybrid system, it is not discussed here. For further information, it is referred to text books on gas turbines [Saravanamuttoo 2001].

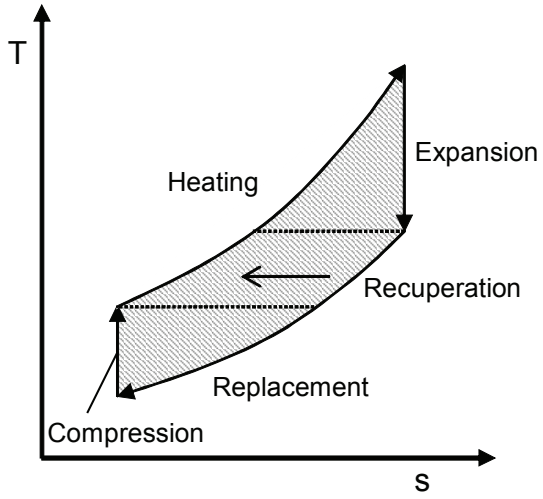

Figure 2-10: Brayton cycle

2.2.1 Compressor

Compression of gases can basically be achieved by volume displacement or fluid-dynamically by turbomachines. Whereas volume displacement machines work reciprocatingly through size changes of closed volumes (e.g. by a piston), turbomachines are continuously working open systems. Static pressure increase is achieved by acceleration of the fluid through a rotor and successive stagnation of the fluid through a stator. In gas turbines, turbomachinery is used due to its simplicity and high reliability. The fact that the gases are less contaminated with lubricants and wear debris than in volume displacement machines makes them suitable for combination with SOFC. Different flow configurations exist; mainly axial, radial (or centrifugal) and axial-radial compressors are known. Axial compressors are used for large mass flows and moderate pressure increase per stage, while radial compressors are suitable for small mass flows, but high pressure increase per stage as they utilise centrifugal forces for compression of the rotating gas. The main parameter of quality for compressors is the isentropic efficiency, which is defined as the ratio of the enthalpy changes of the ideal (isentropic) and the actual compression.

The off-design characteristics of compressors are non-linear and may be expressed through relationships between the main parameters of shaft speed, mass flow,

pressure ratio and isentropic efficiency. Typically, at a certain shaft speed, a higher mass flow will correlate with a lower pressure ratio. A higher shaft speed causes pressure ratio and/or mass flow to increase. The exact behaviour of these relationships is described in *performance maps*.

A critical phenomenon in compressors is called *surge*. If the pressure ratio becomes too high and the mass flow too low, the gas flow in the compressor reverses and flows towards the lower pressure. This causes in turn a rapid drop in pressure ratio and therewith the normal flow direction will be picked up again to repeat the incident. The result is a sudden drop in pressure and violent oscillations that may cause aerodynamic pulsation throughout the whole system. A further phenomenon is called *rotating stall* and appears at high pressure ratio and low mass flow, too [Gravdahl 1998].

2.2.2 Turbine

The turbine, or expander, is basically the opposite of the compressor. The static pressure of the flow is decreased by acceleration through a stator and the kinetic energy is recovered to the shaft by a rotor. Also here, isentropic efficiency is the leading parameter of quality, defined reciprocally to the compressor as the ratio of enthalpy changes of real and isentropic expansion.

A difference lies, however, in the relationship between mass flow and pressure ratio: Above a critical value of mass flow, the inlet of the turbine will be in choked condition, which means that the flow reaches the speed of sound and the mass flow is no more a function of the turbine pressure ratio, but only of the upstream pressure and temperature. In a gas turbine, the mass flow is mainly determined by the turbine.

Another difference is that an axial turbine stage can process a multiple of the pressure ratio that an axial compressor stage is able to produce. This is because accelerated flow as occurs in turbines is less prone to stall than decelerated flow.

2.2.3 Configurations and Control

The configuration of compressor and turbine depends strongly on the size and the type of use. Among the smallest compressor-turbine applications is turbocharging of internal combustion engines. Here, the remaining pressure in the engine exhaust is expanded in a radial turbine. The produced torque is completely transferred to a radial compressor on the same shaft and in the same housing which compresses the engine inlet air and therewith enhances the engine performance.

The next size step is the microturbine, which additionally has a combustor, possibly a recuperator and a generator. These machines are believed to have a great potential for distributed power generation due to their simplicity and reliability.

A different use of gas turbines is in aviation. Here, power is not produced to drive a generator, but to generate thrust for airplane propulsion. Hence, only a part of the pressure is processed by the turbine.

The largest gas turbines are applied in stationary power production, often combined with a steam cycle to enhance the efficiency. Medium-size stationary machines are often derived from aviation engines. However, as the latter focus on low weight while stationary gas turbines rather focus on high efficiency and long life, pure stationary power gas turbine systems are also being developed.

An important issue is to control power of a gas turbine in order to comply with the demand. This is generally done by the fuel flow, which quickly controls the *turbine inlet temperature* (TIT). For part-load, it may be advantageous to also control airflow, in order to achieve an acceptable efficiency. The airflow may be controlled through variable shaft speed or variable inlet guide vanes (VIGV) which influence the characteristics of compressor and turbine.

The former option is problematic for large systems which usually rotate at the grid frequency (50 resp. 60 Hz) in order to omit costly power conditioning. The latter option adds mechanical complexity to the system.

An important design option is the configuration and number of shafts. For higher pressure ratios, the volume flows vary strongly and hence it is advantageous to have several compressors and turbines in series with different rotation speeds in order to achieve optimum component size and efficiency. Modern aviation engines have up to three shafts. An option to solve the problem of air flow variation at constant generator frequency is the so-called *power turbine* concept. It comprises two turbines in series, with the first driving the compressor and the second driving the generator. One shaft is therewith freely adapting its speed towards equilibrium, while the other is controlled to rotate at constant speed.

2.3 Balance of Plant Equipment

2.3.1 Fuel Desulphurisation

The anode catalyst is very sensitive to sulphur and its compounds. The maximum tolerable concentration in the fuel is about 0.1 ppm [Larminie 2000]. If no sulphur-free natural gas is available, the fuel has to be desulphurised before entering the SOFC. The usual approach is to break down any organic sulphur compounds to hydrosulphide (H_2S) by a hydrogenation catalyst, and subsequently absorb H_2S using for example zinc oxide or activated carbon. Fixed bed zinc oxide absorbers are straightforward, using small cylindrical extrudates of zinc oxide and are designed for operation of several months [Kohl 1997].

2.3.2 Heat Exchanger

Heat exchangers are used extensively in the energy and process industry. In power cycles they are called recuperators and their use is to recover heat from exhaust streams for preheating the process streams and therewith saving part of the fuel.

SOFC systems in particular involve recuperation of heat due to the high gas inlet temperatures required and the high amount of heat in the exhaust.

There are different designs and flow configurations, depending on the application. The main design options are tubular and planar types. The choice of a design is depending on many parameters, as flow phase, pressure difference and available space. Planar types such as the welded or extruded plate-fin or the corrugated sheet based primary surface heat exchangers yield high heat transfer surface per volume, whereas tube-shell configurations are more robust against pressure differences.

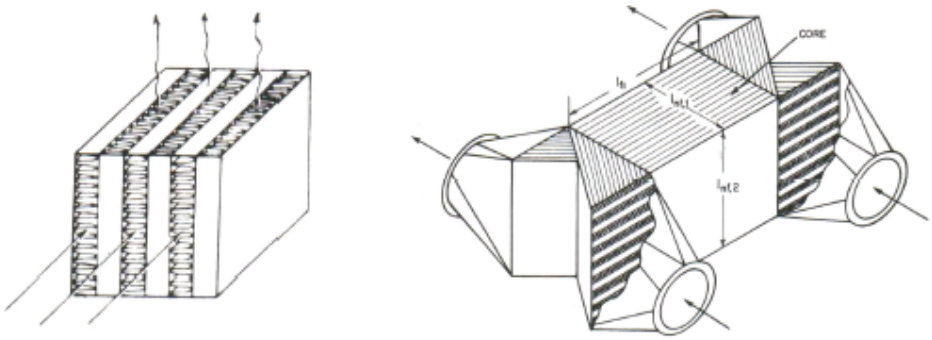

Figure 2-11: Planar plate-fin heat exchangers in cross-flow (left) and counter-flow (right) configuration [Kays 1984]

Analogous to the fuel cell, flow configurations may be co-flow, counter-flow or cross-flow (see Figure 2-11). Exergetically, counter-flow is most efficient, because the cold fluid outlet may closely approach the hot fluid inlet temperature if the flow rates and heat exchange surface are suitably chosen. A co-flow configuration may be more effective for heat exchangers with a huge temperature difference between hot and cold fluid and only small temperature changes. Cross-flow in planar heat exchangers is a mixture between the two configurations and easy to design because of the separate inlets and outlets. For more information it is referred to textbooks on heat exchangers [Kays 1984].

2.3.3 Ejector

Ejectors, or jet pumps, provide "passive" compression of a gas by mixing it with a gas of higher pressure. No moving parts are required, and therefore ejectors may be advantageous when compared to standard compressors under extreme conditions.

In SOFC systems, ejectors are used to recycle part of the anode exhaust gas in order to supply steam for the reforming reaction. The pressure of the recycled, "induced" fluid has to be lifted slightly to overcome the pressure drop in the fuel cell. The compression energy is supplied from the higher pressure of the "actuating" fresh fuel. High temperatures and chemical aggressiveness of the anode exhaust gases restrict the

use of moving parts like in blowers and valves. Furthermore, traces of lubricants and wear debris in the gases could damage the sensitive anode.

The actuating fluid expands through a Laval nozzle and enters the mixing chamber at supersonic condition. According to Lines [1999], the actuating fluid actually expands to a slightly lower pressure, and thereby creates a suction effect. The supersonic actuating fluid then accelerates some of the low speed fluid in the mixing chamber. By deceleration of the mixture in a diffuser, the dynamic pressure surplus is recovered as static pressure, which hence increases above the inlet pressure of the induced fluid. The principle of an ejector is sketched in Figure 2-12.

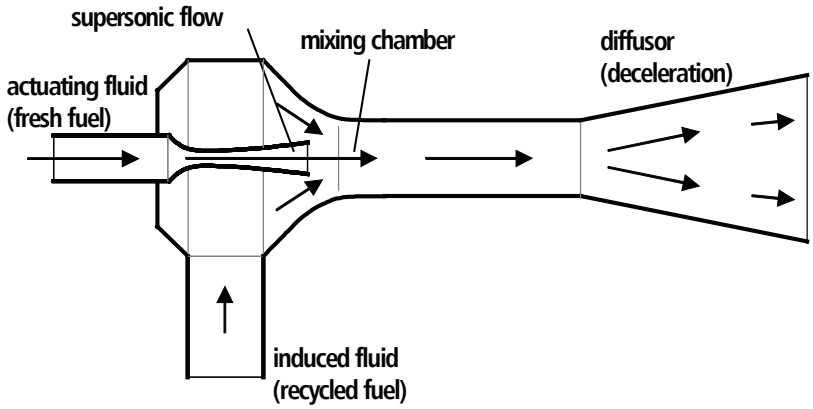

Figure 2-12: Ejector principle

The ejector described above is a subsonic mixing ejector. This type allows for high ratio of induced to actuating fuel, although at only low pressure increase. Another option is supersonic mixing, where a narrow throat in the mixing chamber accelerates the induced fluid to supersonic and a shock wave accomplishes a higher pressure increase. However, as the anode pressure drop is typically very low, subsonic mixing ejectors are better suited for SOFC systems.

The dimensions of the ejector and the state of the entering gases determine the mixing ratio of recycled and fresh fuel and therewith the *steam-to-carbon ratio*. As too low a steam-to-carbon ratio may result in *carbon deposition*, ejector performance is crucial for safe operation of an SOFC system. The behaviour of mixing ratio respectively pressure increase of an ejector is determined by its design and cannot be actively controlled, and hence it must be part of the operation strategy to ensure a sufficient steam-to-carbon ratio.

2.3.4 Reformer

In reformers, part of the incoming hydrocarbons is reformed to carbon monoxide and hydrogen according to **Equation 2-8** and **Equation 2-9**, while the rest is reformed directly at the anode (direct internal reforming, DIR). The intention of reforming upstream the SOFC is to prevent the latter from strong local temperature drops and

high thermal stresses originating from the endothermic reforming reaction. Reformers are reactors that may be supplied with external heat in order to achieve the desired degree of reforming. A reforming catalyst and a large internal surface of the reformer are required for acceptable performance. Reformers that are thermally integrated with the stack are called indirect internal reformers (IIR).

2.3.5 Burner

Because only part of the fuel can be oxidised in the SOFC, an afterburner is necessary to combust the residuals. Depending on the fuel cell design, the combustion may occur directly at the fuel cell exit or in a separate chamber. As the fuel is usually highly diluted, special burner configurations are required for stable combustion [Hermann 2002]. Diffusion burners are normally applied as SOFC afterburners [Pålsson 2002]. In hybrid systems, the introduction of additional fresh fuel to the afterburner is a measure to stabilise the flame and at the same time enhance the turbine power output. Another alternative is to use a catalytic afterburner [Fontell 2004].

2.3.6 Power Electronics

Power electronics is necessary to convert the electric power supplied from SOFC and gas turbine to the required grid voltage and frequency. The SOFC delivers direct current (DC). A turbine system rotating constantly at the net frequency may be directly coupled to the alternate current (AC) grid using a synchronous generator. This is often applied at large power centrals, where the inertia of the rotating mass at the same time provides stabilisation of the grid frequency. The grid can be seen as an "electric shaft prolongation" from the generator to the consumers.

Smaller turbines must, however, rotate faster and possibly with variable speed. It is hence common to convert the generator high-frequency AC to DC with a rectifier. The product is then combined with the DC power from the SOFC and converted to AC at the required conditions with an inverter.

Furthermore, the power electronics carries out the "primary control", i.e. it adapts the system power output to the power demanded by the grid (called the *load*). It has two handles to control the system: The operating point of the SOFC is controlled by the current drawn from the power electronics, and furthermore the shaft speed is controlled by the power drawn from the generator.

In case of off-grid application, a SOFC/GT power plant may not be able to follow large and quick changes in power demand. In addition, the GT shaft does not provide sufficient inertia for stabilisation of frequency and voltage. For these applications, capacitor banks may be required as electronic energy buffers for transient grid stabilisation.

2.3.7 Other Components

The introduced components are most important for the operation of a SOFC/GT hybrid system. However, for startup and shutdown as well as for emergency, several additional components are needed. Such appliances are the following:

- Nitrogen supply system: For startup, shutdown and emergency cases, nitrogen must be provided to flush the anode in order to protect it from air inflow and consequently oxidation.
- Auxiliary steam generator: As long as the system includes anode gas recycling, a steam generator will only be required during startup in order to prevent carbon deposition.
- Auxiliary air blower and buffer: In case of emergency shutdowns, air must be supplied immediately to cool the cell and protect the cathode side.

2.4 Basic SOFC/GT Hybrid Cycle

Figure 2-13 shows the basic configuration of a SOFC/GT hybrid cycle with the components described previously. It is basically a recuperated GT cycle where the combustor has been replaced by a SOFC system. Many variations of this cycle are reported in literature. The most important options are discussed in Chapter 3.4.4.

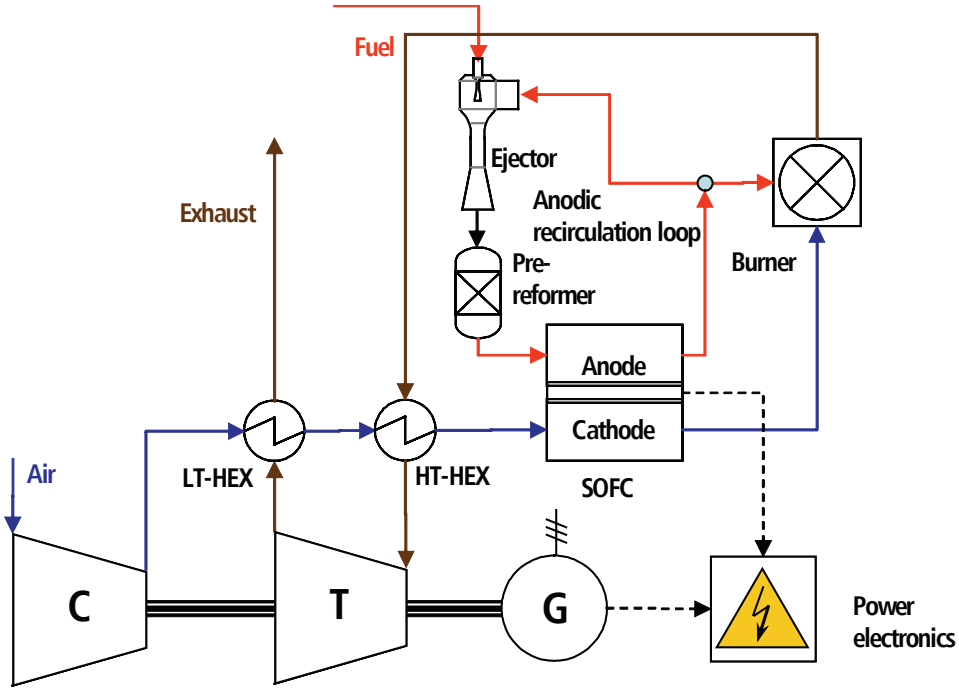

Figure 2-13: Basic hybrid cycle

2.5 Process Control

Control of processes is basically required in order to [Stephanopoulos 1984]:

- Suppress the influence of external disturbances
- Ensure the stability of a process
- Optimise the performance of a process

Speaking of power plants, the most important controlled output is obviously the power (in small grids, a further cascade controls the frequency by manipulating the power). A power setpoint is impressed to the system, and the controller must ensure that the power production adjusts to this setpoint. Furthermore, the system must be maintained at adequate operation conditions, ensuring good performance and safe operation also under the influence of external disturbances such as fuel composition variations, electrical grid instabilities and weather conditions.

2.5.1 Feedback and Feedforward Control

The interfaces between a control system and a process consist usually of controlled and manipulated variables. The two basic control layouts are feedforward and feedback control. They are explained by the example of a heated room, where the room temperature is to be controlled by manipulation of the heat flow:

- A feedforward control layout (see Figure 2-14) requires information about the characteristics of the system (e.g. heat loss as function of outside temperature) and measures the disturbances to the system (e.g. outside temperature). Based on these data, the control signal (e.g. heat flow required for a certain temperature) is calculated. The advantage of this control layout is that if ideally calibrated, it may perfectly stabilise the temperature without any deviation from the setpoint. Furthermore, the system is per se stable as the control signal is not likely to influence the measured variable (the outside temperature is independent from the heat flow into the room). A drawback is that the system cannot react to unforeseen disturbances. If for example the room heat balance is disturbed (e.g. through use of heat intensive equipment, opening of a window), the temperature will deviate from its setpoint.
- In a feedback control layout (see Figure 2-15), the controlled variable strongly (here: room temperature). The measured variable is compared with the setpoint (the difference between measured and setpoint value is called *error*). Based on the error, an action is taken. If e.g. the measured temperature is lower than the setpoint, the heat flow is increased. The slope and shape of the heat flow increase depend on the controller type and its tuning. The advantages of this control layout are that no exact behaviour of the system and disturbances is required and that the setpoint will also be reached if unexpected disturbances occur. A drawback is, however, that the controller at first requires a deviation of

the controlled variable from its setpoint to take an action. Furthermore, due to the feedback of the controller action (closed loop) on the measured variable, stability of the system is an issue. A wrongly tuned feedback controller can lead to instability and damaging of the controlled system.

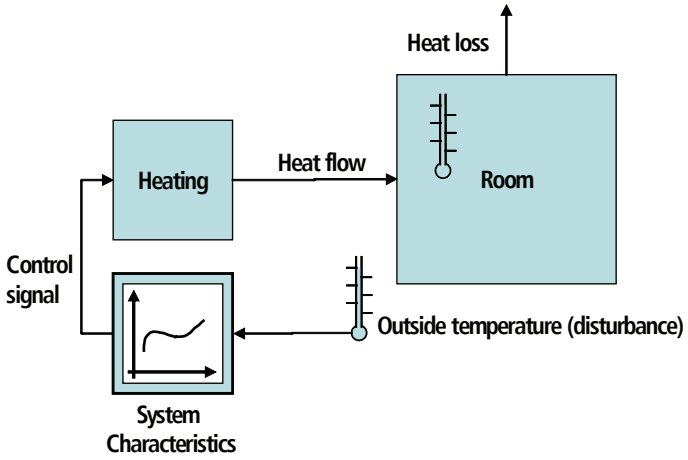

Figure 2-14: Feedforward control layout (open loop)

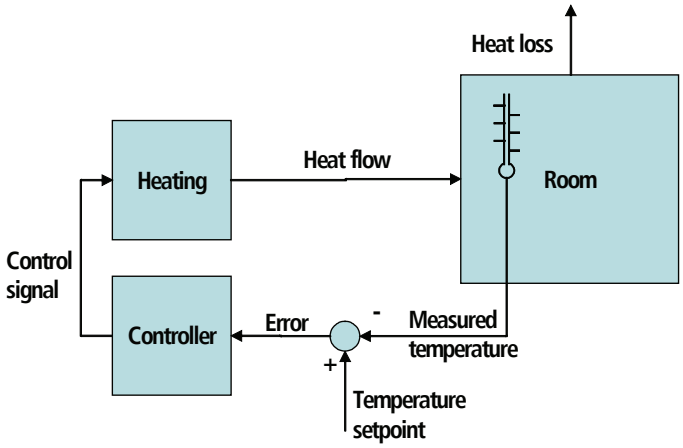

Figure 2-15: Feedback control layout (closed loop)

2.5.2 The PID controller

A feedforward controller is basically a transfer function for calculating an output as a function of an input. Unless dynamics are involved, this transfer function may be of the simple shape $y=f(d)$, where d is the disturbance and y is the controller output.

A typical feedback controller is of PID type, where P stands for proportional, I for integral and D for derivative. The controller output is hence the sum of a term

proportional to the error, a term which integrates the error over time and a term which derives the error to time.

The equation for the controller output y as function of the error e is hence

$$y(t) = K \cdot \left(e + \frac{1}{\tau_I} \int e dt + \tau_D \frac{de}{dt} \right) \qquad \textbf{Equation 2-10}$$

where K is the *proportional gain*, τ_I is the *integral time constant* or *reset time* and τ_D is the *derivative time constant*. These three coefficients characterise the controller and must be tuned carefully for any control purpose in order to grant stability and quick response.

The proportional term provides quick and stable control. However, if it is used alone, a setpoint deviation will remain. The integral term repeats the proportional term action and therewith resets the proportional controller. It causes the controller output to change as long as an error exists in the process output and is therefore suited for exactly achieving a setpoint value. However, if an error cannot be eliminated, the integral controller may keep on changing the output beyond the output limits, which is called *integral windup*.

The derivative term applies a control action proportional to the rate of change of the error and therewith counteracts the anticipated error in the immediate future. It helps to stabilise control systems against the counteractions of proportional and integral term, but is does not react on a constant error and is sensitive to noise in the measured input. For omitting strong control action for a step change in the setpoint (and therewith in error), it is common to derive the measured signal instead of the error.

The mentioned control elements can be combined and applied in multiple ways, such as cascades where a controller output is fed into another controller, and multiple-input multiple-output (MIMO) where several interacting variables are controlled at a time. Control system design and tuning of the controllers are the key tasks in control engineering.

Different mathematical methods exist for examining stability of a control system and optimising controller tuning. However, the classic methods mainly apply to linear or linearised processes. The process that will be investigated in this work is strongly non-linear and linearisation is difficult to accomplish due to its complexity. Controller tuning in this work will thus be based on physical understanding of the process dynamics and trial-and-error methods.

3 SOFC and Hybrid Cycle Modelling – An Overview

This chapter presents an overview of SOFC and hybrid cycle modelling. Firstly, requirements on process modelling in general are formulated. Next, purposes for modelling of SOFC hybrids and their requirements to the models are discussed. Then, the main approaches to SOFC modelling are presented and discussed. Important issues therein are geometry, spatial distribution, reaction kinetics and electric resistance, heat conduction as well as simulation environments and solving methods. Moreover, hybrid cycle models are presented with regard to cycle layout and modelling approaches and currently active groups in hybrid cycle modelling are highlighted.

3.1 Introduction

The research on solid oxide fuel cells has been steadily increasing since the early 1990s. There still is great uncertainty in the optimum geometrical and system configuration, and experiments with fuel cells are expensive. Thus there is great need for mathematical modelling of fuel cells. There are many different approaches to SOFC and hybrid cycle modelling and the complexity and accuracy of the models is increasing steadily with computer performance.

3.1.1 Requirements on Modelling Approach

A large variety of approaches to modelling a physical-chemical process exist. These variations include the degree of spatial distribution, the levels of detail in modelling the occurring phenomena as well as simplification or neglect of side effects. A main quality indicator of any model is indisputably its degree of accuracy in reproducing the true behaviour of a system. Hence, the acceptability of each simplification must be verified.

Generally speaking, the more detailed model is expectably the more reliable model in terms of accuracy. However, obvious restrictions to the level of detail are the time required for calculation and the stability of the mathematical solver. The purpose of the model and the simulation approach often decides the detailing level. If for example an optimisation using a genetic algorithm (GA) is to be performed, a high number of model evaluations and thus a fast model is required. Likewise, if the controllability of a system is to be investigated, linear or linearised models with a low number of state variables are advantageous. The main task of modelling is formulated in the "principle of optimum sloppiness" [Luyben 1990]:

"Make as many simplifying assumptions as reasonable without throwing out the baby with the bath water"

Another important feature of a model is the flexibility with which the problem may be posed. A classical model has input and output variables. However, for example the point of operation of a fuel cell may be determined by either dictating a voltage or a

current as input variable. The free (output) variable is in both cases resulting from the specified one through a non-analytical relationship. For operation, different restrictions on both values exist; hence it is advantageous for most applications if the model is flexible in terms of input and output variables. Using a classical sequential solving approach, this may be realised by adding additional iteration loops for each output variable which is to be changed to an input variable. However, as this boosts simulation time, a better solution is a simultaneous, equation-oriented solving approach.

Summarizing, general requirements on the modelling approach are

- Accuracy of reproducing the true behaviour of a system
- Quick and stable solving
- Flexibility in input-output structure

These requirements are to some extent contradictive. On the other hand, the purpose of the model plays an important role in determining the importance of each single point.

3.1.2 SOFC Modelling Purposes

Due to the contradictive nature of the aforementioned requirements, the selection of modelling approach is dependent on the purpose of the model and the way it should be applied. As for other power plant and energy related systems in pre-commercial stages, the main purposes where a model of a SOFC power plant may be applied are:

- **System understanding and analysis**: The model shall help to understand phenomena observed in a real system and allow analysis of the system behaviour at different conditions. A model for this purpose must obviously cover the phenomena that should be analysed and those they depend on in a sufficient level of detail. Furthermore, it must be verified that the model and the true system agree. On the other hand, quickness of the solver and model flexibility are of secondary importance. Depending on the nature of the analysed phenomena, the system can be of steady-state or dynamic type.
- **Design calculation and optimisation**: Once a system is understood, its components need to be designed in order to achieve an optimum performance. Several objectives may hereby contribute to the optimum; efficiency, specific power output, specific costs and lifetime are only some of them. In an optimisation calculation, typical design values such as physical dimensions and operational parameters are to be optimised and serve as input to the model, while the objectives serve as the output. Several numerical optimisation approaches exist, but they all require a large amount of model evaluations in order to proceed to the optimum. Therefore, models for design should be quick and stable to solve. On the other hand, it must also be provided that critical

issues for the design optimum (e.g. electrical conductivity of materials if the MEA layers' thicknesses are to be optimised) or for system safety (e.g. carbon formation or compressor surge) are modelled accurately. A steady-state model is usually sufficient for design calculations.

- **Operation calculation and optimisation**: Having designed the system and fixed a design point, the next step is to investigate and optimise the behaviour of the system at off-design and under dynamic situations. Here, all parameters that are physically constant in a real system (such as dimensions) must also be kept constant in the simulation. Several global input-output structures are possible:
  - A reverse structure where the desired power output and operational parameters such as temperatures serve as model input and the system inputs (fuel flow, fuel cell current, etc.) serve as model output. This allows a direct calculation of the input parameters required to achieve the desired output.
  - A forward structure where the model and true system inputs and outputs are equal. This is advantageous for mapping valid and invalid operational areas and the stability of the system against malfunction. This structure can be regarded as the numerical equivalent to physical experiments.

  For this purpose, many model evaluations are typically required; hence the model should be lean enough to provide quick and stable solving. Furthermore, for performing different kinds of simulations and evaluating different operation strategies, flexibility of the input-output structure is a great advantage.
- **Control modelling**: A last modelling task is to investigate controllability and to tailor a control design for the developed system. For this task, a dynamic model is required. The input-output structure of model and true system must agree. Conventional methods for analysing system response and controllability require linear input-output models with a limited number of state variables. For a classic feedback control system, the dynamic behaviour of the system is more important than accurate agreement of the steady-state performance. This allows for stronger model simplifications than in the previous cases. As the implementation of the control design adds complexity to the model, it should be provided that the "non-controlled" model is solved quickly and stable.

3.2 SOFC Modelling

3.2.1 Lumped and Distributed Models

The chemical reaction rates in a SOFC depend on temperature and species concentrations. Concurrently, temperature and species concentration are influenced by the reaction rates. This interdependency between chemistry and temperature implies that concentration and local temperatures will vary throughout the fuel cell. In

order to simulate the processes in a detailed way, a *spatially distributed model* [Luyben 1990] where the fuel cell is discretised into a mesh of finite elements is therefore required. Different discretisation methods for distributed models and the resulting partial differential equations exist; the *finite-volume* and *finite-difference methods* are most common here. The finite volume method calculates the values of the variables averaged across so-called control volumes, while the finite difference method calculates the values of spatial gradients of the variables between so-called nodes. The two discretisation methods are similar for sufficient resolution of the discretisation; however, the finite-volume method theoretically does not require a uniform mesh.

It follows that distributed models have the advantage of giving a close insight into the internal processes of the fuel cell. Furthermore, controlling local values of critical parameters, such as temperature or temperature gradients, is facilitated. In addition, these types of models are physically accurate. On the other hand, they are computationally expensive due to the large number of variables in a one- or multi-dimensional distribution.

A model without distributed variables may be called a *lumped model* [Luyben 1990]. It considers the balance equations only at the boundaries of the fuel cell, while the interior is treated as a "black box". Such models are computationally simpler, geometry-independent and they allow easy adjustment to empirical data. However, no insight into the internal processes of the cell is possible.

3.2.2 Cell Configuration

As already presented in Chapter 2.1.3, various geometrical configurations of solid oxide fuel cells exist in practice. Mostly for earlier models, the common approach is rectangular planar geometry with a flat anode-electrode-cathode layer and interconnects which include the gas flow fields.

Models with the cross-flow configuration which allows easy manifolds were particularly published by Karoliussen et al. [1992], Selimovic [2000, 2002b], and Stiller et al. [2005][12]. All of them use the so-called Vayenas approach where the smallest repeated element, namely the crossing between one gas and one fuel channel, is considered as control volume [Karoliussen 1992]. Counter-flow was modelled by Yakabe et al. [2002], and co-flow by Aguiar et al. [2005a,b]. Rechenauer [1993] and Recknagle et al. [2003] introduced models with variable geometry.

Recent models, especially for hybrid applications, rather focus on the tubular configuration from Siemens-Westinghouse [Campanari 2001; Hall 1999; Stiller 2005; Chan 2002] or micro-tubular cells [Ota 2003].

---

[12] This paper represents a precursor to the model described later in this work; see Chapter 1.7.1 (Paper I) and Appendix 1.

Distributed models of novel geometric configurations such as the integrated planar SOFC from Rolls-Royce [Costamagna 2004] or the flattened tubular SOFC from Siemens-Westinghouse [Bharadwaj 2005a; Lu 2005] have been published recently. Costamagna et al. [1998] have developed a model of the circular counter-flow design from Sulzer Hexis where the fuel flows in radial direction from the center to the outside and the air flows in the counter direction. Larrain et al. [2004] have introduced a generalised model for planar flow configurations on the basis of a configuration with punctual gas inlets and outlets.

Furthermore, a large number of lumped models have been published where geometric configuration is not of special interest. Such models have been introduced by many authors, especially with respect to hybrid system and control investigations [Uechi 2001; Costamagna 2001; Chan 2002; Kandepu 2005].

3.2.3 Reforming and Shift Reaction

Most SOFC models use methane or sulphur-free natural gas as fuel, utilising this advantage of the high temperature fuel cell. Exceptions are Costamagna et al. [1998] and Ota et al. [2003] who use hydrogen as fuel.

In order to know the distribution of the reforming across the cell, the kinetics of the reforming and shift reaction must be modelled.

For the rate of the reforming reaction r_{CH4}, Rechenauer [1993] puts up the empirical equation

$$r_{CH_4}\left(mol\,m^{-2}s^{-1}\right) = A \cdot e^{-\frac{E}{RT}} \cdot p_{CH_4} \qquad \textbf{Equation 3-1}$$

with a frequency factor A, the reaction activation energy E, the universal gas constant R_m, the temperature T and the partial pressure of methane p_{CH4}. The values for A and E were empirically determined to

$$A = 4274\frac{mol}{m^2 \cdot bar \cdot s}; \quad E = 82\frac{kJ}{mol}$$

This approach is picked up by Selimovic [2000, 2002b] and Stiller et al. [2005].

Yakabe et al. [2002] developed a similar formula from proper empirical data:

$$r_{CH_4}\left[mol/m^3\right] = A \cdot e^{-\frac{E}{RT}} \cdot {p_{CH_4}}^{1.3} \cdot {p_{H_2O}}^{-1.25} \cdot \rho_a \qquad \textbf{Equation 3-2}$$

with the partial pressure of methane p_{CH4} *(bar)* and steam p_{H2O} *(bar)* and the density of the anode ρ_a, where

$$A = 1.09 \cdot 10^{10}\frac{mol}{kg}; \quad E = 191\frac{kJ}{mol}; \quad \rho_a = 930\frac{kg}{m^3}$$

Others consider the reforming reaction to be always at its chemical equilibrium [e.g. Chan 2002].

The shift reaction is so fast that it is assumed to be at its chemical equilibrium in all reviewed models that include reforming reactions.

3.2.4 Electrochemical Reactions

The electrochemical reaction of hydrogen and oxygen to water is the main reaction in the solid oxide fuel cell (see **Equation 2-3**). Beside hydrogen, carbon monoxide (CO) resulting from the reforming reaction is oxidised to CO_2 electrochemically, but due to the fast water gas shift reaction, most models neglect this. From the investigated models, only Hall [1999] includes the electrochemical reaction of CO.

The kinetics of the electrochemical reactions determines the voltage losses and reaction rates and thus the molar composition distribution of the gases, heat production, current flow distribution and current-voltage characteristics. The reaction kinetics model can therefore be seen as the core of an SOFC model.

The driving mechanism for electrochemical reaction in a fuel cell connected to an external circuit is the difference between the operation voltage and the reversible potential. The latter can be exactly calculated by the standard potential and the well known Nernst equation, which is dependent on the concentration of the reactants and the operation temperature (see Chapter 2.1.1). This voltage difference drives the current and is dissipated by the effects of ohmic, activation and concentration overpotential.

The ohmic resistivity is a mostly temperature-dependent material property. Bossel [1992] summarises formulae for ohmic resistivities of the standard materials, applied by Selimovic [2002b], Rechenauer [1993] and Stiller et al. [2005]. As this approach does not account for contact resistances between the layers, Yakabe et al. [2002] uses proper empirical data for the resistivities. The geometry of the planar interconnect can be expressed by an electrical serial circuit of the different current flow cross-sections [Selimovic 2002b; Rechenauer 1993; Yakabe 2002; Stiller 2005; Chan 2002]. The electric current path in tubular models exhibits a complex three-dimensional pattern. For modelling purposes it is often assumed that current flows only in radial direction in the electrolyte and circumferential direction in the electrodes. Furthermore an even circumferential current distribution in the electrolyte is commonly assumed [Nisancioglu 1989]. Recently, a novel circumferentially discretised approach for current profile calculations has been introduced [Bharadwaj 2005b].

The exact mechanisms of the activation potential are not known to date [Mogensen 2002, Singhal 2003]. Semi-empirical approaches are therefore applied. The activation overpotential η_{act} can be implicitly calculated as a function of the current density j by the Butler-Volmer equation (see **Equation 4-1**).

For currents strongly higher than the exchange current density j_0, the simplified explicit Tafel equation can be used

$$\eta_{act} = A \ln\left(j / j_0 \right) \qquad \textbf{Equation 3-3}$$

where A is a geometry and material dependent factor. This approach is utilised by Selimovic [2002b], Chan et al. [2002], Rechenauer [1993] and Hall [1999]; however, in none of the sources parameters are specified. Karoliussen et al. [1992] state that the relationship between overpotential and current density is nearly constant and put up the empirical approach

$$\eta_{act} = a \cdot j \cdot e^{b/T} \qquad \textbf{Equation 3-4}$$

with the coefficients

$$a = 2.83 \cdot 10^{-4}\,\Omega cm^2; \quad b = 8360K$$

obtained by Solheim from experimental data from Umimura, and the temperature T. This approach is adopted by Selimovic [2000] and Stiller et al. [2005]. Ota et al. [2003] utilise a different empirical approach from Fukunaya.

In many cases the diffusion overpotential η_{diff} is neglected [Selimovic 2000; Stiller 2005; Karoliussen 1992; Ota 2003], as the concentration difference in the thin electrodes is usually low. Others use the standard approach

$$n_{diff} = -B \ln\left(1 - j / j_L \right) \qquad \textbf{Equation 3-5}$$

with the coefficient B and the limiting current density j_L [Kuchonthara 2003; Chan 2002], but no values for B and j_L are usually given. However, these parameters can easily be determined from experimental data.

Yakabe et al. [2002] use a very basic approach with a constant integral activation and diffusion overpotential of 50 mV.

Where good measurement data for the investigated cell exist, an integral empirical approach can be used to formulate a dependency between temperature, concentration, overpotential and current density. The physics of ohmic, activation and concentration overpotential can be disregarded in this case. Such an approach is chosen by Pangalis et al. [2002] and Campanari [2001].

3.2.5 Thermal Model

Another important topic of the model core is the thermal model. It includes the heat flows through conduction, convection and radiation as well as the heat production or consumption by the reactions taking place. As the different approaches are very diverse and difficult to summarise, this review will not go too deep into physical details but rather describe general assumptions and neglects.

Heat conduction through solids of the fuel cell along the thin layers is normally rather weak, as ceramic materials have a low conductivity. Convection and radiation are much stronger [Ota 2003]. For planar cells, heat conduction between the control volumes is considered in all models. For tubular cells, in contrast, Ota et al. [2003] and Hall [1999] neglect the conduction along the tube, while Stiller et al. [2005] include only the axial conduction of the membrane and neglects the air preheat tube.

Heat exchange by convection between the gases and solids is included in all models. Here it is common to consider the flow as fully developed and calculate the convection by Newton's law of cooling which is well documented in the literature. Therefore, specific heat capacity values of the gases are usually considered as temperature-dependent, while heat conductivity and specific heat capacity of solids are seen as constant [Yakabe 2002; Stiller 2005].

Radiation occurs between surfaces that "see" each other through the gas channels. At the high temperatures occurring in the SOFC, radiation is a very effective means of heat transfer. However, for the planar models, Recknagle [2003], Stiller et al. [2005] and Selimovic [2000, 2002b] neglect radiation along the channels, by reasoning that the ratio between length and width of the channels is very high and thus the radiative heat transfer along the flow axis is rather low. Yakabe et al. [2002] and Rechenauer [1993], in contrast, include radiation along the channels, and as a result the temperature variations in the cell are significantly lower than when radiation is neglected. It can be concluded that the models where radiation is neglected are hence rather conservative with respect to temperature gradients. For tubular geometry, Ota et al. [2003] consider radiation between the air feed tube and the membrane inside a control volume, which does not flatten the temperature profile along the tube. In the model presented by Stiller et al. [2005], radiation between adjacent control volumes has been implemented.

As a consequence of high operating temperatures, it can be important to include fuel cell system boundary conditions in the model. Several models consider the boundary as adiabatic [Recknagle 2003; Yakabe 2002], assuming either the cell in the middle of a large stack or a low influence of the heat exchange with the surroundings. Stiller et al. [2005] define a black body to which the planar cell is radiating from its edges, simulating a casing around an infinite stack. The black body temperature is iteratively adjusted by the solver so that the radiation heat meets the pre-reformer heat requirement. Selimovic [2002b] introduces simulations with both adiabatic conditions and radiation from the edges of the cell. Rechenauer [1993] includes convective heat transfer between the cell edges and the surrounding gas additionally to the radiative heat transfer. At the tubular models, no radiation to the surroundings is modelled. Stiller et al. [2005] include a constant sink term in the heat balances of each control volume to meet the heat requirement of the pre-reformer.

3.2.6 Dynamics

Another important characteristic of a model is its capability to simulate transient behaviour of the system. This is of special interest as the SOFC materials are very sensitive to thermal stresses and modern power plants usually must be capable of quick load changes. Transient models are more complex than steady-state models as they include *state variables*. From the reviewed literature, the models of Rechenauer [1993], Bistolfi et al. [1996], Hall [1999], Ota et al. [2003], Recknagle et al. [2003], Kemm et al. [2004], and Magistri et al. [2004a] include transient simulations.

Time-dependent behaviour of SOFCs in non-steady-state arises basically from four phenomena:

- **Thermal inertia of the solids**: This originates from the heat capacities of the solids. The time constants are usually quite high (>100 s) due to slow heat transport and long conduction paths. Thermal inertia modelling is therewith essential for any dynamic SOFC model.
- **Thermal inertia and composition of gases**: The time constants are coupled to the residence times of the gases and usually much smaller than for the solids. However, a neglect of these phenomena implies an instantaneous change of temperature and therewith the SOFC's molar gas content as response to step changes in current. This results in non-physical step changes of pressure where the fuel cell is charged by a gas turbine.
- **Diffusive inertia**: This originates from the diffusion process of the gases from the bulk phase to the three phase boundary and temporarily influences the diffusion overpotential. However, in most cases it is fair to neglect this phenomenon, as time constants are typically below one second [Qi 2005]. In addition, several models presented in literature do not consider diffusion overpotential at all.
- **Gas dynamics**: Inertia originating from the momentum of the gas flows. However, as flow velocities are typically very low in fuel cells, it is fair to neglect the difference between static and dynamic pressure.

Rechenauer [1993] and Kemm et al. [2004] neglect the heat capacity of the gases and consider only the solids. The latter is not clearly stated by other authors.

3.3 Software

There are various ways to implement the discussed modelling approaches: In principle, it can be distinguished between basic programming and process flowsheeting tools.

The latter approach provides graphical user interfaces which facilitate easy cycle setup and modification based on standard components. However, the SOFC has not yet become a standard component of process flowsheeting tools. Hence, most distributed SOFC models are implemented by programming. The FORTRAN language has been

intensively used [Karoliussen 1992; Rechenauer 1993; Selimovic 2000, 2002; Kemm 2004; Stiller 2005]. An advantage of FORTRAN based SOFC modelling is that the compiled code may be integrated in a flow sheet simulation tool for hybrid cycle studies. Selimovic and Pålsson [2000, 2002a] integrated a FORTRAN model into a hybrid cycle modelled in Aspen Plus (AspenTech), and Stiller et al. [2005] did the same with PRO/II (SimSci-Esscor).

The Matlab environment (MathWorks) is becoming more and more popular for all kinds of modelling, due to its numerous intrinsic mathematical functions and tools and the possibility of flowsheeting within the embedded Simulink environment. Furthermore, it provides built-in non-linear and differential equation solvers. The Matlab/Simulink environment was used by Chan et al. [2002] and Magistri et al. [2003].

A comparatively new tool is gPROMS (Process Systems Enterprise). Its main advantage is the equation oriented approach, which in contrast to the sequential modular approach used by most process flowsheeting tools solves all equations simultaneously. This allows for high flexibility in the input-output structure in addition to a significant reduction in computation time. gPROMS has so far not been widely used in the SOFC modelling community. It is currently being used by groups at EPFL [Larrain 2004], Imperial College [Aguiar 2005a,b] and by the author's group.

Computational fluid dynamics (CFD) codes and tools are frequently used, mainly for three-dimensional modelling of the gas flow in fuel cells. Recknagle et al. [2003] use STAR-CD (CD-adapco) for three-dimensional planar stack modelling, while Autissier et al. [2004] and Lockett et al. [2004] rely on FLUENT (Fluent Inc.) for flow field planar SOFCs with non-orthogonal flow field respectively micro-tubular SOFC stacks. Campanari and Iora [2004] used FLUENT to model the velocity field at the air turn point of a tubular SOFC of Siemens-Westinghouse type.

3.4 Hybrid Cycle Modelling

SOFC/GT hybrid cycle models connect a SOFC with gas turbine and balance of plant equipment through dissimilar interfaces, such as material and heat flows. The total model is more complex, and consequently most of the common hybrid cycle models today rely on lumped SOFC models, with only few exceptions [e.g. Pålsson 2001; Song 2005; Stiller 2005].

3.4.1 Turbomachinery

Compressor and turbine are along with the fuel cell important devices in terms of system behaviour. They may in general be modelled either with a distributed fluid-dynamical approach or in a lumped way based on a mathematical representation of empiric results. The former approach is computationally very expensive and therefore usually not used for hybrid cycle modelling. Furthermore, it is common to assume adiabatic conditions and neglect dynamics from thermal inertia and gas dynamics,

resulting in a quasi-steady-state model. Only Hildebrandt [2004] has coupled a one-dimensionally distributed compressor model with a hybrid cycle for non-steady-state analysis of the compressor *surge* phenomenon.

Lumped models for design calculations simply consist of the thermodynamic relationship between input and output flow conditions according to specified performance values for pressure ratio and isentropic efficiency. If off-design operation is to be investigated, pressure ratio and isentropic efficiency will vary. The behaviour of these values as a function of shaft speed and mass flow for a specific turbomachine can be expressed through characteristic steady-state map representations [Campanari 2000; Costamagna 2001; Selimovic 2002a; Chan 2003a,b; Magistri 2004b]. The characteristic maps can be implemented either in a continuous analytical or a grid interpolation representation, depending on the type of solver approach. Because only few characteristic maps are published in open literature, many modellers apply scaling by the law of similitude [Hildebrandt 2005, Magistri 2004b] to adapt the turbomachinery size to the specific hybrid system. A simplification for the expander is to calculate the relationship between mass flow and inlet pressure by assuming choked conditions in the inlet [Campanari 2000, Selimovic 2002a]. However, no relationship for the efficiency can be established with this method.

3.4.2 Heat Exchanger

The recuperative heat exchangers are a further important component for the system characteristics and dynamics, as their effectiveness is dependent on the gas flows. In models, they are usually considered as adiabatic or affected by a small heat loss. Thermal capacity of the solid material has a strong influence on the dynamic behaviour and should thus not be neglected in non steady-state studies.

The simplest approach to model a steady-state heat exchanger is to calculate the outlet temperatures based on inlet conditions and a heat transfer efficiency coefficient. The approach can be used for design calculations. Methods for calculating off-design performance with specified heat exchanger geometry based on a lumped approach for heat transfer are available in literature [Kays 1984] and have been applied by Selimovic et al. [2002a] and Kimijima et al. [2002]. For dynamic behaviour, the lumped approach is, however, problematic: For large exchangers, calculating the heat in the solid based on a single temperature causes significant error in dynamic simulation. This is because in a heat exchanger the solid and gas temperatures at one point are usually very similar, while the temperature differences along the solid are huge. For dynamic simulations, a distributed heat exchanger model is therefore advantageous. A dynamic heat exchanger model has been applied by Magistri et al. [2004b].

3.4.3 Ejector

Ejectors are applied to overcome the pressure loss in an anodic recirculation loop. They are commonly assumed as adiabatic mixers, and must include an energy balance.

For design calculations, the simple specification of a mixing ratio is sufficient, provided that the fuel can be delivered at a pressure high enough to fulfil the momentum conservation. Off-design calculations on the other hand calculate the mixing ratio based on the specified ejector geometry, gas inlet conditions and internal gas dynamical processes. A useful "lumped" calculation approach is to draw section-wise momentum, mass and energy balances, i.e. for the Laval nozzle, mixing chamber and diffuser. Such an approach has been described by Marsano et al. [2004]. Ferrari et al. [2004] have compared a lumped model to a one-dimensional CFD model and achieved good matching. They also found that the transient time constant for an ejector of 1 m length is about 0.04 s. This means that ejector residence time can be neglected for hybrid system investigations.

3.4.4 Cycle Configurations

Most of the hybrid cycle models are based on a recuperated gas turbine process where the combustion chamber is replaced by a SOFC. The fuel cell is thus pressurised. However, many different configuration options for this "standard cycle" exist, most of which are summarised in Figure 3-1 (see also Chapter 2.4).

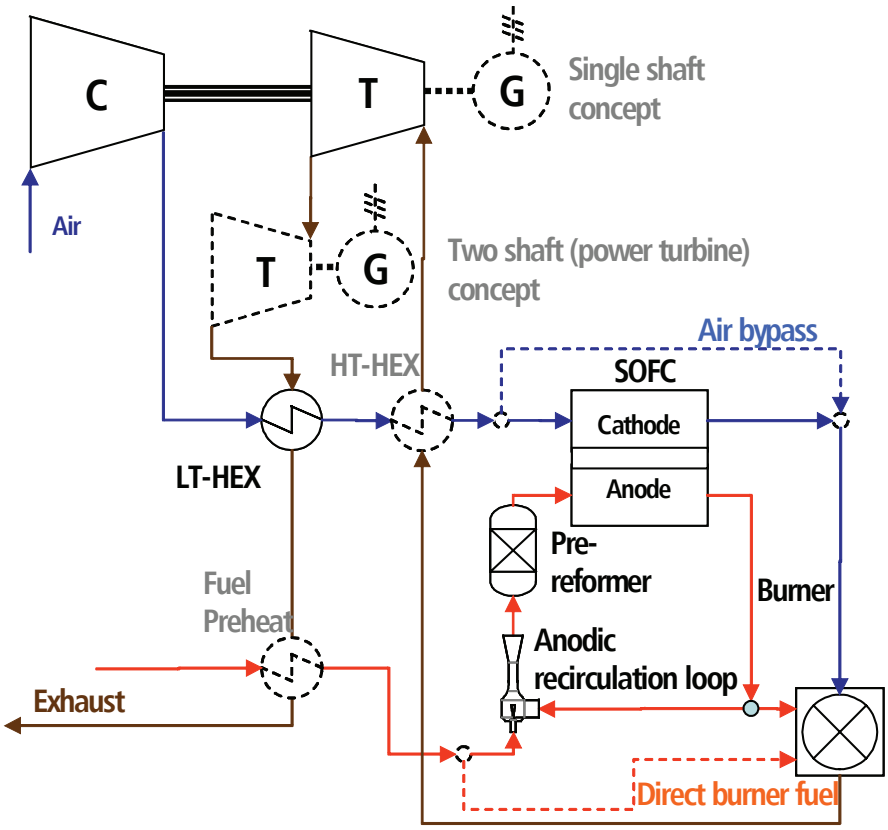

Figure 3-1: Options of the standard cycle

A choice which influences part-load operation and control is the gas turbine configuration. Single-shaft is the most common layout [Campanari 2000, 2004; Costamagna 2001; Uechi 2001; Kimijima 2002; Magistri 2003, 2004; Pålsson 2001; Rao 2001; Song 2005; Stiller 2005]. However, operation strategies with various as well as constant shaft speed pose technical and control problems. A further option is a two-shaft concept which includes a *turbo-charger* (compressor and turbine without generator) and a downstream *power turbine* driving a generator on a separate shaft [Chan 2002, 2003a,b; Rao 2002]. This offers the possibility of running the generator at constant speed and therewith grid synchronisation, although at the cost of a more complex system. A two-shaft system with two separate compressors and turbines has been presented by Yi et al. [2003, 2004]. The two-stage compression has been implemented to facilitate intercooling between the compressor stages.

Another option influencing the system behaviour is the implementation of a high temperature heat exchanger prior to the turbine. It has been modelled as a separate heat exchanger by Campanari [2004], Magistri et al. [2003], Selimovic et al. [2002a] and Stiller et al. [2005]. In the Siemens-Westinghouse tubular design, high temperature recuperation is inherently incorporated. This is reflected in models [Campanari 2000; Costamagna 2001; Magistri 2004; Song 2005].

Further cycle options are preheating of the fuel [Campanari 2000; Chan 2002, 2003b; Costamagna 2001; Magistri 2003, 2004b; Selimovic 2002a; Rao 2001, 2002; Yi 2004; Stiller 2005], variable air bypass around the fuel cell [Chan 2003b, Rao 2002; Yi 2003], and introducing extra fuel directly to the burner [Chan 2003a, b; Uechi 2001; Kimijima 2002; Selimovic 2002a; Rao 2001, 2002; Yi 2003; Stiller 2005].

Apart from the standard cycle and its options, some authors have also introduced significant novelties. Veyo et al. [2003] evaluated several cycle concepts. An interesting option is the indirect SOFC integration, where the turbine exhaust gas at atmospheric pressure is fed into the SOFC, and the exhaust of the SOFC recuperatively heats the compressed gas in order to drive the gas turbine cycle. Other concepts in the paper are turbo-charged SOFC where no generator is applied or an intercooled and reheated gas turbine cycle. The latter improves efficiency compared to the standard cycle, while the two other options decrease it.

Yi et al. [2004] introduced a cycle configuration without heat recuperation. Instead, a higher compression ratio elevates the air inlet temperature of the tubular SOFC to an adequate value. With an optimisation, electric efficiency of 75.8% based on LHV is claimed for a very large system of around 600 MW. Agnew et al. [2003] also presented a recuperator-less configuration for the novel Rolls-Royce integrated planar fuel cell configuration. This design incorporates a cathode recirculation for raising inlet temperatures. The intention is to save investment costs.

Janssen and Dijkstra [2003] have studied the use of membrane-based burners [Janssen 2003] in order to investigate the SOFC's potential for CO_2-free power generation. A

result was that the energetic CO_2 removal penalty was only half as high as for conventional systems.

Further investigations point at integration of SOFC into advanced gas turbine cycles such as humid air turbine (HAT) [Rao 2001; Kuchonthara 2003], combined gas and steam turbine cycles and steam injected gas turbine cycle (STIG) [Kuchonthara 2003]. The intention is to decrease the SOFC share of power production and thus investment costs without efficiency penalty.

3.4.5 Active Groups

Table 3-1 represents and characterises the work groups which are currently known to be active in hybrid system modelling and research in terms of publications. This list is not exhaustive and reflects only the author's knowledge and impression.

Table 3-1: Overview of active groups in hybrid cycle modelling

Institution	Location	Head persons	Models	Current Focuses
TPG	Genova, Italy	Massardo, A.D. Costamagna, P. Magistri, L. Traverso, A.	tubular SOFC IP-SOFC (RR)	part-load, dynamics, control strategy, cycle layout and design
Rolls-Royce	Derby, UK	Agnew, G. Bozzolo, M.		
Politecnico di Milano	Milano, Italy	Campanari, S. Iora, P.	tubular SOFC	cycle design, part-load
VOK-LTH	Lund, Sweden	Assadi, M. Torisson, T. Selimovic, A. Kemm, M. Hildebrandt, A.	planar SOFC, detailed compressor	dynamics, control, compressor surge modelling
SNU	Seoul, Korea	Song, T.W. Sohn, J.L.	tubular SOFC	cycle layout and design
Irvine/NFCRC	Irvine, USA	Rao, A.D. Yi, Y.	tubular SOFC	cycle layout and design
NETL/D.O.E.	Morgantown, USA	Tucker, D. Shelton, M.	lumped model	dynamics, control, startup
NTNU-EPT	Trondheim, Norway	Bolland, O. Thorud, B. Stiller, C.	tubular SOFC	part-load, dynamics, control
NTNU-ITK	Trondheim, Norway	Imsland, L. Kandepu, R.	lumped model	dynamics, control

3.5 Conclusions

A broad variety of models with different approaches is available in literature. The degree of detail to be used must be selected based on the purpose of the model. A flexible input-output structure is advantageous for model that should be used for different simulation modes. In hybrid cycle modelling, many different cycle options have been investigated so far, although the standard option appears to be the pressurised SOFC which replaces the combustion chamber of a recuperated gas turbine.

4 Model Toolbox

This chapter introduces the component models which serve as a "toolbox" for the modelling of SOFC/GT hybrid cycles. First, the common environment and premises for the whole toolbox are introduced. A structure for mathematical model description is introduced for clarity and quick comprehension. Subsequently, all models are explained sequentially in order of decreasing complexity.

The chapter shall describe the models in a mathematical way to allow reproduction by experienced modellers. However, due to the complexity of the work, only the mathematical elements of the models are described, but no detailed comments on implementation are provided.

4.1 Environment and Common Premises

All models are implemented in gPROMS (Process Systems Enterprise), an equation oriented modelling environment. The following section will give a brief introduction into the principles and structure of this tool; for further information it is referred to the gPROMS product page [PSE-online 2004] and the user guide [gPROMS 2004].

The general idea of the approach is that an equation system consisting of *variables* and predefined constants (called *parameters*) is implemented as it would be written on paper, and the solver provides simultaneous solution of all equations. The code is similar to typical programming languages. However, the main difference is that the equations do not have to be explicit as in the assignments of a programming language. Furthermore, the system is analysed and processed as a whole, i.e. the sequence of the problem formulation is irrelevant.

gPROMS allows for an arbitrary number of physical process *models* and connections between those. Complex flowsheet models can thus be decomposed into component sub-models (e.g. SOFC, compressor, etc.). These component models may be linked in higher-ranking *models* in terms of energy, material and information flows. An operation procedure (called *process*) is required to define the inputs to a model and to run it.

Despite being modular, the modelling environment requires common conventions for all models. Such conventions are mainly *variable types*, *connection types* and *physical property packages*. Furthermore, premises on the modelling approach are required that should be consistent throughout the whole model.

Variable Types

The *variable types* (e.g. "pressure", "molar fraction") are arbitrary and comprise lower and upper bounds, a default value for the first iteration and a physical unit. The latter does not indicate any check of the correctness of equations with respect to units; it just serves as a guideline for the programmer. Upper and lower bounds may be crucial with respect to solver stability and solution finding. The default value is only

important if no set of default values from a preceding calculation is available and no preset values are specified in the *process*. Due to the *variable types'* secondary importance for the model results, they are not listed here.

Connection Types

Connection types define the nature of the interfaces (called *ports*) between the *models*. They comprise variable sets which comprise all required data of the exchanged units. The purpose is to provide clear interfaces for the models and furthermore to allow for graphic flowsheeting. The following *connection types* have been defined for this work:

- **Energy** (flowsheeting colour: blue): Used for energy streams. It comprises the amount of power P (W) that is transferred between two units. The energy stream is for example used for the electrical transmission of power or for the connection between shaft and turbomachinery.
- **Material** (flowsheeting colour: orange): This is used where material streams are flowing between models. It comprises temperature T (K), pressure p (Pa), flow rate $\dot{n}$ (mol s^{-1}) and molar fraction of all species $x(1:7)$. Material connectors are applied in each component involving fluid flow.
- **Control** (flowsheeting colour: grey): This denotes an information stream. It comprises a signal variable S. It is used for any information signal transferred between components and the control system (for example flow measurements, control signals) and furthermore for spreading the shaft speed information between rotating components located on a common shaft.
- **Radiation** (flowsheeting colour: red): This is used for calculating the energy transferred by radiation between components. It comprises the temperatures of emitter T_e and recipient T_r (K) and the heat flow $\dot{q}$ (W) as one-dimensional distribution. The equation for the heat flow as a function of the temperatures must be included in one of the involved models. Radiation heat flow is assumed to appear between the SOFC tube and the indirect internal reformer as well as the stack casing.
- **PMap** (flowsheeting colour: green): With this connection type, the performance maps of compressors and turbines are coupled to the higher-ranking models which calculate the thermodynamics. It comprises dimensionless values of reduced mass flow $\overline{\dot{m}}'$, reduced shaft speed $\overline{N}'$, isentropic efficiency η_{is}, as well as the values of pressure ratio π, design pressure ratio π_0 and surge pressure ratio π_s.

Physical Property Package

gPROMS features different physical property packages as well as the ability to include external packages. For the current model, the inbuilt interface of the Multiflash

package (Infochem Computer Services Ltd) is applied. In order to define and customise Multiflash, a definition file with the following specifications is created:

- The Infochem fluids databank "INFODATA" is used as source for pure component data.
- Components included in mixture calculations are nitrogen, oxygen, hydrogen, methane, water, carbon monoxide and carbon dioxide.
- Binary interaction parameters for mixture calculations are based on the "oilandgas" databank.
- A model featuring advanced Soave-Redlich-Kwong with vapour pressure fitting, Peneloux volume shift and van der Waals mixing rules ("rksa psat lden vdw") is applied for fugacity, volume/density and enthalpy/entropy calculation.
- Simple mixing rules are applied for vapour viscosity ("vvs1") and thermal conductivity calculation ("vtc1").

The following functions are obtained from the physical property package:

- $M(x(1{:}7))$: Molecular weight (kg mol^{-1})
- $\rho(T,p,x(1{:}7))$: Vapour density (kg m^{-3})
- $v(T,p,x(1{:}7))$: Vapour molar volume (m^3 mol^{-1})
- $h(T,p,x(1{:}7))$: Vapour enthalpy (J mol^{-1})
- $s(T,p,x(1{:}7))$: Vapour entropy (J K^{-1} mol^{-1})
- $\lambda(T,p,x(1{:}7))$: Vapour thermal conductivity (W m^{-1} K^{-1})
- $\mu(T,p,x(1{:}7))$: Vapour dynamic viscosity (kg m^{-1} s^{-1})
- $c_p(T,p,x(1{:}7))$: Vapour heat capacity (J mol-1 K-1)
- $h_f^0(x(1{:}7))$: Standard enthalpy of formation at 25°C (J mol^{-1})
- $g^0(T,p,x(1{:}7))$: Standard gibbs free energy (J mol^{-1})
- $\kappa(T,p,x(1{:}7))$: Isentropic coefficient

Premises

The following premises apply to the model and all of its submodels:

- All fluids occur in the vapour phase.
- Beside the 7 components specified above, no other fluid components appear anywhere in the system.
- Gas dynamics are generally neglected (except in the ejector), it is assumed that the static pressure equals the total pressure.

4.2 Structure of Model Description

In the following, a recurring structure is used to describe the models in a logic and mathematically clear form. The structure will be described below. The structure items are non-numbered and only listed where they apply. Each model description is self-contained and can be studied independently from other text parts, relying only on Chapter 4.1 and 4.2. Due to the high frequency of occurrence and the low amount of interlinking with other parts of this work, only figures, tables and equations to which it is referred to elsewhere are numbered and catalogued. Likewise, symbols and parameter names will not be listed in the nomenclature. It has been tried to achieve a high degree of accordance between the symbols and names.

Icon

The icon which represents the model in gPROMS flowsheeting is displayed here. The icons will be used in flowsheets in the later chapters. The ports are marked in the icon; triangles with the tip into the icon represent inlet ports, triangles with the tip away from the icon represent outlet ports and squares stand for bi-directional (in/out) ports. Where necessary, port names are specified.

Purpose

This section explains the basic idea and approach of the model and its range of application.

Assumptions

The main assumptions that underlie the model are mentioned here.

Parameters

Parameters in gPROMS must be constant throughout a simulation and therefore do not add mathematical complexity to the problem. Default values may be defined with a parameter, which are used if the parameter is not set in the actual or a higher ranking model. This section shows the parameters of the model in tabular form. Names to be used in the equation section, a definition of the purpose and, where applicable, default values are given.

Distribution Domains

This section lists the domains over which distributed variables are spread. The discretisation method is given, which determines the direction of the finite difference method (FDM): BFDM, CFDM and FFDM stands for backward, centre and forward respectively. A rule of thumb is that variables connected to fluid flow and convectional effects should use FDM in the reverse flow direction (i.e. BFDM if the fluid flows into positive direction), while direction-independent phenomena should be modelled using CFDM. The order of the discretisation and the number of nodes are

furthermore listed. The array dimension of a distributed variable will be one more than the number of nodes.

Ports

The interfaces of the model are depicted in this section. The *port* name, a definition and the *connection type* are listed. Furthermore, the flow direction of each port is assigned as *in*, *out* or *bi-directional(in/out)*. The latter assignment does not influence the solver; it rather marks the natural flow direction of the *port* for the user. A statement about which ports should be connected is provided.

Variables

The model's internal variables are tabulated here. A definition and the unit are given. Where necessary, it is commented on typical input and output variables.

Note that in addition to the listed variables, the variables from the ports are to be used in the model. The variable names can be found in Chapter 4.1 (Connection Types). Port variables will generally be indexed with the respective port name.

Selectors

Selectors are suitable for modelling of asymmetric discontinuities. They can be seen as switches with an arbitrary number of positions. Each position determines a mode where a certain set of equations applies. The mode can be switched manually by a *process* or by automatic switch conditions. A definition of the selector, the modes and the default mode are tabulated.

Equations

The equations which connect the variables are shown here. It has to be pointed out that every equal sign stands for one equation. Variables from *ports* are denoted with the symbol as described in Chapter 4.1 (Connection types) and indexed with the *port* name. Terms where all occurring variables relate to one *port* are for simplicity denoted in brackets with the port name as index. Equations depending on the mode of a *selector* are shown tabularly, along with the mode switch conditions. Conditional equations programmed with *IF..THEN..ELSE* structure are shown as case differentiation.

Comments

Here, additional comments to the model are given. These may include statements on limitations, advices for proper use or particularities observed when using the model.

4.3 SOFC

4.3.1 Tubular SOFC Model

Icon

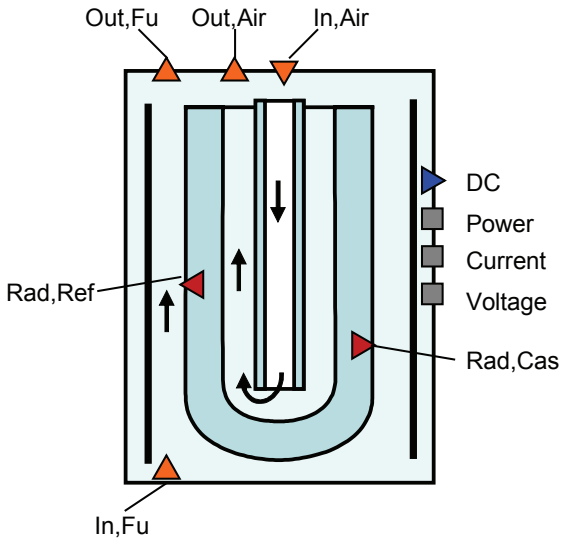

Purpose

The thermo-chemical model of the tubular SOFC is the most complex model of the toolbox. It describes a tubular fuel cell, based on the Siemens-Westinghouse design (see Chapter 2.1.3; Figure 2-4; Figure 2-8; Figure 2-9 for description; Figure 4-1 for geometry breakdown). The model includes convectional heat transfer between gases and solids as well as radiation and conduction between the solid materials. Gas flows are treated as plug flows. Kinetics of reforming and electrochemical reactions are included. The model is discretised in axial direction. The solid materials are furthermore discretised in radial direction, allowing for calculation of radial temperature gradients. The dynamics of heat and mass transfer are taken into account.

The development of the model was started by Bjørn Thorud in the beginning of his PhD project [Thorud 2005]. Thorud initially tried approaches with very high degree of spatial exactness and discretisation. It turned out that these approaches were too complex for the available solvers, and so the geometry was gradually simplified to the quasi-2D approach which is being used now. The model has continuously been updated and debugged by Thorud and the author. Development steps comprise inclusion of pressure losses, radiation heat exchange, energy and mass balance checks, carbon deposition checks, mathematical improvements, detailed kinetics of diffusion and activation and a calibration against available current-voltage data from Siemens-Westinghouse for hydrogen fuel.

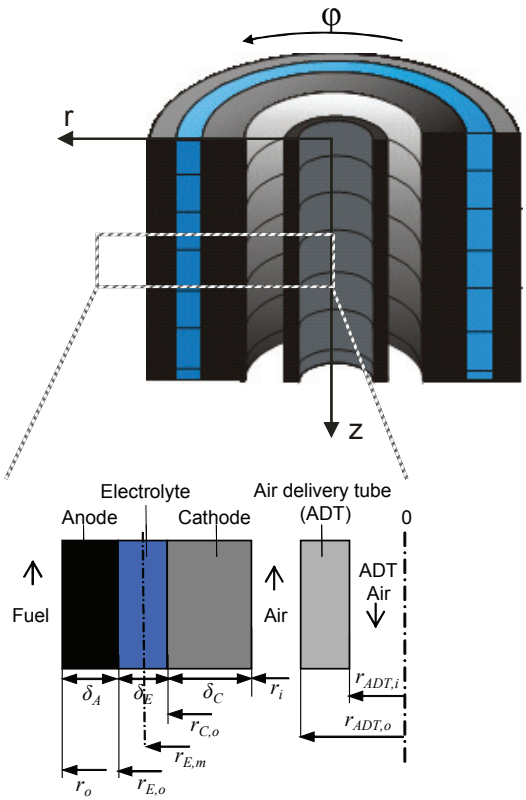

Figure 4-1: Geometry of the SOFC tube

Assumptions

The model describes a bundle of non-interacting fuel cell tubes; no stacking effects are considered. The upper and lower tube ends of the cell tube and ADT are adiabatic. The gas flows are modelled as plug flows. For heat transfer and pressure loss, laminar flow is assumed. The model is not discretised in circumferential direction. Diffusion is modelled steady state. The shift reaction is assumed to be always at equilibrium. The lumped pressure losses from laminar tube friction, inlet and outlet effects are calculated. All heat sources and sinks deriving from the reactions attack at the anode surface.

Parameters

Parameter	Definition	Unit	Default
n_T	Number of tubes	-	1152
l	Tube length	m	1.5
$r_{ADT,i}$	Inner radius of air delivery tube (see Fig. 4-1)	m	0.0025

$r_{ADT,o}$	Outer radius of air delivery tube (see Fig. 4-1)	m	0.004
r_i	Inner radius of cell tube (see Fig. 4-1)	m	0.00866
$r_{C,o}$	Outer radius of cathode layer (see Fig. 4-1)	m	0.01086
$r_{E,o}$	Outer radius of electrolyte layer (see Fig. 4-1)	m	0.01090
$r_{E,m}$	Middle radius of the electrolyte layer (see Fig. 4-1)	m	0.01088
r_o	Outer radius of cell tube (see Fig. 4-1)	m	0.011
δ_C	Thickness of the cathode (see Fig. 4-1)	m	0.0022
δ_E	Thickness of the electrolyte (see Fig. 4-1)	m	0.00004
δ_A	Thickness of the anode (see Fig. 4-1)	m	0.0001
v_C	Volume fraction of the cathode	-	0.933
v_E	Volume fraction of the electrolyte	-	0.019
v_A	Volume fraction of the anode	-	0.048
l_I	Circumferential length of the interconnect	m	0.006
δ_{Fu}	Thickness of a virtual annular fuel channel (to be determined from tube distance in the stack grid)	m	0.0023
A_{el}	Active surface of the fuel cell	m^2	0.0834
l_E	Circumferential length of the electrolyte	m	0.0616
A_{Fu}	Cross-sectional area of the fuel channel	m^2	$1.77 \cdot 10^{-4}$
$d_{Air,hyd}$	Hydraulic diameter of the cathode air channel	m	0.00932
$d_{Fu,hyd}$	Hydraulic diameter of the fuel channel	m	0.010
Nu	Nusselt number for laminar flow [Mills 1995]	-	4.364
Nu_{ADT}	Nusselt number for inner tube (laminar flow in annular ducts) [Rohsenow 1998]	-	10
Nu_C	Nusselt number for outer tube (laminar flow in annular ducts) [Rohsenow 1998]	-	7
Nu_A	Nusselt number for laminar flow between several tubes [Rohsenow 1998]	-	1.8
ξ_{Re}	Correction factor for Reynolds number in annlar ducts [White 2003]	-	1.5
$\zeta_{ADT,in}$	Pressure loss coefficient at ADT inlet (seamless transition to preheat tube)	-	0
$\zeta_{ADT,out}$	Pressure loss coefficient at ADT outlet (sudden area extension and flow direction reversal)	-	1
$\zeta_{C,in}$	Pressure loss coefficient at cathode inlet	-	0.5

	(assumption)		
$\zeta_{C,out}$	Pressure loss coefficient at cathode outlet (assumption)	-	0.5
$\zeta_{A,in}$	Pressure loss coefficient at anode inlet (assumption)	-	0.5
$\zeta_{A,out}$	Pressure loss coefficient at anode outlet (assumption)	-	0.5
$V_{diff}(1:7)$	Diffusion volumes for simple molecules [Reid 1987]	10^{-30} m^3	N_2:18.5 O_2:16.3 H_2: 6.12 CH_4:25.14 H_2O:13.1 CO:18.0 CO_2:26.9
α_{Ox}	Coefficient for the calculation of the oxygen diffusion coefficient	-	-0.069
γ_A, γ_C	Constants for activation polarisation (estimated)	A m^{-2}	$1.955 \cdot 10^{10}$, $1.061 \cdot 10^{10}$
β_A, β_C	Constants for Butler-Volmer equation	-	0.5
$E_{act,A}$, $E_{act,C}$	Activation energy at anode and cathode (estimated)	J mol^{-1}	140019, 48497
ε_C, ε_A	Porosity of cathode and anode	-	0.5, 0.4
τ_C, τ_A	Tortuosity of cathode and anode	-	1.5, 3
$r_{p,C}$, $r_{p,A}$	Pore diameter of cathode and anode	m	$4 \cdot 10^{-6}$, 10^{-6}
ρ_{ADT}	Density of ADT material (Al_2O_3) [Mills 1995]	kg m^{-3}	3970
ρ_C	Bulk density of cathode material [Tanaka 2000]	kg m^{-3}	5300
ρ_E	Density of electrolyte material [Tanaka 2000]	kg m^{-3}	6000
ρ_A	Bulk density of anode material (40% electrolyte material and 60% Nickel with 8900 kg m^{-3}) [Tanaka 2000]	kg m^{-3}	7740
ρ_{IC}	Density of interconnect material (Al_2O_3) [Tanaka 2000]	kg m^{-3}	4300
ρ_{MEA}	Mixed density of the MEA: $v_C\rho_C(1-\tau_C)+v_E\rho_E+v_A\rho_A(1-\tau_A)$	kg m^{-3}	see formula
c_C, c_E, c_A	Heat capacity of the layers [Bossel 1992]	J kg^{-1} K^{-1}	400, 500, 300

c_{MEA}	Mixed heat capacity of the MEA $\frac{v_C\rho_C(1-\tau_C)c_C + v_E\rho_E c_E + v_A\rho_A(1-\tau_A)c_A}{\rho_{MEA}}$	J kg^{-1} K^{-1}	see formula
c_{ADT}	Heat capacity of the ADT [Mills 1995]	J kg^{-1} K^{-1}	1167
k_C, k_E, k_A	Thermal conductivity of the layers [Gemmen 2000]	W K^{-1} m^{-1}	9.6, 2.7, 6.23
$k_{MEA,r}$	Thermal conductivity of the ADT, radial $\frac{\ln r_o / r_i}{\ln \frac{r_{C,o}}{r_i}\cdot\frac{1}{k_C} + \ln \frac{r_{E,o}}{r_{C,o}}\cdot\frac{1}{k_E} + \ln \frac{r_o}{r_{E,o}}\cdot\frac{1}{k_A}}$	W K^{-1} m^{-1}	see formula
$k_{MEA,z}$	Thermal conductivity of the ADT, axial $v_C k_C + v_E k_E + v_A k_A$	W K^{-1} m^{-1}	see formula
k_{ADT}	Thermal conductivity of the ADT [Mills 1995]	W K^{-1} m^{-1}	11.8
$\varepsilon_{Rad,C}$	Radiative emittance of the cathode	-	0.85
$\varepsilon_{Rad,ADT}$	Radiative emittance of the air delivery tube	-	0.85
$\tau_{C\text{-}ADT}$	Radiation transfer factor between ADT and cathode [Mills 1995] $\frac{\varepsilon_{Rad,ADT}}{1+(1-\varepsilon_{Rad,C})\left(\frac{\varepsilon_{Rad,ADT}\cdot r_{ADT,o}}{\varepsilon_{Rad,C}\cdot r_i}\right)}$	-	see formula

Distribution Domains

Domain	Definition	Discretisation	Order	Nodes
z_b	Axial direction (0:l), backward method	BFDM	2	40
z_f	Axial direction (0:l) , forward method	FFDM	2	40
z_c	Axial direction (0:l) , centre method	CFDM	2	40
r_{ADT}	Radial direction of ADT ($r_{ADT,i}$:$r_{ADT,o}$)	CFDM	2	3
r_{MEA}	Radial direction of MEA (r_i:r_o)	CFDM	2	3

Ports

Port	Definition	Type	Direction
In,Air	Inlet of air	Material	In
Out,Air	Outlet of air	Material	Out
In,Fu	Inlet of fuel	Material	In
Out,Fu	Outlet of fuel	Material	Out
Rad,Ref	Radiation to the reformer, distributed over z_c	Radiation	Out
Rad,Cas	Radiation to the casing, distributed over z_c	Radiation	Out
DC	DC power	Energy	Out
Power	Power signal	Control	In/Out
Voltage	Cell voltage	Control	In/Out
Current	Total current	Control	In/Out

The gas inlet or outlet ports must be connected. The radiation ports must be connected, or alternatively the recipient temperatures must be specified.

Variables

Variable	Definition	Unit
Temperatures		
$T_{ADTAir}(z_b)$	Temperature of the air in the ADT	K
$T_{ADT}(r_{ADT},z_c)$	Temperature of the ADT	K
$T_{Air}(z_f)$	Temperature of the air in the cathode channel	K
$T_{MEA}(r_{MEA},z_c)$	Temperature of the MEA	K
$T_{Fu}(z_f)$	Temperature of the fuel	K
Reactions		
$\Delta h_{Elc}(z_c)$	Enthalpy change of the electrochemical reaction	J mol^{-1}
$\Delta hR_{ef}(z_c)$	Enthalpy change of the reforming reaction	J mol^{-1}
$\Delta h_{Shi}(z_c)$	Enthalpy change of the shift reaction	J mol^{-1}
$\dot{r}_{Elc}(z_c)$	Rate of the electrochemical reaction	mol s^{-1}
$\dot{r}_{Ref}(z_c)$	Rate of the reforming reaction	mol s^{-1}
$\dot{r}_{Shi}(z_c)$	Rate of the shift reaction	mol s^{-1}
$K_{Shi}(z_c)$	Equilibrium constant of the shift reaction	-

Gas Properties		
$c_{p,Fu}(z_f)$	Heat capacity of fuel	J mol^{-1} K^{-1}
$c_{p,Air}(z_f)$	Heat capacity of cathode air	J mol^{-1} K^{-1}
$c_{p,ADT,Air}(z_b)$	Heat capacity of delivery tube air	J mol^{-1} K^{-1}
LHV_{In}	Lower heating value of inlet fuel	J mol^{-1}
LHV_{Out}	Lower heating value of outlet fuel	J mol^{-1}
Electrics		
$E^0(z_c)$	Standard potential	V
$E^{rev}(z_c)$	Reversible (open circuit) potential	V
$\eta_{act,A}(z_c)$, $\eta_{act,C}(z_c)$	Activation overpotential of anode and cathode respectively	V
$\eta_{diff,A}(z_c)$, $\eta_{diff,C}(z_c)$	Diffusion overpotential of anode and cathode respectively	V
$\eta_{ohm}(z_c)$	Ohmic overpotential	V
E	Cell voltage	V
$j(z_c)$	Distributed current density	A m^{-2}
J_t	Total current	A
j_t	Total current density	A m^{-2}
Loss Models		
$R_\Omega(z_c)$	Ohmic resistance of cell	Ω
R_D	Resistance added by degradation of the fuel cell (to be specified)	Ω
$J_E(z_c)$, $J_I(z_c)$	Lumped variable for electrolyte and interconnect resistance	-
$\rho_{\Omega,A}$, $\rho_{\Omega,C}$, $\rho_{\Omega,E}(z_c)$	Ohmic resistivity of anode, cathode and electrolyte	Ω m
$j_{0,A}$, $j_{0,C}(z_c)$	Exchange current density for anode and cathode	A m^{-2}
D_{H2}, D_{H2O}, $D_{O2}(z_c)$	Ordinary diffusion coefficients for reacting species	m^2 s^{-1}
$D_{K,H2}$, $D_{K,H2O}$, $D_{K,O2}(z_c)$	Knudsen diffusion coefficients for reacting species	m^2 s^{-1}
$D_{eff,H2}$, $D_{eff,H2O}$	Effective diffusion coefficients for anode species	m^2 s^{-1}
$x_{C,O2}$	Oxygen molar fraction at cathode surface	-
$x_{TPB,O2}$	Oxygen molar fraction at TPB	-
$x_{A,H2}$, $x_{A,H2O}$	Hydrogen and steam molar fraction at anode surface	-

$x_{TPB,H2}$, $x_{TPB,H2O}$	Hydrogen and steam molar fraction at TPB	-
Heat Transfer		
$h_{c,ADTAir\text{-}ADT}(z_b)$	Heat transfer coefficient between air in the ADT and ADT	W m^{-2} K^{-1}
$h_{c,Air\text{-}ADT}(z_f)$	Heat transfer coefficient between cathode air and ADT	W m^{-2} K^{-1}
$h_{c,Air\text{-}C}(z_f)$	Heat transfer coefficient between cathode air and cathode	W m^{-2} K^{-1}
$h_{c,Fu\text{-}A}(z_f)$	Heat transfer coefficient between fuel and anode	W m^{-2} K^{-1}
$\dot{q}_{C-ADT}(z_c)$	Radiation heat flow between cathode and ADT	W
τ_{Ref}	Transfer factor between anode and reformer	-
τ_{Cas}	Transfer factor between anode and casing	-
Flow Variables		
u_{ADTAir}, u_{Air}, u_{Fu}	Flow velocities for ADT air, cathode air and fuel respectively	m s^{-1}
Re_{ADTAir}, Re_{Air},Re_{Fu}	Reynolds numbers for ADT air, cathode air and fuel respectively	
f_{ADTAir},f_{Air},f_{Fu}	Friction coefficients for ADT air, cathode air and fuel respectively	-
Δp_{ADT}, Δp_C, Δp_A	Friction losses in ADT, cathode and anode channel	-
$p_{ADTAir,ref}$, $p_{Air,ref}$, $p_{Fu,ref}$	Reference pressure distribution of ADT air, cathode air and fuel for reactions heat transfer	Pa
$c_{Air}(z_c,7)$, $c_{Fu}(z_c,7)$	Molar concentrations of species in air and fuel	mol m^{-3}
$x_{Air}(z_c,7)$, $x_{Fu}(z_c,7)$	Molar fractions of species in air and fuel	-
Check Variables		
$T_{MEA,Max}$	Maximum local temperature in the MEA	K
$T_{MEA,Mean}$	Mean temperature in the MEA	K
$T_{MEA,Min}$	Minimum local temperature in the MEA	K
$dTdz_{MEA,Max}$	Max local axial temperature gradient in the MEA	K m^{-1}
$dTdr_{MEA,Max}$	Max local radial temperature gradient in the MEA	K m^{-1}
j_{min}	Minimum local current density	A m^{-2}
Δg_{CD}	Gibbs energy change of carbon deposition reaction	J mol^{-1}

ΔE	Relative energy balance around the system	-
ΔM	Relative mass flow balance around the system	-

The degradation resistance R_D must be specified (0 for the assumption of an new cell). Furthermore, the operation point must be specified by either total current J, current density j or the cell voltage E (alternatively the power P). The radiation transfer factors τ_{Ref} and τ_{Cas} must be specified.

Equations

The equation section is subdivided for better overview. For easier reading, a convention is that each axially distributed equation (over z) is valid for all $z \in [0,l]$ unless otherwise noted.

Boundary Equations

Small pressure losses over the flow channels are assumed. The reference pressures for the reactions and heat transfer are hydraulically set before the channel inlets. Hence, the pressure relationships are

$$p_{ADT,ref} = p_{In,Air}$$
$$p_{C,ref} = p_{In,Air} - \Delta p_{ADT}$$
$$p_{Air,Out} = p_{C,ref} - \Delta p_C$$

$$p_{A,ref} = p_{In,Fu}$$
$$p_{Out,Fu} = p_{A,ref} - \Delta p_A$$

The inlet temperatures from the ports are connected to the flow channel entrances (0: top of the tube, l: bottom of the tube)

$$T_{ADTAir}(0) = T_{In,Air}$$
$$T_{Fu}(l) = T_{In,Fu}$$

To account for enthalpy conservation at pressure changes, the outlet temperatures are gained implicitly by enthalpy balances:

$$h\left(T_{Air}(0), p_{C,ref}, x_{Out,Air}\right) = h\left(T_{Out,Air}, p_{Out,Air}, x_{Out,Air}\right)$$
$$h\left(T_{Fu}(0), p_{A,ref}, x_{Out,Fu}\right) = h\left(T_{Out,Fu}, p_{Out,Fu}, x_{Out,Fu}\right)$$

The air from the air delivery tube enters the cathode channel at the cell bottom:

$$h\left(T_{ADTAir}(l), p_{C,ref}, x_{In,Air}\right) = h\left(T_{Air}(l), p_{ADT,ref}, x_{In,Air}\right)$$

The species concentration and molar fraction of fuel and air at the inlet and outlet are calculated with the molar volume function:

$$c_{Air}(l,:) = \frac{x_{Air}(l,:)}{v\left(T_{Air}(l), p_{Air,ref}, x_{Air}(l,:)\right)}$$

$$c_{Fu}(l,:) = \frac{x_{Fu}(l,:)}{v\left(T_{Fu}(l), p_{Fu,ref}, x_{Fu}(l,:)\right)}$$

$$c_{Air}(0,:) = \frac{x_{Air}(0,:)}{v\left(T_{Air}(0), p_{Air,ref}, x_{Air}(0,:)\right)}$$

$$c_{Fu}(0,:) = \frac{x_{Fu}(0,:)}{v\left(T_{Fu}(0), p_{Fu,ref}, x_{Fu}(0,:)\right)}$$

The velocities distributions of the three flows are calculated from the continuity condition for the pressure loss calculation.

$$u_{ADTAir} = \dot{n}_{In,Air} \cdot \frac{v_{In,Air}}{r_{ADT,i}^2 \pi} \qquad -u_{Air} = \dot{n}_{In,Air} \cdot \frac{v\left(T_{Air}(l), p_{Air,ref}, x_{In,Air}\right)}{\left(r_i^2 - r_{ADT,o}^2\right)\pi}$$

$$-u_{Fu} = \dot{n}_{In,Fu} \cdot \frac{v\left(T_{Fu}(l), p_{Fu,ref}, x_{In,Fu}\right)}{A_{Fu}}$$

For the heat and mass transfer, the velocity of a flow path must be assumed as constant due to mathematical reasons. The velocities at the bottom of the tube (l) will be taken for these calculations.

The flow rates at the outputs are calculated according to the continuity equation:

$$\dot{n}_{Out,Air} = -u_{Air} \cdot \sum_{i=1}^{7} c_{Air}(0,i) \cdot \left(r_i^2 - r_{ADT,o}^2\right)\pi \qquad \dot{n}_{Out,Fu} = -u_{Fu} \cdot \sum_{i=1}^{7} c_{Fu}(0,i) \cdot A_{Fu}$$

The lower heating value of the inlet and outlet fuel:

$$LHV_X = x_X(H_2) \cdot \left(0 - h_f^0(H_2O)\right) + x_X(CH_4) \cdot \left(h_f^0(CH_4) - h_f^0(CO_2) - 2h_f^0(H_2O)\right) +$$
$$+ x_X(CO) \cdot \left(h_f^0(CO) - h_f^0(CO_2)\right) \quad \forall\, X \in \{In, Fuel; Out, Fuel\}$$

The upper and lower ends of the air delivery tube and the cell tube are assumed to be adiabatic:

$$\frac{\partial T_{ADT}(r,0)}{\partial z_c} = \frac{\partial T_{ADT}(r,l)}{\partial z_c} = 0 \quad \forall\, r \in \left[r_{ADT,i}, r_{ADT,o}\right]$$

$$\frac{\partial T_{MEA}(r,0)}{\partial z_c} = \frac{\partial T_{MEA}(r,l)}{\partial z_c} = 0 \quad \forall\, r \in \left[r_i, r_o\right]$$

Gas Properties, Heat Transfer and Flow Numbers

The relationship between the species concentration and mole fraction in the reacting gas channels:

$$x_{Air}(z,i)=\frac{c_{Air}(z,i)}{\sum_{j=1}^{7}c_{Air}(z,j)};\quad x_{Fu}(z,i)=\frac{c_{Fu}(z,i)}{\sum_{j=1}^{7}c_{Fu}(z,j)}\quad \forall\, i\in\{1:7\}$$

The heat transfer coefficients for all solid-gas interfaces are based on laminar flow and constant Nusselt number (thermal conductivities from physical property package):

$$h_{c,ADTAir-ADT}(z)=Nu\cdot\lambda\left(T_{ADTAir}(z),p_{ADTAir,ref},x_{In,Air}(:)\right)\cdot\frac{1}{2r_{ADT,i}}$$

$$h_{c,Air-ADT}(z)=Nu_{ADT}\cdot\lambda\left(T_{Air}(z),p_{Air,ref},x_{Air}(z,:)\right)\cdot\frac{r_i+r_{ADT,o}}{2\left(r_i^2-r_{ADT,o}^2\right)}$$

$$h_{c,Air-C}(z)=Nu_C\cdot\lambda\left(T_{Air}(z),p_{Air,ref},x_{Air}(z,:)\right)\cdot\frac{r_i+r_{ADT,o}}{2\left(r_i^2-r_{ADT,o}^2\right)}$$

$$h_{c,Fu-A}(z)=Nu_A\cdot\lambda\left(T_{Fu}(z),p_{Fu,ref},x_{Fu}(z,:)\right)\cdot\frac{2\pi r_o}{4A_{Fu}}$$

The heat capacities are obtained from the physical property package:

$$c_{p,ADTAir}(z)=c_p\left(T_{ADTAir}(z),p_{ADTAir,ref},x_{In,Air}(:)\right)$$

$$c_{p,Air}(z)=c_p\left(T_{Air}(z),p_{Air,ref},x_{Air}(z,:)\right)$$

$$c_{p,Fu}(z)=c_p\left(T_{Fu}(z),p_{Fu,ref},x_{Fu}(z,:)\right)$$

The Reynolds numbers are calculated at the entrances and assumed to be constant along the flow paths:

$$Re_{ADTAir}=\frac{\dot{n}_{In,Air}\cdot M_{In,Air}}{r_{ADT,i}^2\pi}\cdot\frac{2r_{ADT,i}}{\mu\left(T_{ADTAir}(0),p_{ADTAir,ref},x_{In,Air}(:)\right)}$$

$$Re_{Air}=-\frac{1}{\xi_{Re}}u_{Air}\cdot\sum_{i=1}^{7}c_{Air}(l,i)\cdot M\left(x_{Air}(:)\right)\cdot\frac{d_{Air,hyd}}{\mu\left(T_{Air}(l),p_{Air,ref},x_{Air}(l,:)\right)}$$

$$Re_{Fu}=-u_{Fu}\cdot\sum_{i=1}^{7}c_{Fu}(l,i)\cdot M\left(x_{Fu}(:)\right)\cdot\frac{d_{Fu,hyd}}{\mu\left(T_{Fu}(l),p_{Fu,ref},x_{Fu}(l,:)\right)}$$

Pressure Loss

The friction factors are calculated for laminar flow [Mills 1995]:

$$f_X=\frac{64}{Re_X}\quad \forall\, X\in\{ADTAir,Air,Fuel\}$$

Together with the friction coefficients at the entrances, the pressure losses in the gas channels are:

$$\Delta p_{ADT} = \left(\zeta_{ADT,in} + f_{ADTAir} \cdot \frac{l}{2r_{ADT,i}} + \zeta_{ADT,out} \right) \cdot \tfrac{1}{2} \cdot \rho\left(T_{ADTAir}(l), p_{ADTAir,ref}, x_{In,Air}(:)\right) \cdot u_{ADTAir}^2$$

$$\Delta p_C = \left(\zeta_{C,in} + f_{Air} \cdot \frac{l}{d_{Air,hyd}} + \zeta_{C,out} \right) \cdot \tfrac{1}{2} \cdot \rho\left(T_{Air}(l), p_{Air,ref}, x_{Air}(z,:)\right) \cdot u_{Air}^2$$

$$\Delta p_A = \left(\zeta_{A,in} + f_{Fu} \cdot \frac{l}{d_{Fu,hyd}} + \zeta_{A,out} \right) \cdot \tfrac{1}{2} \cdot \rho\left(T_{Fu}(l), p_{Fu,ref}, x_{Fu}(z,:)\right) \cdot u_{Fu}^2$$

Reactions

The heat of the reactions is:

$$\begin{aligned}
\Delta h_{Ref}(z) &= 3 \cdot \left(0 + h(H_2)\right) + \left(h_f^0(CO) + h(CO)\right) \\
&\quad - \left(h_f^0(CH_4) + h(CH_4)\right) - \left(h_f^0(H_2O) + h(H_2O)\right) \\
\Delta h_{Shi}(z) &= \left(0 + h(H_2)\right) + \left(h_f^0(CO) + h(CO)\right) \\
&\quad - \left(h_f^0(CO) + h(CO)\right) - \left(h_f^0(H_2O) + h(H_2O)\right) \\
\Delta h_{Elc}(z) &= \left(h_f^0(H_2O) + h(H_2O)\right) - \tfrac{1}{2}\left(h_f^0(O_2) + h(O_2)\right) \\
&\quad - \left(0 + h(H_2)\right) + 2 \cdot E \cdot F
\end{aligned}$$

with the enthalpy values at the middle electrolyte temperature $T_{MEA}(r_{E,m})$ and the reference pressure of the respective gas channel, i.e. $p_{Air,ref}$ for O_2, all other species $p_{Fu,ref}$.

Note that for the electrochemical reaction, a part of the enthalpy change is turned into electric power.

The reaction rate of the reforming reaction is determined using the common kinetic approach of Rechenauer [Achenbach 1994].

$$\dot{r}_{Ref}(z) = 4274 \cdot e^{-\frac{82000}{R_m \cdot T_{MEA}\left(r_{E,m},z\right)}} \cdot x_{Fu}(z, CH_4) \cdot \frac{p_{Fu,ref}}{10^6\,Pa} \cdot A_{el}$$

The shift reaction is assumed to be always at equilibrium. The equilibrium constant is determined from the change in standard Gibbs energy [Moran 2004]:

$$\ln\left(K_{Shi}(z)\right) = -\frac{g^0(H_2) + g^0(CO_2) - g^0(CO) - g^0(H_2O)}{R_m T_{MEA}\left(r_{E,m}, z\right)}$$

The reaction rate for the shift reaction is then

$$\dot{r}_{Shi}(z) = 10^4 \left(x_{Fu}(z, CO) \cdot x_{Fu}(z, H_2O) - \frac{x_{Fu}(z, H_2) \cdot x_{Fu}(z, CO_2)}{K_{Shi}(z)} \right) \quad \forall\, z \in [0, l)$$

$$\dot{r}_{Shi}(l) = 0$$

Note that the factor 10^4 is a sufficient proportional "gain" to ensure that the reaction rate is close to equilibrium. Higher numbers do not significantly increase the approach of equilibrium, but may cause solver problems. The reaction rate equation is coupled with the molar balance equations. As the molar composition at the fuel entrance ($z=l$) is specified, the reaction rate value at this point is meaningless.

The electrochemical reaction rate is calculated from the distributed current density

$$\dot{r}_{Elc}(z) = \frac{j(z) \cdot A_{el}}{2 \cdot F}$$

Electrics and Electrochemistry

The standard potential is calculated from the standard Gibbs energy:

$$E^0(z) = -\frac{g^0(H_2O) - \frac{1}{2} g^0(O_2) - g^0(H_2)}{2 \cdot F}$$

The reversible potential is calculated from the Nernst equation, applying Dalton's law:

$$E^{rev}(z) = E^0(z) - \frac{R_m T_{MEA}(r_{E,m}, z)}{2 \cdot F} \cdot \ln\left(\frac{x_{Fu}(z, H_2O)}{x_{Fu}(z, H_2)} \cdot \sqrt{\frac{10^5 Pa}{x_{Air}(z, O_2) \cdot p_{Air,ref}}} \right)$$

The total voltage balance is

$$S_{Voltage} = E = E^{rev}(z) - \eta_{ohm}(z) - \eta_{act,A}(z) - \eta_{act,C}(z) - \eta_{diff,A}(z) - \eta_{diff,C}(z)$$

The total current:

$$S_{Current} = J_t = \frac{A_{el}}{l} \int_{z=0}^{l} j(z) dz$$

The average current density:

$$j_t = \frac{J_t}{A_{el}}$$

The electric power:

$$S_{Power} = P_{DC} = E \cdot J_t$$

Ohmic Losses

The ohmic overpotential including degradation resistance is

$$\eta_{ohm}(z) = j(z) \cdot A_{el} \cdot \left(R_\Omega(z) + R_D \right)$$

The ohmic resistance by the layers is determined by an analytic representation for even distributed current from Nisancioglu [1989].

$$R_\Omega(z)=\frac{1}{l}\cdot\left(\frac{\left(\left(\frac{\rho_A(z)}{\delta_A}\right)^2+\left(\frac{\rho_C(z)}{\delta_C}\right)^2\right)\cosh(J_E)+\frac{\rho_A(z)\rho_C(z)}{\delta_A\delta_C}\left(2+J_E(z)\sinh(J_E(z))\right)}{2\left(\frac{1}{\rho_E(z)\delta_E}\right)^{1/2}\left(\frac{\rho_A(z)}{\delta_A}+\frac{\rho_C(z)}{\delta_C}\right)^{3/2}\sinh(J_E(z))}+\frac{\sqrt{\rho_I\delta_I\left(\frac{\rho_C}{\delta_C}\right)}}{2\tanh(J_I(z))}\right)$$

where

$$J_E(z)=\frac{l_E}{2}\sqrt{\frac{1}{\rho_E(z)\delta_E}\left(\frac{\rho_A(z)}{\delta_A}+\frac{\rho_C(z)}{\delta_C}\right)};\qquad J_I(z)=\frac{l_I}{2}\sqrt{\frac{1}{\rho_I\delta_I}\cdot\frac{\rho_A(z)}{\delta_A}}$$

This approach assumes that current flows only in radial direction in the electrolyte and circumferential direction in the electrodes and furthermore an even circumferential current distribution in the electrolyte.

The layer resistivity values are calculated temperature dependent [Bossel 1992]:

$$\rho_E(z)=2.994\cdot10^{-5}\cdot e^{\frac{10300}{T_{MEA}(r_{E,m},z)}}$$

$$\rho_A(z)=1.053\cdot10^{-8}\cdot T_{MEA}(r_{E,m},z)\cdot e^{\frac{1150}{T_{MEA}(r_{E,m},z)}}$$

$$\rho_C(z)=2.381\cdot10^{-8}\cdot T_{MEA}(r_{E,m},z)\cdot e^{\frac{1200}{T_{MEA}(r_{E,m},z)}}$$

The resistivity of the interconnect layer is assumed to be temperature independent. The value from Nisancioglu [1989] is used:

$$\rho_I\delta_I=2\cdot10^{-7}\ \Omega m^2$$

Activation Losses

A relationship between activation overpotential and current is the Butler-Volmer equation for anode and cathode:

$$j(z)=j_{0,A}(z)\cdot\left(e^{\frac{\beta_A\cdot2F}{R_mT_{MEA}(r_o,z)}\eta_{act,A}(z)}-e^{-\frac{(1-\beta_A)\cdot2F}{R_mT_{MEA}(r_o,z)}\eta_{act,A}(z)}\right)$$

$$j(z)=j_{0,C}(z)\cdot\left(e^{\frac{\beta_C\cdot2F}{R_mT_{MEA}(r_i,z)}\eta_{act,C}(z)}-e^{-\frac{(1-\beta_C)\cdot2F}{R_mT_{MEA}(r_i,z)}\eta_{act,C}(z)}\right)$$

Equation 4-1

The therefore required exchange current densities for the anode and cathode are:

$$j_{0,A}(z)=\gamma_A\cdot\left(x_{Fu}(z,H_2)+x_{Fu}(z,CO)\right)^{\beta_A}\cdot\left(x_{Fu}(z,H_2O)+x_{Fu}(z,CO_2)\right)^{1-\beta_A}\cdot e^{-\frac{E_{act,A}}{R_mT_{MEA}(r_i)}}$$

$$j_{0,C}(z)=\gamma_C\cdot x_{Air}(z,O_2)^{\beta_A}\cdot e^{-\frac{E_{act,C}}{R_mT_{MEA}(r_o)}}$$

The coefficients γ_A and γ_C and the activation energy values $E_{act,A}$ and $E_{act,C}$ have been defined by Thorud [2005] applying parameter estimation with Siemens-Westinghouse experimental results.

Diffusion Losses

The diffusion losses arise from the fact that the concentration of the reacting species, i.e. O_2, H_2 and H_2O, at the triple phase boundary (TPB) varies from the bulk concentration due to diffusion resistance in the porous electrodes. The voltage corrections for anode and cathode based on the Nernst equation are

$$\eta_{diff,A}(z) = \frac{R_m T_{MEA}(r_o, z)}{2 \cdot F} \cdot \ln\left(\frac{x_{Fu}(z, H_2)}{x_{TPB,H_2}(z)} \cdot \frac{x_{TPB,H_2O}(z)}{x_{Fu}(z, H_2O)} \right)$$

$$\eta_{diff,C}(z) = \frac{R_m T_{MEA}(r_i, z)}{2 \cdot F} \cdot \ln\left(\frac{x_{Air}(z, O_2)}{x_{TPB,O_2}(z)} \right)$$

Diffusion is a transient phenomenon, but the expected time constants are below one second [Qi 2005] and thus a steady-state approach is chosen.

Two serial diffusion phenomena occur in the cell; one between the bulk gas phase to the electrode surface and one in the porous electrode, i.e. between electrode surface and TPB.

On the air side, a binary gas mixture is present where only oxygen is diffusing. The diffusion coefficient from the bulk phase to the cathode surface can thus be determined by the Fuller equation [Reid 1987]:

$$D_{O_2}(z) = \frac{1.43 \cdot 10^{-7} \cdot T_{Air}(z)^{1.75}}{\frac{p_{Air,ref}}{10^5\,Pa} \cdot \left(\frac{2}{M(O_2)^{-1} + M(N_2)^{-1}} \right)^{1/2} \cdot \left(V_{diff}(O_2)^{1/3} + V_{diff}(N_2)^{1/3} \right)^2}$$

Therewith the oxygen concentration at the cathode surface is

$$x_{C,O_2}(z) = 1 + \left(x_{Air}(z, O_2) - 1 \right) \cdot e^{\frac{j(z) R_m T_{MEA}(r_i, z)}{4F \cdot p_{Air,ref} \cdot D_{O_2}(z)} \cdot \frac{r_i - r_{ADT,o}}{2}}$$

The Knudsen model is applied for diffusion in the porous electrode. The diffusion coefficient is

$$D_{K,O_2}(z) = \frac{2}{3} r_{p,C} \cdot \sqrt{\frac{8RT_{MEA}(r_i, z)}{\pi M_{O_2}}}$$

where the square root expresses the average molecular speed of the oxygen. The oxygen molar fraction at the TPB is specified implicitly by

$$\frac{\left(D_{K,O_2}(z)\cdot\left(\alpha x_{C,O_2}(z)-1\right)-D_{O_2}(z)\right)\cdot\left(x_{TPB,O_2}(z)-1\right)}{\left(D_{K,O_2}(z)\cdot\left(\alpha x_{TPB,O_2}(z)-1\right)-D_{O_2}(z)\right)\cdot\left(x_{C,O_2}(z)-1\right)}=$$

$$=e^{\frac{\tau_C R_m j(z)\cdot T_{MEA}(r_i,z)\cdot\left(D_{O_2}(z)-(\alpha-1)D_{K,O_2}(z)\right)}{4F\varepsilon_C D_{O_2}(z)\cdot D_{K,O_2}(z)}\cdot\delta_C}$$

On the fuel side, hydrogen and steam are diffusing. As five species are present, a mixing rule must be applied for the calculation of the diffusion coefficient from the bulk phase to the anode surface [Mills 1995].

$$D_i(z)=\frac{1-x_{Fu}(z,i)}{\sum_j \frac{x_{Fu}(z,i)}{D_{i,j}}}$$

with the following species for i and j:

i	j
H2	CH4, H2O, CO, CO2
H2O	H2, CH4, CO, CO2

Applying the Fuller equation for the mutual diffusion coefficients $D_{i,j}$, the above equation is extended to:

$$D_i(z)=\frac{1-x_{Fu}(z,i)}{\sum_j \frac{x_{Fu}(z,i)\cdot\frac{p_{Fu,ref}}{10^5\,Pa}\cdot\left(\frac{2}{M(i)^{-1}+M(j)^{-1}}\right)^{1/2}\cdot\left(V_{diff}(i)^{1/3}+V_{diff}(j)^{1/3}\right)^2}{1.43\cdot10^{-7}\cdot T_{Fu}(z)^{1.75}}}$$

The mole fractions at the anode surface are:

$$x_{A,i}(z)=x_{Fu}(z,i)-\frac{j(z)R_m T_{MEA}(r_o,z)}{2F\cdot p_{Fu,ref}\cdot D_i(z)}\cdot\frac{\delta_{Fu}}{2}\quad\forall\, i\in\{H_2,H_2O\}$$

The Knudsen diffusion coefficients in the porous anode material are:

$$D_{K,i}(z)=\frac{2}{3}r_{p,A}\cdot\sqrt{\frac{8RT_{MEA}(r_o,z)}{\pi M_i}}\quad\forall\, i\in\{H_2,H_2O\}$$

The ordinary and Knudsen diffusion coefficient yield the effective diffusion coefficient:

$$D_{eff,i}(z)=\frac{D_i(z)\cdot D_{K,i}(z)}{D_i(z)+D_{K,i}(z)}\cdot\frac{\varepsilon_A}{\tau_A}\quad\forall\, i\in\{H_2,H_2O\}$$

The molar fractions at the TPB can therewith be expressed explicitly:

$$x_{TPB,i}(z) = x_{A,i}(z) - \frac{j(z) R_m T_{MEA}(r_o, z)}{2F \cdot p_{Fu,ref} \cdot D_{eff,i}(z)} \cdot \delta_A \quad \forall\, i \in \{H_2, H_2O\}$$

Heat Transfer

Beginning in the middle of the tubular cell, the heat transport equation for the air in the air delivery tube (ADT) is:

$$\sum_{i=1}^{7} c_{Air}(l,i) \cdot c_{p,ADTAir}(z) \cdot \left(\frac{dT_{ADTAir}(z)}{dt} + u_{ADTAir}(l) \cdot \frac{\partial T_{ADTAir}(z)}{\partial z_b} \right)$$
$$= \frac{2}{r_{ADT,i}} \cdot h_{c,ADTAir-ADT}(z) \cdot \left(T_{ADT}(r_{ADT,i}, z) - T_{ADTAir}(z) \right) \quad \forall\, z \in (0, l]$$

Note that because no reactions occur in the ADT, the concentrations at the cathode air entry are used.

The boundary heat transfer between ADT air and ADT:

$$k_{ADT} \cdot \frac{\partial T_{ADT}(r_{ADT,i}, z)}{\partial r_{ADT}} = h_{c,ADTAir-ADT}(z) \cdot \left(T_{ADT}(r_{ADT,i}, z) - T_{ADTAir}(z) \right) \quad \forall\, z \in (0, l)$$

The heat conduction in radial and axial direction inside the ADT:

$$c_{ADT} \cdot \rho_{ADT} \cdot \frac{dT_{ADT}(r,z)}{dt}$$
$$= k_{ADT} \cdot \left(\frac{\partial^2 T_{ADT}(r,z)}{\partial {z_c}^2} + \frac{\partial \left(r \cdot \partial T_{ADT}(r,z) \right)}{r \cdot \partial {r_{ADT}}^2} \right) \quad \forall\, r \in (r_{ADT,i}, r_{ADT,o}), z \in (0, l)$$

The boundary heat transfer between ADT and cathode air (including radiation from the cathode surface):

$$k_{ADT} \cdot \frac{\partial T_{ADT}(r_{ADT,o}, z)}{\partial r_{ADT}} = -h_{c,Air-ADT}(z) \cdot \left(T_{ADT}(r_{ADT,o}, z) - T_{Air}(z) \right) + \frac{\dot{q}_{C-ADT}(z)}{2\pi r_{ADT,o} l} \quad \forall\, z \in (0, l)$$

The heat transport in the cathode air:

$$\sum_{i=1}^{7} c_{Air}(z,i) \cdot c_{p,Air}(z) \cdot \left(\frac{dT_{Air}(z)}{dt} + u_{Air}(l) \cdot \frac{\partial T_{Air}(z)}{\partial z_f} \right)$$
$$= \frac{2 \cdot r_{ADT,o}}{r_i^2 - r_{ADT,o}^2} \cdot h_{c,Air-ADT}(z) \cdot \left(T_{ADT}(r_{ADT,o}, z) - T_{Air}(z) \right)$$
$$+ \frac{2 \cdot r_i}{r_i^2 - r_{ADT,o}^2} \cdot h_{c,Air-C}(z) \cdot \left(T_{MEA}(r_i, z) - T_{Air}(z) \right) \qquad \forall\, z \in (0, l)$$

The boundary heat transfer between cathode air and cathode (including radiation to the ADT surface):

$$k_{MEA,r} \cdot \frac{\partial T_{MEA}(r_i,z)}{\partial r_{MEA}} = h_{c,Air-C}(z) \cdot \left(T_{MEA}(r_i,z) - T_{Air}(z)\right) + \frac{\dot{q}_{C-ADT}(z)}{2\pi r_i l} \quad \forall\, z \in (0,l)$$

The heat transfer in radial and axial direction inside the MEA (note different heat conductivities in radial and axial direction)

$$c_{MEA} \cdot \rho_{MEA} \cdot \frac{dT_{MEA}(r,z)}{dt} = k_{MEA,z} \cdot \frac{\partial^2 T_{MEA}(r,z)}{\partial z_c^{\,2}} + k_{MEA,r} \cdot \frac{\partial\left(r \cdot \partial T_{MEA}(r,z)\right)}{r \cdot \partial r_{MEA}^{\,2}} \quad \forall\, r \in (r_i,r_o), z \in (0,l)$$

The boundary heat transfer between the anode and the fuel (including heat of reactions and radiation to the reformer and the casing):

$$k_{MEA,r} \cdot \frac{\partial T_{MEA}(r_o,z)}{\partial r_{MEA}} = -h_{c,Fu-A}(z) \cdot \left(T_{MEA}(r_o,z) - T_{Fu}(z)\right) - \frac{\dot{r}_{Ref}\Delta h_{Ref} + \dot{r}_{Shi}\Delta h_{Shi} + \dot{r}_{Elc}\Delta h_{Elc} + \dot{q}_{Rad,Ref}(z) + \dot{q}_{Rad,Cas}(z)}{2\pi r_o l} \quad \forall\, z \in (0,l)$$

Finally, the heat transport in the fuel:

$$\sum_{i=1}^{7} c_{Fu}(z,i) \cdot c_{p,Fu}(z) \cdot \left(\frac{dT_{Fu}(z)}{dt} + u_{Fu}(l) \cdot \frac{\partial T_{Fu}(z)}{\partial z_f}\right) = \frac{2\pi \cdot r_o}{A_{Fu}} \cdot h_{c,Fu-A}(z) \cdot \left(T_{MEA}(r_o,z) - T_{Fu}(z)\right) \quad \forall\, z \in [0,l)$$

Mass Transfer

On the air side, only for oxygen a sink term exists:

$$\frac{dc_{Air}(z,O_2)}{dt} + u_{Air}(l)\frac{\partial c_{Air}(z,O_2)}{\partial z_c} = \frac{-\frac{1}{2}\dot{r}_{Elc}(z)}{l \cdot \left(r_i^2 - r_{ADT,o}^2\right)\pi} \quad \forall\, z \in [0,l)$$

for all other components i:

$$\frac{dc_{Air}(z,i)}{dt} + u_{Air}(l)\frac{\partial c_{Air}(z,i)}{\partial z_c} = 0 \quad \forall\, z \in [0,l), i \in \{N_2, H_2, CH_4, H_2O, CO, CO_2\}$$

On the fuel side, no source or sink terms exists for nitrogen and oxygen:

$$\frac{dc_{Fu}(z,i)}{dt} + u_{Fu}(l)\frac{\partial c_{Fu}(z,i)}{\partial z_c} = 0 \quad \forall\, z \in [0,l), i \in \{N_2, O_2\}$$

The mass transfer equations for the remaining species are:

$$\frac{dc_{Fu}(z,H_2)}{dt}+u_{Fu}(l)\frac{\partial c_{Fu}(z,H_2)}{\partial z_c}=\frac{3\dot{r}_{Ref}(z)+\dot{r}_{Shi}(z)-\dot{r}_{Elc}(z)}{l\cdot A_{Fu}} \quad \forall\, z\in[0,l)$$

$$\frac{dc_{Fu}(z,CH_4)}{dt}+u_{Fu}(l)\frac{\partial c_{Fu}(z,CH_4)}{\partial z_c}=\frac{-\dot{r}_{Ref}(z)}{l\cdot A_{Fu}} \quad \forall\, z\in[0,l)$$

$$\frac{dc_{Fu}(z,H_2O)}{dt}+u_{Fu}(l)\frac{\partial c_{Fu}(z,H_2O)}{\partial z_c}=\frac{-\dot{r}_{Ref}(z)-\dot{r}_{Shi}(z)+\dot{r}_{Elc}(z)}{l\cdot A_{Fu}} \quad \forall\, z\in[0,l)$$

$$\frac{dc_{Fu}(z,CO)}{dt}+u_{Fu}(l)\frac{\partial c_{Fu}(z,CO)}{\partial z_c}=\frac{\dot{r}_{Ref}(z)-\dot{r}_{Shi}(z)}{l\cdot A_{Fu}} \quad \forall\, z\in[0,l)$$

$$\frac{dc_{Fu}(z,CO_2)}{dt}+u_{Fu}(l)\frac{\partial c_{Fu}(z,CO_2)}{\partial z_c}=\frac{\dot{r}_{Shi}(z)}{l\cdot A_{Fu}} \quad \forall\, z\in[0,l)$$

Radiation

The radiation heat flow between the cathode and the ADT is:

$$\dot{q}_{C-ADT}(z)=\tau_{C-ADT}\cdot\sigma_B\cdot\left(T_{MEA}(r_i,z)^4-T_{ADT}(r_{ADT,o},z)^4\right)$$

The radiation heat flow from the anode surface to the reformer is

$$\dot{q}_{Rad,Ref}(z)=\tau_{Ref}\cdot\sigma_B\cdot\left(T_{e,Ref}(z)^4-T_{r,Ref}(z)^4\right)$$

where the recipient temperature from the radiation port *Ref* is specified in the reformer (IIR) model and the emitter temperature is

$$T_{e,Ref}(z)=T_{MEA}(r_o,z)$$

The radiation heat flow from the anode surface to the stack casing is analogously

$$\dot{q}_{Rad,Cas}(z)=\tau_{Cas}\cdot\sigma_B\cdot\left(T_{e,Cas}(z)^4-T_{r,Cas}(z)^4\right)$$

and also here the recipient temperature is specified in the connected model (casing) and the emitter temperature is

$$T_{e,Cas}(z)=T_{MEA}(r_o,z)$$

Note that all heat flows are related to the whole length of the tube.

Check Variables

The check variables are outputs not required elsewhere in the equation system. Their purpose is the surveillance of important physical parameters as well as the correctness of the model.

The local temperature maximum and minimum in the MEA is

$$T_{MEA,Max} = \max\left(T_{MEA}\right) \qquad T_{MEA,Min} = \min\left(T_{MEA}\right)$$

Assuming $r_o - r_i \ll r_i$, the mean temperature over the MEA is

$$T_{MEA,Mean} = \frac{1}{l \cdot \left(r_o - r_i\right)} \int_{z=0}^{l} \int_{r=r_i}^{r_o} T_{MEA}\left(r,z\right) dr\, dz$$

The local heat gradient maxima in radial and axial direction of the MEA are

$$dTdz_{MEA,Max} = \max\left(\frac{\partial T_{MEA}\left(r,z\right)}{\partial z_c}\right); \qquad dTdr_{MEA,Max} = \max\left(\frac{\partial T_{MEA}\left(r,z\right)}{\partial r_{MEA}}\right)$$

The minimum current density occurring in the cell is

$$j_{min} = \min\left(j\right)$$

The change in Gibbs energy for carbon deposition is

$$\Delta g_{CD}\left(z\right) = \left(2 \cdot g_{0,C} + g_0\left(z,CO_2\right) + 2 \cdot g_0\left(z,H_2\right) - g_0\left(z,CH_4\right) - 2 \cdot g_0\left(z,CO_2\right)\right) + R_m T_{MEA}\left(r_o,z\right) \cdot \ln\frac{x_{Fu}\left(z,CO_2\right) \cdot x_{Fu}\left(z,H_2\right)^2}{x_{Fu}\left(z,CH_4\right) \cdot x_{Fu}\left(z,CO\right)^2}$$

Note that the reaction for which the Gibbs energy change has been calculated is

$$CH_4 + 2CO \rightleftharpoons 2C + 2H_2 + CO_2$$

This reaction is the sum of the Boudouard reaction

$$2CO \rightleftharpoons C + CO_2$$

and the methane cracking reaction

$$CH_4 \rightleftharpoons C + 2H_2$$

It is assumed that if the combined reaction moves to the left, carbon deposition is not an issue (if one reaction produces carbon, the other reaction will immediately consume it). Carbon deposition occurs if the calculated Gibbs energy change is negative.

The relative overall energy balance is

$$\Delta E = 1 - \frac{\dot{n}_{Out,Air} h_{Out,Air} + n_{Out,Fu}\left(h_{Out,Fu} + LHV_{Out}\right) + P + \frac{1}{l}\int_{z=0}^{l} \dot{q}_{Rad,Ref} + \dot{q}_{Rad,Cas} dz}{\dot{n}_{In,Air} h_{In,Air} + n_{In,Fu}\left(h_{In,Fu} + LHV_{In}\right)}$$

The relative overall mass balance is

$$\Delta M = 1 - \frac{\dot{n}_{Out,Air} M_{Out,Air} + \dot{n}_{Out,Fu} M_{Out,Fu}}{\dot{n}_{In,Air} M_{In,Air} + \dot{n}_{In,Fu} M_{In,Fu}}$$

Mass and energy balance should in steady state operation be zero. A deviation of 0.01 (=1%) for the energy and 0.005 (=0.5%) for the mass balance is regarded as tolerable.

Comments

The fuel cell model involves several thousand variables and is therewith the largest model of the toolbox. Furthermore, it has many non-linear equations and hence the solver stability is an issue with this model.

A general problem in detailed modelling is the lack of accurate data of the fuel cells. Hence it is easy to put up a physical approach for most of the occurring phenomena, but it is difficult to calibrate the model without reliable information about properties of the applied materials and experimental results. A small comfort is, however, that the hybrid cycle is rather insensitive to the exact fuel cell character, and also internal effects are expected to at least show qualitatively correct trends.

In the Siemens-Westinghouse configuration, the tubes are connected to burner and air preheater at the top of the cell. The assumption of adiabatic tube ends is nevertheless fair, as the tube thicknesses and hence heat conduction in axial direction is small. Experiments showed a temperature change of not more than 1K at the node next to the boundary. The large axial temperature gradients at the boundaries are not regarded as critical, as there will be no electrolyte and anode material at this section.

Due to the limited number of nodes, the energy balance can show deviation of up to 1% in some operation points.

4.4 Turbomachinery

4.4.1 Compressor and Turbine

The models of compressor and turbine are very similar and are thus treated together here.

Icons

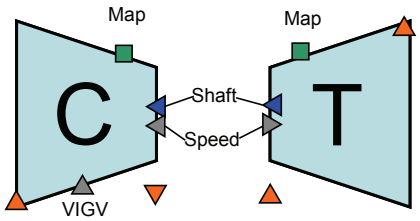

Purpose

The compressor and turbine models provide the standard thermodynamic equations for the input-output relationships of the working fluid based on pressure ratio and isentropic efficiency. The latter values are determined by performance map models which are linked to the compressor and turbine models. The models furthermore provide scaling of the turbomachinery. This implies the existence of dimensionless and design point variables. For the compressor, a simple approach to variable inlet guide vanes (VIGV) has been implemented: The VIGV linearly scale the mass flow, while no other parameters are affected. This simplification has been decided by considering literature data on a small centrifugal compressor [Ishino 1999] and has also been implemented by other modellers [Ulfsnes 2006]. In gas turbine cycles, the changed relationship between mass flow and pressure will cause a change in the operation point and therewith also a different pressure.

The basic model was developed by Ragnhild Ulfsnes [Ulfsnes 2006].

Assumptions

The models are steady state, which is regarded as sufficient for turbomachinery calculations (see Chapter 3.4.1). The variable inlet guide vane affects only the mass flow variable of the compressor performance.

Ports

Port	Definition	Type	Direction
In	Inlet port	Material	In
Out	Outlet port	Material	Out
Shaft	Shaft power	Energy	In
Speed	Shaft speed	Control	In
Map	Performance map interface	PMap	In/Out
VIGV (*only compressor*)	Position of the variable inlet guide vane	Control	In

One material port and all other ports must be connected.

Variables

Variable	Definition	Unit
$\dot{m}$	mass flow through the turbomachine	kg/s
T_s	Isentropic endpoint temperature	K
Δh	Specific enthalpy change	J K^{-1} mol^{-1}
$T_{In,0}$	Design point inlet temperature	K
$p_{In,0}$	Design point inlet pressure	Pa
$\dot{m}_0$	Design point mass flow	kg/s
$M_{In,0}$	Design point inlet molar weight	kg mol^{-1}
κ_0	Design point isentropic coefficient	-
N_0	Design point shaft speed	s^{-1}
$\overline{T}_{In}$	Dimensionless inlet temperature	-
$\overline{p}_{In}$	Dimensionless inlet pressure	-
$\overline{M}_{In}$	Dimensionless inlet molar weight	-
$\overline{\kappa}_{In}$	Dimensionless inlet isentropic coefficient	-
$\overline{\dot{m}}$	Dimensionless mass flow	-
$\overline{N}$	Dimensionless shaft speed	-
$\overline{\pi}$	Dimensionless pressure ratio	-

In design mode, all dimensionless values must be assigned unity. This grants that the compressor is in design point and a set of design point values for off-design mode can be obtained. In off-design mode, all design point variables must be assigned.

Equations

Boundaries

Flow rate and composition at inlet and outlet are equal

$$\dot{n}_{In} = \dot{n}_{Out}; \quad x_{In}(:) = x_{Out}(:)$$

The pressure relationship:

Compressor $\frac{p_{Out}}{p_{In}} = \pi_{Map}$ Turbine $\frac{p_{In}}{p_{Out}} = \pi_{Map}$

The mass flow is calculated as:

$$\dot{m} = \left(\dot{n} \cdot \sum_{i=1}^{7} M(i) x(i) \right)_{In}$$

Outlet temperature and power

The isentropic endpoint temperature T_s is determined by

$$s\left(T_s, p_{Out}, x_{Out}\left(:\right)\right) = s_{In}$$

The enthalpy change:

Compressor $\Delta h \cdot \eta_{is,Map} = h\left(T_s, p_{Out}, x_{Out}\left(:\right)\right) - h_{In}$

Turbine $\dfrac{\Delta h}{\eta_{is,Map}} = h\left(T_s, p_{Out}, x_{Out}\left(:\right)\right) - h_{In}$

The real outlet temperature is determined by

$$\Delta h = h\left(T_{Out}, p_{Out}, x_{Out}\left(:\right)\right) - h_{In}$$

The power the turbomachine consumes/produces is

Compressor $P_{Shaft} = \dot{n} \cdot \Delta h$ Turbine $P_{Shaft} = -\dot{n} \cdot \Delta h$

Boundaries for the performance map

Dimensionless inlet gas properties and pressure ratio are calculated from actual and design point values:

$$\overline{p}_{In} = \frac{p_{In}}{p_{In,0}};\ \overline{T}_{In} = \frac{T_{In}}{T_{In,0}};\ \overline{M}_{In} = \frac{M_{In}}{M_{In,0}};\ \overline{\kappa}_{In} = \frac{\kappa_{In}}{\kappa_{In,0}};\ \overline{N} = \frac{N}{N_0};\ \overline{\pi} = \frac{\pi_{Map}}{\pi_{0,Map}}$$

For the dimensionless mass flow, in case of the compressor the position of the variable inlet guide vane has to be considered:

Compressor $\overline{\dot{m}} \cdot S_{VIGV} = \dfrac{\dot{m}}{\dot{m}_0}$ Turbine $\overline{\dot{m}} = \dfrac{\dot{m}}{\dot{m}_0}$

The reduced dimensionless mass flow:

$$\overline{\dot{m}}'_{Map} = \overline{\dot{m}} \cdot \frac{\sqrt{\dfrac{\overline{T}_{In}}{\overline{M}_{In}\overline{\kappa}_{In}}}}{\overline{p}_{In}}$$

The reduced dimensionless shaft speed:

$$\overline{N}'_{Map} = \overline{N} \cdot \frac{1}{\sqrt{\overline{T} \cdot \overline{\kappa} \big/ \overline{M}}}$$

4.4.2 Performance Maps for Compressor and Turbine

Icon

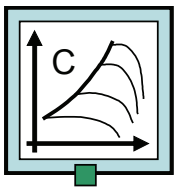

Map

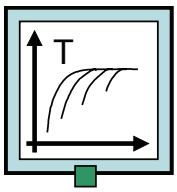

Map

Purpose

The performance map models provide analytic representations of the operational characteristics of a turbomachine. They incorporate expressions for the reduced mass flow $\dot{m}'^{*}$, efficiency η^{*} and pressure ratio π^{*} of the original machine performance they were derived from, all as a functions of the reduced dimensionless shaft speed $\bar{N}'$ and the parameter β. The latter presents an auxiliary coordinate in the two-dimensional maps.

The original values are scaled down to dimensionless values using a set of scaling factors. Except the mass flow function of the turbine, all performance data may be sufficiently modelled by polynomials of 4th or 5th or lower degree, as for example

$$\pi^{*} = \sum_{i=0,\,j=0}^{n} c_{ij} \left(\bar{N}'\right)^{i} \left(\beta\right)^{j}.$$

The turbine inlet will be choked above a certain pressure ratio, meaning that the mass flow is no longer a function of the pressure ratio respectively the parameter β. This constant mass flow cannot be satisfactorily represented by a polynomial function. An elliptic approach of the kind

$$\left(\frac{\dot{m}'}{a}\right)^{z} + \left(\frac{1-\beta}{b}\right)^{z} = 1$$

or explicitly

$$\dot{m}' = a \cdot \left(1 - \left(\frac{1-\beta}{b}\right)^{z}\right)^{1/z} \quad \text{with the exponent } z = c_0 + c_1 \bar{N}' + c_2 \bar{N}'^{2}.$$

is sufficient to represent this behaviour. The coefficients for all approaches can be fitted to performance data with adequate software for multi-dimensional curve fitting. The Matlab function *nlinfit* has been used for this task. The found representation is described in Chapter 5.

Independent from the scaling factors, the resulting pressure ratio must always be greater than unity. In order to assure this, the pressure ratio is scaled around unity. For

this scaling, a dimensionless pressure ratio is not sufficient. Hence, the absolute and design pressure ratios must be supplied by the turbomachine model.

Parameters

Parameter	Definition	Unit	Default
π_{Scale}	Pressure ratio for scaling	-	-
$\dot{m}'_{Scale}$	Reduced mass flow rate for scaling	kg/s	-

If the turbomachine is at the design point, all calculated values must equal their design values. For the performance map interface, this means that the dimensionless reduced mass flow $\bar{\dot{m}}' = 1$ and the pressure ratio $\pi = \pi_0$. Considering **Equation 4-2** and **Equation 4-3** below, this implies that to choose a design point β_D on the line $\bar{N}' = 1$, the parameters π_{Scale} and $\dot{m}'_{Scale}$ must be set in a way that

$$1 = \frac{\dot{m}'^{*}\left(\bar{N}' = 1, \beta = \beta_D\right)}{\dot{m}'_{Scale}}$$

and

$$\pi_{0,Map} = 1 + \frac{\pi^{*}\left(\bar{N}' = 1, \beta = \beta_D\right) - 1}{\pi_{Scale} - 1} \cdot \left(\pi_{0,Map} - 1\right) \text{ or } \pi_{Scale} = \pi^{*}\left(\bar{N}' = 1, \beta = \beta_D\right)$$

Ports

Port	Definition	Type	Direction
Map	Interface to thermodynamic model	PMap	In/Out

Map must be connected to the thermodynamic compressor or turbine model.

Variables

Variable	Definition	Unit
β	Beta parameter from performance equation	-
$\dot{m}'^{*}$	Original reduced mass flow from performance equation	-
π^{*}	Original pressure ratio from performance equation	-
π_s^{*} (only compressor)	Original surge pressure ratio from performance equation	-

Equations

The polynomial or elliptic performance equations for the values of the original machine:

$$\dot{m}'^{*} = f\left(\bar{N}'_{Map}, \beta\right)$$

$$\eta_{Map} = f\left(\bar{N}'_{Map}, \beta\right)$$

$$\pi^{*} = f\left(\bar{N}'_{Map}, \beta\right)$$

The original surge pressure is expressed as function of the reduced mass flow (only compressor map model)

$$\pi_s^{*} = f\left(\bar{\dot{m}}'^{*}\right)$$

The dimensionless mass flow for the thermodynamic model interface:

$$\bar{\dot{m}}'_{Map} = \frac{\dot{m}'^{*}}{\dot{m}'_{Scale}} \qquad \textbf{Equation 4-2}$$

The scaled pressure ratio for the thermodynamic model interface:

$$\pi_{Map} = 1 + \frac{\pi^{*} - 1}{\pi_{Scale} - 1} \cdot \left(\pi_{0,Map} - 1\right) \qquad \textbf{Equation 4-3}$$

The scaled surge pressure (only compressor map model):

$$\pi_{s,Map} = 1 + \frac{\pi_s^{*} - 1}{\pi_{Scale} - 1} \cdot \left(\pi_{0,Map} - 1\right)$$

Comments

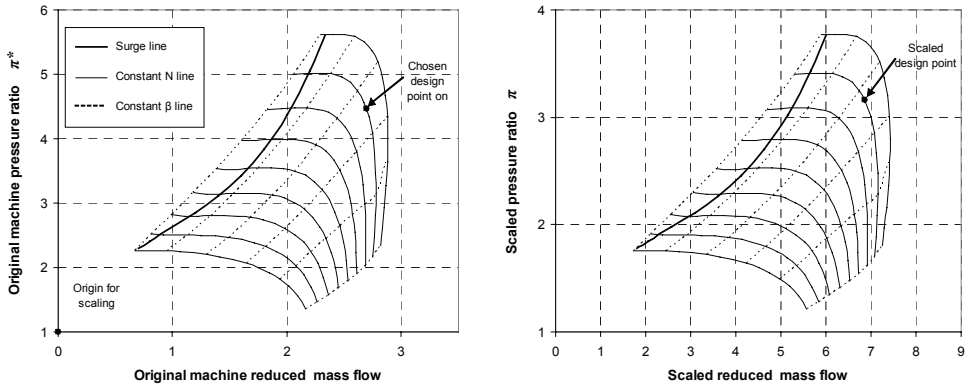

Figure 4-2: Example for scaling of compressor map from original machine data

Figure 4-2 shows an exemplary compressor map of an original machine (left) and a scaled (right). The polynomial representation varies partly from the original. However, it is seen as sufficient as long as general turbomachinery behaviour is to be modelled and scaling is used. As soon as the true, non-scaled behaviour of a real turbomachine

shall be modelled, a more exact representation, as for example lookup tables and interpolation, can be interesting.

As extrapolation of compressor data is not tolerable, it must be assured that the coordinates for reduced speed and β are always inside the range where original data exist. This can be realised by defining variable bounds for the mentioned parameters.

Solver problems are expected in ranges where a certain reduced mass flow at given speed can be achieved with more than one pressure ratios, i.e. in the regime of high shaft speed. However, such problems were never observed during the simulations.

4.4.3 Shaft

Icon

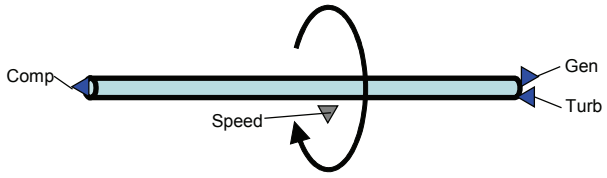

Purpose

The shaft model accounts for the coupling of compressor, turbine and generator with respect to speed and power. Dynamics of mass inertia of the shaft and the rotating components is included. The model was taken over from Ragnhild Ulfsnes [Ulfsnes 2006].

Assumptions

The mass inertia is calculated by assuming a mass rotating at a certain radius. The power delivered by the turbine is transferred to the shaft at a constant mechanical efficiency.

Parameters

Parameter	Definition	Unit	Default
m_{rot}	Rotating mass	kg	-
r_{rot}	Mean radius of rotating mass	m	-
η_{mech}	Mechanical efficiency of the shaft (based on turbine power)	-	0.99

Ports

Port	Definition	Type	Direction
Turb	Turbine power	Energy	In
Comp	Compressor power	Energy	Out
Gen	Generator power	Energy	Out
Speed	Shaft speed	Control	In/Out

Three ports must be connected.

Variables

Variable	Definition	Unit
ω	Angular speed	rad s^{-1}
ΔP	Power balance	W
I	Moment of inertia	kg m^2

Equations

The moment of inertia is

$$I = \frac{1}{2} \cdot m_{rot} \cdot r_{rot}^2$$

The angular speed is

$$\omega = 2\pi \cdot S_{Speed}$$

The power balance is

$$\Delta P = -\eta_{mech} \cdot P_{Turb} - P_{Comp} - P_{Gen}$$

The power balance dictates change in shaft speed:

$$\frac{d\omega}{dt} = \frac{\Delta P}{I \cdot \omega}$$

4.5 Heat Exchangers

4.5.1 Plate-Fin Heat Exchanger

Icon

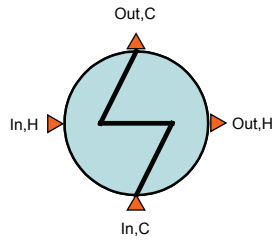

Purpose

For heat exchange between gaseous fluids, a large surface per volume ratio is required for achieving satisfactory compactness of the component. The model describes such a compact counter-flow plate-fin heat exchanger, see Figure 4-3. The gas flows are 1-dimensionally discretised in flow direction. The wall is discretised 2-dimensionally in flow direction and to its thickness. The fins are considered for the heat transfer calculation according to Kays and London [1984].

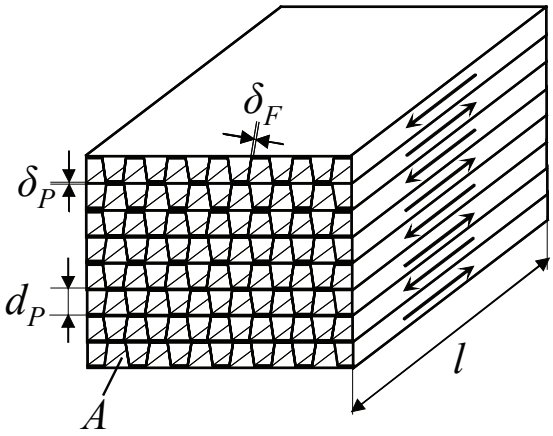

Figure 4-3: Heat exchanger geometry

The model was developed by Inge Fosse during a summer project [Fosse 2003].

Approaches different from the fuel cell and its derivate models were used for heat transfer. This is because a heat exchanger features a more complex geometry and furthermore usually operates in turbulent flow regime.

Assumptions

The surface geometry *11.1* [Kays 1984], which correlates to 11.1 fins per inch, is applied. The heat exchanger is adiabatic. Hence all gas channels of the hot and cold sides respectively have the same temperature distribution and do not exchange heat with each other. Heat transfer by convection and conduction is included, while radiation is neglected. The gas flows are fully developed and modelled as plug flow. Dynamics of gas composition due to residence time is neglected. Only the mass of the flat plate accounts for thermal inertia of the heat exchanger; other parts such as fins are neglected. The contribution of the fins to heat transfer is described by geometrical considerations and the fin efficiency method. Pressure loss is included. The generic geometry of the heat exchanger implies symmetry of hot and cold sides, resulting in velocity differences.

Parameters

Parameter	Definition	Unit	Default
ρ_P	Bulk density of plate (Stainless steel AISI 302 at 300 K [Incropera 2002])	kg m^{-3}	8055
c_P	Heat capacity of the plate [Incropera 2002]	J kg^{-1} K^{-1}	480
k_P	Thermal conductivity of the plate [Incropera 2002]	W K^{-1} m^{-1}	15.1
d_P	Plate space [Kays 1984] (see Figure 4-3)	m	0.00635
r_{hyd}	Hydraulic radius [Kays 1984]	m	0.000771
δ_F	Fin thickness [Kays 1984] (see Figure 4-3)	m	0.000152
δ_P	Plate thickness [Kays 1984] (see Figure 4-3)	m	0.0003
β	Rate of heat transfer area to volume between plates [Kays 1984]	m^{-1}	1204
α	Rate of heat transfer area to total volume $\frac{d_p \cdot \beta}{2d_P + 2\delta_P}$	m^{-1}	575
a_G	Rate of free flow area to frontal area $\alpha \cdot r_{hyd}$	-	0.443
a_F	Ratio of fin area to total heat transfer area [Kays 1984]	-	0.756
ζ_{In}	Pressure loss coefficient at entry [Kays 1984]	-	0.5
ζ_{Out}	Pressure loss coefficient at exit [Kays 1984]	-	0.25

Distribution Domains

Domain	Definition	Discretisation	Order	Nodes
z_b	Flow direction (0:l), backward method	BFDM	2	30
z_c	Flow direction (0:l) , centre method	CFDM	2	30
z_f	Flow direction (0:l), forward method	FFDM	2	30
y	Plate thickness direction (0:δ_P)	CFDM	2	3

Ports

Port	Definition	Type	Direction
In,C	Inlet of cold flow	Material	In
Out,C	Outlet of cold flow	Material	Out
In,H	Inlet of hot flow	Material	In
Out,H	Outlet of hot flow	Material	Out

The gas inlet or outlet ports must be connected.

Variables

Variable	Definition	Unit
l	Length of heat exchanger (see Figure 4-3)	m
A	Frontal area of heat exchanger (see Figure 4-3)	m²
$T_H(z_b)$	Temperature of the hot flow	K
$T_C(z_F)$	Temperature of the cold flow	K
$T_P(y,z_c)$	Temperature of the wall	K
$c_H(z_b)$, $c_C(z_f)$	Total concentration of hot and cold flow	mol m^{-3}
$T_{m,H}$, $T_{m,C}$	Arithmetic mean temperature of hot and cold flow	K
$p_{m,H}$, $p_{m,C}$	Arithmetic mean pressure of hot and cold flow	Pa
$h_{c,H}$, $h_{c,C}$	Heat transfer coefficient of hot and cold flow	W m^{-2} K^{-1}
$\eta_{F,H}$, $\eta_{F,C}$	Fin effectiveness on hot and cold side	-
$\eta_{S,H}$, $\eta_{S,C}$	Surface effectiveness on hot and cold side	-
$K_{Shi}(z_c)$	Equilibrium constant of the shift reaction	-
$c_{p,H}(z_b)$, $c_{p,C}(z_f)$	Heat capacity of hot and cold flow	J mol^{-1} K^{-1}
$\rho_H(z_b)$, $\rho_C(z_f)$	Density of hot and cold flow	kg m^{-3}
$\rho_{m,H}$, $\rho_{m,C}$	Mean density of hot and cold flow	kg m^{-3}
$\dot{m}_H$, $\dot{m}_C$	Mass flow of hot and cold flow	kg s^{-1}

g_H, g_C	Mass flux of hot and cold flow	kg s^{-1} m^{-2}
$u_{H,max}$, $u_{C,max}$	Maximum velocity of hot and cold flow	m s^{-1}
f_H, f_C	Friction factors for hot and cold flow	-
St_H, St_C	Stanton number of hot and cold flow	-
Pr_H, Pr_C	Prandtl number of hot and cold flow	-
Re_H, Re_C	Reynolds number of hot and cold flow	-
ΔT_{LM}	Logarithmic mean temperature difference	K
ΔE	Relative energy balance around the system	-

In design mode, a flow parameter (such as velocity or pressure loss) and a thermal parameter (such as logarithmic mean temperature difference or an output temperature) must be specified and the frontal area and length are calculated as result. In off-design mode, the frontal area and length must be specified.

Equations

Temperatures from the ports are connected to the ends of the heat exchanger (hot flow from 0 to l; cold flow from l to 0):

$$T_H(0) = T_{In,H} \qquad T_C(l) = T_{In,C}$$
$$T_H(l) = T_{Out,H} \qquad T_C(0) = T_{Out,C}$$

The compositions at inlet and outlet are set equal:

$$x_{In,H}(:) = x_{Out,H}(:) \qquad x_{In,C}(:) = x_{Out,C}(:)$$

The mass flow rates are:

$$\dot{m}_H = \dot{n}_{In,H} \cdot M_{In,H} \qquad \dot{m}_C = \dot{n}_{In,C} \cdot M_{In,C}$$

The mass fluxes are:

$$g_H = \frac{\dot{m}_H}{A \cdot a_g} \qquad g_C = \frac{\dot{m}_C}{A \cdot a_g}$$

The maximum velocities are expected to occur at the hot end:

$$u_{H,max} = \frac{g_H}{\rho_H(0)} \qquad u_{C,max} = \frac{g_C}{\rho_C(0)}$$

The species concentration and the flows at the inlet and outlet are connected with the density:

$$c_H(0) = \frac{\dot{n}_{In,H}}{n_P} \cdot \frac{\rho_H(0)}{\dot{m}_H} \qquad c_C(l) = \frac{\dot{n}_{In,C}}{n_P} \cdot \frac{\rho_C(l)}{\dot{m}_C}$$

$$c_H(l) = \frac{\dot{n}_{Out,H}}{n_P} \cdot \frac{\rho_H(l)}{\dot{m}_H} \qquad c_C(0) = \frac{\dot{n}_{Out,C}}{n_P} \cdot \frac{\rho_C(0)}{\dot{m}_C}$$

The front and rear end of the plate are assumed to be adiabatic:

$$\frac{\partial T_P(y,0)}{\partial y} = \frac{\partial T_P(y,l)}{\partial y} = 0 \quad \forall\, y \in [0, \delta_P]$$

Distributed heat capacities and densities are obtained from Multiflash:

$$\begin{aligned} c_{p,H}(z) &= c_p\left(T_H(z), p_H(z), x_{In,H}(:)\right) \\ c_{p,C}(z) &= c_p\left(T_C(z), p_C(z), x_{In,C}(:)\right) \\ \rho_{p,H}(z) &= \rho\left(T_H(z), p_H(z), x_{In,H}(:)\right) \\ \rho_{p,C}(z) &= \rho\left(T_C(z), p_C(z), x_{In,C}(:)\right) \end{aligned} \quad \forall\, z \in [0,l]$$

The arithmetic mean values of pressure, temperature and density are approximated assuming linear profiles:

$$p_{m,H} = \frac{p_{In,H} + p_{Out,H}}{2} \qquad p_{m,C} = \frac{p_{In,C} + p_{Out,C}}{2}$$

$$T_{m,H} = \frac{T_{In,H} + T_{Out,H}}{2} \qquad T_{m,C} = \frac{T_{In,C} + T_{Out,C}}{2}$$

$$\rho_{m,H} = \rho\left(T_{m,H}, p_{m,H}, x_H(:)\right) \qquad \rho_{m,C} = \rho\left(T_{m,C}, p_{m,C}, x_C(:)\right)$$

The Reynolds numbers are:

$$Re_H = \frac{4 \cdot r_{hyd} \cdot g_H}{\mu\left(T_{m,H}, p_{m,H}, x_{In,H}(:)\right)} \qquad Re_C = \frac{4 \cdot r_{hyd} \cdot g_C}{\mu\left(T_{m,C}, p_{m,C}, x_{In,C}(:)\right)}$$

The Prandtl numbers are:

$$Pr_H = \frac{\mu\left(T_{m,H}, p_{m,H}, x_{In,H}(:)\right) \cdot c_{P,H}(0)}{\lambda\left(T_{m,H}, p_{m,H}, x_{In,H}(:)\right)}$$

$$Pr_C = \frac{\mu\left(T_{m,C}, p_{m,C}, x_{In,C}(:)\right) \cdot c_{p,C}(l)}{\lambda\left(T_{m,C}, p_{m,C}, x_{In,C}(:)\right)}$$

The Stanton numbers are determined implicitly by fitting data from Kays and London [1984] for the Colburn factor $St \cdot Pr^{2/3}$ for the surface geometry *11.1*:

$$St_x \cdot Pr_x^{2/3} = \min\left(\begin{array}{l} 2.126\cdot 10^{-3} + \dfrac{12.687}{Re_x} - \dfrac{2.9070\cdot 10^4}{Re_x^2} + \\ + \dfrac{3.1751\cdot 10^7}{Re_x^3} - \dfrac{1.48954\cdot 10^{10}}{Re_x^4}, 0.00840 \end{array}\right) \quad \forall\, x \in \{H, C\}$$

The moody friction factors are also determined by data fitting from Kays and London [1984]:

$$f_x = 8.034\cdot 10^{-3} + \frac{8.6701}{Re_x} + \frac{2433.8}{Re_x^2} \quad \forall\, x \in \{H, C\}$$

The pressure losses become then:

$$p_{In,x} - p_{Out,x} = \frac{g_x^2}{2\rho_{In,x}} \cdot \left(\begin{array}{l} \zeta_{In} + 1 - a_F^2 + 2\left(\dfrac{\rho_{In,x}}{\rho_{Out,x}} - 1\right) + \\ + f_x \alpha l \cdot \dfrac{\rho_{In,x}}{\rho_{m,x}} - \left(1 - a_F^2 - \zeta_{Out}\right)\dfrac{\rho_{In,x}}{\rho_{Out,x}} \end{array}\right) \quad \forall\, x \in (H, C)$$

The heat transfer coefficients are calculated from the Stanton numbers:

$$h_{c.H} = St_H \cdot g_H \cdot c_{p,H}(0) \qquad h_{c.C} = St_C \cdot g_C \cdot c_{p,C}(l)$$

The fin efficiencies are [Kays 1984]:

$$\eta_{F,H} = \frac{\tanh\left(\dfrac{d_P}{2}\cdot\sqrt{\dfrac{2h_{c,H}}{k_P\delta_F}}\right)}{\dfrac{d_P}{2}\cdot\sqrt{\dfrac{2h_{c,H}}{k_P\delta_F}}} \qquad \eta_{F,C} = \frac{\tanh\left(\dfrac{d_P}{2}\cdot\sqrt{\dfrac{2h_{c,C}}{k_P\delta_F}}\right)}{\dfrac{d_P}{2}\cdot\sqrt{\dfrac{2h_{c,C}}{k_P\delta_F}}}$$

The surface efficiencies are:

$$\eta_{S,H} = 1 - a_F \cdot (1 - \eta_{F,H}) \qquad \eta_{S,C} = 1 - a_F \cdot (1 - \eta_{F,C})$$

The heat transport equations for the flows are:

$$-a_G \cdot \rho_H \cdot c_{p,H}(z) \cdot \frac{dT_H(z)}{dt} = \alpha \cdot \eta_{S,H} h_{c,H} \cdot \left(T_H(z) - T_P(z)\right) + \frac{\dot{m}_H}{A} \cdot c_{p,H}(z) \cdot \frac{dT_H(z)}{dz_c} \quad \forall\, z \in (0, l_T]$$

$$a_G \cdot \rho_C \cdot c_{p,C}(z) \cdot \frac{dT_C(z)}{dt} = \alpha \cdot \eta_{S,C} h_{c,C} \cdot \left(T_P(z) - T_C(z)\right) + \frac{\dot{m}_C}{A} \cdot c_{p,C}(z) \cdot \frac{dT_C(z)}{dz_c} \quad \forall\, z \in (0, l_T]$$

The boundary heat transfer between the flows and the plate are:

$$-(1 - a_F) \cdot k_P \cdot \frac{\partial T_P(0,z)}{\partial y} = \eta_{S,H} h_{c,H} \left(T_H(z) - T_P(0,z)\right) \quad \forall\, z \in (0, \delta_P)$$

$$\left(1-a_F\right)\cdot k_P\cdot\frac{\partial T_P\left(\delta_P,z\right)}{\partial y}=\eta_{S,C}h_{c,C}\left(T_C\left(z\right)-T_P\left(\delta_P,z\right)\right)\quad\forall\, z\in\left(0,\delta_P\right)$$

The heat balance equation for the plate is:

$$\frac{\partial^2 T_p\left(y,z\right)}{\partial y^2}+\frac{\partial^2 T_p\left(y,z\right)}{\partial z_c^2}=\frac{\rho_P c_P}{k_P}\cdot\frac{dT_p\left(y,z\right)}{dt}\quad\forall\, y\in\left(0,\delta_P\right),z\in\left(0,l\right)$$

The molar balances for the cold and hot flows are:

$$\frac{dc_H\left(z\right)}{dt}+g_H\cdot\rho_{m,H}\cdot\frac{\partial c_H\left(z\right)}{\partial z_b}=0\quad\forall\, z\in\left[0,l_T\right)$$

$$\frac{dc_C\left(z\right)}{dt}-g_C\cdot\rho_{m,C}\cdot\frac{\partial c_C\left(z\right)}{\partial z_f}=0\quad\forall\, z\in\left(0,l_T\right]$$

The mean logarithmic temperature difference is:

$$\Delta T_{LM}=\frac{\left(T_{In,H}-T_{Out,C}\right)-\left(T_{Out,H}-T_{In,C}\right)}{\log\left(\frac{T_{In,H}-T_{Out,C}}{T_{Out,H}-T_{In,C}}\right)}$$

The total relative energy balance is

$$\Delta E=1-\frac{\dot{n}_{Out,C}h_{Out,C}+n_{Out,H}h_{Out,H}}{\dot{n}_{In,C}h_{In,C}+n_{In,H}h_{In,H}}$$

The energy balance should in steady state operation be zero. A deviation of 0.01 (=1%) is regarded as tolerable.

Comments

It has been observed that the discretisation method for the flow temperatures is crucial. For backward/forward discretisation, the temperature distributions look smooth, but energy balance mismatch is quite high (>0.1). For centre discretisation, the energy balance looks better, but the temperature curves are zigzagged. Nevertheless, central method was chosen, with a distribution of 30 nodes.

Due to the plate heat conduction in axial direction, a certain length of the exchanger is indispensable for achieving close temperature approaches. A long exchanger with a smaller frontal area, however, causes stronger pressure drop.

4.5.2 Preheat Tube

Icon

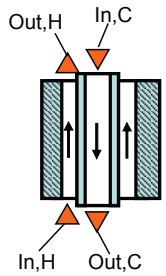

Purpose

The preheat tube is a typical tube-shell heat exchanger configuration as it appears in the Siemens-Westinghouse configuration (see Figure 2-9). The tubes are the extension of the air delivery tube on top of the cell. The cold stream (air) runs downwards through the tubes and is preheated by the burner exhaust gas running upwards outside the tube. Downwards, the tube enters the cell tube where it exchanges further heat.

The model is based on the tubular SOFC core model, i.e. the premises concerning spatial distribution, and heat transfer are equal. The radial temperature distribution in the solid has been removed.

Assumptions

The model describes a number of non-interacting, axially distributed tube-shell heat exchangers; no bundling effects are considered. The upper and lower tube ends are adiabatic; no heat conduction to the prolongation of the tube inside the fuel cell (ADT) occurs. Dynamics of gas composition due to residence time is neglected. The gas flows are modelled as plug flows. The velocity is calculated from the continuity equation at arithmetic mean gas temperature and is assumed to be constant along the flow path. For heat transfer, laminar flow is assumed. The lumped pressure losses from laminar tube friction, inlet and outlet effects are calculated. Only the heat capacity of the tubes is considered; the shells are neglected.

Parameters

Parameter	Definition	Unit	Default
n_T	Number of tubes	-	1152
r_i	Inner radius of tube	m	0.0025
r_o	Outer radius of tube	m	0.004
r_S	Radius of the shell	m	0.0055
Nu_T	Nusselt number for laminar flow inside a tube	-	4.364

	[Mills 1995]		
Nu_S	Nusselt number for inner tube (laminar flow in annular ducts) [Rohsenow 1998]	-	10
$d_{H,hyd}$	Hydraulic diameter of the hot flow	m	0.003
ξ_{Re}	Correction factor for Reynolds number in annlar ducts [White 2003]	-	1.5
$\zeta_{C,in}$	Pressure loss coefficient at cold inlet (assumption)	-	0.5
$\zeta_{C,out}$	Pressure loss coefficient at cold outlet (seamless transition to ADT)	-	0
$\zeta_{H,in}$	Pressure loss coefficient at hot inlet (assumption)	-	0.5
$\zeta_{H,out}$	Pressure loss coefficient at hot outlet (assumption)	-	0.5
ρ_T	Density of tube material (Al_2O_3) [Mills 1995]	kg m^{-3}	3970
c_T	Heat capacity of the tube [Mills 1995]	J kg^{-1} K^{-1}	1167
k_T	Thermal conductivity of the tube [Mills 1995]	W K^{-1} m^{-1}	11.8

Distribution Domains

Domain	Definition	Discretisation	Order	Nodes
z_b	Axial direction (0:l_T), backward method	BFDM	2	20
z_f	Axial direction (0:l_T) , forward method	FFDM	2	20
z_c	Axial direction (0:l_T) , centre method	CFDM	2	20

Ports

Port	Definition	Type	Direction
In,*C*	Inlet of cold flow	Material	In
Out,*C*	Outlet of cold flow	Material	Out
In,*H*	Inlet of hot flow	Material	In
Out,*H*	Outlet of hot flow	Material	Out

Port quantities refer to the total number of tubes. The gas inlet or outlet ports must be connected.

Variables

Variable	Definition	Unit

l_T	Tube length	m
$T_C(z_b)$	Temperature of the cold flow inside the tube	K
$T_H(z_f)$	Temperature of the hot flow outside the tube	K
$T_T(z_c)$	Temperature of the tube	K
$T_{m,C}$, $T_{m,H}$	Mean temperature of cold and hot flow	K
$c_{p,C}(z_b)$	Heat capacity of fuel	J mol^{-1} K^{-1}
$c_{p,H}(z_f)$	Heat capacity of cathode air	J mol^{-1} K^{-1}
Re_C, Re_H	Reynolds number of hot and cold flow	-
f_C, f_H	Friction coefficients of hot and cold flow	-
Δp_C, Δp_H	Friction losses on hot and cold side	-
$h_{c,C}(z_b)$	Heat transfer coefficient between cold flow and the tube	W m^{-2} K^{-1}
$h_{c,H}(z_f)$	Heat transfer coefficient between hot flow and the tube	W m^{-2} K^{-1}
u_C, u_H	Flow velocities for cold and hot flow respectively	m s^{-1}
$c_C(z_c)$, $c_H(z_c)$	Total molar concentrations in cold and hot flow	mol m^{-3}
ΔT_C, ΔT_H	Difference between inlet and outlet for hot and cold flow respectively	K
ΔE	Relative energy balance around the system	-

In design mode, a thermal parameter (such temperature difference or an output temperature) must be specified and the length is calculated as result. In off-design mode, the length must be specified.

Equations

For easier reading, a convention is that each axially distributed equation (over z) is valid for all $z \in [0, l_T]$ unless otherwise noted.

The pressure at inlets and outlets are connected through the pressure loss:

$$p_{Out,C} = p_{In,C} - \Delta p_C; \quad p_{Out,H} = p_{In,H} - \Delta p_H$$

The inlet temperatures from the ports are connected to the flow channel entrances (0: top of the tube, l: bottom of the tube)

$$T_C(0) = T_{In,C}; \quad T_H(l_T) = T_{In,H}$$

To account for enthalpy conservation at pressure changes of a real gas, the outlet temperatures are gained implicitly by enthalpy balances:

$$h\left(T_C\left(l\right), p_{In,C}, x_{Out,C}\right) = h\left(T_{Out,C}, p_{Out,C}, x_{Out,C}\right)$$
$$h\left(T_H\left(0\right), p_{In,H}, x_{Out,H}\right) = h\left(T_{Out,H}, p_{Out,H}, x_{Out,H}\right)$$

Compositions at inlets and outlets are set equal

$$x_{In,C}\left(:\right) = x_{Out,C}\left(:\right); \quad x_{In,H}\left(:\right) = x_{Out,H}\left(:\right)$$

The mean temperatures of hot and cold flows are taken in the middle of the tube:

$$T_{m,H} = T_H\left(\frac{l_T}{2}\right) \qquad T_{m,C} = \left(\frac{l_T}{2}\right)$$

The Reynolds numbers are calculated at the entrances and assumed to be constant along the flow paths:

$$Re_C = \frac{\dot{n}_{In,C} \cdot M_{In,C}}{r_i^2 \pi} \cdot \frac{2r_i}{\mu\left(T_{m,C}, p_{In,C}, x_{In,C}\right)}; \quad Re_H = \frac{\dot{n}_{In,H} \cdot M_{In,C}}{\left(r_S^2 - r_o^2\right)\pi} \cdot \frac{d_{H,hyd}}{\mu\left(T_{m,H}, p_{In,H}, x_{In,H}\right)}$$

The friction factors are calculated for laminar flow [Mills 1995]:

$$f_X = \frac{64}{Re_X} \quad \forall\, X \in \{C, H\}$$

Together with the friction coefficients at the entrances, the pressure losses in the gas channels are:

$$\Delta p_C = \left(\zeta_{C,in} + f_C \cdot \frac{l}{2r_i} + \zeta_{C,out}\right) \cdot \tfrac{1}{2} \cdot \rho\left(T_{C,m}, p_{In,C}, x_{In,C}\right) \cdot u_C^2$$

$$\Delta p_H = \left(\zeta_{H,in} + f_H \cdot \frac{l}{d_{H,hyd}} + \zeta_{H,out}\right) \cdot \tfrac{1}{2} \cdot \rho\left(T_{H,m}, p_{In,H}, x_{In,H}\right) \cdot u_H^2$$

The total molar concentration of hot and cold flows at the inlets is calculated from molar volume, utilising the arithmetic mean temperature:

$$c_C\left(0\right) = \frac{1}{v\left(T_{m,C}, p_{In,C}, x_{In,C}\right)} \qquad c_H\left(l_T\right) = \frac{1}{v\left(T_{m,H}, p_{In,H}, x_{In,H}\right)}$$

The velocities of the flows are assumed as constant along the flow paths and calculated from the continuity condition, assuming the arithmetic mean temperatures of the flows:

$$u_C = \frac{\dot{n}_{In,C}}{n_T} \cdot \frac{v\left(T_{m,C}, p_{In,C}, x_{In,C}\right)}{r_i^2 \pi} \qquad -u_H = \frac{\dot{n}_{In,H}}{n_T} \cdot \frac{v\left(T_{m,H}, p_{In,H}, x_{In,H}\right)}{\left(r_S^2 - r_o^2\right)\pi}$$

Note that the port flow rates are total flow rates and have to be divided by the number of tubes.

The flow rates at the flow outlets are calculated according to the continuity equation:

$$\dot{n}_{Out,C} = n_T \cdot u_C \cdot c_C\left(l_T\right) \cdot r_i^2 \pi \qquad \dot{n}_{Out,H} = -n_T \cdot u_H \cdot c_H\left(0\right) \cdot \left(r_S^2 - r_o^2\right)\pi$$

The upper and lower ends of the tube are assumed to be adiabatic:

$$\frac{\partial T_T\left(0\right)}{\partial z_c} = \frac{\partial T_T\left(l_T\right)}{\partial z_c} = 0$$

The heat transfer coefficients between the flows and the tube are based on laminar flow and constant Nusselt number (thermal conductivities from physical property package):

$$h_{c,C}\left(z\right) = Nu_T \cdot \lambda_{In,C} \cdot \frac{1}{2r_i}; \qquad h_{c,H}\left(z\right) = Nu_S \cdot \lambda_{In,H} \cdot \frac{r_S + r_o}{2\left(r_S^2 - r_o^2\right)}$$

The heat capacities are obtained from the physical property package:

$$c_{p,C}\left(z\right) = c_p\left(T_C\left(z\right), p_{In,C}, x_{In,C}\right); \qquad c_{p,H}\left(z\right) = c_p\left(T_H\left(z\right), p_{In,H}, x_{In,C}\right)$$

The heat transport equation for the cold flow in the tube is:

$$c_C\left(z\right) \cdot c_{p,C}\left(z\right) \cdot \left(\frac{dT_C\left(z\right)}{dt} + u_C \cdot \frac{\partial T_C\left(z\right)}{\partial z_b}\right) = \frac{2}{r_i} \cdot h_{c,C}\left(z\right) \cdot \left(T_T\left(z\right) - T_C\left(z\right)\right) \quad \forall\, z \in \left(0, l_T\right]$$

The heat balance equation for the tube:

$$-c_{ADT} \cdot \rho_{ADT} \cdot \frac{dT_{ADT}\left(r,z\right)}{dt} + k_{ADT} \cdot \left(\frac{\partial^2 T_T\left(z\right)}{\partial {z_c}^2}\right) =$$

$$= \frac{2r_i \cdot h_{c,C} \cdot \left(T_T\left(z\right) - T_C\left(z\right)\right) + 2r_o \cdot h_{c,H} \cdot \left(T_T\left(z\right) - T_H\left(z\right)\right)}{r_o^2 - r_i^2} \quad \forall\, z \in \left(0, l_T\right)$$

The heat transport in the hot flow outside the tube:

$$c_H\left(z\right) \cdot c_{p,H}\left(z\right) \cdot \left(\frac{dT_H\left(z\right)}{dt} + u_H \cdot \frac{\partial T_H\left(z\right)}{\partial z_f}\right) = \frac{2 \cdot r_o}{r_S^2 - r_o^2} \cdot h_{c,H}\left(z\right) \cdot \left(T_T\left(z\right) - T_H\left(z\right)\right) \quad \forall\, z \in \left(0, l_T\right)$$

The boundary heat transfer between cathode air and cathode (including radiation to the ADT surface):

$$k_{MEA,r} \cdot \frac{\partial T_{MEA}\left(r_i, z\right)}{\partial r_{MEA}} = h_{c,Air-C}\left(z\right) \cdot \left(T_{MEA}\left(r_i, z\right) - T_{Air}\left(z\right)\right) + \frac{\dot{q}_{C-ADT}\left(z\right)}{2\pi r_i l} \quad \forall\, z \in \left[0, l_T\right)$$

The molar balance for the cold flow is:

$$\frac{dc_C\left(z\right)}{dt} + u_C \frac{\partial c_C\left(z\right)}{\partial z_c} = 0 \quad \forall\, z \in \left(0, l_T\right]$$

The molar balance for the hot flow is analogously:

$$\frac{dc_H(z)}{dt} + u_H \frac{\partial c_H(z)}{\partial z_c} = 0 \quad \forall\, z \in [0, l_T)$$

The temperature differences between inlet and outlet of the flows are:

$$\Delta T_C = T_{Out,C} - T_{In,C}; \qquad \Delta T_H = T_{Out,H} - T_{In,H}$$

The total relative energy balance is

$$\Delta E = 1 - \frac{\dot{n}_{Out,C} h_{Out,C} + n_{Out,H} h_{Out,H}}{\dot{n}_{In,C} h_{In,C} + n_{In,H} h_{In,H}}$$

The energy balance should in steady state operation be zero. A deviation of 0.01 (=1%) is regarded as tolerable.

Comments

The model does not account for gas residence times, as a delay in the gas composition does not have any influence in the prospected application: The cold flow is air and the hot flow is burner exhaust gas which is entering the turbine downstream.

4.6 Balance of Plant Equipment

4.6.1 Indirect Internal Reformer

Icon

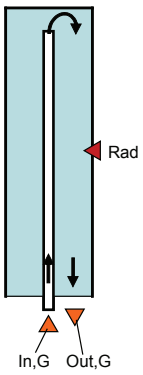

Purpose

The indirect internal reformer is used for pre-reforming the methane to a certain degree before the fuel enters the fuel cell. Heat is supplied to the reformer by radiation from the SOFC tube surface. The current model is a rectangular reformer of the same

height as the fuel cell tube, which is to be situated next to the tubes in the bundle in order to receive radiation heat along its whole body. The model is discretised in direction of the tube axes. The wall is furthermore discretised to its thickness. The geometry is depicted in Figure 4-4.

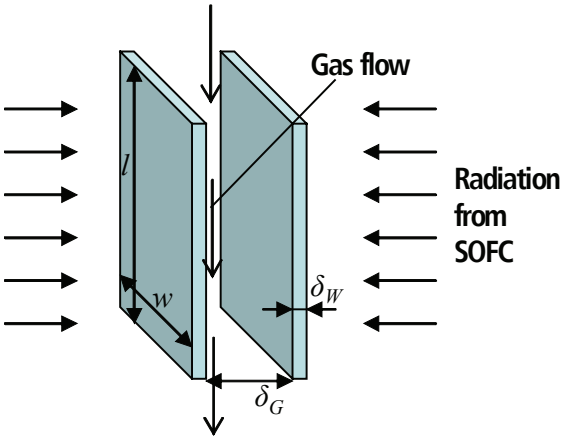

Figure 4-4: Geometry of the IIR

The model is based on chemical equilibrium calculation. For including non-equilibrium, a temperature difference between the actual and the equilibrium temperature may be specified.

It is assumed that the gas flow enters the IIR at the top and leaves at the bottom. In case the gas is fed from the bottom by a tube (see icon), the heat transfer between tube and the reforming gas is neglected.

The model is a derivate of the tubular SOFC model and was developed in order to model the reforming more accurately (previously, a non-discretised reformer model including radiation heat flow had been applied).

Geometry and materials of the IIR used by Siemens-Westinghouse are uncertain and may vary substantially from the approach modelled here.

Assumptions

The upper and lower ends of the reformer are adiabatic. The gas enters the reformer from the top and leaves it at the bottom. The reformer has two symmetric outer walls and one gas channel between (Figure 4-4). The internal gas flow is modelled as plug flow. The velocity is calculated from the continuity equation at arithmetic mean gas temperature and flow rate and is assumed to be constant along the flow path. Laminar flow is assumed. Pressure loss is calculated assuming a constant flow coefficient. The model is not discretised into the width direction. The reactions are based on equilibrium calculations. Only the steam reforming reaction of methane

$$CH_4 + H_2O \Leftrightarrow 3H_2 + CO$$

and the water-gas shift reaction

$$CO + H_2O \Leftrightarrow CO_2 + H_2$$

occur in the reformer. A reforming degree is defined as the reformed amount divided by the supplied amount of methane.

The outer wall of the reformer receives only radiation heat from the fuel cell tubes. A radiation distribution over the length of the reformer is calculated in the tubular SOFC model. Convective heat transfer by gas outside the reformer is neglected.

Parameters

Parameter	Definition	Unit	Default
n_R	Number of reformers	-	16
l	Length	m	1.5
w	Width	m	0.6
δ_W	Wall thickness	m	0.0025
δ_G	Gas channel thickness	m	0.02
Nu	Nusselt number for laminar flow in rectangular ducts. Average value for constant heat flow; constant temperature, ratio a/b=8;infinite [Incropera 2002]	-	7.5
ρ_W	Bulk density of wall (bulk Nickel)	kg m^{-3}	8900
c_W	Heat capacity of the wall (bulk Nickel)	J kg^{-1} K^{-1}	444
k_W	Thermal conductivity of the wall (bulk Nickel)	W K^{-1} m^{-1}	90.7

Distribution Domains

Domain	Definition	Discretisation	Order	Nodes
z_b	Axial direction (0:l), backward method	BFDM	2	40
z_c	Axial direction (0:l) , centre method	CFDM	2	40
y	Wall thickness direction (0:δ_W)	CFDM	2	3

Ports

Port	Definition	Type	Direction
In,*G*	Inlet	Material	In
Out,*G*	Outlet	Material	Out
Rad	Radiation from the SOFC, distributed over z_c	Radiation	In

Port quantities refer to the total number of reformers. The gas inlet port must be connected. The radiation port must be connected, to a model where radiation heat flow is calculated. Alternatively, the heat flow and emitter temperature (without effect) must be specified.

Variables

Variable	Definition	Unit
$T_G(z_b)$	Temperature of the gas	K
$T_W(y,z_c)$	Temperature of the wall	K
$T_{m,G}$	Mean temperature of the gas	K
ΔT_{eq}	Temperature difference between actual and equilibrium	K
Δp_{abs}	Absolute pressure drop	Pa
Δp_{rel}	Relative pressure drop	-
c	Flow coefficient	m^2
$\Delta hR_{ef}(z_c)$	Enthalpy change of the reforming reaction	J mol^{-1}
$\Delta h_{Shi}(z_c)$	Enthalpy change of the shift reaction	J mol^{-1}
$\dot{r}_{Ref}(z_c)$	Rate of the reforming reaction	mol s^{-1}
$\dot{r}_{Shi}(z_c)$	Rate of the shift reaction	mol s^{-1}
$K_{Ref}(z_c)$	Equilibrium constant of the reforming reaction	-
$K_{Shi}(z_c)$	Equilibrium constant of the shift reaction	-
$c_{p,G}(z_b)$	Heat capacity of gas	J mol^{-1} K^{-1}
LHV_{In}	Lower heating value of inlet gas	J mol^{-1}
LHV_{Out}	Lower heating value of outlet gas	J mol^{-1}
$h_{c,G}(z_b)$	Heat transfer coefficient between the gas and the wall	W m^{-2} K^{-1}
u_G	Flow velocity of gas	m s-1
$c_{Gr}(z_c,7)$	Molar concentrations of species in gas	mol m-3
$x_G(z_c,7)$	Molar fractions of species in gas	-
ΔE	Relative energy balance around the system	-
ΔM	Relative mass flow balance around the system	-
γ_R	Degree of methane reforming	-

In design mode, the reforming degree and the absolute or relative pressure loss must be specified. In off-design mode, the equilibrium temperature difference and the flow

coefficient must be specified. An alternative design possibility is the coefficient for the radiation energy exchange in the SOFC model.

Equations

For easier reading, a convention is that each axially distributed equation (over z) is valid for all $z \in [0,l]$ unless otherwise noted.

The inlet temperatures from the port are connected to the upper end of the reformer:

$$T_G(0) = T_{In,G}$$

The absolute pressure loss is determined through:

$$\Delta p_{abs} = p_{In,G} - p_{Out,G} = c \cdot \frac{\left(\dot{n}_{In,G} \cdot M_{In,G}\right)^2}{\rho_{In,G}}$$

The relative pressure drop is

$$\Delta p_{rel} = \frac{\Delta p_{abs}}{p_{In,G}}$$

To account for enthalpy conservation at pressure changes, the outlet temperature is gained implicitly by an enthalpy balance:

$$h\left(T_G(l), p_{In,G}, x_{Out,G}\right) = h\left(T_{Out,G}, p_{Out,G}, x_{Out,G}\right)$$

The mean temperature for the velocity calculation is taken in the middle of the flow path:

$$T_{m,G} = T_G\left(\frac{l}{2}\right)$$

The species concentrations at the inlet are calculated from the molar volume at arithmetic mean temperature:

$$c_G(0,:) = \frac{x_{In,G}(:)}{v\left(T_{m,G}, p_{In,G}, x_{In,G}\right)}$$

The relationship between mole fractions and species concentrations in the gas:

$$x_G(z,i) = \frac{c_G(z,i)}{\sum_{j=1}^{7} c_G(z,j)} \quad \forall\, i \in \{1:7\}$$

The velocity of the gas flow is assumed as constant along the flow path and calculated from the continuity condition at assuming the arithmetic mean temperature and the inlet flow rate:

$$u_G = \frac{\dot{n}_{In,G}}{n_R} \cdot \frac{v\left(T_{m,G}, p_{In,G}, x_{In,G}\right)}{w\delta_G}$$

Note that the port flow rates are total flow rates and have to be divided by the number of reformers. The change in flow rate by the reactions is neglected for the average velocity.

Flow rate and composition at the output are:

$$\dot{n}_{Out,G} = \frac{\dot{n}_{In,G}}{v\left(T_{m,G}, p_{In,G}, x_{In,G}\right)} \sum_{i=1}^{7} c_G\left(l,i\right) \qquad x_{Out,G}\left(:\right) = x_G\left(l,:\right)$$

The lower heating value of the inlet and outlet gas:

$$LHV_X = x_X\left(H_2\right) \cdot \left(0 - h_f^0\left(H_2O\right)\right) + x_X\left(CH_4\right) \cdot \left(h_f^0\left(CH_4\right) - h_f^0\left(CO_2\right) - 2h_f^0\left(H_2O\right)\right) +$$
$$+ x_X\left(CO\right) \cdot \left(h_f^0\left(CO\right) - h_f^0\left(CO_2\right)\right) \quad \forall\, X \in \left\{In,G;Out,G\right\}$$

The upper and lower ends of the reformer wall are assumed to be adiabatic:

$$\frac{\partial T_W\left(y,0\right)}{\partial y} = \frac{\partial T_W\left(y,l\right)}{\partial y} = 0 \quad \forall\, y \in \left[0,\delta_W\right]$$

The relationship between the species concentration and mole fraction in the gas channel:

$$x_G\left(z,i\right) = \frac{c_G\left(z,i\right)}{\sum_{j=1}^{7} c_G\left(z,j\right)}$$

The heat transfer coefficients for all solid-gas interfaces are based on laminar flow and constant Nusselt number (thermal conductivities from physical property package):

$$h_{c,G}\left(z\right) = Nu \cdot \lambda\left(T_G\left(z\right), p_{In,G}\left(z\right), x_G\left(z,:\right)\right) \cdot \frac{w + \delta_C}{2w\delta_C}$$

The heat capacities are obtained from the physical property package:

$$c_{p,G}\left(z\right) = c_p\left(T_G\left(z\right), p_{In,G}\left(z\right), x_G\left(z,:\right)\right)$$

The heat of the reactions is:

$$\Delta h_{Ref}\left(z\right) = 3 \cdot \left(0 + h\left(H_2\right)\right) + \left(h_f^0\left(CO\right) + h\left(CO\right)\right)$$
$$- \left(h_f^0\left(CH_4\right) + h\left(CH_4\right)\right) - \left(h_f^0\left(H_2O\right) + h\left(H_2O\right)\right)$$
$$\Delta h_{Shi}\left(z\right) = \left(0 + h\left(H_2\right)\right) + \left(h_f^0\left(CO\right) + h\left(CO\right)\right)$$
$$- \left(h_f^0\left(CO\right) + h\left(CO\right)\right) - \left(h_f^0\left(H_2O\right) + h\left(H_2O\right)\right)$$

with the enthalpy values at the inner wall $T_W(0)$ and at the pressure of the gas channel $p_{In,G}$.

The reactions are assumed to be at equilibrium of the actual temperature minus the equilibrium temperature difference $T_G - \Delta T_{eq}$. The equilibrium constants are determined from the change in standard Gibbs energy at this temperature [Moran 2004]:

$$\ln\left(K_{Shi}(z)\right) = -\frac{g^0(H_2) + g^0(CO_2) - g^0(CO) - g^0(H_2O)}{R_m\left(T_G(0,z) - \Delta T_{eq}\right)}$$

$$\ln\left(K_{Ref}(z)\right) = -\frac{3g^0(H_2) + g^0(CO) - g^0(CH_4) - g^0(H_2O)}{R_m\left(T_G(0,z) - \Delta T_{eq}\right)}$$

The reaction rates are then

$$\dot{r}_{Shi}(z) = 1 \cdot \left(x_G(z,CO) \cdot x_G(z,H_2O) - \frac{x_G(z,H_2) \cdot x_G(z,CO_2)}{K_{Shi}(z)} \right) \quad \forall\, z \in (0,l]$$

$$\dot{r}_{Shi}(0) = 0$$

$$\dot{r}_{Ref}(z) = 1 \cdot \left(x_G(z,CH_4) \cdot x_G(z,H_2O) - \frac{x_G(z,H_2)^3 \cdot x_G(z,CO)}{K_{Ref}(z)} \right) \quad \forall\, z \in (0,l]$$

$$\dot{r}_{Ref}(0) = 0$$

Note that the factor 1 is a sufficient proportional "gain" to ensure that the reaction rate is close to equilibrium. Higher numbers do not significantly increase the approach of equilibrium, but may cause solver problems. The reaction rate equation is coupled with the molar balance equations. As the molar composition at the fuel entrance (z=0) is specified, the reaction rate value at this point is meaningless.

The heat transport equation for the gas is:

$$\sum_{i=1}^{7} c_G(z,i) \cdot c_{p,G}(z) \cdot \left(\frac{dT_G(z)}{dt} + u_G \cdot \frac{\partial T_G(z)}{\partial z_b} \right) = \frac{2}{\delta_C} \cdot h_{c,G}(z) \cdot \left(T_W(0,z) - T_G(z) \right) \quad \forall\, z \in (0,l]$$

Note that there are two reformer walls for one gas channel.

The boundary heat transfer between gas and wall is:

$$k_W \cdot \frac{\partial T_W(0,z)}{\partial y} = h_{c,G}(z) \cdot \left(T_W(0,z) - T_G(z) \right) + \frac{\dot{r}_{Ref} \Delta h_{Ref} + \dot{r}_{Shi} \Delta h_{Shi}}{2wl} \quad \forall\, z \in (0,l)$$

The heat conduction in width and length direction inside the wall is:

$$c_W \cdot \rho_W \cdot \frac{dT_W(y,z)}{dt} = k_W \cdot \left(\frac{\partial^2 T_W(y,z)}{\partial z_c^{\,2}} + \frac{\partial^2 T_W(y,z)}{\partial y^2} \right) \quad \forall\, y \in (0,\delta_W), z \in (0,l)$$

The boundary heat transfer at the outer side of the wall (including radiation from the tube) is:

$$k_W \cdot \frac{\partial T_W(\delta_W, z)}{\partial y} = \frac{\dot{q}_{Rad}(z)}{n_R \cdot 2wl} \quad \forall\, z \in (0,l)$$

Regarding the mass transfer, no source or sink terms exists for nitrogen and oxygen:

$$\frac{dc_G(z,i)}{dt} + u_G \frac{\partial c_G(z,i)}{\partial z_c} = 0 \quad \forall\, z \in (0,l], i \in \{N_2, O_2\}$$

The mass transfer equations for the remaining species are:

$$\frac{dc_G(z,H_2)}{dt} + u_G \frac{\partial c_G(z,H_2)}{\partial z_c} = \frac{3\dot{r}_{Ref}(z) + \dot{r}_{Shi}(z)}{lw\delta_G} \quad \forall\, z \in (0,l]$$

$$\frac{dc_G(z,CH_4)}{dt} + u_G \frac{\partial c_G(z,CH_4)}{\partial z_c} = \frac{-\dot{r}_{Ref}(z)}{lw\delta_G} \quad \forall\, z \in (0,l]$$

$$\frac{dc_G(z,H_2O)}{dt} + u_G \frac{\partial c_G(z,H_2O)}{\partial z_c} = \frac{-\dot{r}_{Ref}(z) - \dot{r}_{Shi}(z)}{lw\delta_G} \quad \forall\, z \in (0,l]$$

$$\frac{dc_G(z,CO)}{dt} + u_G \frac{\partial c_G(z,CO)}{\partial z_c} = \frac{\dot{r}_{Ref}(z) - \dot{r}_{Shi}(z)}{lw\delta_G} \quad \forall\, z \in (0,l]$$

$$\frac{dc_G(z,CO_2)}{dt} + u_G \frac{\partial c_G(z,CO_2)}{\partial z_c} = \frac{\dot{r}_{Shi}(z)}{lw\delta_G} \quad \forall\, z \in (0,l]$$

The recipient temperature from the radiation port *Rad* equals the outside temperature of the wall:

$$T_{r,Rad}(z) = T_W(\delta_W, z)$$

The methane reforming degree is:

$$\gamma_R = 1 - \frac{\left(\dot{n} \cdot x(CH_4)\right)_{Out}}{\left(\dot{n} \cdot x(CH_4)\right)_{In}}$$

The relative overall energy balance is:

$$\Delta E = 1 - \frac{n_{Out,G}\left(h_{Out,G} + LHV_{Out}\right) + \frac{1}{l}\int_{z=0}^{l} \dot{q}_{Rad}\, dz}{n_{In,G}\left(h_{In,G} + LHV_{In}\right)}$$

The relative overall mass balance is:

$$\Delta M = 1 - \frac{\dot{n}_{Out,G} M_{Out,G}}{\dot{n}_{In,G} M_{In,G}}$$

Mass and energy balance should in steady state operation be zero. A deviation of 0.01 (=1%) for the energy and 0.005 (=0.5%) for the mass balance is regarded as tolerable.

Comments

The assumptions taken for the integrated internal reformer are quite vague, as few data exist on geometry and materials. However, the expected influence on system performance is expected to be low, provided that a certain degree of reforming can be achieved for a design case by choosing area and transfer factors for the heat exchange. Bulk nickel has been assumed as material for the walls. Dynamic behaviour of the reformer will strongly depend on the amount of heat inertia and thus thickness and material properties of the wall.

4.6.2 Adiabatic Reformer

Icon

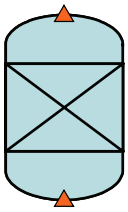

Purpose

The adiabatic reformer is a lumped reformer model based on chemical equilibrium calculation. For including non-equilibrium, a temperature difference between the actual and the equilibrium temperature may be specified. Adiabatic pre-reformers are applied in SOFC systems (such as Siemens-Westinghouse) to reform possibly available higher hydrocarbons in the fuel and part of the methane. Heat for the reactions must be supplied by an upstream mixing of fresh fuel with (hot) recycled anode gas.

Assumptions

The mixer is adiabatic and at steady state. Pressure drop is calculated assuming a constant flow coefficient. Only the steam reforming reaction of methane

$$CH_4 + H_2O \Leftrightarrow 3H_2 + CO$$

and the water-gas shift reaction

$$CO + H_2O \Leftrightarrow CO_2 + H_2$$

occur in the reformer.

Ports

Port	Definition	Type	Direction
In	Gas inlet	Material	In
Out	Gas outlet	Material	Out

One port must be connected.

Variables

Variable	Definition	Unit
ΔT_{eq}	Temperature difference between outlet and equilibrium	K
Δp_{abs}	Absolute pressure drop	Pa
Δp_{rel}	Relative pressure drop	-
c	Flow coefficient	m^2
K_{Ref}, K_{Shi}	Equilibrium constants for steam reforming and water-gas shift reaction	-
γ_R	Degree of methane reforming	-

In design mode, the reforming degree and the absolute or relative pressure drop must be specified. In off-design mode, the equilibrium temperature difference and the flow coefficient must be specified.

Equations

The absolute pressure loss is determined through:

$$\Delta p_{abs} = p_{In} - p_{Out} = c \cdot \frac{\left(\dot{n}_{In} \cdot M_{In}\right)^2}{\rho_{In}}$$

The relative pressure drop is

$$\Delta p_{rel} = \frac{\Delta p_{abs}}{p_{In}}$$

The reactions are assumed to be at equilibrium of the actual temperature minus the equilibrium temperature difference $T_G - \Delta T_{eq}$. The equilibrium constants are determined from the change in standard Gibbs energy at this temperature [Moran 2004]:

$$\ln\left(K_{Shi}\right) = -\frac{g^0\left(H_2\right) + g^0\left(CO_2\right) - g^0\left(CO\right) - g^0\left(H_2O\right)}{R_m\left(T_{Out} - \Delta T_{eq}\right)}$$

$$\ln\left(K_{Ref}\right) = -\frac{3g^0\left(H_2\right) + g^0\left(CO\right) - g^0\left(CH_4\right) - g^0\left(H_2O\right)}{R_m\left(T_{Out} - \Delta T_{eq}\right)}$$

In order to achieve equilibrium, the following relationships must be satisfied at the outlet:

$$K_{Ref} = \frac{x_{Out}(CO) \cdot x_{Out}(H_2)^3}{x_{Out}(CH_4) \cdot x_{Out}(H_2O)} \cdot \left(p_{In}[bar]\right)^2$$

$$K_{Shi} = \frac{x_{Out}(CO_2) \cdot x_{Out}(H_2)}{x_{Out}(CO) \cdot x_{Out}(H_2O)}$$

The molar flow of oxygen and nitrogen does not change:

$$\dot{n}_{Out} \cdot x_{Out}(N_2) = \dot{n}_{In} \cdot x_{In}(N_2) \qquad \dot{n}_{Out} \cdot x_{Out}(O_2) = \dot{n}_{In} \cdot x_{In}(O_2)$$

The molar outlet flows of the reacting species are determined implicitly by the conservation of elements C, H, and O. For carbon, the relationship is:

$$\dot{n}_{Out} \cdot \left(x(CH_4) + x(CO) + x(CO_2)\right)_{Out} = \dot{n}_{In} \cdot \left(x(CH_4) + x(CO) + x(CO_2)\right)_{In}$$

For hydrogen, the relationship is:

$$\dot{n}_{Out} \cdot \left(2 \cdot x(CH_4) + x(H_2) + x(H_2O)\right)_{Out} = \dot{n}_{In} \cdot \left(2 \cdot x(CH_4) + x(H_2) + x(H_2O)\right)_{In}$$

For oxygen, the relationship is:

$$\dot{n}_{Out} \cdot \left(2 \cdot x(CO_2) + x(CO) + x(H_2O)\right)_{Out} = \dot{n}_{In} \cdot \left(2 \cdot x(CO_2) + x(CO) + x(H_2O)\right)_{In}$$

The missing relationship to determine the outlet molar flow is:

$$\sum_{i=1}^{7} x_{Out}(i) = 1$$

The outlet temperature is determined implicitly over an energy balance:

$$\left(\dot{n} \cdot \left(h + h_f^0\right)\right)_{Out} = \left(\dot{n} \cdot \left(h + h_f^0\right)\right)_{In}$$

The methane reforming degree is:

$$\gamma_R = 1 - \frac{\left(\dot{n} \cdot x(CH_4)\right)_{Out}}{\left(\dot{n} \cdot x(CH_4)\right)_{In}}$$

Comments

The equilibrium temperature difference must not be below zero. Else, the gas equilibrium temperature would be higher than the actual outlet temperature, which is violating the second law of thermodynamics, unless the gas has been at a temperature higher than the outlet temperature inside the reformer.

4.6.3 Casing

Icon

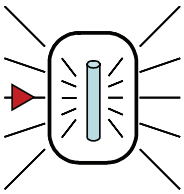

Purpose

The model is applied to calculate radiation heat losses distributed over the axial length of the SOFC stack. It receives radiation heat from an inner component and releases it to the environment. A heat transfer series consisting of inner radiation, heat conduction in the casing material and outer radiation is modelled. The distribution was included in order to achieve a correct spatial distribution of radiation for components with steep temperature profile.

Assumptions

The casing is one-dimensional. Steady state is assumed, i.e. heat holdup in the casing is neglected. Heat conduction along the wall direction is neglected, as the heat conductivity of the casing material will be typically very small. An emissivity of unity is assumed for the radiation to the environment. Assuming a cylindrical vessel as casing of the SOFC stack, only the circumferential wall is considered for heat loss. The calculation of inner radiation is not included in the model; it must be included in the radiation partner model (SOFC).

Parameters

Parameter	Definition	Unit	Default
l	Length of casing (distributed direction)	m	1.5
A	Area of the wall	m^2	12.5
k	Thermal conductivity of the insulation material	$W\ m^{-1}\ K^{.1}$	0.17 [13]
d	Thickness of the casing	m	0.15

Distribution Domains

Domain	Definition	Discretisation	Order	Nodes
z	Axial direction (0:l)	CFDM	2	40

[13] **Typical value for high temperature insulation materials [Abis 2005]**

Ports

Port	Definition	Type	Direction
Rad,SOFC	Radiation from the SOFC, distributed over z	Radiation	In

The radiation port must be connected.

Variables

Variable	Definition	Unit
$T_I(z)$	Inner wall temperature	K
$T_O(z)$	Outer wall temperature	K
T_∞	Ambient temperature	K
$\dot{q}_t$	Total heat flow	W

The ambient temperature must be specified.

Equations

The inner wall temperature equals the recipient temperature from the radiation port:

$$T_i = T_{R;Rad,SOFC}$$

The heat conduction chain is described by

$$\dot{q}_{Rad,SOFC}(z) = k \cdot \frac{A}{d} \cdot \left(T_I(z) - T_O(z)\right) = \sigma A \cdot \left(T_O(z)^4 - T_\infty^4\right) \quad \forall\, z \in [0;l]$$

The total heat flow is

$$\dot{q}_t = \frac{1}{l} \int_{z=0}^{l} \dot{q}_{Rad,SOFC}(z)$$

Comments

The model is based on heat transfer in a simplified geometry; however, no data on the true nature of a SOFC stack casing are available and the parameters are guessed. A parameter to adjust the integral heat loss is the coefficient for the radiation between casing and SOFC which is specified in the SOFC model. The casing parameters have an influence on the temperature of the radiation recipient and hence on the distribution of radiation along the SOFC tube.

4.6.4 Ejector

Icon

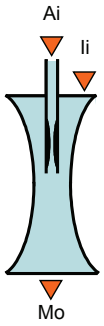

Purpose

The model describes an ejector with supersonic nozzle and subsonic mixing. It is based on mass and energy balances in the nozzle critical section (c), at the nozzle exit (n), at the mixing section entry (m) and exit (d) and at the diffuser exit (o) and furthermore on a momentum balance at the mixing section (see Figure 4-5). It has been calibrated against data from Marsano et al. [2004]. The model may be run in design and off-design mode. It was originally developed by Inge Fosse during a semester project [Fosse 2003].

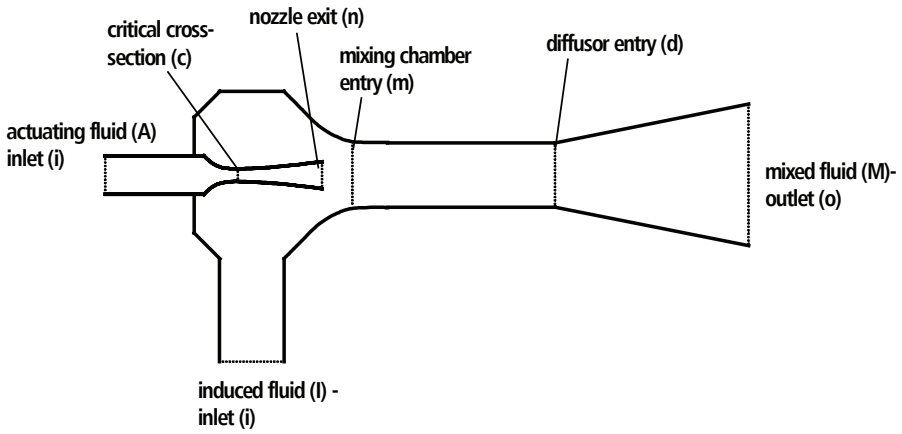

Figure 4-5: Fluids and balance points of the ejector model

Assumptions

The ejector is a steady state model. Constant cross-section mixing is assumed. Stagnation (no movement) of the fluids entering and leaving the ejector is assumed in order to match the energy conservation of the other system components where dynamic pressure is neglected. The expansion of the actuating fluid is regarded as

isentropic. The pressure of the actuating fluid must be higher than the pressure of the inducing fluid at the mixing section entry. Losses are accounted for by total pressure loss coefficients in the mixing section and diffuser.

Parameters

Parameter	Definition	Unit	Default
c_{pm}	Pressure recuperation coefficient mixing	-	0.8 [14]
c_{pd}	Pressure recuperation coefficient diffuser	-	0.75 [14]

Ports

Port	Definition	Type	Direction
Ai	Actuating fluid inlet	Material	In
Ii	Induced fluid inlet	Material	In
Mo	Mixed fuel outlet	Material	Out

Composition and temperature of two streams must be specified. If geometry is assigned (off-design mode), either pressure or mass flow of each of two flows must be specified. Otherwise (in design mode), pressure and flow rates must be specified.

Variables

Variable	Points (see Figure 4-5)	Definition	Unit
A	c, n, m, d, o	Cross-sectional area at balance points	m^2
T	Ac, An, Am, Im, Md_{is}, Md	Temperature at balance points	K
p	Ac, An, Am, Im, Md_{is}, Md	Pressure at balance points	Pa
u	Ac, An, Am, Im, Md_{is}, Md, Mo	Velocity at balance points	$m\ s^{-1}$
Ma	n	Mach number at nozzle exit	-
$\dot{m}$	A,C,M	Mass flow	$kg\ s^{-1}$
R	A,C,M	Gas constant	$J\ K^{-1}\ kg^{-1}$
η_{pd}		Ideal pressure recuperation efficiency diffuser	-

In off-design mode, the areas of critical section, nozzle exit, mixing chamber and diffuser outlet must be specified. In design mode, a different set of 4 variables must be specified, for example the two remaining flow rate/pressure variables of the inlet streams, the velocity of the induced fluid at the mixing chamber entry v_{Im} and the

[14] **Adapted to fit the ejector performance of Marsano et al. [2004]**

velocity of the mixed fluid at the diffuser outlet v_{Mo}. The latter should be rather small in order to justify the stagnation assumption.

Equations

Constant area mixing section is assumed:

$$A_m = A_{d,is} = A_d$$

Boundaries

The gas constants:

$$(R)_{I,A,O} = \frac{R_m}{(M)_{I,A,O}}$$

The mass flows of the streams:

$$\dot{m}_I = M_I \cdot \dot{n}_{Ii}; \quad \dot{m}_A = M_A \cdot \dot{n}_{Ai}; \quad \dot{m}_M = M_M \cdot \dot{n}_{Mo}$$

The composition of the mixed stream:

$$\left(\dot{n} \cdot x(:)\right)_{Mo} = \left(\dot{n} \cdot x(:)\right)_{Ii} + \left(\dot{n} \cdot x(:)\right)_{Ai}$$

Critical Cross-Section (c)

Sonic flow in the critical cross-section is assumed. The velocity is hence:

$$u_{Ac} = \sqrt{\kappa_{Ac} R_A T_{Ac}}$$

The mass balance of the actuating fluid:

$$\dot{m}_A = \rho_{Ac} \cdot A_c \cdot u_{Ac}$$

The enthalpy at the critical cross-section (implicitly specifying the temperature T_{Ac}):

$$h\left(T_{Ac}, p_{Ac}, x_{Ac}(:)\right) - h_{Ai} = -\tfrac{1}{2} M_A u_{Ac}^2$$

Isentropic expansion is assumed (implicitly specifying the pressure p_{Ac}):

$$s\left(T_{Ac}, p_{Ac}, x_{Ac}(:)\right) - s_{Ai} = 0$$

Nozzle Exit (n)

Supersonic flow (Ma_n>1) is assumed. The velocity at the nozzle exit:

$$u_{An} = Ma_n \sqrt{\kappa_{An} R_A T_{An}}$$

Temperature, pressure and density are determined analogously to the critical cross-section:

$$h_{An} - h_{Ac} = \tfrac{1}{2} M_A \left(u_{Ac}^2 - u_{An}^2\right)$$

$$s_{An} - s_{Ac} = 0$$

$$\dot{m}_A = \rho_{An} \cdot A_n \cdot u_{An}$$

Mixing Section Entry (m)

It is assumed that the jet of actuating fluid has the same pressure, temperature, velocity and consequently area at the mixing section entry as at the nozzle exit.

$$(h, s, T, p, \rho, u)_{An} = (h, s, T, p, \rho, u)_{Am}$$

The induced fluid is assumed to be subsonic and the following relations apply:

$$h_{Im} - h_{Ii} = -\frac{1}{2} M_I u_{Im}^2$$

$$s_{Im} - s_{Ii} = 0$$

$$\dot{m}_I = \rho_{Im} \cdot (A_m - A_n) \cdot u_{Im}$$

However, one equation to calculate mass flow and velocity is missing and will be determined in the mixing section.

Ideal Mixing Section (d_{is})

It is assumed that induced and actuating fluid enter the mixing section unmixed and exit it ideally mixed. No friction is assumed.

The enthalpy balance over the mixing section:

$$\dot{n}_{Mm*} h_{Mm*} - \dot{n}_{Am} h_{Am} - \dot{n}_{Im} h_{Im} = \frac{1}{2}\left(\dot{m}_{Am} u_{Am}^2 + \dot{m}_{Im} u_{Im}^2 - \dot{m}_{Mm*} u_{Mm*}^2\right)$$

The momentum balance over the mixing section:

$$A_n \cdot p_{Am} + (A_m - A_n) \cdot p_{Im} - A_d \cdot p_{Mm*} = \dot{m}_{Mm*} u_{Mm*} - \dot{m}_{Am} u_{Am} - \dot{m}_{Im} u_{Im}$$

Total Pressure Loss / Diffuser Entry (d)

In this section a loss of total pressure is calculated with the Bernoulli equation, including a pressure recuperation coefficient of the mixing section:

$$p_{Md} + \frac{1}{2} \rho_{Md} u_{Md}^2 = p_{Mm*} + \frac{1}{2} c_{pm} \rho_{Mm*} u_{Mm*}^2$$

The other parameters are determined through mass and energy balance:

$$\rho_{Md} \cdot u_{Md} = \rho_{Mm*} \cdot u_{Mm*}$$

$$h_{Md} - h_{Mm*} = \frac{1}{2}\left(M_{Mm*} u_{Mm*}^2 - M_{Md} u_{Md}^2\right)$$

The mass balance and continuum equation over the mixing section:

$$\dot{m}_M = \dot{m}_I + \dot{m}_A = \rho_{Md} \cdot A_d \cdot u_{Md}$$

Diffuser / Outlet (o)

The efficiency of total pressure conservation in an ideal diffuser is [White 2003]:

$$\eta_{pd} = 1 - \left(\frac{A_d}{A_o} \right)^2$$

Together with a coefficient for a real diffuser and assuming stagnation at the outlet, the Bernoulli equation for the diffuser yields

$$p_{Mo} = p_{Md} + \tfrac{1}{2} \eta_{pd} c_{pd} \rho_{Md} u_{Md}^2$$

The outlet temperature T_{Mo} is determined by the enthalpy balance

$$h\left(T_{Mo}, p_{Mo}, x_{Mo}(:)\right) - h_{Md} = \tfrac{1}{2} M_{Md} u_{Md}^2$$

The true outlet velocity is finally calculated by the continuum equation

$$\dot{m}_M = \rho_{Mo} \cdot A_o \cdot u_{Mo}$$

Comments

Due to the choked nozzle, the flow rate of actuating fluid is directly depending on its inlet pressure (next to molar weight and temperature).

To ensure correct physical behaviour of the model, it must be checked that the pressure of the actuating fluid is equal or higher than the pressure of the induced fluid in the mixing section entry. A lower actuating fluid pressure causes a strong reduction in induced flow rate, while a higher actuating flow pressure does not significantly increase induced fluid flow rate [Johannesen 1951].

4.6.5 Burner

Icon

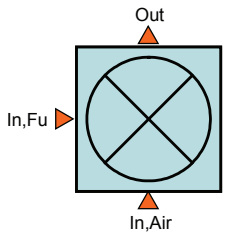

Purpose

The model describes an ideal burner. It mixes two streams and turns all occurring methane, hydrogen, and carbon monoxide to carbon dioxide and steam.

Assumptions

The burner is adiabatic, steady state and frictionless. Pressure loss for both inlets is calculated assuming constant flow coefficients. Complete reaction of all combustibles is assumed.

Variables

Variable	Definition	Unit
$\Delta p_{abs,Fu}$, $\Delta p_{abs,Air}$	Absolute pressure drop for fuel and air	Pa
$\Delta p_{rel,Fu}$, $\Delta p_{rel,Air}$	Relative pressure drop for fuel and air	-
c_{Fu}, c_{Air}	Flow coefficient of fuel and air	m^2

In design mode, either relative or absolute pressure drop for fuel and air must be specified. In off-design mode, the flow coefficients must be specified.

Ports

Port	Definition	Type	Direction
In,Fu	Fuel inlet	Material	In
In,Air	Air inlet	Material	In
Out	Outlet	Material	Out

The inlet ports must be connected.

Equations

The absolute pressure losses are determined through:

$$\Delta p_{abs,Fu} = p_{In,Fu} - p_{Out} = c_{Fu} \cdot \frac{\left(\dot{n}_{In,Fu} \cdot M_{In,Fu}\right)^2}{\rho_{In,Fu}}$$

$$\Delta p_{abs,Air} = p_{In,Air} - p_{Out} = c_{Air} \cdot \frac{\left(\dot{n}_{In,Air} \cdot M_{In,Air}\right)^2}{\rho_{In,Air}}$$

The relative pressure drops are

$$\Delta p_{rel,Fu} = \frac{\Delta p_{abs,Fu}}{p_{In,Fu}}; \qquad \Delta p_{rel,Air} = \frac{\Delta p_{abs,Air}}{p_{In,Air}}$$

As for mass balances, Nitrogen flow rates are simply added:

$$\left(\dot{n} \cdot x\left(N_2\right)\right)_{Out} = \left(\dot{n} \cdot x\left(N_2\right)\right)_{In,Fu} + \left(\dot{n} \cdot x\left(N_2\right)\right)_{In,Air}$$

Outlet flow rates of methane, hydrogen and carbon monoxide are zero:

$$x\left(CH_4\right)_{Out} = x\left(H_2\right)_{Out} = x\left(CO\right)_{Out} = 0$$

Atomic balance of hydrogen:

$$\left(\dot{n}\cdot\left(2\cdot x\left(CH_4\right)+x\left(H_2\right)+x\left(H_2O\right)\right)\right)_{In,Fu}+\left(\dot{n}\cdot\left(2\cdot x\left(CH_4\right)+x\left(H_2\right)+x\left(H_2O\right)\right)\right)_{In.Air}$$
$$=\left(\dot{n}\cdot\left(2\cdot x\left(CH_4\right)+x\left(H_2\right)+x\left(H_2O\right)\right)\right)_{Out}$$

Atomic balance of carbon:

$$\left(\dot{n}\cdot\left(x\left(CH_4\right)+x\left(CO\right)+x\left(CO_2\right)\right)\right)_{In,Fu}+\left(\dot{n}\cdot\left(x\left(CH_4\right)+x\left(CO\right)+x\left(CO_2\right)\right)\right)_{In.Air}$$
$$=\left(\dot{n}\cdot\left(x\left(CH_4\right)+x\left(CO\right)+x\left(CO_2\right)\right)\right)_{Out}$$

Atomic balance of oxygen:

$$\left(\dot{n}\cdot\left(2\cdot x\left(O_2\right)+2\cdot x\left(CO_2\right)+x\left(CO\right)+x\left(H_2O\right)\right)\right)_{In,Fu}$$
$$+\left(\dot{n}\cdot\left(2\cdot x\left(O_2\right)+2\cdot x\left(CO_2\right)+x\left(CO\right)+x\left(H_2O\right)\right)\right)_{In.Air}$$
$$=\left(\dot{n}\cdot\left(2\cdot x\left(O_2\right)+2\cdot x\left(CO_2\right)+x\left(CO\right)+x\left(H_2O\right)\right)\right)_{Out}$$

The sum of components at the outlet must yield unity:

$$\sum_{i=1}^{7}x_{Out}\left(i\right)=1$$

The energy balance:

$$\left(\dot{n}\cdot\left(h+h_f^0\right)\right)_{Out}=\left(\dot{n}\cdot\left(h+h_f^0\right)\right)_{In,Fu}+\left(\dot{n}\cdot\left(h+h_f^0\right)\right)_{In,Air}$$

Comments

The model treats air and fuel inlets equally. As all combustibles are converted, a premise is that at least the stoichiometric rate of oxygen must be available. Else, the outlet oxygen molar fraction will turn negative. With adequate variable bounds, no solution will be found in this case. In the applications investigated here, there should from an operational point of view, however, always be a certain air excess and this limitation is thus tolerable.

4.6.6 Mixer

Icon

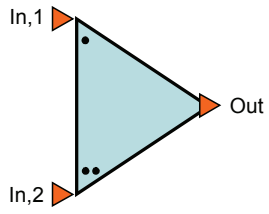

Purpose

The mixer model is applied to unify material streams of equal pressure.

Assumptions

The mixer is adiabatic, steady state and frictionless.

Ports

Port	Definition	Type	Direction
In,1	Inlet port 1	Material	In
In,2	Inlet port 2	Material	In
Out	Outlet port	Material	Out

Two ports must be connected. However, not more than one pressure must be assigned.

Equations

Pressure of all ports is set equal:

$$p_{In,1} = p_{In,2} = p_{Out}$$

Flow rates are added:

$$\dot{n}_{Out} = \dot{n}_{In,1} + \dot{n}_{In,2}$$

Specific enthalpy and composition are mixed:

$$\left(\dot{n} \cdot h\right)_{Out} = \left(\dot{n} \cdot h\right)_{In,1} + \left(\dot{n} \cdot h\right)_{In,2}$$

$$\left(\dot{n} \cdot x(:)\right)_{Out} = \left(\dot{n} \cdot x(:)\right)_{In,1} + \left(\dot{n} \cdot x(:)\right)_{In,2}$$

4.6.7 Splitter

Icon

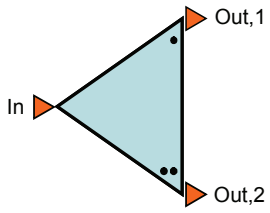

Purpose

The splitter model is applied where streams are split with a certain ratio.

Assumptions

The splitter is adiabatic, steady state and frictionless.

Ports

Port	Definition	Type	Direction
In	Inlet port	Material	In
Out,1	Outlet port 1	Material	Out
Out,2	Outlet port 2	Material	Out

The inlet port must be connected.

Variables

Variable	Definition	Unit
ψ_1	Split ratio Out,1	-
ψ_2	Split ratio Out,2	-

One split ratio must be specified.

Equations

Temperature, pressure and composition of all ports are set equal.

The split ratios are coupled to the flow rates

$$\psi_1 = \frac{\dot{n}_{Out,1}}{\dot{n}_{In}}; \quad \psi_2 = \frac{\dot{n}_{Out,2}}{\dot{n}_{In}}$$

The mass balance is:

$$\psi_1 + \psi_2 = 1$$

4.6.8 Throttle

Icon

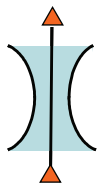

Purpose

The throttle model describes the off-design behaviour of a fixed throttle. The purpose is to model orifices adjusted to achieve a certain pressure loss, which represents an

option for dimensioning the anode recycle loop. It may be operated in design mode with specified pressure loss or in off-design mode with specified flow coefficient.

Assumptions

The throttle in steady state, i.e. no heat and mass inertia are considered. A constant flow coefficient is assumed. Incompressible fluid is assumed, i.e. the model is only accurate for small relative pressure drop.

Ports

Port	Definition	Type	Direction
In	Inlet port	Material	In
Out	Outlet port	Material	Out

Either the inlet or the outlet port must be connected.

Variables

Variable	Definition	Unit
Δp_{abs}	Absolute pressure drop	Pa
Δp_{rel}	Relative pressure drop	-
c	Flow coefficient	m^2

One variable must be specified.

Equations

Flow rate and molar composition of input and output are set equal. Temperatures are coupled through the energy balance equation

$$h_{In} = h_{Out}$$

The absolute pressure loss is determined through:

$$\Delta p_{abs} = p_{In} - p_{Out} = c \cdot \frac{\left(\dot{n}_{In} \cdot M_{In}\right)^2}{\rho_{In}}$$

The relative pressure drop is

$$\Delta p_{rel} = \frac{\Delta p_{abs}}{p_{In}}$$

Comments

The model assumes a constant pressure loss coefficient and is hence not suitable for modelling pressure loss in pipes. For modelling of orifices it is, however, sufficient.

Negative flow coefficients must be avoided because they lead to pressure increase and hence violate the second law of thermodynamics.

4.6.9 Generator/Alternator

Icon

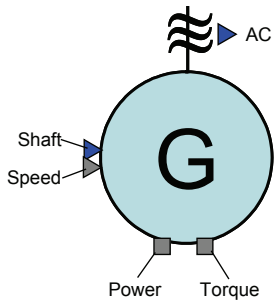

Purpose

The generator model represents the conversion from mechanical to electrical energy. Manipulation of either torque or power by a control system is possible.

Assumptions

The generator has a constant efficiency and is instantaneously reacting on any control signal manipulating power or torque.

Parameters

Parameter	Definition		Default
η_{gen}	Generator efficiency		0.95

Ports

Port	Definition	Type	Direction
Shaft	Shaft power (gross)	Energy	In
AC	AC power (net)	Energy	Out
Speed	Shaft speed (s^{-1})	Control	In
Torque	Generator torque (Nm)	Control	In/Out
Power	Generator power (gross; W)	Control	In/Out

Shaft and *Speed* should be assigned. Either *Torque* or *Power* should be assigned.

Equations

The power values are coupled:

$$\frac{P_{AC}}{\eta_{Gen}} = P_{Shaft} = S_{Power}$$

The torque is coupled to shaft speed and power:

$$S_{Torque} = \frac{P_{Shaft}}{2\pi \cdot S_{Speed}}$$

4.6.10 Pipe

Icon

Purpose

The purpose of the pipe model is to account for gas residence times in the pipes and ducts.

Assumptions

The pipe model is adiabatic. Pressure drop is neglected, as 1st order approximations resulted in very small pressure drop (<0.1%/m) for a flow velocity of ~20 ms^{-1}. Input pressure equals output pressure at any time. The speed is constant over the pipe.

Parameters

Parameter	Definition	Unit	Default
r	pipe radius	m	-
l	pipe length	m	-

Distribution Domains

Domain	Definition	Discretisation	Order	Nodes
z	Axial direction (0:l)	BFDM	1	5

Ports

Port	Definition	Type	Direction
In	Inlet port	Material	In
Out	Outlet port	Material	Out

The inlet port must be connected.

Variables

Variable	Definition	Unit
u_{gas}	Flow velocity	m s^{-1}
$T_{gas}(z)$	Flow temperature	K
$c(z,7)$	Concentration	mol m^{-3}
τ	Delay	s

All variables are output variables.

Equations

Pressures at inlet and outlet are equal:

$$p_{In} = p_{Out}$$

Concentrations at the pipe ends are coupled to the inlet and outlet streams by the ideal gas law:

$$c(:,0) = \frac{x_{In}(:)}{v_{In}} \text{ and } c(:,l) = \frac{x_{Out}(:)}{v_{Out}}$$

The gas temperatures at the pipe ends equal the inlet and outlet temperatures:

$$T_{gas}(0) = T_{In} \text{ and } T_{gas}(l) = T_{Out}$$

Inlet and outlet flow rate are coupled by the flow velocity:

$$\left(\frac{\dot{n}RT}{p}\right)_{In} = v_{gas} \cdot r^2\pi = \left(\frac{\dot{n}RT}{p}\right)_{Out}$$

The delay time is coupled to velocity and length:

$$\tau = \frac{l}{u_{gas}}$$

The transport equations are as follows:

$$\frac{\partial T_{gas}(z)}{\partial t} + u_{gas}\frac{\partial T_{gas}(z)}{\partial z} = 0 \quad \forall\, z \in (0,l]$$

$$\frac{\partial c(:,z)}{\partial t} + u_{gas}\frac{\partial c(:,z)}{\partial z} = 0 \quad \forall\, z \in (0,l]$$

Comments

A drawback of the model is that temperature and concentration are smoothed over time; i.e. a step function of the input is turned into a ramp function of the output. This is a consequence of the finite number of nodes and can be mitigated by a higher number of nodes (see Figure 4-6). Due to the computation time consumption, a

number of 5 nodes is nevertheless considered as sufficient for modelling gas residence time in pipes. A similar smoothing effect would to some extent occur in a real tube due to flow turbulence; however, this is an awkward justification.

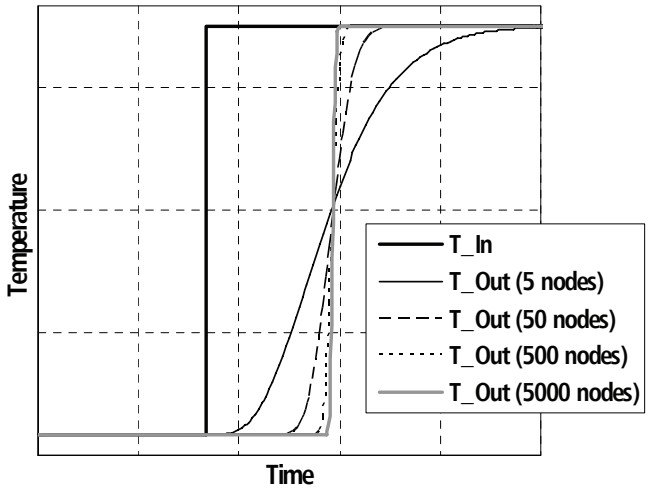

Figure 4-6: Smoothing of pipe outlet temperature for different numbers of nodes

4.6.11 Power Electronics

Icon

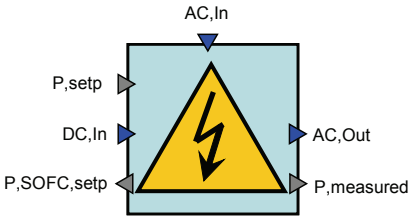

Purpose

The model provides the conversion of produced power to net power. It furthermore calculates the power required from the SOFC at a given generator power to supply a certain net power. This signal will be used for primary control of the SOFC (see Chapter 6.3).

Assumptions

The conversion efficiencies are constant parameters. The generator AC power is at first rectified and then inverted to the grid frequency. An auxiliary power requirement may compensate for conversion efficiency decrease at lower load. For the calculation of required SOFC power, it is assumed that the exact performance of the power

conversion is known to the system, i.e. an immediate determination of the new required SOFC power after a setpoint change is possible.

Parameters

Parameter	Definition	Unit	Default
$\eta_{AC\text{-}DC}$	Efficiency AC to DC	-	0.95
$\eta_{DC\text{-}AC}$	Efficiency DC to AC	-	0.95
P_{aux}	Auxiliary power requirement	W	5000

Ports

Port	Definition	Type	Direction
DC,In	DC from SOFC	Energy	In
AC,In	AC from generator	Energy	In
AC,Out	Net AC output	Energy	Out
P,measured	Measured net power	Control	Out
P,setp	Power Setpoint	Control	In
P,SOFC,setp	Power required from SOFC	Control	Out

The inlet ports must be connected.

Equations

Net power:

$$P_{AC,Out} = S_{P,meas} = P_{AC,in}\eta_{AC-DC}\eta_{DC-AC} + P_{DC,in}\eta_{DC-AC} - P_{aux}$$

Required power from the SOFC to reach a certain net power (relevant for control strategy):

$$S_{P,setp} = P_{AC,in}\eta_{AC-DC}\eta_{DC-AC} + S_{P,SOFC,setp}\eta_{DC-AC} - P_{aux}$$

4.6.12 Source

Icon

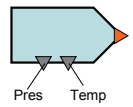

Purpose

The model represents a material source. Control signal outputs for temperature and pressure of the material stream are supplied for flowsheeting.

Ports

Port	Definition	Type	Direction
Out	Outlet	Material	Out
Temp	Temperature of the material stream	Control	Out
Pres	Pressure of the material stream	Control	Out

The material outlet port must be fully defined by temperature, pressure, flow rate and composition.

Equations

Pressure and temperature signals:

$$S_{Pres} = p_{Out} \qquad S_{Temp} = T_{Out}$$

4.6.13 Sink

Icon

Purpose

The model represents a material sink for flowsheeting purpose.

Ports

Port	Definition	Type	Direction
In	Inlet	Material	In

The material inlet port must be connected.

4.7 Control Equipment

4.7.1 PID-Controller

Icon

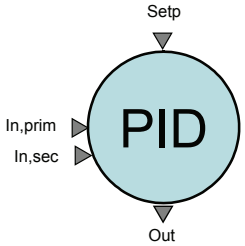

Purpose

The model describes a general PID controller as explained in Chapter 2.5.2. The controller class (P, I, D, PI, PID, PD) can be switched by the user. To prevent windup of the integral part, the latter is stopped if the output variable is at its upper or lower bound. A *manual mode* allows directly specifying the controller output.

Optionally, a secondary control input can be connected and boundaries specified. The controller then supervises that the secondary controlled variable is kept within its boundaries. This function is called *constrained control* and for example useful in a control task where the fuel flow (output) is manipulated to control the fuel utilisation (primary input), but at the same time it must be assured that the ejector is in a valid operation regime (secondary input/constraint).

The PID controller was basically taken over from the gPROMS process model library. However, some adaptations were done concerning secondary control input, port setup and switch criteria for the anti-windup function.

Parameters

Parameter	Definition	Unit	Default
h_{WP}	Hysteresis of windup protection	-	0.05
h_{sec}	Hysteresis of secondary input boundary control switch	-	0.001

Ports

Port	Definition	Type	Direction
In,prim	Primary control input (obligatory)	Control	In
Setp,ext	External setpoint signal for primary control input	Control	In
In,sec	Secondary control input (optional)	Control	In
Out	Controller output signal	Control	Out

All ports must be connected or the signal variables assigned. If no secondary control input is required, it must be connected to a dummy signal.

Variables

Variable	Definition	Unit
K	Proportional gain	-
K_{sec}	Proportional gain of secondary input boundary control	-
τ_I	Reset time of integral term	s
τ_D	Rate time of derivative term	s
ω	Bandwidth limit of derivative term (should be very small)	s^{-1}
A	Controller action (-1 for reverse action; +1 for direct action)	-

S_{prim}^{max}, S_{prim}^{min}	Upper and lower bound of the primary control input signal	-
S_{sec}^{max}, S_{sec}^{min}	Upper and lower bound of the secondary control input signal	-
S_{Out}^{max}, S_{Out}^{min}	Upper and lower bound of the controller output signal	-
S_{Out}^{m}	Output signal in manual mode	-
S_{Setp}	Internal setpoint	-
S_{Out}^{c}	Calculated, unclipped output	-
I	Integral term	-
ΔI	Change in integral term	s^{-1}
P	Proportional term	-
P_{sec}	Proportional term for bound control of secondary control input	-
E	Error	-
D	Derivative term	-
D_{aux}	Auxiliary variable for derivative term calculation	-
B	Bias to be superposed to control signal	-
$D_{swt,WP}$	Absolute switch threshold of windup protection	-
$D_{swt,sec}$	Absolute switch threshold of secondary input boundary control	-

All variables from the top to the manual output signal must be specified. If the controller is in *automatic mode*, the internal setpoint must be further specified.

Selectors

Selector	Definition	Possible modes	Default
Class	Class of controller	P, PI, PID, PD, D, I	I
Mode	Operation mode	manual, automatic, cascade	cascade
Windup_Bound	Anti-windup mode and secondary input boundary control	normal, Windup, C2max, C2Min	normal

Equations

The error is calculated from the relative difference between setpoint and primary input:

$$E \cdot \left(S_{Prim}^{max} - S_{Prim}^{min} \right) = A \cdot \left(S_{Setp} - S_{In,prim} \right)$$

The proportional term equals the error:

$$P = E$$

The derivative term is principally $D=dE/dt$, but because the error must not be derived due to equation system integrity reasons, it is calculated indirectly: The term in the

innermost bracket specifies the relative measured signal. This term is used instead of the error E to avoid strong amplitudes in case of setpoint step changes.

$$D = \frac{dD_{aux}}{dT}; \quad \omega D = \left(\tau_D \left(-\frac{A \cdot S_{In,prim}}{S_{prim}^{\max} - S_{prim}^{\min}} \right) - D_{aux} \right)$$

The secondary proportional term is zero as long as the second control input is within its bounds. It is treated together with the change in integral term by the windup protection and secondary input boundary control:

Selector: *Windup_Bound*		
Mode	Equation	Switch to mode
normal	$\Delta I = \frac{E}{\tau_I}$ $P_{sec} = 0$	Windup *if* $\left(S_{Out}^{c} < \left(S_{Out}^{\min} - D_{sw}\right) \cap E < 0\right) \cup \left(S_{Out}^{c} > \left(S_{Out}^{\max} + D_{sw}\right) \cap E > 0\right)$ C2max *if* $S_{In,sec} > S_{sec}^{\max} + D_{swt,sec}$ C2min *if* $S_{In,sec} < S_{sec}^{\min} - D_{swt,sec}$
Windup	$\Delta I = 0$ $P_{sec} = 0$	normal *if* $\left(\left(S_{Out}^{c} > S_{Out}^{\min}\right) \cap \left(S_{Out}^{c} < S_{Out}^{\max}\right)\right) \cup \left(S_{Out}^{c} < \left(S_{Out}^{\min} - D_{sw}\right) \cap E > 0\right) \cup \left(S_{Out}^{c} > \left(S_{Out}^{\max} + D_{sw}\right) \cap E < 0\right)$ C2max *if* $S_{In,sec} > S_{sec}^{\max} + D_{swt,sec}$ C2min *if* $S_{In,sec} < S_{sec}^{\min} - D_{swt,sec}$
C2max	$\Delta I = \min\left(\frac{E}{\tau_I}, 0\right)$ $P_{sec} = \frac{S_{sec}^{\max} - S_{In,sec}}{S_{sec}^{\max} - S_{sec}^{\min}}$	normal *if* $S_{In,sec} \le S_{sec}^{\max}$
C2min	$\Delta I = \max\left(\frac{E}{\tau_I}, 0\right)$ $P_{sec} = \frac{S_{sec}^{\min} - S_{In,sec}}{S_{sec}^{\max} - S_{sec}^{\min}}$	normal *if* $S_{In,sec} \ge S_{sec}^{\min}$

where

$$D_{swt,WP} = h_{WP} \cdot \left(S_{Out}^{\max} - S_{Out}^{\min}\right)$$

and

$$D_{swt,sec} = h_{sec} \cdot \left(S_{sec}^{\max} - S_{sec}^{\min} \right)$$

The calculated output and integral term depend on the controller class:

Selector: *Class*		
Mode	Equation 1	Equation 2
PID	$S_{Out}^{c} = K \cdot \left(P + I + D + K_{sec} \cdot P_{sec} \right) \cdot \left(S_{Out}^{\max} - S_{out}^{\min} \right) + B$	$\frac{dI}{dt} = \Delta I$
PI	$S_{Out}^{c} = K \cdot \left(P + I + K_{sec} \cdot P_{sec} \right) \cdot \left(S_{Out}^{\max} - S_{out}^{\min} \right) + B$	$\frac{dI}{dt} = \Delta I$
P	$S_{Out}^{c} = K \cdot \left(P + K_{sec} \cdot P_{sec} \right) \cdot \left(S_{Out}^{\max} - S_{out}^{\min} \right) + B$	$\frac{dI}{dt} = 0$
PD	$S_{Out}^{c} = K \cdot \left(P + D + K_{sec} \cdot P_{sec} \right) \cdot \left(S_{Out}^{\max} - S_{out}^{\min} \right) + B$	$\frac{dI}{dt} = 0$
D	$S_{Out}^{c} = K \cdot \left(D + K_{sec} \cdot P_{sec} \right) \cdot \left(S_{Out}^{\max} - S_{out}^{\min} \right) + B$	$\frac{dI}{dt} = 0$
I	$S_{Out}^{c} = K \cdot \left(I + K_{sec} \cdot P_{sec} \right) \cdot \left(S_{Out}^{\max} - S_{out}^{\min} \right) + B$	$\frac{dI}{dt} = \Delta I$

The controller output signal is the calculated or the manual signal clipped to the bounds:

Selector: *Mode*		
Mode	Equation 1	Equation 2
manual	$S_{Out} = \max\left(S_{Out}^{\min}, \min\left(S_{Out}^{\max}, S_{Out}^{m} \right) \right)$	$S_{Setp} = S_{In,prim}$
automatic	$S_{Out} = \max\left(S_{Out}^{\min}, \min\left(S_{Out}^{\max}, S_{Out}^{c} \right) \right)$	S_{Setp} must be specified in this mode
cascade	$S_{Out} = \max\left(S_{Out}^{\min}, \min\left(S_{Out}^{\max}, S_{Out}^{c} \right) \right)$	$S_{Setp} = S_{Setp,ext}$

In manual mode, the internal setpoint is set to the measured primary input signal in order to avoid windup of the integral term.

Comments

It must be noted that the controller action must be specified through the variable *A* which may only have the values of {-1;1}. Any other value will lead to a scaling of the error and cause distortion of the controller settings. The output port of the controller must be connected but not assigned. This is in order to numerically allow the derivation of the integral term, which is coupled to the output signal.

If the controller class is switched, bumps of the output signals may occur that may be omitted by recalculating a bias value simultaneously with the switch command.

The controller features many discontinuities. Each discontinuity causes a reinitialisation of the dynamic solver stepsize and therewith increases computation time.

4.7.2 Power Controller

Icon

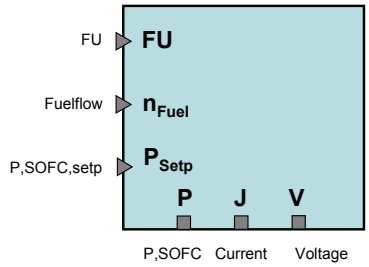

Purpose

The model describes a constrained multi-mode controller of the SOFC power. In normal mode, it forwards a power setpoint to the power electronics which control the SOFC. If a bound on fuel utilisation or voltage is reached, it diverges from setpoint power and specifies either current or voltage to keep the constraint at its bound. As soon as it is possible again to reach the setpoint power without violating any bounds, it switches back to normal mode. Additionally, it features a mode where a voltage can be specified manually. The model was developed after analysis of the system with respect to controllability (see Chapter 6.3) and will be applied in the controlled system.

Parameters

Parameter	Definition	Unit	Default
V_{min}	Minimum voltage bound	V	0.52
FU_{min}	Minimum fuel utilisation bound	-	0.75
FU_{max}	Maximum fuel utilisation bound	-	0.90

Ports

Port	Definition	Type	Direction
FU	Fuel utilisation	Control	In
Fuelflow	Actual fuel flow	Control	In
P,SOFC,setp	Required power from SOFC	Control	In

P,SOFC	Power signal SOFC	Control	In/Out
Current	Current signal SOFC	Control	In/Out
Voltage	Voltage signal SOFC	Control	In/Out

All ports must be connected.

Variables

Variable	Definition	Unit
V_{man}	Voltage signal for manual operation	-
γ_{H_2}	Molar hydrogen yield per reformed mole of fuel (4 for methane)	-

All variables must be specified.

Selectors

Selector	Definition	Possible modes	Default
Mode	Control mode	normal, maxFU, minFU, minV, manualV	normal

Equations

Selector: *Control mode*		
Mode	Equation	Switch to mode
normal	$P = P_{Setp}$	maxFU $if\ FU > FU_{max}$ minFU $if\ FU < FU_{min}$ minV $if\ V < V_{min}$
maxFU	$J = FU_{max} \cdot \gamma_{H_2} \cdot 2F \cdot \dot{n}_{Fuel}$	normal $if\ \ P > P_{Setp}$ minV $if\ V < V_{min}$
minFU	$J = FU_{min} \cdot \gamma_{H_2} \cdot 2F \cdot \dot{n}_{Fuel}$	normal $if\ \ P < P_{Setp}$ minV $if\ V < V_{min}$
minV	$V = V_{min}$	normal $if\ \ P > P_{Setp}$ maxFU $if\ FU > FU_{max}$ minFU $if\ FU < FU_{min}$
manualV	$V = V_{man}$	

4.7.3 Control Valve

Icon

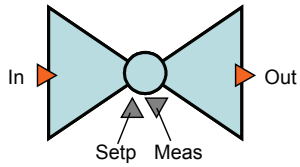

Purpose

The model represents a simple control valve, which can be used for the control of fuel flow or any other flows. It controls the flow rate and simulates inertia of the control system by an asymptotic approach of the setpoint value, based on a time constant. Commercially available gas flow valves are very fast and reach any setpoint in less than a second without over- or undershooting [Bronkhorst 2005]. A measurement error variable is included in order to simulate malfunction in the flow measurement of the valve.

Assumptions

The valve is adiabatic and no fluid inertia is considered. The true flow rate approaches the setpoint asymptotically.

Parameters

Parameter	Definition	Unit	Default
τ	Time constant of the control	s	1

Ports

Port	Definition	Type	Direction
In	Gas inlet	Material	In
Out	Gas outlet	Material	Out
Meas	Measured gas flow signal (mol/s)	Control	Out
Setp	Setpoint gas flow signal (mol/s)	Control	In

The gas inlet and outlet and the setpoint must be connected.

Variables

Variable	Definition	Unit
e	Relative measurement error	-

The error must be specified.

Equations

Flow rate and molar composition of input and output are set equal. The measured signal is determined by

$$S_{Meas} = \dot{n}_{In} \cdot (1 + e)$$

The flow rate signal is obtained by:

$$\frac{dS_{Meas}}{dt} = \frac{S_{Setp} - S_{Meas}}{\tau}$$

Temperatures are coupled through the energy balance equation:

$$h_{In} = h_{Out}$$

Comments

It must be noted that there is no fix relationship between the inlet and outlet pressure of the valve. A control valve acts by throttling the pressure to any level to reach the flow rate setpoint. The value of the pressure is here determined by the downstream pressure-flow rate characteristics. Consequently, the downstream pressure must be determined elsewhere. Another particularity of the model in this context is that there is no check of the second law of thermodynamics; i.e. if the upstream pressure is too low to achieve a certain flow rate with the actual downstream pressure-flow rate characteristics, the valve will have a higher outlet than inlet pressure. This is physically not feasible.

A limitation of the model is that for a change of feed pressure or downstream characteristics (for example by adjustment of a second valve) there would in reality be a short-time deviation of the measured flow rate from the setpoint, which is not covered by the model. However, in case of the fuel flow, where this valve is applied, these incidents are not likely to occur.

4.7.4 Characteristic Line

Icon

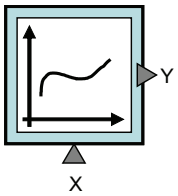

Purpose

The model is basically a flowsheet representation of an arbitrary polynomial function $Y=f(X)$ within the upper and lower bound of the input X. It is used to calculate and represent characteristic lines required for operation and feed forward control.

Assumptions

A polynomial function is applied on an input signal. If the values of the input signal exceed the boundaries, the function value resides at the boundary value.

Ports

Port	Definition	Type	Direction
X	Input signal	Control	In
Y	Output signal	Control	Out

The input port must be connected.

Variables

Variable	Definition	Unit
$c(0:5)$	Polynomial coefficients	-
$S_{X,max}$, $S_{X,min}$	Input signal bounds	-

The parameters define the curve shape and boundaries and must be specified.

Equations

The output signal:

$$S_Y = \begin{cases} \sum_{i=0}^{5} c(i) \cdot \left(S_{X,\min}\right)^i & if\ S_X < S_{X,\min} \\ \sum_{i=0}^{5} c(i) \cdot \left(S_X\right)^i & if\ S_{X,\min} \le S_X \le S_{X,\max} \\ \sum_{i=0}^{5} c(i) \cdot \left(S_{X,\max}\right)^i & if\ S_X > S_{X,\max} \end{cases}$$

Comments

Due to the directionless nature of the equation oriented approach, the model may in the same manner calculate an input signal based on the output signal. However, no solution may be found if the output signal value exceeds the range of possible output signals. If the inverse function of the polynomial is not unique, the solver may be trapped with an insufficient solution. This has, however, not been observed yet.

4.7.5 Rate Limiter

Icon

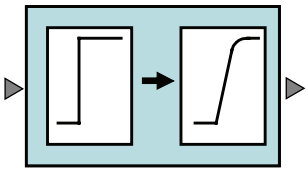

Purpose

The rate limiter smoothes control signals. Unsteady inputs are transferred to steady outputs with a maximum rate and an asymptotic approach of the target based on an integral time constant. The purpose is to increase stability of control systems. A further purpose can be to stabilise the solver where step changes occur or to solve mathematical problems with assignment of state variables. It was derived from the gPROMS inbuilt Process Model Library (PML).

Assumptions

Three cases of operation exist: normal operation, operation at maximum increase rate and operation at maximum decrease rate. No hysteresis is assumed for the switch between the cases.

Ports

Port	Definition	Type	Direction
In,ext	External input signal	Control	In
Out	Output Signal	Control	Out

The input port must be connected. The output is a state variable and must not be assigned.

Variables

Variable	Definition	Unit
τ	Time constant	s
$\dot{S}_{out}^{\max}$	Maximum rate of output signal	s^{-1}
$S_{In,man}$	Manual input signal	-
$\dot{S}_{out}^{n}$	Derived output signal in normal mode	s^{-1}
S_{In}	Input signal	-

The first three variables must be assigned.

Selectors

Selector	Definition	Possible modes	Default
Operation	Operational case	normal, max, min	normal
Mode	Operation mode	automatic, manual	automatic

Equations

The input signal is

Selector: *Mode*	
Mode	Equation
automatic	$S_{In} = S_{In,ext}$
manual	$S_{In} = S_{In,man}$

The derived output signal in normal operation is:

$$\dot{S}_{Out}^{n} = \frac{S_{In} - S_{Out}}{\tau}$$

The input-output connection is depending on the *Operation* selector:

Selector: *Operation*		
Mode	Equation	Switch to mode
normal	$\frac{dS_{Out}}{dt} = \dot{S}_{Out}^{n}$	max $if\ \dot{S}_{Out}^{n} > \dot{S}_{Out}^{\max}$ min $if\ \left(-\dot{S}_{Out}^{n}\right) > \dot{S}_{Out}^{\max}$
max	$\frac{dS_{Out}}{dt} = \dot{S}_{Out}^{\max}$	normal $if\ \dot{S}_{Out}^{n} < \dot{S}_{Out}^{\max}$
min	$\frac{dS_{Out}}{dt} = -\dot{S}_{Out}^{\max}$	normal $if\ \left(-\dot{S}_{Out}^{n}\right) < \dot{S}_{Out}^{\max}$

4.7.6 Signal Mixer

Icon

Purpose

The signal mixer adds two control signals and clips the output to a maximum and minimum bound.

Ports

Port	Definition	Type	Direction
In,1	Input signal 1	Control	In
In,2	Input signal 2	Control	In
Out	Output Signal	Control	Out

Two ports must be connected.

Variables

Variable	Definition	Unit
$S_{out,max}$	Maximum output signal	-
$S_{out,min}$	Minimum output signal	-

All variables must be specified.

Equations

The output signal is

$$S_{Out} = \min\left(S_{Out,max}, \max\left(S_{Out,min}, S_{In,1} + S_{In,2}\right)\right)$$

4.7.7 Flow and Temperature Measurement

The two models are similar and thus treated together.

Icons

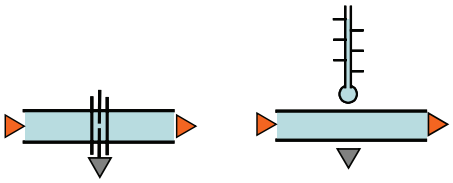

Purpose

The models represent measurement points in flowsheeting. To simulate measurement failure, a relative error is included that must be assigned.

Ports

Port	Definition	Type	Direction
In	Inlet port	Material	In
Out	Outlet port	Material	Out
Meas	Measured signal	Control	Out

One material port must be connected.

Variables

Variable	Definition	Unit
e	Relative measurement error	-

The error must be specified.

Equations

Inlet and outlet ports are set equal.

The measured signal is determined by

$S_{Meas} = T_{In} \cdot (1 + e)$ respectively $S_{Meas} = \dot{n}_{In} \cdot (1 + e)$

4.8 Author's Contribution to Modelling

The author has developed the following models:

- Performance maps for compressor and turbine
- Preheat tube
- Indirect internal reformer
- Adiabatic reformer
- Casing
- Burner
- Mixer
- Splitter
- Throttle
- Generator/Alternator
- Pipe
- Power electronics
- Power controller
- Control valve
- Characteristic line
- Rate limiter
- Signal mixer
- Flow and temperature measurement

For existing models and models developed in collaboration with others, the author has done the following contributions:

- SOFC tubular core model: pressure losses, radiation heat exchange, revision of the shift reaction equilibrium thermodynamics, energy and mass balance check, carbon deposition check, mathematical improvements (equation scaling, initial conditions, variable boundaries).
- Compressor and Turbine: Adaptation of the models for calculating molar flows, restructuring of the interfaces and inclusion of scaling options.
- Plate-fin heat exchanger: Rearrangement of the model with respect to interfaces and inclusion of physical property calculations with Multiflash
- Ejector: Revision, adaptation and calibration.
- PID controller: Inclusion of a second control objective, modification of port setup and switch conditions

5 Hybrid Cycles

This chapter describes models for different hybrid cycle configurations to be investigated. The hybrid cycle models make use of the model toolbox from Chapter 4 and further provide performance parameters for the system. Basics for operation are discussed. Requirements for system design are derived with respect to performance and safety. Interactions between design objectives and parameters are detected, and a set of objectives for the directly integrated cycle is developed.

5.1 Hybrid Cycle Models

5.1.1 Configurations

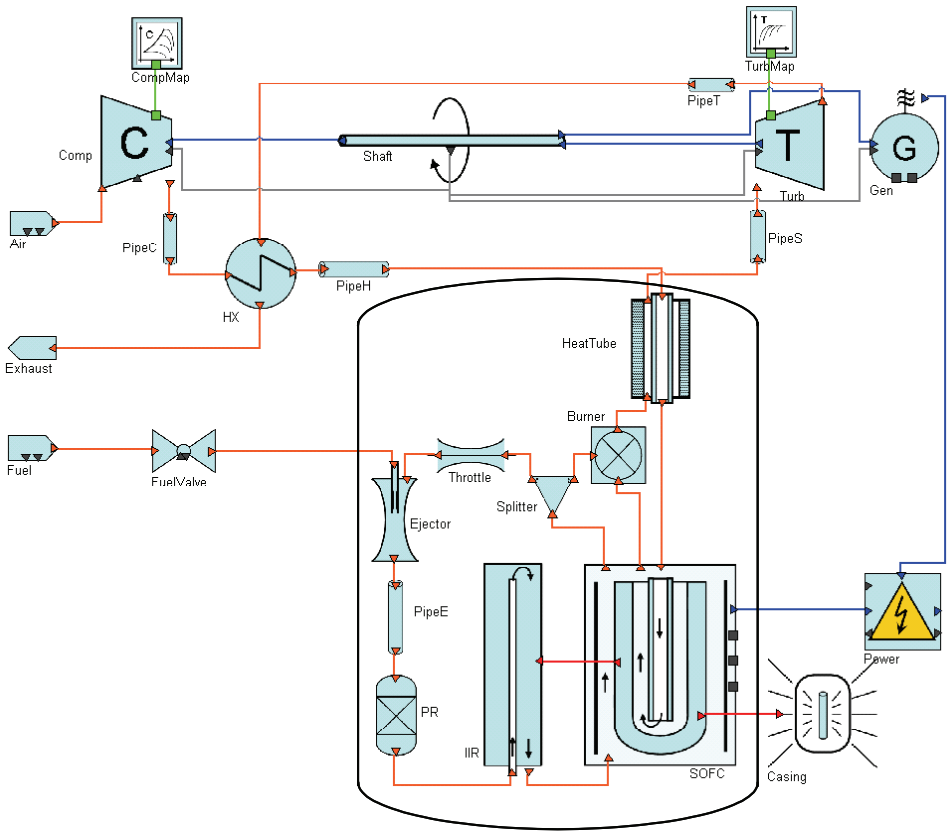

Figure 5-1: Cycle with directly integrated (pressurised) SOFC (DIC)

In the following studies, three different cycle configurations will be investigated:

- Directly integrated SOFC cycle (DIC): In this configuration, the SOFC system replaces the combustion chamber of a recuperated gas turbine cycle. Consequently, the SOFC system is pressurised. From the literature study, this

cycle emerges as the standard cycle (Chapter 3.4.4). The DIC is shown in Figure 5-1.

- Directly integrated SOFC cycle with two-shaft gas turbine (DIC-2T): The cycle configuration is equal to the DIC on the gas side. The expansion is split up into two turbines, where the first is connected to the compressor (so-called *turbocharger*) and the second to the generator (so-called *power turbine*). While the steady state performance is similar to the single expansion DIC, a different control design for dynamic operation is required. The DIC-2T is shown in Figure 5-2.

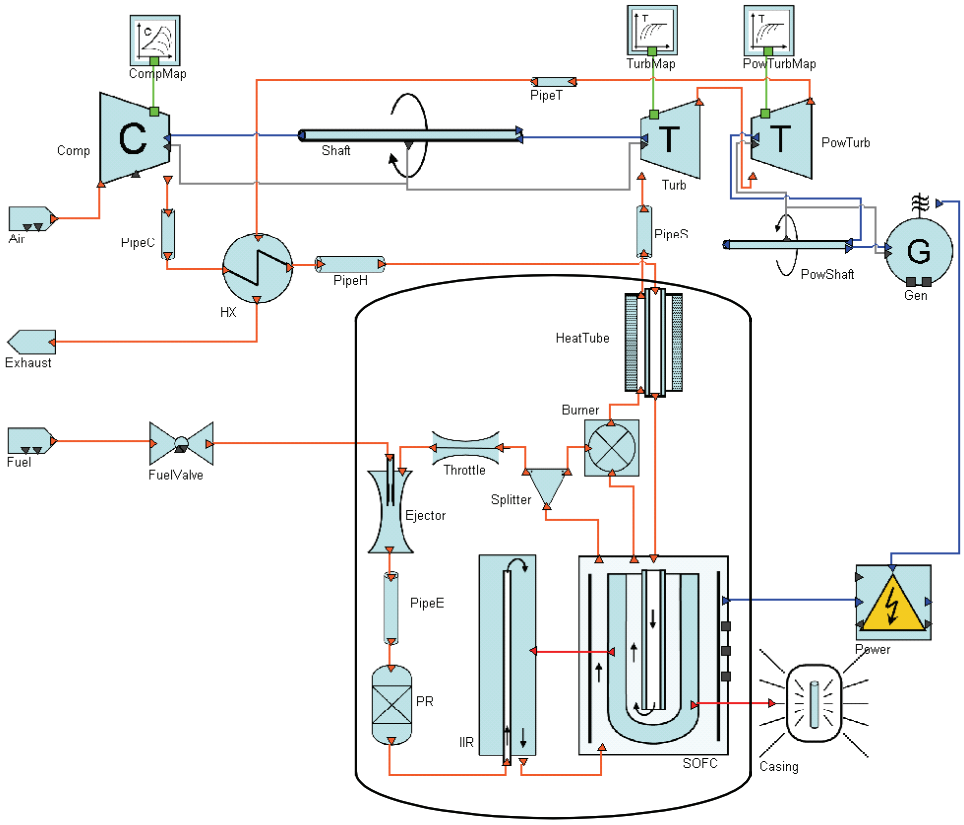

Figure 5-2: Cycle with directly integrated SOFC and two turbines (DIC-2T)

- Indirectly integrated SOFC cycle (IIC): Here, the air is expanded in the turbine before it is fed into the SOFC system. The SOFC system exhaust heats the compressed air. The SOFC is therewith operating at atmospheric pressure. Steady-state performance differs from the DIC due to different temperature relationships and SOFC pressure. However, dynamic and control behaviour are expected to be similar. The IIC is shown in Figure 5-3.

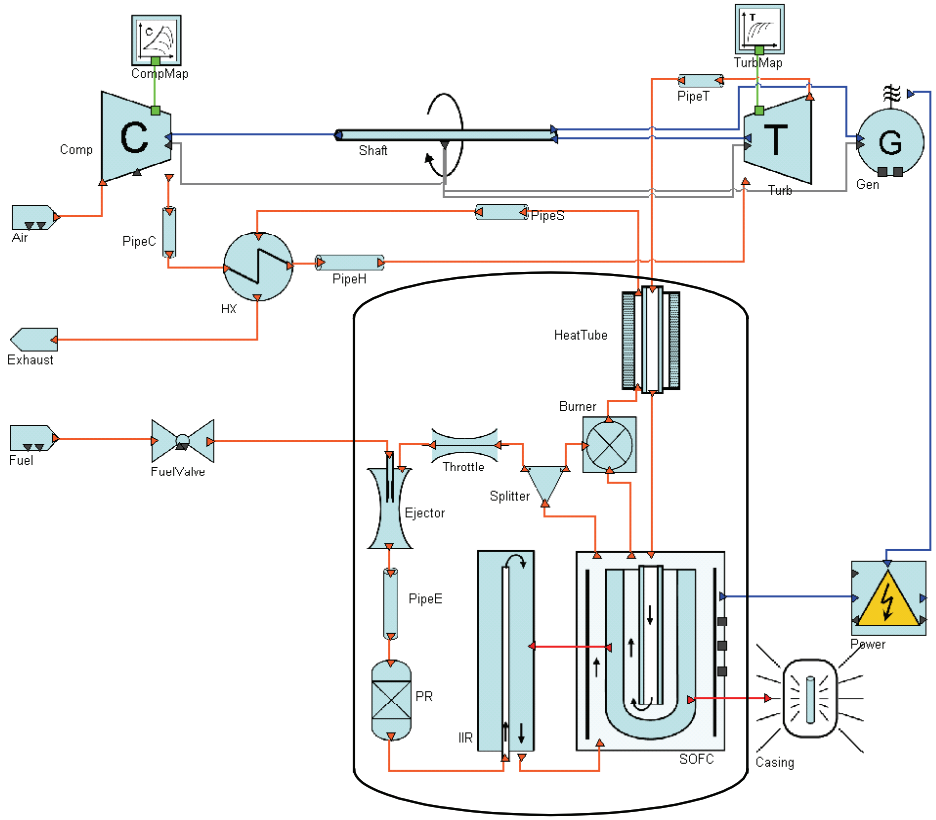

Figure 5-3: Cycle with indirectly integrated (atmospheric) SOFC (IIC)

Figure 5-1 to 5-3 depict the mentioned configurations. They represent hybrid cycle models, which mainly consist of connections between the instances of component models. The component names are highlighted. Orange colour is used for *Material* ports and connections, blue for *Energy*, red for *Radiation,* grey for *Control* and green for the compressor and turbine *Map*.

The black contour indicates the vessel for the SOFC system, which is equal for all three cycle options. It represents the Siemens-Westinghouse system.

The DIC is regarded as the standard cycle, and most of the following studies will refer to it. In Chapter 7, peculiarities of the DIC-2T and IIC as compared to the DIC will be developed and discussed, and an evaluation of the three processes will be conducted.

5.1.2 Hierarchy and Addressing

For simplicity reasons, the whole cycles are integrated in one model each. Thus mainly two hierarchy levels exist, the hybrid cycle level and the component level. All variables and parameters will in the following be addressed with the downstream hierarchy path ahead and finally the name, separated by dots. For example, the electric power of the

fuel cell would be *SOFC.P*, while the scaling pressure ratio of the compressor would be $CompMap.\pi_{Scale}$.

5.1.3 Additional Parameters

Beside the declaration of the units and their connections, the hybrid cycle models provide calculation of overall performance parameters. This subchapter describes these parameters and how they are determined.

- Fuel utilisation (*FU*): The fraction of the fuel entering the system which is utilised in the fuel cell.

  $$FU = \frac{SOFC.J_t}{2F \cdot \dot{n}_{Fuel} \cdot \gamma_{H_2}}$$

  Note that a molar hydrogen yield per mole of fuel is assumed, $\gamma_{H2} = 4$. The *FU* will be an input to the control system described in Chapter 6.3 and hence only practically measurable variables may be used for calculating it (a theoretical approach would also take the molar composition of the fuel into account; see **Equation 2-6**).

- Stoichiometric air ratio (λ) for the complete oxidisation of fuel.

  $$\lambda = \frac{\dot{n}_{Air} \cdot x_{Air}(O_2)}{\dot{n}_{Fuel} \cdot \left(2x_{Fuel}(CH_4) + \frac{1}{2}x_{Fuel}(CO) + \frac{1}{2}x_{Fuel}(H_2)\right)}$$

- Gross power (P_{Gr}): the total power produced by the GT shaft and SOFC.

  $$P_{Gr} = Shaft.P_{Load} + SOFC.P$$

- Net power (P_{Net}): the power which is available for the consumer

  $$P_{Net} = Power.P_{AC,Out}$$

- Net electric efficiency (η_{Net}):

  $$\eta_{Net} = \frac{P_{Net}}{\dot{n}_{Fuel} \cdot LHV_{Fuel}}$$

- Contribution of the gas turbine to the total gross power (p_{GT})

  $$p_{GT} = \frac{Shaft.P_{Load}}{P_{Gr}}$$

- Total degree of methane pre-reforming in both reformers (γ_R)

  $$\gamma_R = 1 - \frac{IIR.\dot{n}_{Out} \cdot IIR.x_{Out}(CH_4)}{PR.\dot{n}_{In} \cdot PR.x_{In}(CH_4)}$$

- Ratio of steam to carbon in methane and CO at the reforming section inlet (γ_{SC})

$$\gamma_{SC} = \frac{PR.x_{In}\left(H_2O\right)}{PR.x_{In}\left(CH_4\right) + PR.x_{In}\left(CO\right)}$$

- Compressor surge margin (SM): Calculated from the compressor pressure ratio and the surge pressure ratio at the actual mass flow. Surge occurs if the value falls below zero.

$$SM = \frac{Comp.\pi_{s,Map} - Comp.\pi_{Map}}{Comp.\pi_{Map}}$$

- Minimum Gibbs energy for carbon deposition reaction (CD): If this value is greater than zero, no carbon deposition occurs at any point of the fuel cell.

$$CD = \min\left(SOFC.\Delta g_{CD}\right)$$

- Pressure difference between actuating and induced fluid at the ejector mixing section entry (Δp_{Ej}) This value must be greater than zero in order to ensure correct ejector operation. It is assumed that it can in a real system be calculated from ejector design and measurable pressures. Thus the true pressures are used:

$$\Delta p_{Ej} = Ejector.p_{Am} - Ejector.p_{Im}$$

- Dimensionless fuel flow ($\overline{\dot{n}}_{Fuel}$), relating to the design point fuel flow

$$\overline{\dot{n}}_{Fuel} = \dot{n}_{Fuel} \Big/ \dot{n}_{Fuel,0}$$

- Dimensionles air flow ($\overline{\dot{n}}_{Air}$), relating to the design point air flow

$$\overline{\dot{n}}_{Air} = \dot{n}_{Air} \Big/ \dot{n}_{Air,0}$$

- Dimensionless net power ($\overline{P}_{Net}$), relating to the design point net power

$$\overline{P}_{Net} = P_{Net} \Big/ P_{Net,0}$$

- Dimensionless shaft speed ($\overline{N}$), relating to the design point speed

$$\overline{N} = Comp.\overline{N}$$

5.1.4 Calculation Time

The resulting hybrid cycle models consist of approximately 14,000 algebraic and 2300 state variables. The simulations are performed on a 2.5 Ghz Intel Pentium-4 processor PC. To calculate a steady state operation point, a time of approximately 5-10 seconds is required.

The *SRADAU* solver used for dynamic calculations [gPROMS 2004] varies the time increments according to convergence behaviour of the model in the current state.

Thus, no fixed relationship between simulation time and simulated time can be established. A general rule is that high fluctuation rate of the variables (as after a step load change) slows down simulation speed, while for a system at almost steady-state, dynamic simulations are very fast. Furthermore, discontinuities caused by switches of *Selectors* or conditional equations generally provoke reinitialisation of the time increment to a low value and are thus substantially delaying the simulation progress. All performed simulation experiments could be obtained in times between 5 minutes and 12 hours.

5.1.5 Limitations of the Hybrid Cycle Models

Compared to most other hybrid cycle models available in open literature, the models used here are based on a very detailed approach. It features a combination of discretised models for the main components and mainly off-design models for the other components and dynamic effects where necessary. This results in a mathematical complexity which only few simulation environments can tackle. The most important limitations of the models are:

- SOFC bundle: Only one tube is modelled, i.e. heat transfer between the tubes in a tube bundle is neglected. In a real tube bundle, each tube is in a different thermal state depending on its position and therewith the view factors to casing, IIR and adjacent tubes. The innermost tubes will have a higher temperature than the outer ones. This has been neglected and therefore, the difference between local maximum and minimum temperatures will likely be underestimated by the model.
- Gas flow modelling: Plug flow was assumed, i.e. diffusion in the flow channels and uneven flow velocity and temperature profiles along its cross-section are neglected. Furthermore, a constant speed is assumed along the flow channels, which is necessary for the applied dynamic approach. The true velocity is depending on the specific gas volume and therewith on temperature and pressure. This leads to misestimating gas residence times and flow channel pressure losses.
- No calculation of thermal stress is included. An extended model for thermal stress calculation has been developed and is available [Nakajo 2005], but it has not been applied for the hybrid cycle calculations. This is because it implies an enhanced exactness of the spatial discretisation, resulting in a more complex mathematical problem. Furthermore, the results are based on geometric simplifications and include strong uncertainties about material properties.
- GT model. Compressor and turbine have been scaled to achieve good matching between the components and furthermore to supply the required air flow and pressure. There is uncertainty whether such components are available in practice and whether they can be designed to achieve the assumed design and off-design

conditions. This is not a limitation of the modelling approach itself, but rather a limitation on authenticity of the modelled system.

- Assumptions: Non-physical assumptions have been taken, such as the SOFC heat loss, the radiation view factors or the pressure losses in the burner and the reformers. There is uncertainty about the validity of these assumptions.
- Material properties: The correctness of the assumed material properties is uncertain. The values can vary significantly in different references. As no reference with a comprehensive, coherent set of material properties could be found, the values were taken from unlike sources.
- Ejector: Little literature on the steady-state and dynamic behaviour of the ejector was found. Even though the steady-state behaviour could be validated against another model from Marsano et al. [2004], uncertainty remains about the off-design performance and whether transient behaviour can be neglected.
- IIR: The IIR was modelled using an equilibrium approach, as there is great uncertainty about geometry and materials of the IIR used by Siemens-Westinghouse.

It can be concluded that obviously more verification and calibration work is required to ensure a 1:1 reproduction of a true system. The SOFC model has been calibrated against available data by Thorud [2005]. A calibration of the other important components would be desirable, but difficult to achieve as few data are available. It is, however, assumed that the model is able to predict qualitatively how a true system would respond to steady-state and dynamic operation cases. It is hence a useful tool to evaluate design options and operation strategies. Furthermore, it can be calibrated to real components and a real cycle once experimental results are available.

5.2 Basics for Operation of the Hybrid Cycle Models

5.2.1 Operation Parameters

The models describe the internal physical phenomena of the components and the hybrid cycle. In order to run simulations with the models, further parameters must be specified describing the case the system is operated at. The combination of the set of specifications depends on the operation mode. The parameters can be divided into 4 classes:

- **Design premises**: These are parameters that describe boundary conditions and fixed assumptions for the system. The latter include geometrical dimensions that have not yet been defined in with the component models and are of minor interest for the design process. Premises are not supposed to change under normal operation and must always be specified. Examples are ambient conditions or the number of SOFC tubes.

- **Design objectives**: These are operational parameters which represent quantitative objectives for the system at its design point. They must be specified in design calculations, whereas they are output variables in off-design calculations. Examples are process temperatures (such as turbine inlet temperature), relative pressure drops in the components where a constant pressure loss coefficient approach is used, or velocities in the ejector sections. It must be mentioned that many possibilities for a set of design objectives exist. For example, either the steam-to-carbon ratio or the anode gas recycle ratio can be specified during a design calculation.
- **Design parameters**: These are the counterpart to design objectives. Hence, they are output variables in design calculations and must be specified in off-design calculations. Consequently, the number of design parameters must equal the number of design objectives. Despite interactions among them, design objectives and parameters can mostly be coupled pair-wise. For example, a demanded steam-to-carbon ratio (design objective) can be best satisfied by adapting the pressure loss coefficient in the throttle (design parameter). Alternatively, it is also dependent on the ejector dimensions (interaction). Further examples for design parameters are pressure loss coefficients, geometrical dimensions or design values of air and fuel flow.
- **Operation point parameters**: These parameters define the actual operation point of the system. Hence, for each degree of freedom in system operation, one parameter must be specified. Examples are SOFC current or GT shaft speed. It must be mentioned that also here, many possibilities exist for defining the operation point (e.g. SOFC current *or* voltage). A set of operation point parameters must be specified for any operation, either directly or through an operation objective.

The chosen set of parameters for each of the classes will be described in Chapter 5.4.

5.2.2 Operation Modes

The hybrid cycle models are to be operated at three modes (see also Chapter 3.1.2):

- **Steady-state design**: Used for design and optimisation of the system. The system is designed to meet the design objectives and furthermore the performance can be optimised. In steady-state simulations, all time derivatives of the dynamic models must be replaced with zeroes.
- **Steady-state off-design**: Used for calculating off-design performance of the system at given design conditions, for example for part-load purposes.
- **Dynamic off-design**: Used for the dynamic response of the system to changes, e.g. load changes. The load changes are implied by changes of the operation point parameters. Therefore, additional operation objectives are required, either

through simple assumptions for the parameter change (such as ramp functions) or through a control system.

The mentioned operation modes are successive. For steady-state off-design calculations, a set of design parameters from the design calculations are required. For dynamic simulations, an operation objective is required which should be determined from the steady-state off-design behaviour.

5.3 Design and Operation Considerations

5.3.1 Requirements for a Hybrid Cycle Power Plant

The basic scale of the hybrid system investigated here is determined based on the Siemens-Westinghouse stack design which incorporates 1152 tubular cells and achieves a power output of 220 kW [Yi 2003]. It will be primarily operated with natural gas.

It shall be applied in distributed generation scenarios. These include grid- and off-grid applications as well as supply of residential and industrial consumers. For the power plant, the main difference between these applications lies in the type of load changes it is exposed to: A plant included into a large grid must be capable of a certain load change speed, but during normal operation, no step load changes will occur, as load steps by single consumers will be divided among all power plants. Furthermore, power plants with constant speed synchronous generators grant primary control of grid frequency and voltage through the inertia of the spinning shafts (see Chapter 2.3.6). Off-grid applications for residential supply must be able to perform load changes of about 5-10 kW, as this is the maximum load that may be switched in a private household (e.g. electric heater). In addition, they must have the ability to operate at low part-load, as the power demand of private consumers varies strongly throughout a day. The ability to operate in low part-load (app. 25%) is considered as necessary. The off-grid supply of industrial consumers poses the highest requirements to load change ability. Depending on the type of application, very high step load changes can occur. An example is the supply on offshore platforms, where large pumps or compressors are switched.

A further objective is that the system should be as simple as possible. For small-scale systems, a large amount of components is a strong driver for costs and size and furthermore complicates the controlling and increases malfunction rate.

5.3.2 System Safety Issues

In a hybrid system, several incidents can appear that cause degradation, reduced lifetime or even breakdown. The most critical incidents are discussed in this subchapter. Causes and consequences are commented, and associated model parameters are mentioned which are suitable for surveying them during the simulations.

Cell Cracking

Ceramic materials as used for SOFCs are brittle and thus prone to cracking when exposed to high stresses. Cracks in whatever layer and direction cause degradation of the electric cell performance by creating contact resistances and leakage current.

Mechanical stresses in the SOFC materials mainly derive from differences in the layers' coefficients of thermal expansion. The temperature at which the materials are adjoined during the production process is called *zero stress temperature*. It is typically higher than the cell operation temperature, i.e. at around 1400 K. This means that especially for low temperatures, the thermal stress and therewith likelihood of cracking increases. A further cause for thermal cracking and decomposition of the layers for tubular cells is the temperature gradient in radial direction [Nakajo 2005].

The exact relationships between thermal cracking likelihood and temperature state depend on exact design and material data where sparse information exists and are thus afflicted with high uncertainty [Nakajo 2005]. The maximum radial temperature gradient ($SOFC.dTdr_{MEA,Max}$) and the minimum local temperature of the MEA ($SOFC.T_{MEA,Min}$) will be monitored for supervision of the likelihood of cell cracking. However, due to the mentioned uncertainty, neither target values nor fix limits for these monitored parameters are given. They will be used as a qualitative means to evaluate certain operation points in terms of SOFC thermal cracking danger.

Compressor Surge

If the pressure ratio a compressor has to work against is too high for its current speed, it runs into surge (see also Chapter 2.2.1). Mostly too high turbine inlet temperatures are responsible for the occurrence of surge. It can cause violent oscillations in the gas path of the system the compressor is connected to and can therewith damage the system. In order to avoid compressor surge, a control strategy is required which grants suitable turbine inlet temperature at any operation condition. For monitoring, the surge margin *SM* was defined (see Chapter 5.1.3). It describes the distance from the compressor operation point to the regime where surge occurs. A value of equal or smaller to zero must be omitted under any operational instance.

Carbon Deposition

For certain gas compositions, temperatures and pressures, elementary carbon can be formed by the Boudouard and the methane cracking reactions. (see Chapter 4.3.1, Equations-Check Variables). The carbon deposits at the anode and causes covering of the catalyst and clogging of the pores required for gas diffusion. Cell performance will therewith degrade, even though the phenomenon is reversible in principle. Carbon formation can be avoided by supplying a suitable steam to carbon ratio.

The occurrence of carbon deposition in the SOFC can be monitored by the *CD* parameter (see Chapter 5.1.3). However, the phenomenon can also occur in the reformers where it is not surveyed. Therefore, the steam to carbon ratio γ_{SC} (see

Chapter 5.1.3) should be monitored additionally. The parameters will be used as a means to evaluate certain operation points in terms of SOFC degradation danger.

Anode Oxidation

If the activated anode is in a reactive state (i.e. at high temperature) and exposed to oxygen, the nickel catalyst will oxidise and thus be deactivated. Oxygen can reach the anode mainly due to backflow of gas from the burner into the anode channel and reversal of the electrochemical reaction. The former can occur when the system is exposed to quick pressure increase. The large volume and low flow rate in the anode channels cause that the pressure increases faster in the cathode channel than in the anode and hence oxygen-containing gas can flow from the burner back to the anode. The second phenomenon, reversal of the electrochemical reaction, occurs if the cell operation voltage is higher than the local reversible potential of the cell, which again can be a consequence of high operation voltage or low reactant/high product concentration. Electrolysis will occur where oxygen is produced at the anode.

In order to survey this incident, the parameters of fuel flow to the burner $Burner.\dot{n}_{In,Fu}$ and the minimum SOFC current $SOFC.j_{min}$ are monitored. The burner fuel flow rate may only be problematic during quick load increase.

Overheating

Overheating can attack in different components: In the SOFC, too high temperatures may cause irreversible changes in the electrode structure such as recombination of the nickel catalyst. For metallic components with high thermal load, i.e. recuperator and turbine, too high temperatures may lead to material failure which inevitably leads to system breakdown. Sufficient cooling air flow must be supplied to avoid overheating of the mentioned components. In order to survey this incident, the maximum MEA temperature $SOFC.T_{MEA,Max}$ as well as turbine inlet and outlet temperatures $Turb.T_{In}$, $Turb.T_{Out}$ must be monitored.

Thermal Fatigue

The mechanical stress in the SOFC is related to the temperature distribution. Hence, changes in temperature imply changes in the stresses, which lead to fatigue in materials. Fatigue fractures can occur which degrade the cell performance.

In order to minimise thermal fatigue, temperature changes must be minimised. This can be achieved with a control strategy which assures a fairly constant temperature in the SOFC under all operation conditions. The mean MEA temperature $T_{MEA,mean}$ is the major indicator for the SOFC temperature and will serve for the assessment of control strategies with respect to thermal fatigue.

Ejector Malfunction

If the pressure of the actuating fluid is lower than the pressure of the induced fluid in the mixing section entry of the ejector (see Chapter 4.6.4, Comments), the nozzle flow can knock over to sub-sonic flow. This would cause the ejector performance and therewith the steam-to-carbon ratio to drop strongly, and could furthermore expose the system to vibrations. The pressure difference can be calculated from the ejector design and the pressure of actuating and induced fluid. The resulting variable Δp_{Ej} is be used for surveying the ejector. The problem occurs mainly during load decrease at low fuel flow rates, as the actuating fluid pressure is low in this case.

5.4 System Design

The first step to investigate a hybrid cycle is the selection of a design case. In the design process, the dimensions and design values of all components are determined. In order to find a satisfying design point, design objectives are required. This chapter will at first introduce and define design premises for a 220 kW system based on the DIC process. Then, key design objectives for hybrid cycles and the design tasks for the components are discussed. Finally, the design case as defined through the chosen set of design parameters and objectives is presented together with the key system parameters.

Note that the design objectives for the other cycle options DIC-2T and IIC are very similar to the standard cycle (DIC). Their particularities will be discussed in Chapter 7.

5.4.1 Design Premises

In order to keep the design process concise, some of the input data are fixed during all kinds of operation and called design premises. Most of the premises are determined externally (such as ambient conditions), or inherently through the choice of fixed components (such as the Siemens-Westinghouse SOFC). Others are of secondary importance and expected not to vary strongly during design and therefore taken out of the design process (such as pipe diameters). A last group are operation conditions predetermined in order to match common values (such as fuel utilisation).

The premises in detail:

- Inlet air conditions: ISO conditions are assumed. Hence, air temperature $Air.T = 288$ K and pressure $Air.p = 1.013 \cdot 10^5$ Pa. The air is assumed to consist of 21% oxygen and 79% nitrogen.
- Fuel conditions: Fuel feed pressure $Fuel.p = 3 \cdot 10^6$ Pa, temperature $Fuel.T = 288$ K. The fuel is assumed to be pure methane.
- Exhaust pressure: $Exhaust.p = 1.03 \cdot 10^5$ Pa.
- Ambient temperature for stack casing: $Casing.T_\infty = 293$ K.

- Shaft Inertia: When aiming at 220 kW system power, the turbine will contribute with app. 70 kW. This is a typical microturbine power output. The rotating parts are thus assumed to have a mass $Shaft.m_{rot}$ = 10 kg and an average radius $Shaft.r_{rot}$ = 0.07 m.
- Piping dimensions: The pipe diameters have been estimated to achieve a flow velocity of $PipeX.u_{gas} \approx 20$ m s^{-1}. An exception is *PipeE*, modelling the gas delay in the pre-reformer *PR*; here, $PipeE.u_{gas} \approx 0.6$ m s^{-1} shall be achieved. The pipe radii are thus:

Instance	Radius r
PipeC	0.05 m
PipeH	0.08 m
PipeS	0.10 m
PipeT	0.15 m
PipeE	0.05 m

  All pipes have a length of $PipeX.l$ = 1 m.
- Number of SOFC tubes: $SOFC.n_T$ = 1152.
- Number of indirect internal reformers: $IIR.n_R$ = 16.
- Equilibrium temperature difference of the reformers:
  $PR.\Delta T_{eq}$ = 20 K; $IIR.\Delta T_{eq}$ = 20 K,
- Fuel utilisation: FU = 0.85 (fixed only for the steady state analyses)
- Ohmic resistance by degradation of the fuel cell: $SOFC.R_D$ = 0 Ω
- Compressor performance map representation (*CompMap.*): The compressor performance is derived from the performance map of a centrifugal compressor [Kurzke 2004]. The original map data are available for relative shaft speeds from 0.45 to 1.06. In order to be able to increase airflow sufficiently above the design value, the coefficients have been recalculated for a design speed of 0.95 on the original map. The compressor performance map is therefore valid for dimensionless speed between 0.47 and 1.12. The following values and equations were used for obtaining the normalised map:

  π_{Scale} = 3.59288

  $\dot{m}'_{Scale}$ = 0.97729

  $$\dot{m}'^{*} = \sum_{i=0,\,j=0}^{n} c_{ij} \left(\bar{N}'\right)^{i} \left(\beta\right)^{j}$$

c_{ij}	i=0	i=1	i=2	i=3	i=4	i=5
j=0	-0.30519	2.8408	-4.1098	2.0676	2.5571	-2.0523

j=1	-0.19331	1.5230	-4.3663	5.5993	-2.5319	
j=2	-1.9402	4.3347	-6.7041	4.2079		
j=3	1.6719	-0.52059	-1.3500			
j=4	-0.90747	-2.5197				
j=5	-0.01212					

$$\pi^* = \sum_{i=0,j=0}^{n} c_{ij} \left(\bar{N}'\right)^i (\beta)^j$$

c_{ij}	i=0	i=1	i=2	i=3	i=4	i=5
j=0	-1.9927	15.335	-23.420	3.8066	21.969	-12.981
j=1	0.70555	4.0334	-18.931	32.233	-15.86	
j=2	-6.8716	26.918	-45.627	25.551		
j=3	0.60501	3.8626	-6.2892			
j=4	-0.86869	2.1959				
j=5	-0.31402					

$$\eta = \sum_{i=0,j=0}^{n} c_{ij} \left(\bar{N}'\right)^i (\beta)^j$$

c_{ij}	i=0	i=1	i=2	i=3	i=4	i=5
j=0	0.17735	1.00605	-1.6972	2.4423	-1.2327	-0.09065
j=1	4.3718	-5.5747	-0.02450	3.2927	-1.5422	
j=2	-9.8266	16.0942	-8.5886	2.2426		
j=3	7.1352	-9.7270	1.9921			
j=4	-1.7701	2.2826				
j=5	-0.13016					

$$\pi_s^* = 0.95176 + 2.9385 \cdot \bar{m}'^* \text{ -1.9018} \cdot \left(\bar{m}'^*\right)^2 + 0.64316 \cdot \left(\bar{m}'^*\right)^3$$

- The design inlet data of the compressor (as these are only dependent on the ambient conditions):
- $Comp.T_{In,0}$ = 288 K
- $Comp.p_{In,0}$ = $1.013 \cdot 10^5$ Pa
- $Comp.M_{In,0}$ = 28.8504 kg kmol^{-1}
- $Comp.\kappa_0$ = 1.40088
- Turbine performance map representation (*TurbMap*): The turbine performance is derived from a turbine map of a radial NASA turbine [Kurzke 2005]. The original map data are available for relative shaft speeds from 0.7 to 1.5. For a

better fit to the shaft speed range of the compressor, the coefficients have been recalculated for a design speed of the 1.4 on the original map. The turbine performance map is therefore valid for dimensionless speed between 0.5 and 1.07. Furthermore, the efficiency has been downscaled by a factor of 0.95.

- $\pi_{Scale} = 4.3423$
- $\dot{m}'_{Scale} = 0.338999$
- $\dot{m}' = 0.339 \cdot \left(1 - \left(\frac{1-\beta}{1.018} \right)^{z} \right)^{1/z}$, where $z = 1.4451 + 1.9401\bar{N}' + 11.643\bar{N}'^{2}$
- $\pi^{*} = \sum_{i=0,j=0}^{n} c_{ij} \left(\bar{N}' \right)^{i} (\beta)^{j}$

c_{ij}	i=0	i=1	i=2
j=0	2.1746	-4.3715	4.9184
j=1	-7.2205	23.860	-13.938

- $\eta = \sum_{i=0,j=0}^{n} c_{ij} \left(\bar{N}' \right)^{i} (\beta)^{j}$

c_{ij}	i=0	i=1	i=2	i=3	i=4	i=5
j=0	0.01936	1.4133	0.2550	-2.4639	1.8896	-0.4345
j=1	6.1466	-8.5852	2.1441	4.5212	-3.1627	
j=2	-19.466	21.949	-11.255	4.2032		
j=3	26.023	-16.531	0.6757			
j=4	-17.062	6.5010				
j=5	4.0180					

- The design speed of compressor and turbine is assumed to be 70000 RPM, i.e. $Comp.N_0 = Turb.N_0 = 1667\ s^{-1}$

Note that for scaling the turbomachinery, design parameters are required. A representation of the absolute performance of compressor and turbine is given below in Figure 6-2 and Figure 6-3.

5.4.2 Key Design Objectives

For safe and efficient operation of a hybrid cycle plant, several system parameters must be kept in valid bounds. During the design process, special attention must be paid to these parameters. They are thus called *key design objectives*. The following section comments on practical importance, usual values and the influence of these parameters on the design process.

SOFC Current Density ($SOFC.j_t$)

The current density of the SOFC has a direct influence on the power density, but it also affects the efficiency and the cell lifetime. Current density values found in hybrid cycle literature range from 2500 [Chan 2002] to 4450 A m^{-2} [Costamagna 2000]. Sources related to Siemens-Westinghouse report 2900 [Yi 2003] and 3300 A m^{-2} [Veyo 2002]. A value of 3000 A m^{-2} has been assumed for the present study.

Turbine Inlet Temperature ($Turb.T_{In}$)

The turbine inlet temperature (TIT) is a key number for the efficiency of a gas turbine cycle. However, especially small turbines without blade cooling impose material strength limitations on the TIT. McDonald [2003] shows values of app. 1220 K for state of the art microturbines. Values found in hybrid cycle literature range from 1003 K [Yi 2003] to 1309 K [Chan 2002]. For the present study, 1173 K is assumed.

Turbine Outlet Temperature ($Turb.T_{Out}$)

For a given TIT, the turbine outlet temperature (TOT) determines the enthalpy difference which can be converted to power in the GT. It is closely coupled to the GT pressure ratio. For the hybrid cycles, the desired SOFC system air inlet temperature imposes a boundary on the TOT. For the directly integrated cycle (DIC), the temperature stability of the heat exchanger is a further criterion. Metallic heat exchangers, which are much cheaper than ceramic ones, have a maximum temperature stability of app. 900 K [Sarawanamuttoo 2001, Romier 2004]. McDonald [2003] assumed the feasibility of steel heat exchangers for a temperature of 1023 K. A turbine outlet temperature of 923 K is assumed for the DIC.

Mean MEA Temperature ($SOFC.T_{MEA,mean}$)

The mean MEA temperature determines the current-voltage characteristics of the fuel cell and therewith the efficiency. A common value for SOFC operating temperature is 1273 K [Yi 2003, Chan 2002, Campanari 2004]. This value has also been chosen for this study.

Steam to Carbon ratio (γ_{SC})

The steam to carbon ratio at the ejector outlet is important to allow for the desired reforming reactions and to omit carbon deposition. A commonly used value is 2.0 [Chan 2002, Campanari 2004], which has also been chosen for this study.

Reforming Degree (γ_R)

The reforming degree of the fuel at the cell entrance strongly influences the cell temperature profile. Reported numbers for the latter range usually around 30 [Selimovic 2002a]. However, higher reforming degrees flatten the profile of temperature and current density in the cell [Pålsson 2002, Thorud 2005]. Furthermore,

Song et al. [2004] report that the IIR exhaust gas includes only a small amount of unreformed methane. A reforming degree of 80% is chosen for the design point.

5.4.3 Component Design

The following section will discuss the remaining design tasks.

Fuel Flow, Air Flow, Power

Design fuel flow $\dot{n}_{Fuel,0}$ and air flow $\dot{n}_{Air,0}$ are important design parameters for the hybrid system.

With given fuel utilisation, the fuel flow is directly coupled to the SOFC current. The current density $SOFC.j_t$ is hence chosen as a design objective for the fuel flow. The fuel flow is the main handle to adjust the electric power output. Electric power output could also directly serve as design objective; however, the SOFC current density is a more pragmatic value.

The air flow is the main source of cooling and thus closely coupled to the key temperatures in the system. The mean SOFC temperature $SOFC.T_{MEA,mean}$ has been selected as design objective for the air flow. The desired value is 1273 K.

The design net electric power $P_{net,0}$ is designed by setting the corresponding dimensionless net power $\overline{P}_{net}$ to unity.

Heat Exchanger

The design parameters of the heat exchanger are its length $HX.l$ and frontal area $HX.A$. The latter is strongly coupled to the maximum flow velocity of the hot gas $HX.u_{H,max}$, which should not be too high in order to obtain an acceptable pressure loss. A design value of 20 m s^{-1} is chosen. The remaining design objective to determine the length is the mean logarithmic temperature difference $HX.\Delta T_{LM}$. In order to keep the heat exchanger size reasonable, a value of 50 K is chosen. As a comparison, Campanari et al. [2004] chose 45 K as the minimum approach temperature of the heat exchanger. The heat exchanger could be further optimised for minimum pressure loss or minimum volume, which is not done here.

Throttle

The throttle is mounted into the anode gas recycle stream in order to adjust the pressure loss and therewith adjust the steam to carbon ratio. Its loss coefficient $Thro.c$ (technically the opening of an orifice) is adjusted during the design process and remains constant during operation. The connected design objective is the steam to carbon ratio γ_{SC}.

Casing

The radiation coefficient from the SOFC to the casing $SOFC.\tau_{Cas}$ is to be designed in order to meet an assumed heat loss to the surroundings $Casing.\dot{q}_t$ at design case. No information on heat loss of the Siemens-Westinghouse SOFC was found. 10 kW is assumed to be a realistic value.

IIR

The radiation coefficient from the SOFC to the indirect internal reformer $SOFC.\tau_{Ref}$ is to be designed in order to meet a desired reforming degree γ_R.

Pressure Losses

In the devices where pressure loss is modelled through a constant loss coefficient (i.e. IIR, PR, Burn), the coefficients c have to be designed in order to meet a certain relative pressure drop Δp_{rel}. A relative pressure drop for all components of 1% at design point is chosen.

Preheat Tube

The preheat tube mainly decides about the temperature drop between burner and turbine. The shape is given through the assumptions about the Siemens-Westinghouse design; only the length l_T may be designed. A suitable design objective is the turbine inlet temperature $Turb.T_{In}$. Attention should be paid that the length of the tube does not take unreasonable values; a range of 0.3-0.6 m is rated as reasonable in terms of SOFC system design.

Ejector

For the ejector model, four cross-section areas must be designed: The critical cross-section $Ejec.A_c$, the nozzle exit $Ejec.A_{n,}$ the mixing chamber $Ejec.A_m$ and the outlet $Ejec.A_o$. At a given flow rate of the induced fluid, $Ejec.A_c$ can be determined by specifying a design inlet pressure $Ejec.p_{Ai}$. Even though the fuel feed is at 30 bar, a value of 24 bar has been used as design pressure in order to allow for higher fuel flows at transient or peaking operation.

$Ejec.A_n$ is a function of the static pressure at the nozzle exit $Ejec.p_{An}$. This pressure must be low enough to ensure supersonic flow in the nozzle and high enough not to undershoot the static pressure of the induced fluid at any operation condition (see Chapter 4.6.4). A value of 11 bar has been chosen. $Ejec.A_m$ and $Ejec.A_o$ can be calculated by selecting velocities $Ejec.u_{Im}$ and $Ejec.u_{Mo}$ respectively. In order to achieve good mixing at low friction, an intermediate velocity of 100 m s^{-1} is selected for the mixing section. The assumed exhaust velocity of 10 m s^{-1}.

Compressor

The compressor characteristics are described by the map representation. The design parameters of the inlet gas have been declared according to the constant inlet gas conditions in Chapter 5.4.1. The design flow rate is defined with the design system air flow rate $\dot{n}_{Air,0}$. Hence, only the design pressure ratio $Comp.\pi_{0,Map}$ remains as design parameter. The corresponding design objective is the dimensionless pressure ratio $Comp.\overline{\pi}$ which by definition must be unity at the design point.

Turbine

Unlike the compressor, the turbine inlet gas conditions depend on the system design. Thus, design parameters of temperature $Turb.T_{in,0}$, pressure $Turb.p_{In,0}$, molar mass $Turb.M_{In,0}$ and isentropic coefficient $Turb.\kappa_{In,0}$ and furthermore the mass flow rate $Turb.\dot{m}_0$ must be determined. As corresponding design objectives, the dimensionless values of the mentioned parameters are set to unity during the design process.

An important design parameter of the turbine is the design pressure ratio $Turb.\pi_{0,Map}$, which decides the pressure level of the GT system and therewith strongly influences the key temperatures. As the temperature drop over the turbine is directly depending on the pressure ratio, the turbine outlet temperature $Turb.T_{Out}$ has been chosen as a corresponding design objective.

5.4.4 Operation Point Parameters

The operation point parameters determine the operation point of the system as compared to the design point. For each degree of freedom in operation, one parameter must be specified. For performing design calculations, it must be assured that the operation point equals the design point. Hence, it is practical to set the dimensionless parameters to unity. In the actual case, the dimensionless fuel flow $\overline{\dot{n}}_{Fuel}$ and the dimensionless air flow $\overline{\dot{n}}_{Air}$ must be set to unity. As the used compressor provides two degrees of freedom for controlling the air flow (shaft speed $\overline{N}$ and variable inlet guide vane position $Comp.S_{VIGV}$), in addition one of these parameters must be set to unity. The other parameter will be calculated and at a proper design calculation the result must be unity.

6 The Directly Integrated SOFC Cycle (DIC)

This chapter is dedicated to part-load performance and control of the directly integrated SOFC cycle, which is regarded as the standard hybrid cycle (see Chapter 5.1.1). Shutdown and startup as well as fuel flexibility of the system is furthermore investigated.

6.1 The Design Case

Table 6-1: Design objectives and parameters

Design Objective	Value	Design Parameter	Value
$\overline{P}_{net}$	1	$P_{net,0}$	221032 W
$SOFC.j_t$	3000 A m^{-2}	$\dot{n}_{Fuel,0}$	0.4394 mol s^{-1}
$Turb.T_{In}$	1173 K	$PHT.l_T$	0.4776 m
$Turb.T_{Out}$	923 K	$Turb.\pi_{0,Map}$	3.543
$SOFC.T_{MEA,mean}$	1273 K	$\dot{n}_{Air,0}$	13.60 mol s^{-1}
$HX.\Delta T_{LM}$	50 K	$HX.l$	1.8491
$HX.u_{H,max}$	20 m s^{-1}	$HX.A$	0.1139
γ_{SC}	2.0	$Thro.c$	149669
$Casing.\dot{q}_t$	10000 W	$SOFC.\tau_{Cas}$	0.0001254
γ_R	0.8	$SOFC.\ \tau_{Ref}$	0.0005780
$IIR.\Delta p_{rel}$	0.01	$IIR.c$	486812
$PR.\Delta p_{rel}$	0.01	$PR.c$	535362
$Burn.\Delta p_{rel,Air}$	0.01	$Burn.c_{Air}$	28881
$Burn.\Delta p_{rel,Fu}$	0.01	$Burn.c_{Fu}$	$3.342 \cdot 10^6$
$Ejec.p_{Ai}$	24 bar	$Ejec.A_c$	$1.727 \cdot 10^{-6}$ m^2
$Ejec.p_{An}$	11 bar	$Ejec.A_n$	$1.738 \cdot 10^{-6}$ m^2
$Ejec.u_{Im}$	100 m s^{-1}	$Ejec.A_m$	0.0005089 m^2
$Ejec.u_{Mo}$	10 m s^{-1}	$Ejec.A_o$	0.006460 m^2
$Comp.\overline{\pi}$	1	$Comp.\pi_{0,Map}$	3.803
$Turb.\overline{\dot{m}}$	1	$Turb.\dot{m}_0$	0.399 kg s^{-1}

$Turb.\overline{T}_{In}$	1	$Turb.T_{In,0}$	1173 K
$Turb.\overline{p}_{In}$	1	$Turb.p_{In,0}$	3.775 bar
$Turb.\overline{M}_{In}$	1	$Turb.M_{In,0}$	28.45 g mol^{-1}
$Turb.\overline{\kappa}_{In}$	1	$Turb.\kappa_{In,0}$	1.308

The design objectives and parameters and their values as discussed in Chapter 5.4 are displayed in Table 6-1.

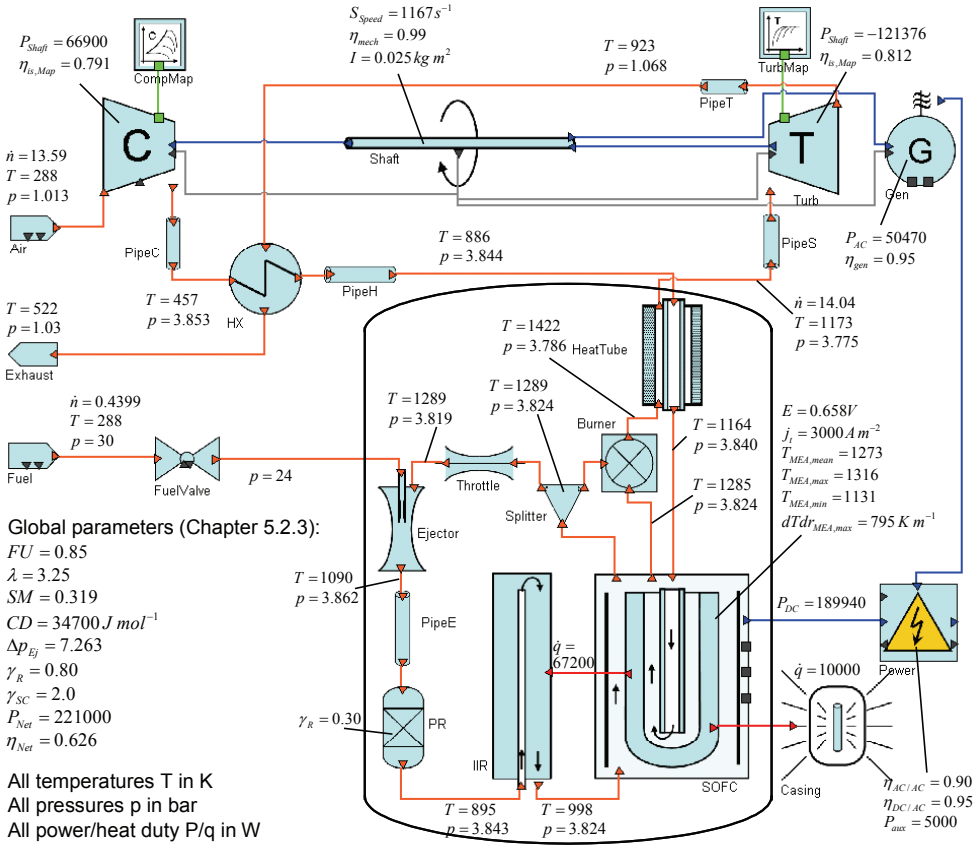

Figure 6-1: Main operation parameters at design point

Figure 6-1 depicts all important cycle and process parameters at the design point of the system. Considering all losses, the system has a net LHV-based electric efficiency of 62.6% at design point. Most published values in literature [Chan 2003; Magistri 2004; Costamagna 2001; Campanari 2000] range between 57% [Veyo 2002] and 66.5% [Kimijima 2002]. The efficiency might be raised by few percentage points through an optimisation process. This was, however, not performed, because for a relevant optimisation, economic data about the component costs must also be considered.

The pressure ratio of app. 3.8 is common and many other authors [Kimijima 2002; Magistri 2004; Companari 2000, 2004; Costamagna 2001] have proposed similar values.

With the design parameters fixed, the scaled absolute performance of the designed compressor and turbine can be displayed; see Figure 6-2 and Figure 6-3.

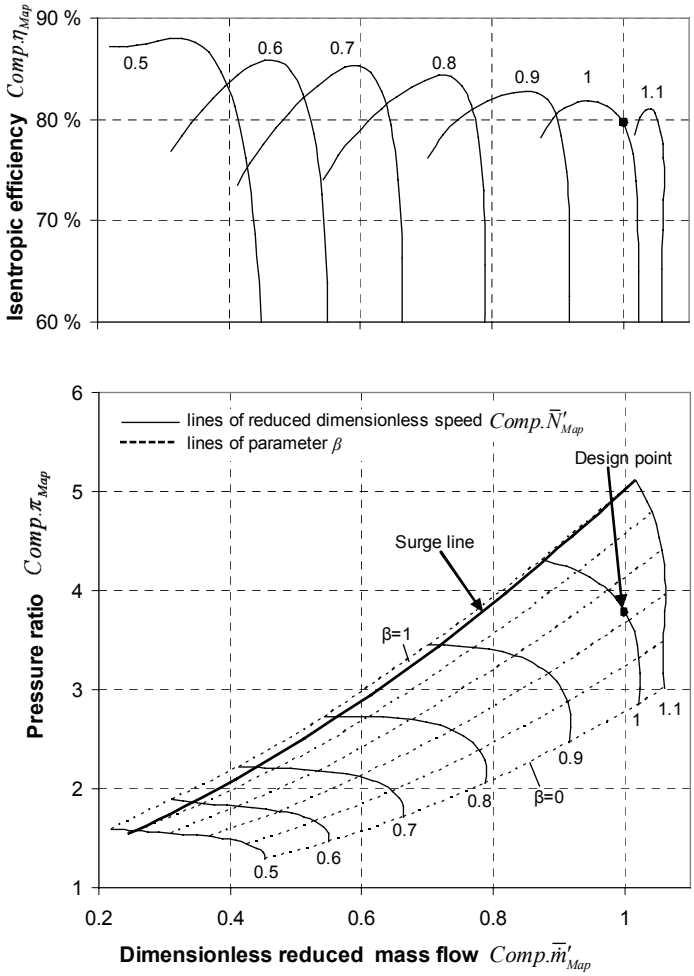

Figure 6-2: Performance of the designed compressor

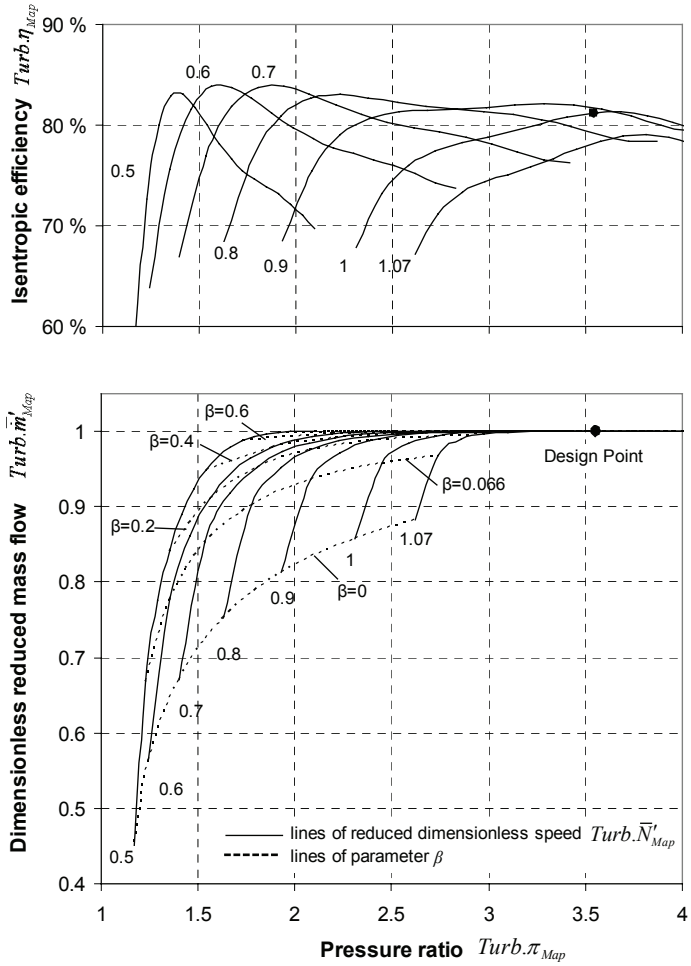

Figure 6-3: Performance of the designed turbine

6.2 Steady-State Part-Load Operation

After defining the system design, the next step is to investigate the off-design behaviour, i.e. when the system is in part-load. In this subchapter, strategies for part-load operation are discussed and a suitable strategy is chosen. Operation boundaries with respect to safety are given, and part-load performance within the valid boundaries is visualised. A suitable steady-state operation line is chosen.

6.2.1 Strategies for Part-Load Operation

In off-design simulations, the *design parameters* highlighted in Table 6-1 must be specified, while the *design objectives* are calculation results. The system deviates from its design point when any of the system parameters given from "outside" differs from its

design value. Such parameters may be premises for the system (Chapter 5.4.1) as the ambient conditions or the composition of the fuel, or *operation point parameters* (Chapter 5.4.4) which are modified on purpose when the system runs at part-load. Thinking of the defined operation point parameters, there are three degrees of freedom for part-load operation with the current cycle:

- Variation of air flow $\overline{\dot{n}}_{Air}$ through shaft speed $\overline{N}$
- Variation of air flow $\overline{\dot{n}}_{Air}$ through compressor variable inlet guide vanes $Comp.S_{VIGV}$
- Variation of fuel flow $\overline{\dot{n}}_{Fuel}$

A theoretical further degree of freedom is the fuel utilisation (FU) respectively current or voltage of the SOFC. Fuel utilisation and current are coupled via the fuel flow rate, while current and voltage are coupled via the fuel cell characteristics. However, large variations in FU are not recommendable, as low FU leads to low steam content in the anode recycle and high TIT, while high FU leads to steep internal temperature gradients in the fuel cell. Therefore, it is chosen to operate at constant FU of 85% in steady-state (see Chapter 5.4.1).

The two methods of air flow variation provoke different operation lines on the GT performance maps:

- For shaft speed variation, the operation point on the compressor map (Figure 6-2) will move to the lower left. The turbine inlet temperature determines the exact operation point on the new speed line (note that the inlet temperature has an influence on the reduced speed; hence reduced speeds in compressor and turbine are not necessarily equal). With a suitable TIT, a strong air flow reduction can be achieved at acceptable efficiency.
- Closed variable guide vanes will scale the compressor mass flow, i.e. shrink the map in horizontal direction. As the turbine map is not modified, it will "grow" compared to the compressor. This causes the pressure and isentropic efficiencies to decrease as both compressor and turbine operation points will move towards β=0 on the design speed line. Furthermore, the mass flow reduction through the compressor scaling is partially compensated by the shape of the speed line. Simulations have shown that this effect is especially strong at slow speeds due to the flat shape of the lines. A combined variation of shaft speed and VIGV is hence not effective.

As a conclusion, compressor variable inlet guide vanes are not suitable for air flow variation within wide bounds. It is hence chosen only to vary the shaft speed, while the VIGV are always fully open. This helps simplifying the system in practise.

The remaining free parameters, air flow (through shaft speed) and fuel flow, may be varied independently from each other within certain limits. Each combination determines a certain operation point of the system. Thus, two-dimensional matrices of

the interesting system parameter steady-state values over the two free parameters can be produced and displayed in performance maps.

6.2.2 Limitations for Steady-State Operation

Theoretically, the system can be exposed to any combination of air flow and fuel flow. However, at some regimes, the system may be damaged due to the safety issues discussed in Chapter 5.3.2. A matrix of steady state simulations with the designed system has detected the following safety issues to occur at certain regimes:

- Overheating appears for high fuel flow and low air flow. At this regime, steady-state simulations could not be solved. Dynamic simulations revealed that the temperature is steadily climbing far beyond the valid range and additionally causing compressor surge. This is because enhanced effectiveness of the heat recuperation loop and lower air excess ratio at lower air flow causes the TIT to increase.
- For the opposite case of high air flow and low fuel flow, the fuel cell is cooled down strongly and therefore the voltage is low. It is not recommendable to operate in this regime due to low efficiency and furthermore the risk of thermal cracking due to low temperatures.
- The compressor and turbine maps are only valid within their given bounds. At maximum and minimum air flow, these bounds are approached. The regimes where they are exceeded are blinded out in order to ensure validity of the turbomachinery behaviour.
- At low fuel flow, the ejector pressure difference Δp_{Ej} becomes negative. Hence the nozzle flow may change to subsonic, resulting in ejector malfunction.

The regimes where these issues occur are mapped in Figure 6-4. The white area enframed by the non-valid regimes demarks the window where safe steady-state operation is possible.

Anode oxidation, carbon deposition and compressor surge do not imply any restrictions to the valid operation regime for the investigated system.

Now, the non-quantified parameters monitoring the safety issues thermal cracking and overheating can be plotted inside the operation window in order to further restrict the area where part-load operation is recommendable.

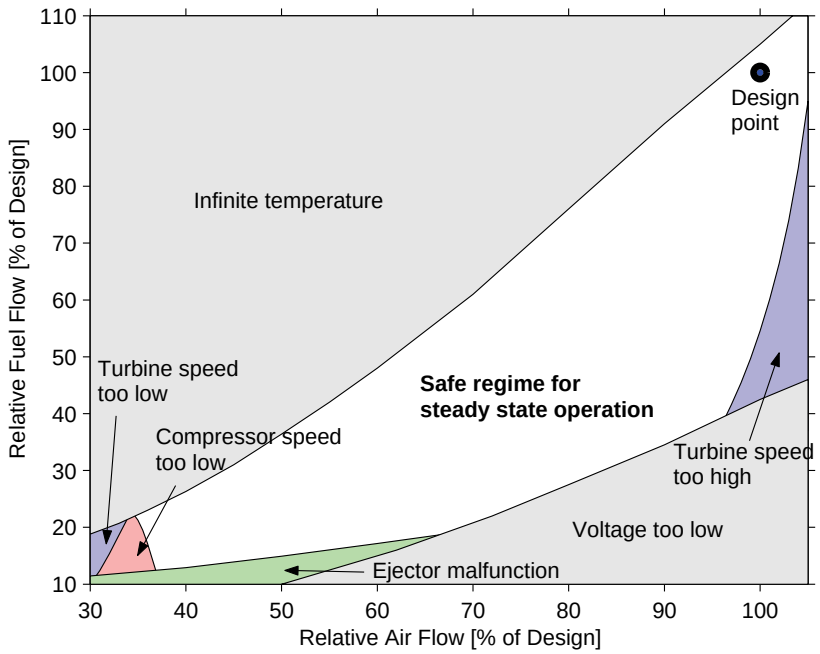

Figure 6-4: Regimes where safety issues occur

Figure 6-5 depicts the temperatures to monitor danger of component overheating. Except the upper right corner, all temperatures are below the design point values. The system is hence safe from overheating in steady-state for air and fuel flow values within the operation windows. Note that overheating can still occur during transients.

Parameters to monitor thermal cracking and fatigue are shown in Figure 6-6. It can be seen that towards the lower fuel flow area, the minimum MEA temperature (denoted as "min SOFC T") decreases, which in principle increases thermal stresses. The maximum local radial temperature gradient has a hump at intermediate temperature; hence it is advantageous to operate the system either in higher or lower temperatures. However, also here, the design value represents the highest value. Thermal fatigue is a purely transient phenomenon; however, it can be assumed that maintaining a fairly constant steady-state MEA (SOFC) temperature in the entire load range will reduce thermal cycling during transient operation and therewith mitigate thermal fatigue.

The steam-to-carbon ratio can be seen in Figure 6-7. During any part-load, it will be higher than the design value. This indicates that also carbon deposition in the reformers is not critical during steady-state part-load for the calculated ejector behaviour.

Concerning all issues about system safety and fuel cell conservation, it seems most recommendable to always operate at fairly constant SOFC temperature, i.e. close to the upper margin of the operation window.

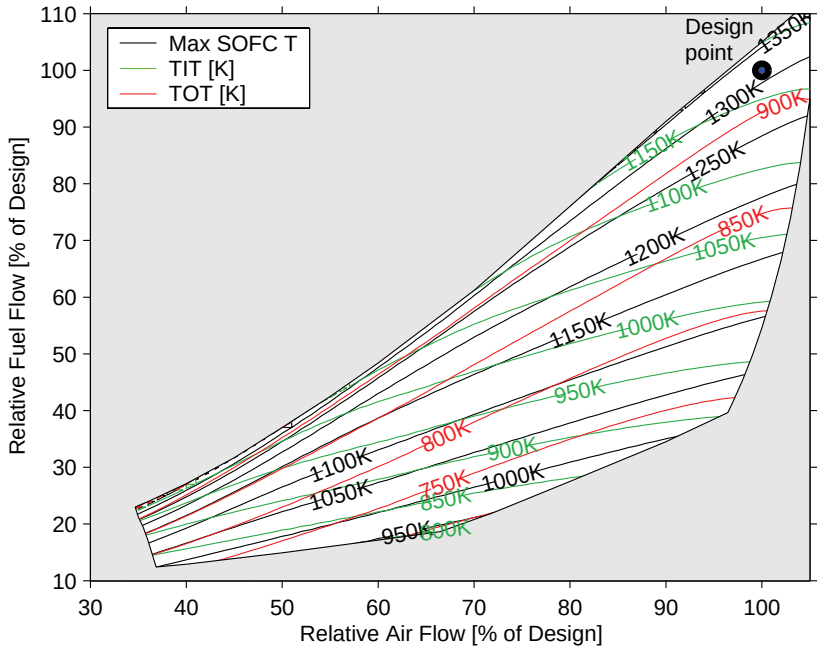

Figure 6-5: Parameters concerning component overheating

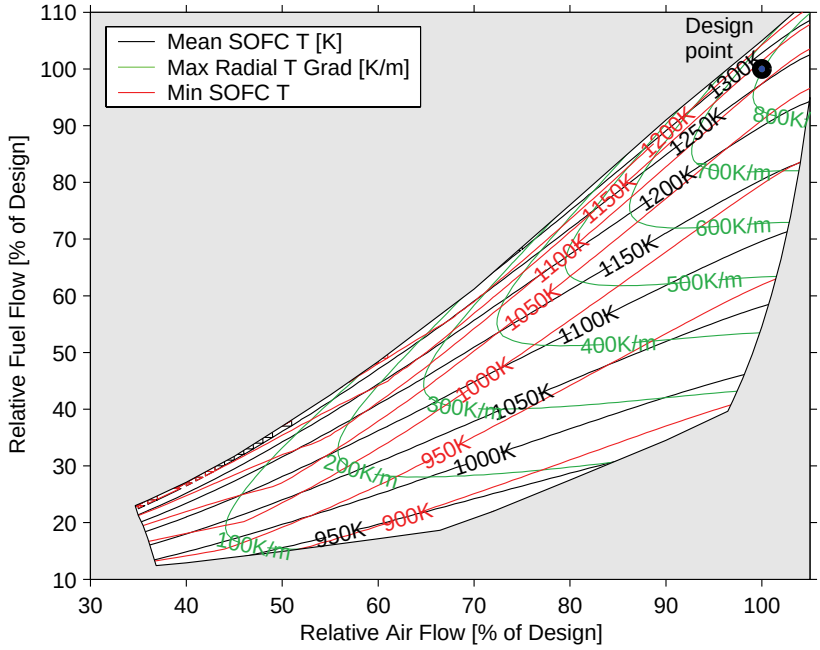

Figure 6-6: Parameters concerning thermal cracking and fatigue

6.2.3 Steady-State Part-Load Performance

Beside safety issues, the performance of the system is a further important criterion for choosing a part-load strategy, mostly in terms of high efficiency and ability for operation at low part-load.

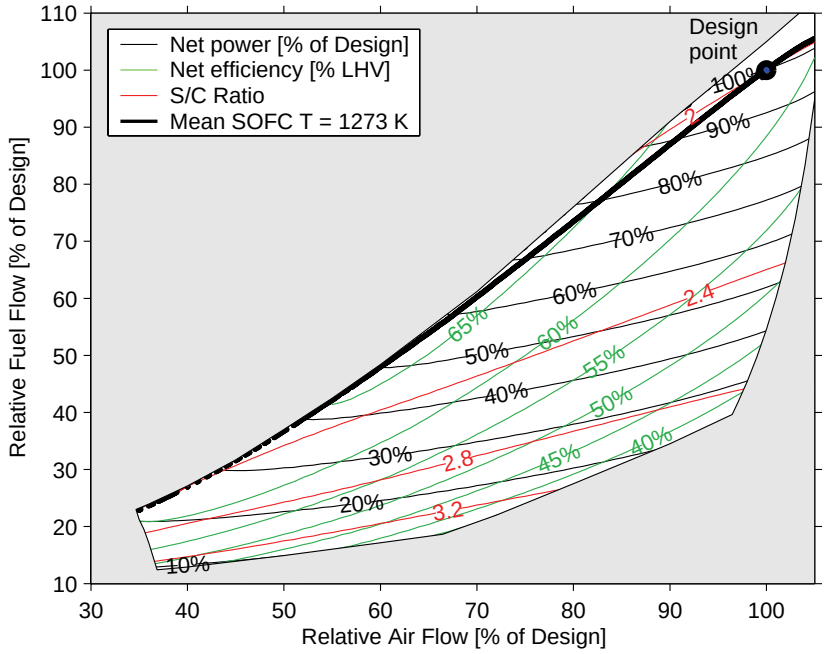

Figure 6-7: System performance parameters

Figure 6-7 depicts the behaviour of net power, efficiency and the steam-to-carbon ratio (see above). Along the bulk black line, the mean SOFC temperature is at its design value of 1273 K. Not surprisingly, the highest part-load efficiency can be achieved at high temperatures. At the same time, the power can be reduced down to app. 21% of its design value, which is also satisfactory.

In order to achieve zero power output without system shutdown ("hot standby"), a further reduction of the air flow must be facilitated by the turbomachinery or other means such as a bypass. A problems for hot standby could for example be caused by the ejector operation boundary (see Figure 6-4).

Parameters related to the gas turbine system are shown in Figure 6-8. Pressure and shaft speed are closely related to the airflow and hence the lines are steep. The relative gas turbine power contribution (p_{GT}) decreases with the airflow. This is a consequence of reduced turbine inlet temperature. The influence on total efficiency is, however, low due to the higher SOFC voltage. Furthermore it can be seen that operation along the constant temperature line yields a significant change in pressure and shaft speed.

As steep pressure gradients may represent a risk during transient operation, this issue must be addressed by a suitable control strategy.

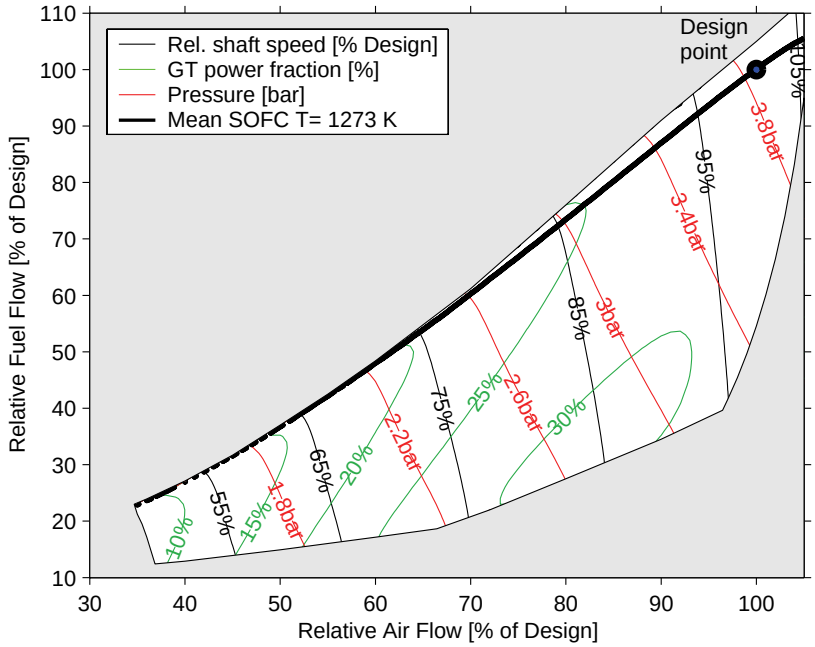

Figure 6-8: Gas turbine related parameters

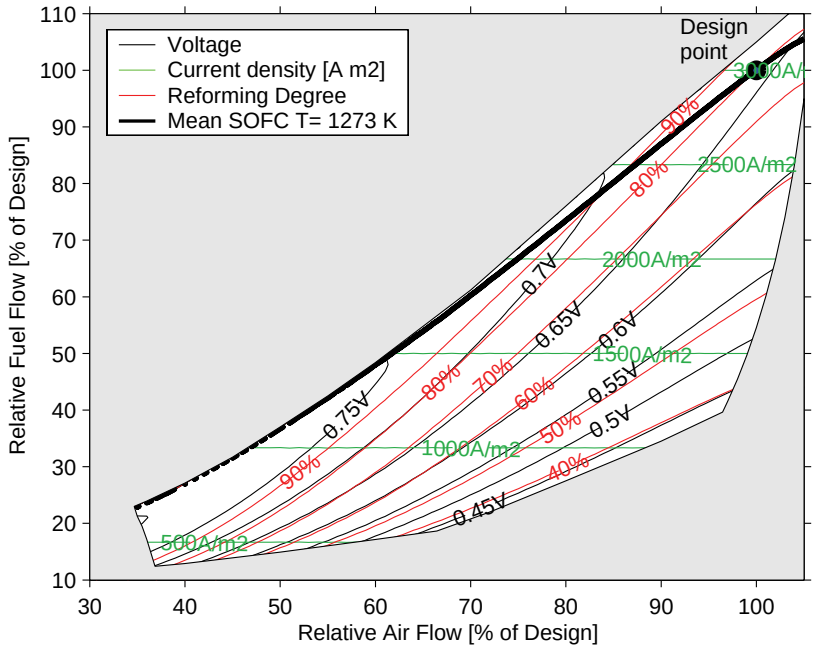

Figure 6-9: SOFC system related parameters

Figure 6-9 depicts relevant parameters for the SOFC system. The current density is only a function of the fuel flow, as the two parameters are coupled by the fuel utilisation. Voltage increases when going to part-load at high temperature, indicating a high conversion efficiency of the fuel cell. Also the methane reforming degree increases for high-temperature part-load, because the heat duty and therewith the temperature drop between SOFC and reformer are lower.

Concluding, a part-load strategy which maintains the mean SOFC temperature constant in the entire load range is optimal in terms of system safety, efficiency and part-load ability. Thorud [2005] has already investigated this strategy and drawn a similar conclusion regarding dynamic operation.

It must be mentioned that the shown behaviour is a product of the characteristics of all applied components and assumptions of the cycle. The displayed quantitative data are model results and may differ for a real system. However, the trends are expected to be similar for a real system and furthermore the demonstrated methods can be applied, once an accurate model of the real system's behaviour is available.

6.2.4 Steady-State Operation Line

Operation at constant mean MEA temperature shall be pursued as a part-load strategy. The behaviour of the parameters for the chosen operation line can be estimated from the maps shown in Chapter 6.2.2 and 6.2.3. For convenience, the most important parameters are plotted against the dimensionless net power in Figure 6-10.

The net electric efficiency of the system in steady-state ranges from 59.6% at minimum load to a maximum of 65.8% at intermediate load (59%) and back to 62.6% at full load.

It can be seen that at minimum power output, the maximum MEA temperature and turbine outlet temperatures are considerably above the design point values (41 K resp. 33 K). This could be relieved by correcting the operation line towards a lower fuel flow in low part-load, which is, however, not regarded as necessary here.

Note that the minimum MEA temperature has a sharp bend at 68% power. This is because the locus of the minimum jumps between top and bottom end of the tube at this point. Figure 6-11 shows SOFC axial temperature profiles at different loads which confirm this.

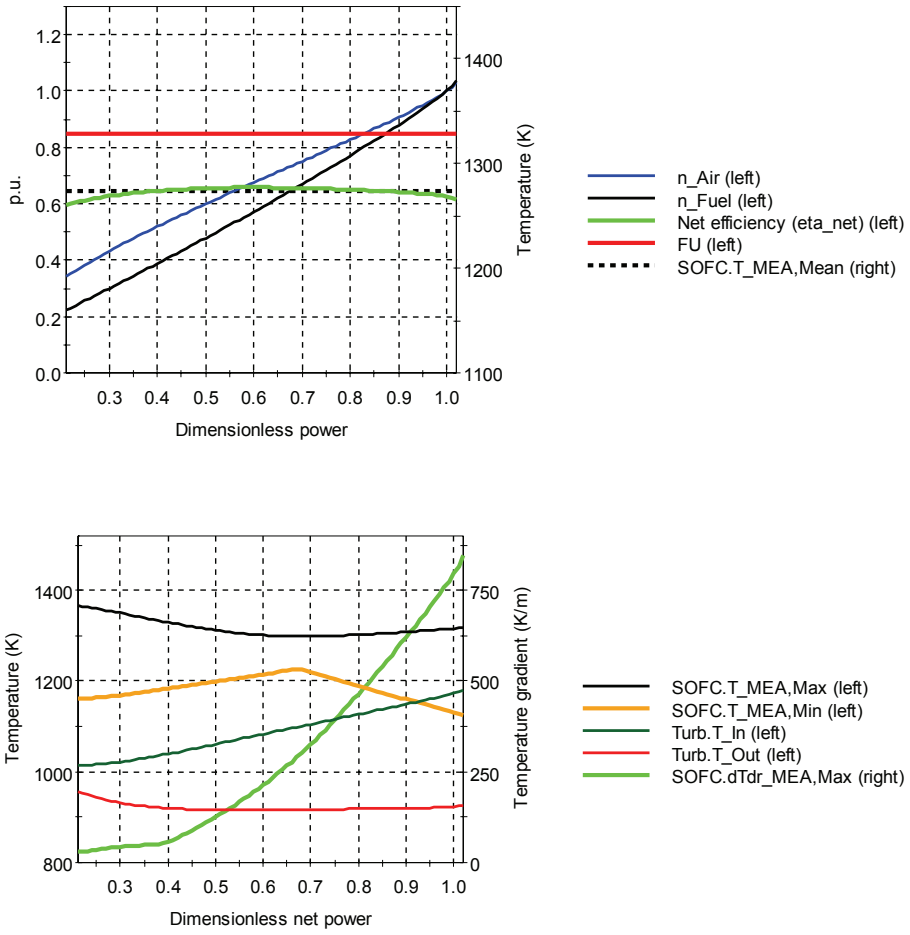

Figure 6-10: System and thermal parameters over dimensionless power

6.2.5 Conclusions

Assuming constant fuel utilisation, the main degrees of freedom for operating the system are fuel and air flow. A "window" where steady-state operation is safe can be plotted and is confined by overheating, compressor and turbine map bounds, ejector malfunction and low voltage. Within the operation window, a part-load strategy where the mean MEA temperature is constant at 1273 K throughout the whole load range seems most promising in terms of safety, lifetime and performance. The ability for low part-load mainly depends on the ability of the GT system to reduce the air flow. With the current system, a minimum part-load of 21% can be achieved at app. 35% of the design air flow. The LHV-based net electric efficiency is between 59.6 and 65.8% throughout the whole load range.

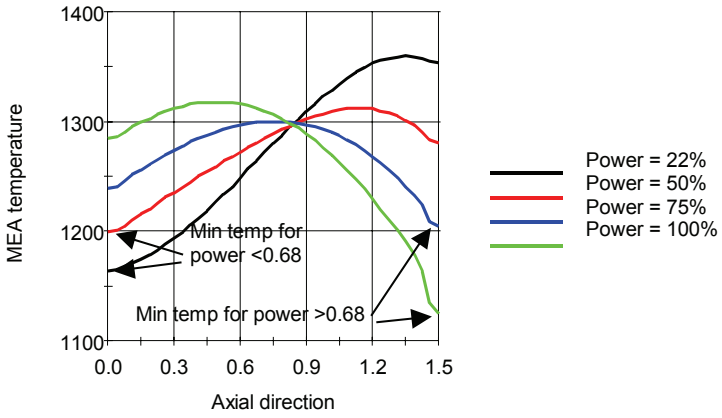

Figure 6-11: Temperature profiles along the SOFC tube (left: top/gas exhaust, right: bottom/gas entry)

6.3 Transient Operation - The Controlled Hybrid System

Having determined an operation line for steady-state, the next task is to control the system during transients in a way that it returns to the operation line after load changes. The control strategy hence determines the way the system proceeds from one operation point to another. In the following subchapter, requirements for a suitable control strategy are defined. Based on system analyses, a control layout is proposed and the response to various transient processes is investigated.

6.3.1 Requirements for a Control Strategy

A suitable control strategy for normal operation must meet the following requirements:

- **Safe and gentle operation of the system**: Incidents which may cause damage or degradation to the fuel cell or other components (see Chapter 5.3.2) must be avoided or mitigated.
- **Quick load following**: A control strategy should facilitate to follow a load profile quickly and accurately. The load profiles a power plant is exposed to depend on the type of application; see Chapter 5.3.1.
- **High efficiency**: High efficiency of the system must be ensured by the control strategy through keeping the operation conditions in favourable regimes.
- **Governing external influences and malfunction**: The system must react on external disturbances such as ambient conditions or malfunction of components. Furthermore, it should to a certain extent be able to compensate changes in

component performance, caused for example by fuel cell degradation or compressor fouling.

6.3.2 System Analysis and Control Layout Development

Output and Input Variables

Outputs are system variables which shall be varied in a certain desired manner. The system has only one output variable relevant for the user, which is the net power, $\overline{P}_{Net}$ (dimensionless number is used for convenience). However, the part-load operation strategy discussed previously shall be implemented, and thus also fuel utilisation FU and mean SOFC temperature SOFC.$T_{MEA,mean}$ are regarded as system outputs in need of control.

The input variables to the system which can be manipulated to control the outputs are the SOFC power output signal $SOFC.S_{Power}$, fuel flow $\overline{\dot{n}}_{Fuel}$ and the generator power signal $Gen.S_{Power}$. Note that other variable sets are also valid, such as the SOFC current instead of the SOFC power, or the generator torque instead of the generator power. However, it is assumed that the power electronics can instantaneously reach a power setpoint for the components and hence power is treated as input.

RGA Analysis and Control Loop Pairing

The system is a so-called multiple input multiple output (MIMO) system. In order to determine which output should be controlled with which input, a relative gain array (RGA) analysis can be performed [Skogestad 2005]. This method is based on the steady-state partial derivative of a system output y_i to an input u_j, namely

$$\frac{\partial y_i}{\partial u_j}$$

The quotient of these derivatives for the cases

1. that all inputs u other than u_j are set constant (the control loops are open)
2. that the input u_j and all outputs y other than y_i are set constant (perfect control with closed loops),

is

$$\left(\frac{\partial y_i}{\partial u_j}\right)_{u_k=const;k\neq j} \Bigg/ \left(\frac{\partial y_i}{\partial u_j}\right)_{y_k=const;k\neq i}.$$

It is called the *relative gain* and is calculated for every i and j in an array. A general rule is that the inputs and outputs which have a relative gain close to unity should be paired in control loops.

To perform an RGA analysis, a system which is stable under all pairings of input and output specifications is required. However, with a specified generator power the system is unstable, as for example a power value lower than the GT power balance would infinitely accelerate the shaft. However, the generator power is strictly coupled to the air flow. Hence it can be substituted with the air flow $\overline{\dot{n}}_{Air}$ as an input variable for the RGA analysis.

Another issue is that for an RGA analysis, strictly a linearised model is required, which is difficult to build from the current model due to its complexity. However, the checksums for each variable are sufficiently close to unity to assume that the RGA analysis of the non-linear model is valid in this case.

RGA results for different load cases are sketched in Table 6-2 to Table 6-4. The soliciting pairings between input and output variables are marked bold. First of all, it can be seen that in all cases, the air flow is the adequate parameter to control the SOFC temperature. For the remaining four variables, the optimum pairing depends on the load case. The choice becomes simpler when looking at the requirements for the control system and transient behaviour of the system: Quick and accurate control is more important for power output than for fuel utilisation. Hence the power output should be controlled by the input it responds faster to. This is doubtlessly the SOFC power, as it is directly connected to the total power. The system response to fuel flow will in contrast be delayed because of the fuel valve dynamics and gas residence times.

Table 6-2: RGA analysis at low load

$\overline{P}_{Net} = 21\%$	$\overline{P}_{Net}$	FU	$SOFC.T_{MEA,mean}$	Checksum
$SOFC.S_{Power}$	**0.60**	0.40	0.00	1.00
$\overline{\dot{n}}_{Fuel}$	0.30	**0.39**	0.30	1.00
$\overline{\dot{n}}_{Air}$	0.10	0.21	**0.69**	0.99
Checksum	1.00	1.00	0.99	

Table 6-3: RGA analysis at medium load

$\overline{P}_{Net} = 60\%$	$\overline{P}_{Net}$	FU	$SOFC.T_{MEA,mean}$	Checksum
$SOFC.S_{Power}$	0.36	**0.65**	-0.03	0.98
$\overline{\dot{n}}_{Fuel}$	**0.72**	0.31	-0.03	1.00
$\overline{\dot{n}}_{Air}$	-0.08	0.03	**1.10**	1.05
Checksum	1.00	0.99	1.04	

Table 6-4: RGA analysis at full load

$\bar{P}_{Net} = 100\%$	$\bar{P}_{Net}$	FU	$SOFC.T_{MEA,mean}$	Checksum
$SOFC.S_{Power}$	0.38	**0.73**	-0.17	0.95
$\bar{\dot{n}}_{Fuel}$	**1.26**	-0.49	0.20	0.97
$\bar{\dot{n}}_{Air}$	-0.65	0.74	**0.91**	1.00
Checksum	0.99	0.98	0.94	

Concluding, the control system will have the following loops:

1. **Power loop**: Net Power is controlled by the SOFC power due to its quick dynamics
2. **Fuel utilisation loop**: Fuel utilisation is controlled by the fuel flow
3. **Temperature loop and air flow loop**: SOFC temperature is controlled by the generator power, using a cascade with the air flow being the connecting variable.

The resulting control layout is sketched in Figure 6-12.

Control Loop Interactions

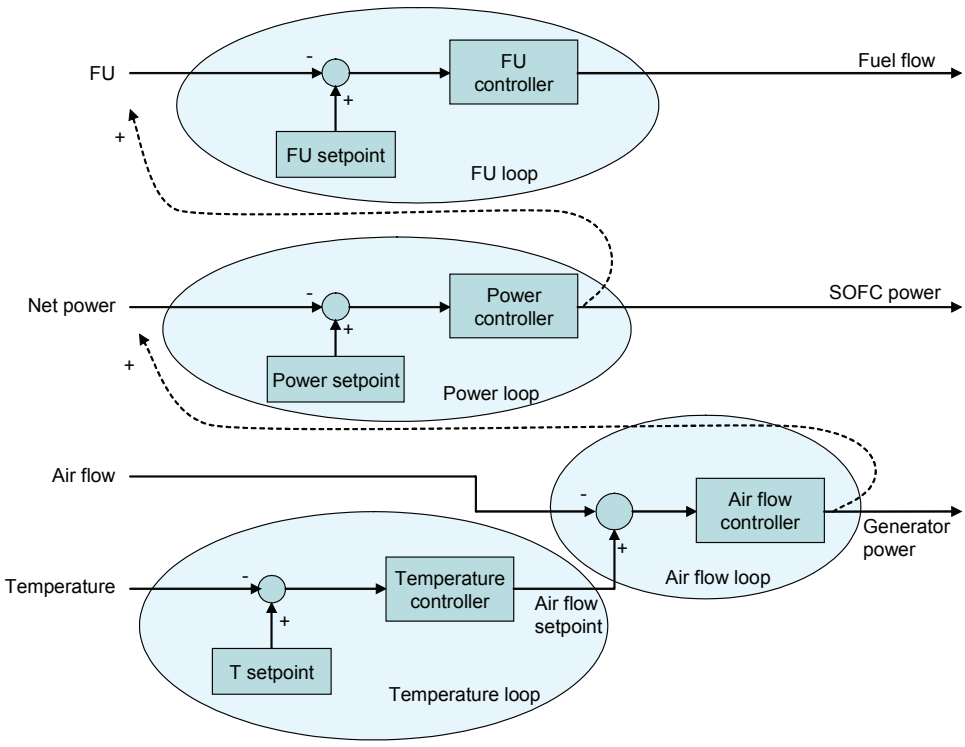

Figure 6-12: Basic control loop layout

The RGA analysis shows that there is a high degree of interaction between the loops. In Figure 6-12, the direct interactions between the loops are marked with dotted lines.

This can be accounted for by decoupling of the loops [Stephanopoulos 1984]. However, if the response time constants of the loops differ sufficiently from each other, no compensation is required.

Temperature Loop

The responses of the system outputs to step functions of the inputs are displayed in Figure 6-13 to Figure 6-15. In Figure 6-13, the response of the mean MEA temperature to a step of +1% of air flow is shown at high and low load. The other outputs (FU and net power) are specified, i.e. perfect control[15] of the closed loops is assumed. The time until a new steady state is reached is about 10,000 s at high load and increases to about 220,000 s at low load. A slow control of the temperature is hence required to avoid instability. Furthermore, especially for realising large load changes without strongly deflecting SOFC temperature, in addition to the feedback controller, a feedforward controller will be advantageous which "knows" the system and can predict the required air flow for a certain load case. The feedback controller should be of PI type for responding adequately to temperature deviations caused by quick load changes and slow incidents such as modification of system characteristics variation due to ambient conditions or performance degradation.

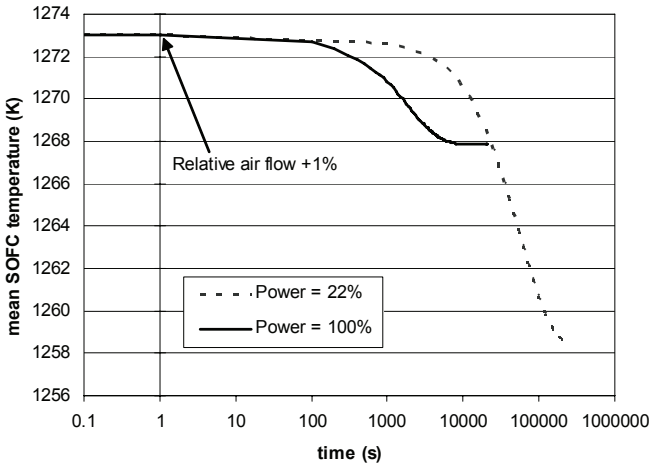

Figure 6-13: Response of mean MEA temperature to step change in air flow (all other loops closed)

[15] **Perfect control: Control of a variable in a way that it never deviates from its setpoint**

A further issue about the temperature controller is that the mean MEA temperature, which it controls, cannot be measured in practice. However, related temperatures can be measured. With a characteristic relationship, the mean SOFC temperature can be estimated based on the measured temperature. This method is called *inferential control* [Stephanopoulus 1984]. However, the relationship of most measurable temperatures to the mean SOFC temperature depends on further unknown parameters. In addition, exact measurement of high temperatures is difficult. In this study, it is chosen to measure the temperature of the fuel leaving the cell, because its relationship to the mean SOFC temperature was found to be least dependent on transient effects.

An alternative to direct temperature measurement could be estimation of the turbine inlet temperature through pressure measurement and GT characteristics. However, this method can fail due to GT degradation and changes in ambient condition.

Fuel Utilisation Loop

The response of the fuel utilisation to a step change of +0.1% in fuel flow is shown in Figure 6-14. For this calculation, the air flow is specified, i.e. the temperature loop is open. To assume a perfectly controlled SOFC temperature would be misleading here, as the time scale of interest is so small that a real temperature controller would practically not react. The power loop is closed, i.e. the net power is specified, as this loop is expected to react quicker than the FU loop. It can be seen that the FU reacts immediately on a change in fuel flow ("primary response"). This is obvious, as the FU is a value calculated from the fuel flow and the SOFC current. After the step, the FU shows a "secondary response" where it continues to decrease, which is a consequence of the changing thermal conditions and therewith current-voltage characteristics triggered by the fuel flow change. It can be concluded that manipulating fuel flow is a quick means to control the FU. The controller should react quick enough not to interfere with the secondary response. In order to avoid oscillations and unwanted steep changes in the flow channels, the controller should be of pure integral type.

An additional constraint on the controller action is that ejector malfunction must be prevented. Therefore, the controller must provide that the ejector pressure difference Δp_{Ej} does not fall below zero.

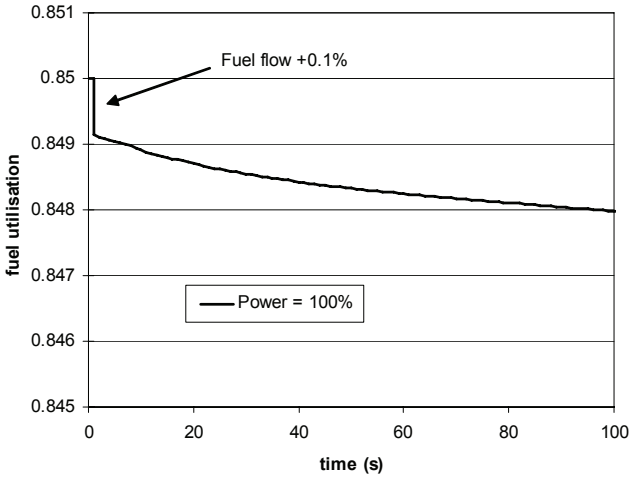

Figure 6-14: Response of fuel utilisation to step change in fuel flow (temperature loop open; power loop closed)

Power Loop

Figure 6-15 shows the response of the net power to a step of +0.1% in SOFC power output. In this case, the system inputs (air and fuel flow) have been specified, representing open loops. Assuming closed loops and perfect control would be misleading in this case, as the time scale of interest is again considerably smaller than for the above mentioned loops. It can be seen that the power reacts instantaneously, which confirms the hypothesis that the net power can be quickly controlled by manipulating the SOFC power. The required SOFC power for producing a certain power can be directly calculated from a power balance (see Chapter 4.6.11). Hence, the calculated SOFC power demand can be forwarded to the controller output and no feedback controller is required. However, not each required power value can be supplied immediately because constraints on FU and voltage must be respected to protect the SOFC.

Air Flow Loop

With a fixed constant generator power, the system is unstable: Departing from steady state, for example, a step increase of the generator power will lead to deceleration of the shaft speed. No new equilibrium will be found within the valid bounds of shaft speed. A robust PID controller is hence required to stabilise the air flow loop. The controller output signal is the generator power which is forwarded to the power electronics. Time constants for power electronics are low enough to assume instantaneous adjustment of the generator power to this value.

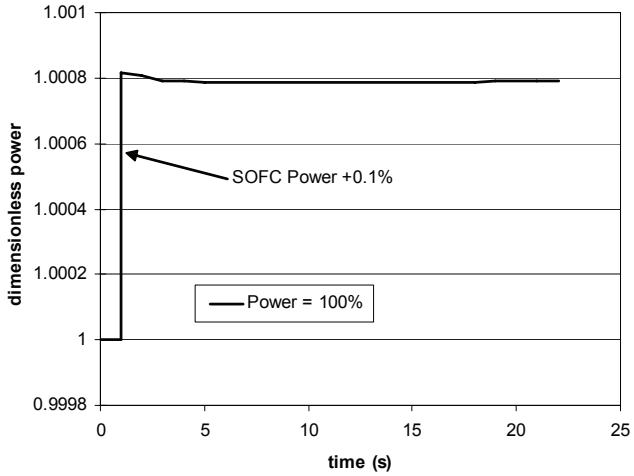

Figure 6-15: Response of net power to step change in SOFC power (all loops open)

It must be granted that the controller action is not too strong, as a quick change of the air flow rate may lead to anode backflow, inverse reaction of system power due to high amplitudes in generator power and instability due to interference with other control loops. A rate limiter for the controller input signal may be used to smooth the air flow transients.

Air flow and shaft speed are directly coupled. However, their relationship is influenced by several parameters. Therefore a constraint on the controller is that the shaft speed is within its bounds.

6.3.3 Proposed Control Layout

The control layout that has been developed based on the previous analyses is sketched in Figure 6-16. Its ports are connected to the ports/variables mentioned in the boxes. Paths refer to the model names (see Figure 6-1; Chapter 4); if no path is included, the additional system parameters are addressed (see Chapter 5.1.3).

The loops are basically shaped as described in Figure 6-12. Ports with additional constraints are indented. A difference lies in the power loop, as here the input is already the power required from the SOFC as calculated from the power electronics (see Chapter 4.6.11).

The used control equipment will be defined in the following subchapters.

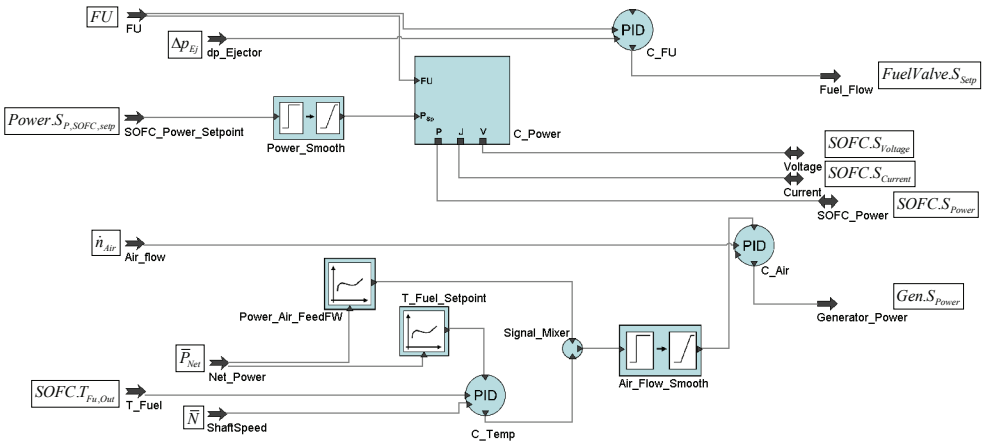

Figure 6-16: Flowsheeting layout of the control system

C_Power (Power Controller)

The *power controller* model described in Chapter 4.7.2 is applied here. The upper and lower bounds of the fuel utilisation are 0.9 and 0.75 respectively. These bounds are essentially determining the maximum step load change the system can tackle. However, setting the bounds too wide results in risk of too low steam content in the anode recycle loop and therewith carbon deposition at low FU, and steep SOFC temperature gradients and the risk of thermal cracking at high FU. Furthermore, the bound values influence the maximum error of the FU controller and therewith the maximum load change rate.

The lower bound for the voltage is set to 0.52 V. This voltage was chosen because it is close to the voltage where the SOFC reaches maximum power output. The hydrogen yield of the methane fuel is set to $\gamma_{H2} = 4$. The value of the manual voltage signal V_{man} does not have any effect unless the controller is in *manualV* mode.

Power_Smooth (Rate Limiter)

This instance of the *rate limiter* model (see Chapter 4.7.5) is only used for mitigating step changes in power down to very steep ramps in order to increase solver stability. The variable values:

Variable	Definition	Value
τ	Time constant	0.1 s
$\dot{S}_{out}^{\max}$	Maximum rate of output signal	1000000 s^{-1}
$S_{In,man}$	Manual input signal	arbitrary

C_FU (PID Controller)

The fuel utilisation controller is an instance of the *PID controller* (see Chapter 4.7.1). It is in *I* class and manipulates the fuel flow to control the fuel utilisation. It is in *automatic* mode, hence it follows an internal setpoint. An additional constraint is the pressure difference in the ejector which must be kept above zero. The values of the specified variables:

Variable	Definition	Value
K	Proportional gain	1
K_{sec}	Proportional gain of secondary input boundary control	100
τ_I	Reset time of integral term	10 s
τ_D	Rate time of derivative term	arbitrary
ω	Bandwidth limit of derivative term (should be very small)	arbitrary
A	Controller action (-1 for reverse action; +1 for direct action)	-1
S_{prim}^{max}, S_{prim}^{min}	Upper and lower bound of the primary control input signal	0.9; 0.79
S_{sec}^{max}, S_{sec}^{min}	Upper and lower bound of the secondary control input signal (constraint)	$3 \cdot 10^6$; 10^4
S_{Out}^{max}, S_{Out}^{min}	Upper and lower bound of the controller output signal	0.55; 0.03
S_{Out}^{m}	Output signal in manual mode	arbitrary
S_{Setp}	Internal setpoint	0.85

Note that the reset time of the FU controller is deciding the maximum slope of the fuel flow and is thus essential for the load change rate of the system.

Power_Air_FeedFW (Characteristic Line)

This module is an instance of the *characteristic line* model (see Chapter 4.7.4). It represents the feed forward part of the temperature control loop. It calculates the dimensionless air flow as a function of the dimensionless net power for steady state operation as shown in Figure 6-10 (blue line) with a polynomial function. The coefficients of the polynomial function have been estimated by curve fitting. The dimensionless net power was chosen because it is a controlled and stabilised variable and does not tend to oscillate or overshoot its target value in transient operation.

This feedforward controller implements the chosen operation line at constant temperature (Figure 6-7) into the control strategy. The specified variables:

Variable	Definition	Value
c(0)	Polynomial coefficient	0.07800
c(1)	Polynomial coefficient	1.4808

c(2)	Polynomial coefficient	-1.1860
c(3)	Polynomial coefficient	0.6266
c(4)	Polynomial coefficient	0
c(5)	Polynomial coefficient	0
$S_{X,max}$, $S_{X,min}$	Input signal bounds	1.05; 0.15

T_Fuel_Setpoint (Characteristic Line)

The module represents the inferential control of the mean SOFC temperature. It calculates the required SOFC outlet fuel temperature $SOFC.T_{Fu,Out}$ for a mean MEA temperature of 1273 K with a polynomial function fitted to the system performance. The dimensionless net power is the input variable. The calculated temperature serves as a setpoint to the temperature controller. The specified variables:

Variable	Definition	Value
c(0)	Polynomial coefficient	1147
c(1)	Polynomial coefficient	40.684
c(2)	Polynomial coefficient	19.070
c(3)	Polynomial coefficient	-8.9845
c(4)	Polynomial coefficient	0
c(5)	Polynomial coefficient	0
$S_{X,max}$, $S_{X,min}$	Input signal bounds	1.05; 0.15

C_Temp (PID Controller)

The temperature controller is an instance of the *PID controller*. It is in *PI* class and manipulates the air flow setpoint to control the SOFC outlet fuel temperature. It is in *cascade* mode, as it receives an external setpoint from the *T_fuel_setpoint* module. An additional constraint is the dimensionless shaft speed, which must be kept within its bounds. The values of the specified variables:

Variable	Definition	Value
K	Proportional gain	1
K_{sec}	Proportional gain of secondary input boundary control	100
τ_I	Reset time of integral term	20,000 s
τ_D	Rate time of derivative term	arbitrary
ω	Bandwidth limit of derivative term (should be very small)	arbitrary
A	Controller action (-1 for reverse action; +1 for direct	-1

	action)	
S_{prim}^{max} , S_{prim}^{min}	Upper and lower bound of the primary control input signal	1300; 1100
S_{sec}^{max} , S_{sec}^{min}	Upper and lower bound of the secondary control input signal	1.05; 0.47
S_{Out}^{max} , S_{Out}^{min}	Upper and lower bound of the controller output signal	0.15; -0.15
S_{Out}^{m}	Output signal in manual mode	arbitrary

Signal_Mixer

The signal mixer (see Chapter 4.7.6) adds the signals of the feedforward and feedback temperature controllers to the dimensionless air flow setpoint. The maximum output signal is 1.20 and the minimum signal is 0.20.

Air_Flow_Smooth (Rate Limiter)

This instance of the *rate limiter* model is used to limit the steepness of air flow and therewith pressure transients to avoid unwanted effects. The maximum rate is tuned in a way that an air flow transient from minimum to maximum takes app. 100 s. The specified variables:

Variable	Definition	Value
τ	Time constant	1 s
$\dot{S}_{out}^{max}$	Maximum rate of output signal	0.0074 s^{-1}
$S_{In,man}$	Manual input signal	arbitrary

C_Air (PID Controller)

The temperature controller is an instance of the *PID controller*. It is in *PID* class and manipulates the generator power to control the dimensionless air flow. It is in *cascade* mode, as it receives a smoothened setpoint from the *Air_flow_smooth* module. The values of the specified variables:

Variable	Definition	Value
K	Proportional gain	8
K_{sec}	Proportional gain of secondary input boundary control	no secondary input
τ_I	Reset time of integral term	18 s
τ_D	Rate time of derivative term	0.85 s^{-1}
ω	Bandwidth limit of derivative term (should be very small)	0.001 s^{-1}

A	Controller action (-1 for reverse action; +1 for direct action)	-1
S_{prim}^{max}, S_{prim}^{min}	Upper and lower bound of the primary control input signal	1.05; 0.34
S_{sec}^{max}, S_{sec}^{min}	Upper and lower bound of the secondary control input signal (constraint)	no secondary input
S_{Out}^{max}, S_{Out}^{min}	Upper and lower bound of the controller output signal	70,000; 0
S_{Out}^{m}	Output signal in manual mode	arbitrary

6.3.4 Response of the Controlled Hybrid System

The control system described above has incorporated a maximum of the posed requirements to load change and part-load ability as well as safe and gentle operation. The response of the resulting controlled hybrid cycle system to a wide variety of incidents happening in power plant operation is tested in the following subchapters.

Residential Applications

Small distributed networks supplying private households are assumed to have a maximum power step change of about 10 kW, corresponding to a dimensionless power of 4.5% of the system. Figure 6-17 to Figure 6-20 show the system response to these step decreases and increases of the power setpoint at high and low load on logarithmic time axes (setpoint power is changed at time 1 s). The time until the new setpoint power is reached varies from app. 1-2 s at high load to app. 4 s at low load.

It can be seen that the setpoint change immediately causes a deviation of the fuel utilisation *FU* from its setpoint of 0.85. This is caused by the power controller *C_Power* which manipulates the SOFC current. Except in Figure 6-17, *FU* reaches its upper or lower bound, which indicates that *C_Power* switches to the *maxFU* resp. *minFU* mode. *FU* is then reset to its setpoint by the *FU* controller *C_FU* in the time range of 2-10 s (note that at low load, FU is reset faster, as the fuel flow change rate is constant). The air flow is adapted to the value calculated for the new power by the feedforward module *Power_Air_FeedFW* in a time of app. 10 s.

The thermal parameters do not vary strongly during the small load changes. However, during the load increase at high load, there is a slight peak of the maximum radial thermal gradient in the MEA at app. 500 s, which exceeds the design value by app. 1%. All other safety parameters mentioned in Chapter 5.3 do not show any alarming deviations.

From the time directly after the setpoint power is changed until the new setpoint is reached, there is a deficit of power during load increase resp. excess power during load decrease. The missing/excessive work can be determined by integrating the power deviation over time. The result is that for a small load increase, the work deficit is app.

11 kWs, while for decrease, app. 7 kWs of excess work are produced. For off-grid applications where stable voltage and frequency are required, this implies an additional power source to stabilise the grid during load transients. Such can be batteries or capacitor banks. These could be loaded during load decreases and unloaded during load increases.

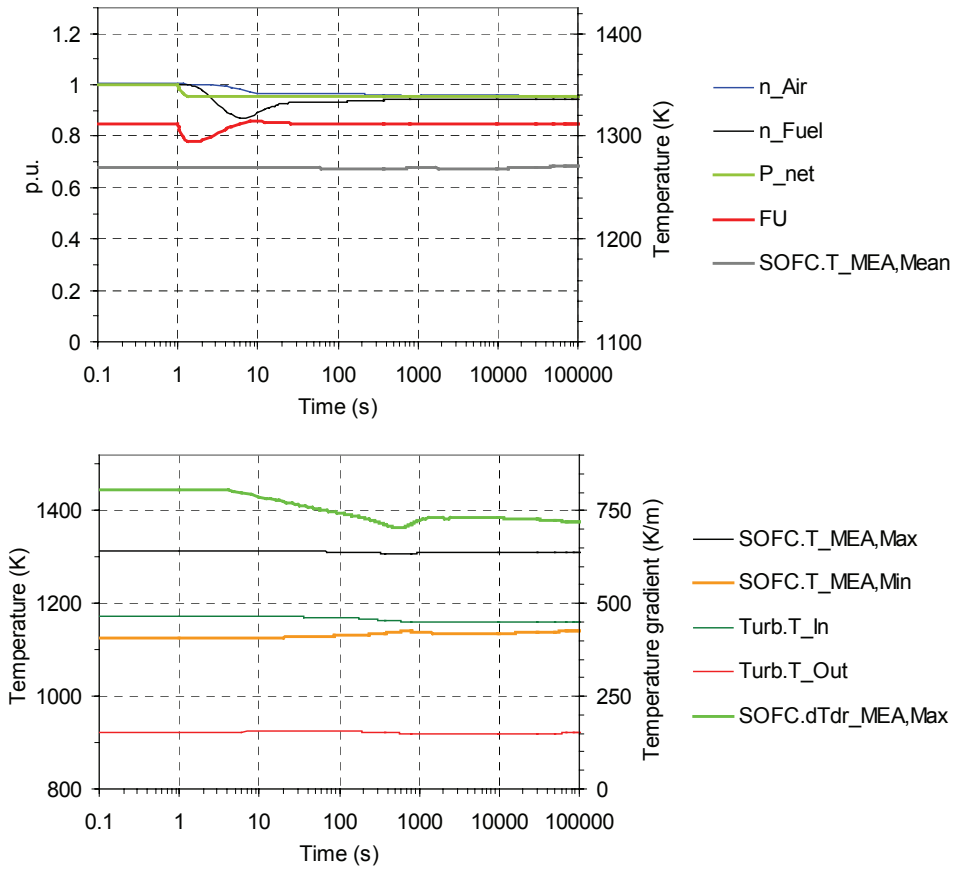

Figure 6-17: Response to small load decrease at high load (100% to 95.5%)

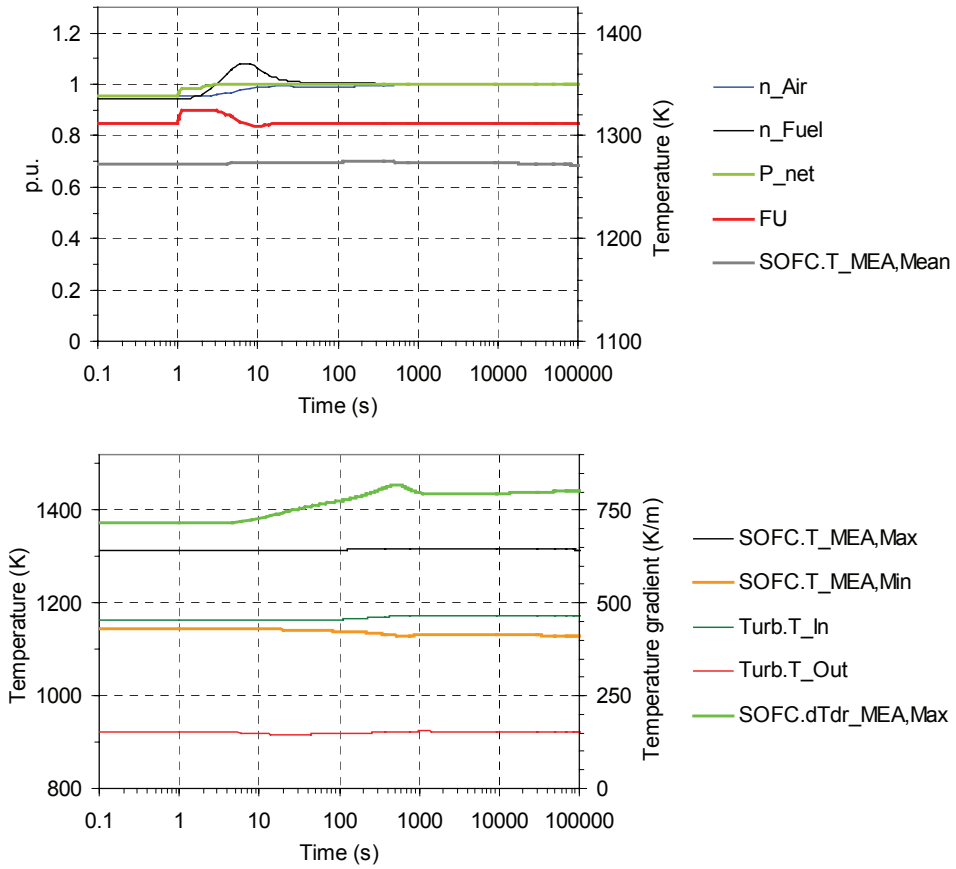

Figure 6-18: Response to small load increase at high load (95.5% to 100%)

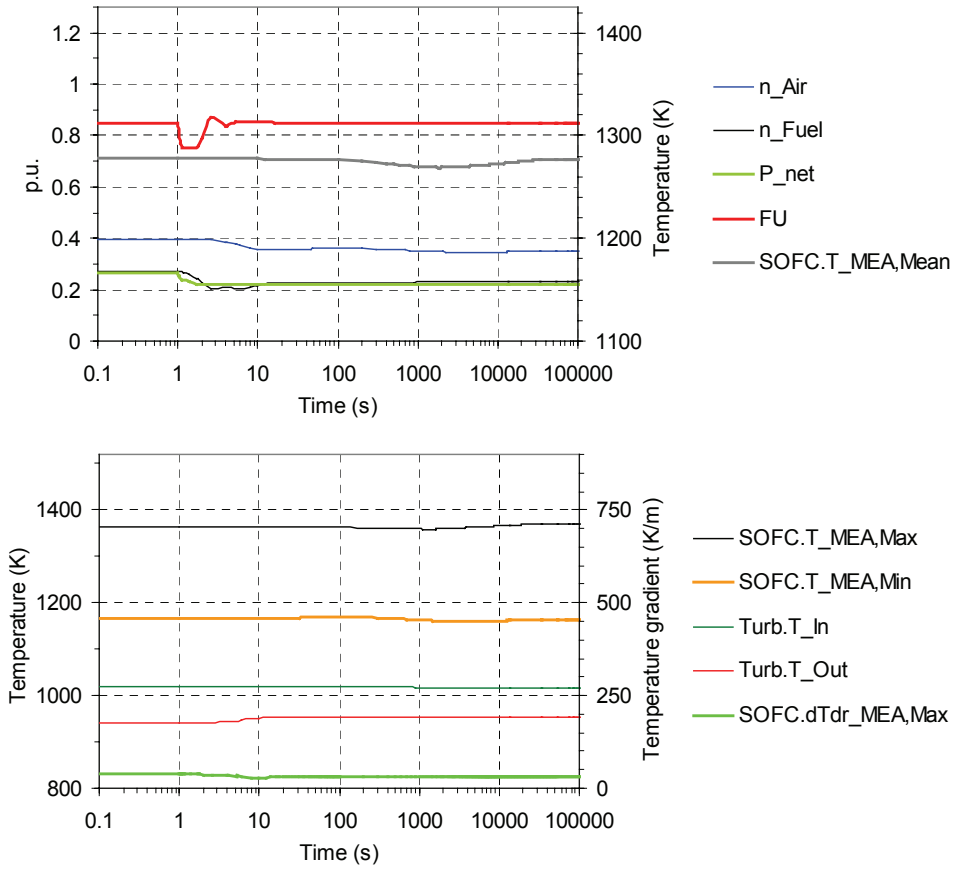

Figure 6-19: Response to small load decrease at low load (26.5% to 22%)

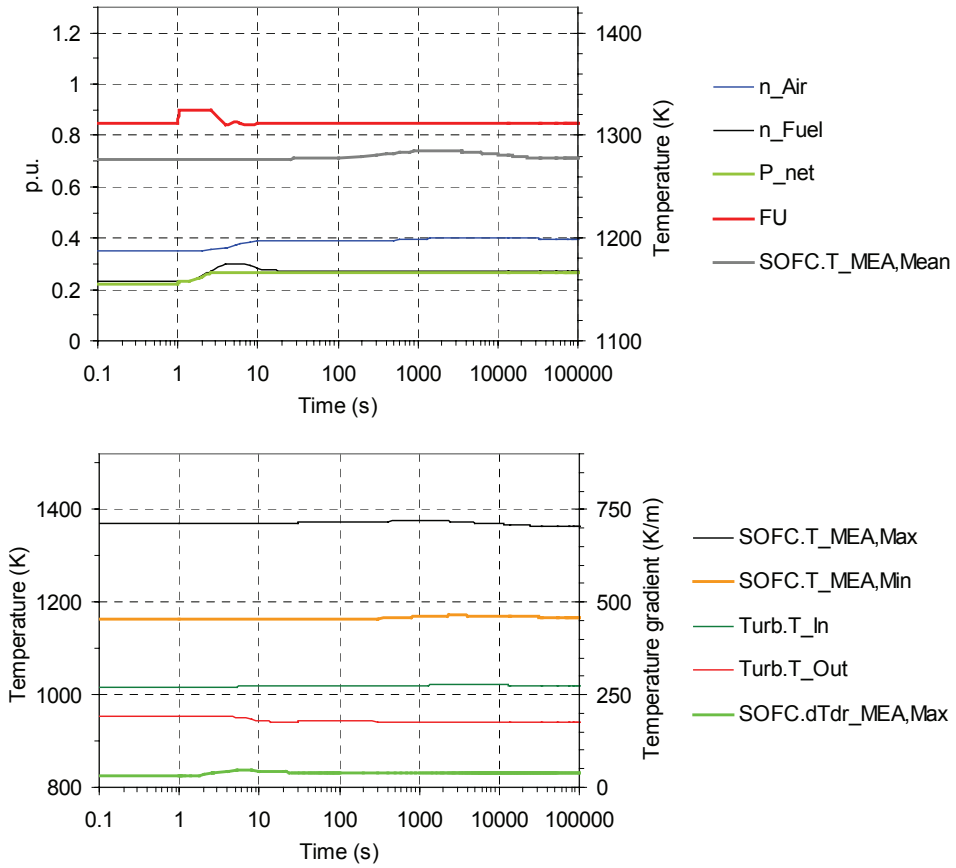

Figure 6-20: Response to small load increase at low load (22% to 26.5%)

The system response to a 24 h load following cycle is shown in Figure 6-21. The load profile is a randomly generated sequence of step load changes with a maximum step size of 10 kW, respectively 4.5%, and an average time of 150 s between two changes. The whole power range of the system is covered. The mean MEA temperature is maintained between 1236 and 1299 K during the whole cycle. The other temperatures and parameters do not exceed their steady-state operation line boundaries significantly. It may be concluded that the system is suitable for load following operation with small step changes. The average load during the cycle was 63% and the total net efficiency was 64.4%.

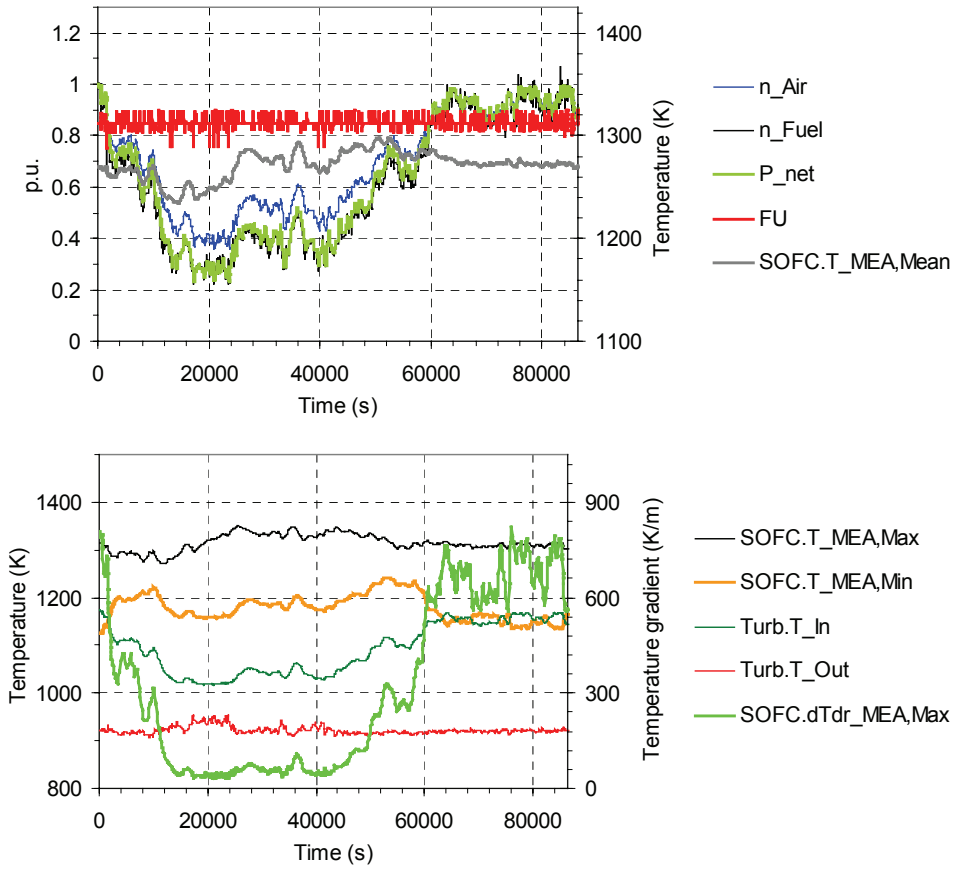

Figure 6-21: Response to residential load profile (24 h, maximum load change 4.5%)

Industrial Applications

For industrial applications, larger load changes than the above will typically occur. Figure 6-22 and Figure 6-23 show load changes between the minimum and the design load (step change of 172 kW, corresponding to 78% of the system's total net power output). The setpoint power is reached after app. 73 and 57 s for the load decrease and increase, respectively. Load decrease is per se faster than load increase due to the greater difference between minimum and setpoint FU (0.1) than between maximum and setpoint FU (0.05). However, the large load decrease is delayed by the constraint on the ejector pressure difference (see Chapter 5.3.2) which is slowing down the fuel flow decrease in the time 10-73 s after the load change. A quicker load decrease could be achieved if an inert gas would be mixed to the fuel during this transient in order to keep the ejector at the desired working condition and at the same time reduce the combustible input. At load increase, the minimum voltage is reached and the controller switches to *minV* mode 19 s after the load increase, where it remains for

12 s (note that FU falls below its maximum value in this period). The fuel flow is at its maximum value (fuel valve fully open) between 30 and 70 s after the load change. The air flow is adapted by the calculated feedforward value for the new power during app. 60 s after the load change. As the measured SOFC outlet fuel temperature $SOFC.T_{Fu,Out}$ at this time has not reached its steady value, the proportional term of the feedback temperature control corrects the airflow to an intermediate level before it approaches a steady value at approximately 2000 s.

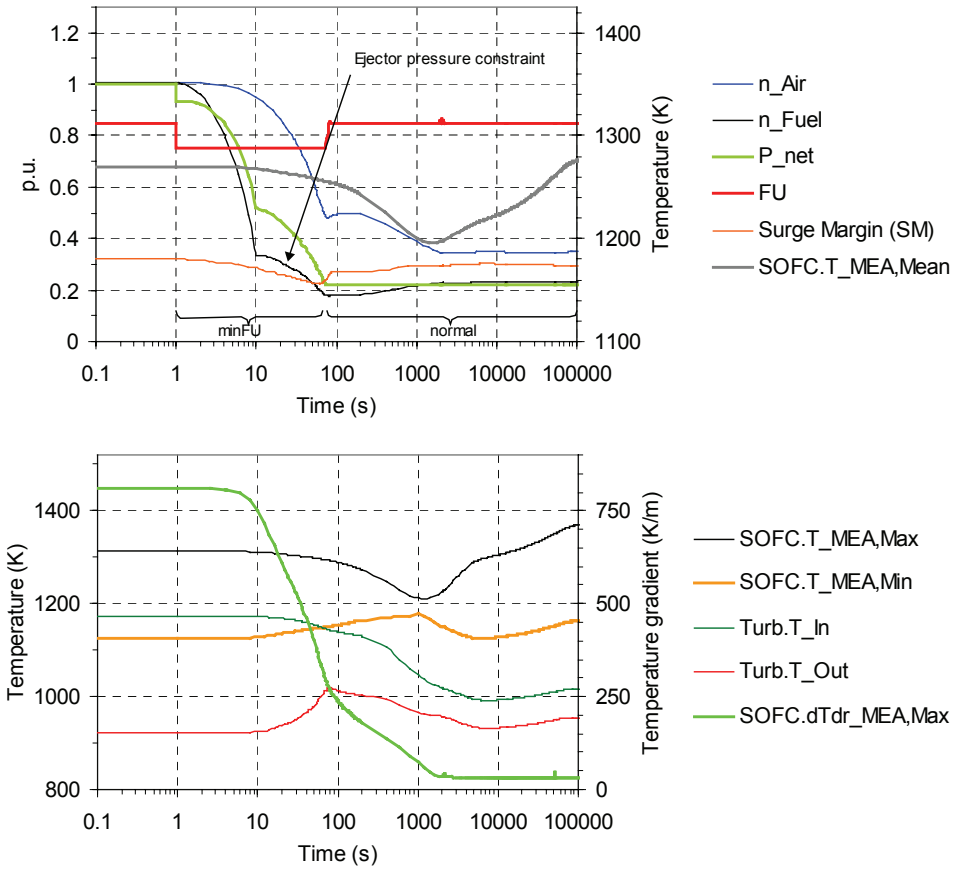

Figure 6-22: Response to large load decrease (100% to 22%)

The compressor surge margin is also shown in Figure 6-22 and Figure 6-23. It is rather stable, but reaches a transient maximum during load increase and a minimum during decrease. This is because of the fairly constant TIT during speed change, which is caused by the high thermal capacity of the SOFC system. Risk of surge during load decrease has also been observed by Hildebrandt and Assadi [2005]. This is particularly interesting because in a regular non-recuperated gas turbine, the opposite trend occurs.

Looking at the temperatures, it can be noticed that after load increase, the system needs about 10,000 s to reach a new thermal steady state, while after the load decrease it stabilises after app. 90,000 s. This large difference can be explained through the higher gas and energy turnover in the system after at high load (i.e. after load increase). It has been reported previously by Achenbach [1995].

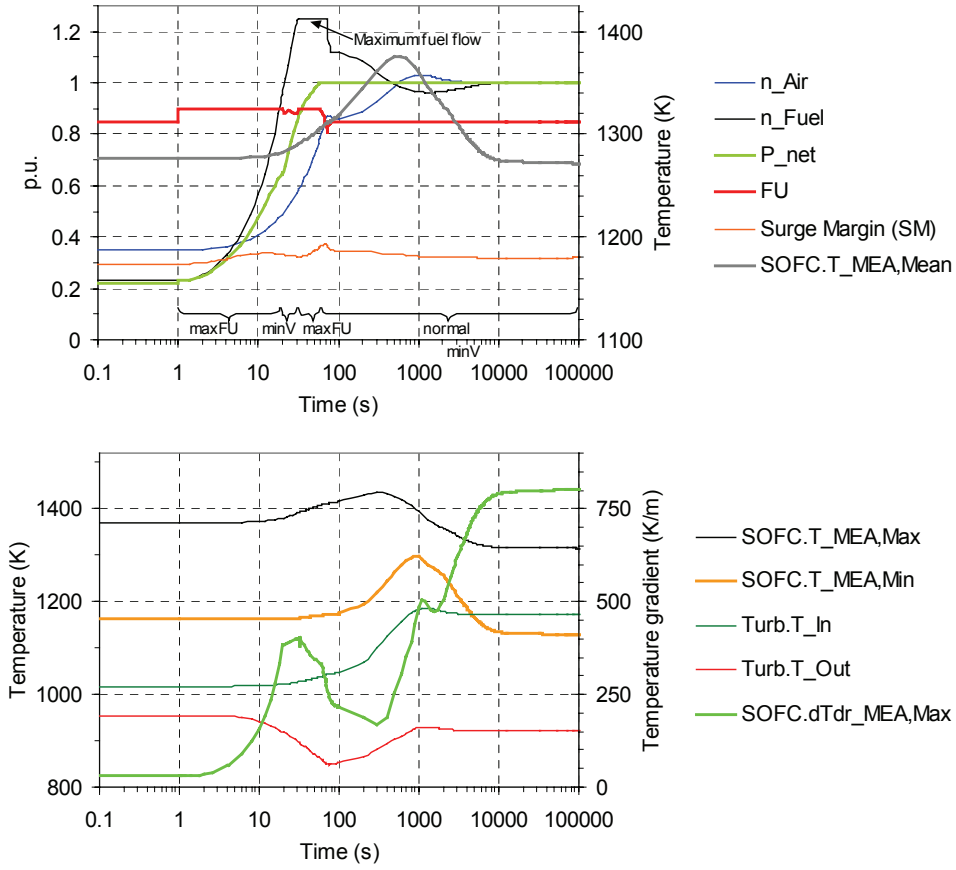

Figure 6-23: Response to large load increase (22% to 100%)

During load decrease, the mean MEA temperature has a minimum of app. 1200 K at app. 1500 s, while at load increase it has a maximum of app. 1375 K at app. 600 s. These strong temporary deviations from its setpoint of 1273 K are mainly caused by the thermal capacity of the integrated indirect reformer (IIR). The thermal capacity induces that the reforming degree needs between 600 and 1500 s to achieve its new steady state value. Therewith, after a load increase the SOFC sends less heat to the IIR than in steady state, and this causes the temperature to peak.

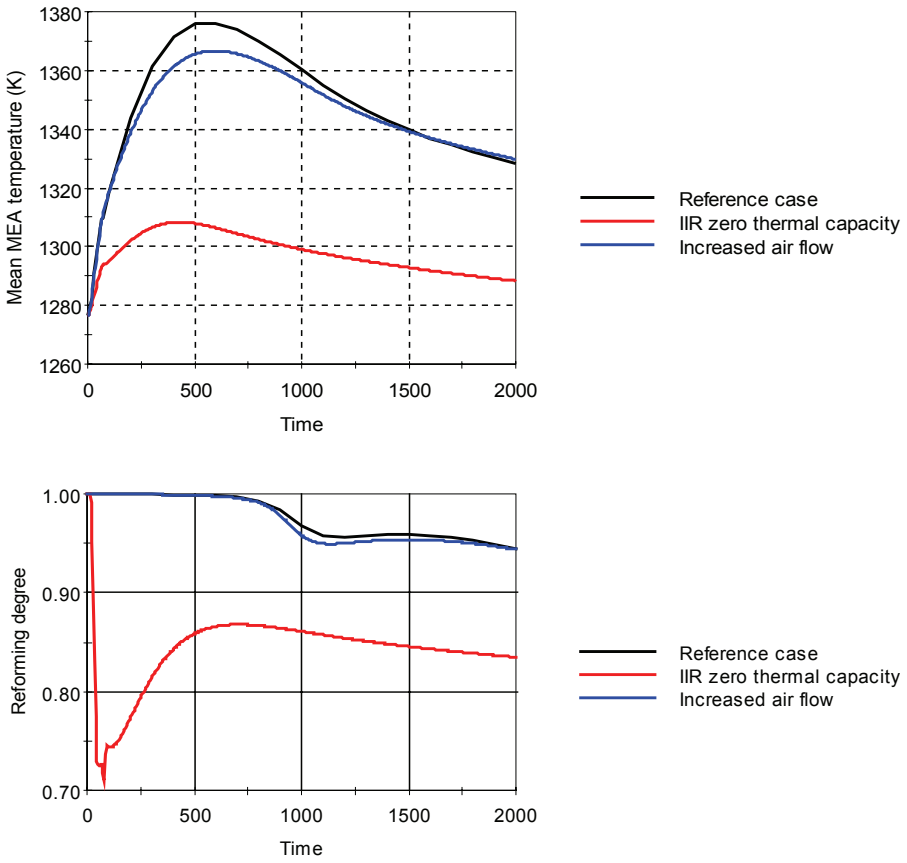

Figure 6-24: Mean MEA temperature and reforming degree for large load change with different options

Figure 6-24 shows the mean MEA temperature and reforming degree response for a load increase simulation with an IIR model without thermal capacity. The peak is reduced by app. 70% (i.e. 70 K). In another simulation, the airflow was forced to immediately proceed to the final value, which decreased the peak only about app. 10 K. Increased air flow rate is hence not very effective to mitigate these peaks.

The maximum MEA temperature has a peak value of 1433 K during load increase. This is yet below the critical temperature of 1473 K where the SOFC materials become unstable (see Chapter 2.1.2). However, it may be concluded that a system with frequent large load changes is exposed to stronger thermal cycling and may therewith have a shorter lifetime than a system with slower load transients.

A further issue is the steam to carbon ratio γ_{SC} during the load decrease, which undershoots its design value of 2.0 for app. 120 s and reaches a minimum value of app. 1.4. This may cause carbon deposition in the reformers. However, as this incident is

principally reversible, no conclusion can be drawn on how critical this is for a real system. Experiments are required here.

During load decrease, the turbine outlet temperature $Turb.T_{Out}$ reaches a peak of 1019 K. According to the McDonald [2003], this is yet an acceptable inlet value for modern steel heat exchangers.

The minimum current density is advancing very close to zero during load increase, at app. 20 s after the step change. The progress of the current density distribution during the first 100 s after the load change is depicted in Figure 6-25. The minimum appears at the cell exit. However, it is due to a high fuel depletion during the transient and considering the low voltage of 0.52 V at the time of 20 s, there is no danger for reversal of the electrochemical reaction.

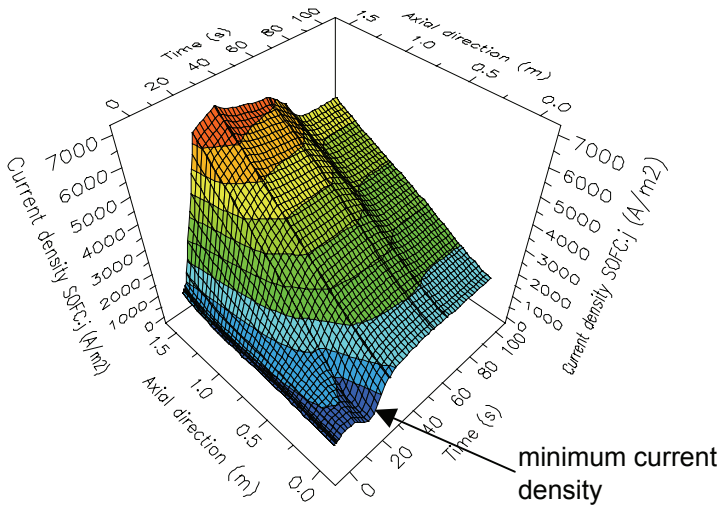

Figure 6-25: Current density distribution during the first 100 s after large load increase (axial direction – 0: top/gas exhaust; 1.5: bottom/gas entry)

At the load increase, the work deficit between demand (setpoint) and supply is app. 3200 kWs, while at the decrease, app. 3150 kWs of excess work are produced. For off-grid solutions where a stable voltage is desired, this value gives a hint on the required capacity of an additional power source/sink. A bank of capacitors for this power should be compact enough, as modern super-capacitors have a power density of up to 17 kWs/l [Epcos 2005].

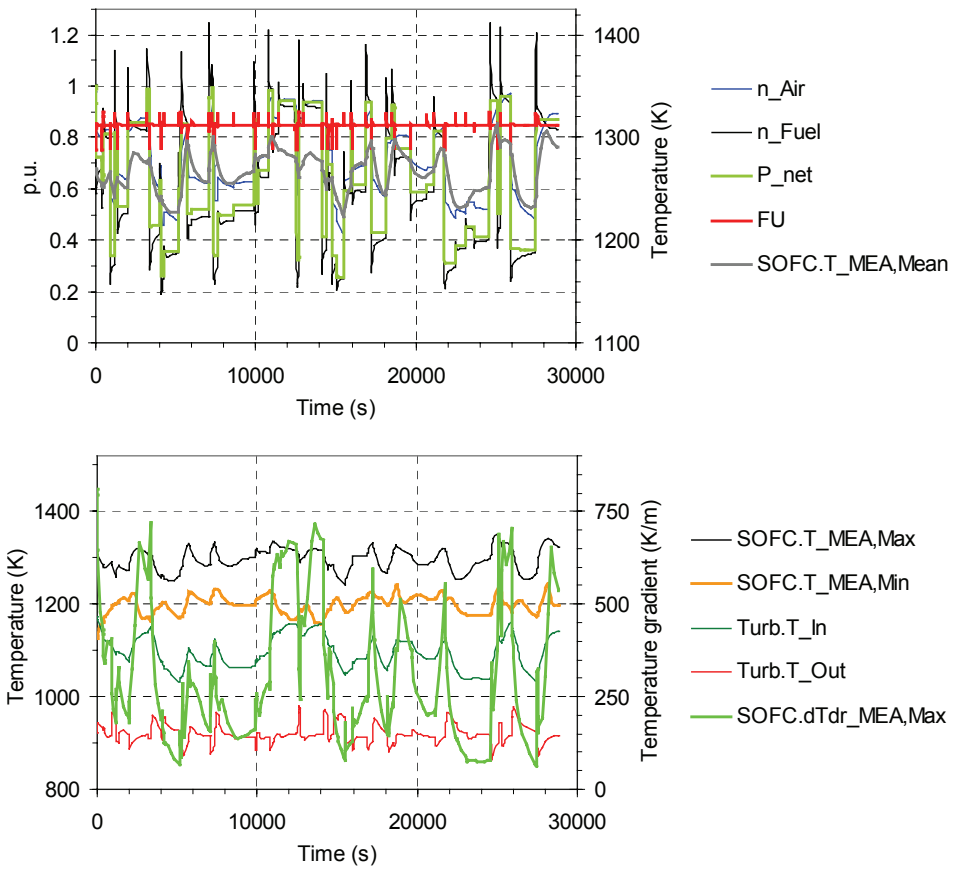

Figure 6-26: Response to industrial load profile (8 h, maximum load change 78%)

Figure 6-26 shows the response of the system to a fictive eight hour load profile for an industrial application. The profile consists of random load changes at random times. It can be seen that all parameters stay in within the ranges spanned by the large load changes and no accumulation occurs. Moreover, the quick succeeding load changes seem to mitigate the temperature extremes: The mean MEA temperature stays within the range from 1222 to 1313 K and the maximum MEA temperature stays between 1242 to 1351 K.

For the simulated industrial load profile, the average load was 65% and an average net electric efficiency of 64.3% was achieved. As this is close to the steady-state efficiency, it may be concluded that there is no significant efficiency penalty for operation with strongly fluctuating load.

Peak Power

In both residential and industrial applications, it is advantageous if a power plant can supply a surplus to its nominal power for a limited period. This ability allows for smaller nominal power and therewith a smaller power plant for a certain application. For the current system, the power output of the GT can hardly be increased as it operated close to the maximum permitted shaft speed at the design point. However, the SOFC power output can be increased as long as the diffusion limit of current density is not reached. However, sufficient air to maintain constant mean MEA temperature cannot be provided, and hence the temperatures will increase.

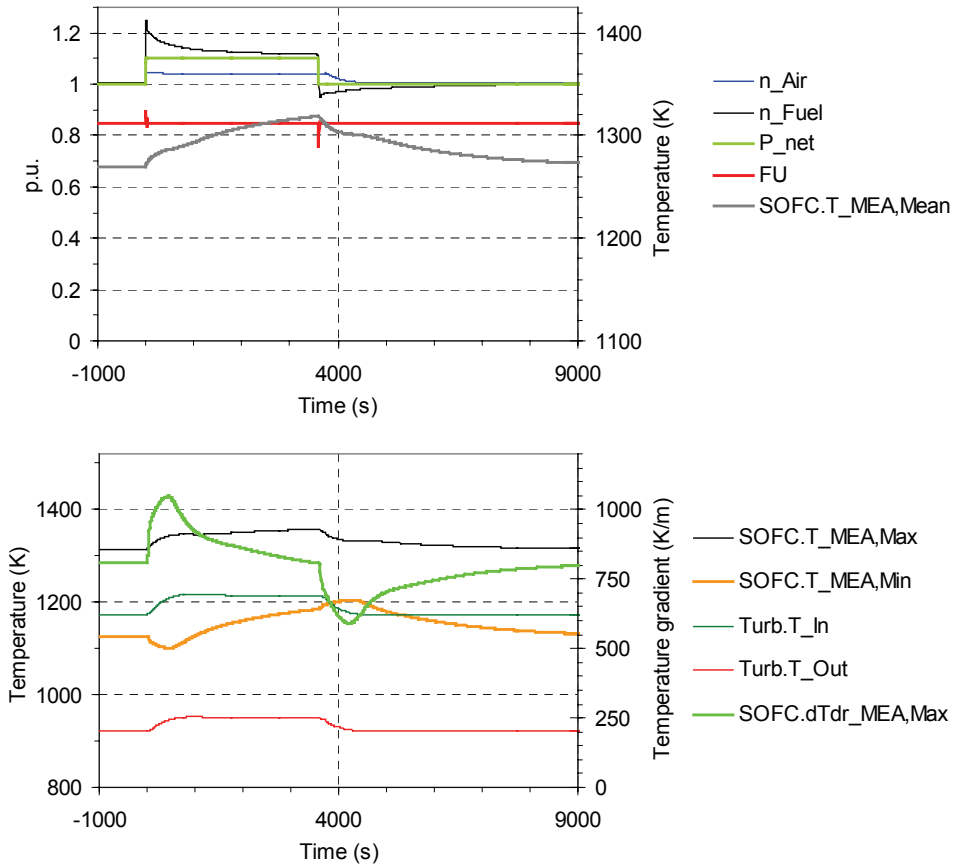

Figure 6-27: Response to peak power (1h at 110%)

Figure 6-27 shows the system response for a case where the power is increased to 110% for one hour and then decreased back to its design value. It can be seen that the SOFC temperatures constantly increase during the peak power; the mean MEA temperature has increased to 1358 K after one hour. It recovers to its design value app. one hour after the end of the peak power period. More critical might be the peak of

the maximum radial temperature gradient of 30% above the design value at the initiation of the peak load.

Theoretically, even higher peak power could be supplied; for the current system, only the maximum fuel flow is limiting the power. As the connection between fuel cell degradation and its thermal state is generally difficult to predict, reasonable peak power limits in terms of degradation must be determined by experiments and operation experience.

Ambient Conditions, Malfunction and Degradation

The system is in practice exposed to external disturbances such as variation in ambient pressure and temperature, or variation of the fuel quality. These provoke that the system deviates from its design performance. For example, the feedforward parts of the control strategy are not accurate anymore. In addition, degradation of the components influences the system behaviour. Fouling of the compressor reduces for example its isentropic efficiency and mass flow, and the heat production in a degraded SOFC is higher than in a new one. In order to inspect the control stability and response of a system under external disturbances and degradation, the following four scenarios were investigated:

- **Ambient conditions**: Ambient temperature increase by 15 K and simultaneous pressure decrease by 20 mbar. This provokes a decrease in air density of app. 7% and therewith a variation of the GT performance.
- **Error in fuel quality**: 5 mol-% nitrogen is added to the methane fuel. The molar hydrogen yield γ_{H2} remains unchanged (it is assumed that the changed fuel quality is not known to the operator). This equals an overestimation of the fuel flow of app. 5%, as it may be caused by a malfunctioning measurement device. It provokes an error in the calculation of fuel utilisation and therewith influences the thermal balance of SOFC and GT.
- **Compressor degradation**: The mass flow and efficiency of the compressor map are scaled down to 95% each. This provokes a changed operation line in the GT performance maps.
- **Fuel cell degradation**: A contact resistance $SOFC.R_D = 2 \cdot 10^{-4}\ \Omega$ is assumed. For the design current of app. 250 A per tube, this equals a voltage drop of 0.05 V. The reduced voltage increases heat production in the SOFC.

The feedforward parts of the controller, i.e. the characteristic lines for air flow and SOFC air exhaust temperature, remain unchanged. Figure 6-28 depicts the new mean MEA temperature and system net efficiency over the dimensionless net power in steady-state. The black dashed line gives the reference scenario (note that the slight slope of the mean MEA temperature as compared to Figure 6-10 is due to limited precision of the polynomial in *T_Fuel_Setpoint*). It can be seen that the ambient conditions, fuel cell and compressor degradation scenarios provoke a steeply

increasing temperature at high load. This is because the selected scenarios lead to a reduced compressor air flow. Once the GT has reached its maximum speed, it cannot supply more cooling air and thus the temperatures rise as the load increases, comparably to the peak power described above. A conclusion is that the GT system should be capable to deliver a considerably higher air flow than the design value.

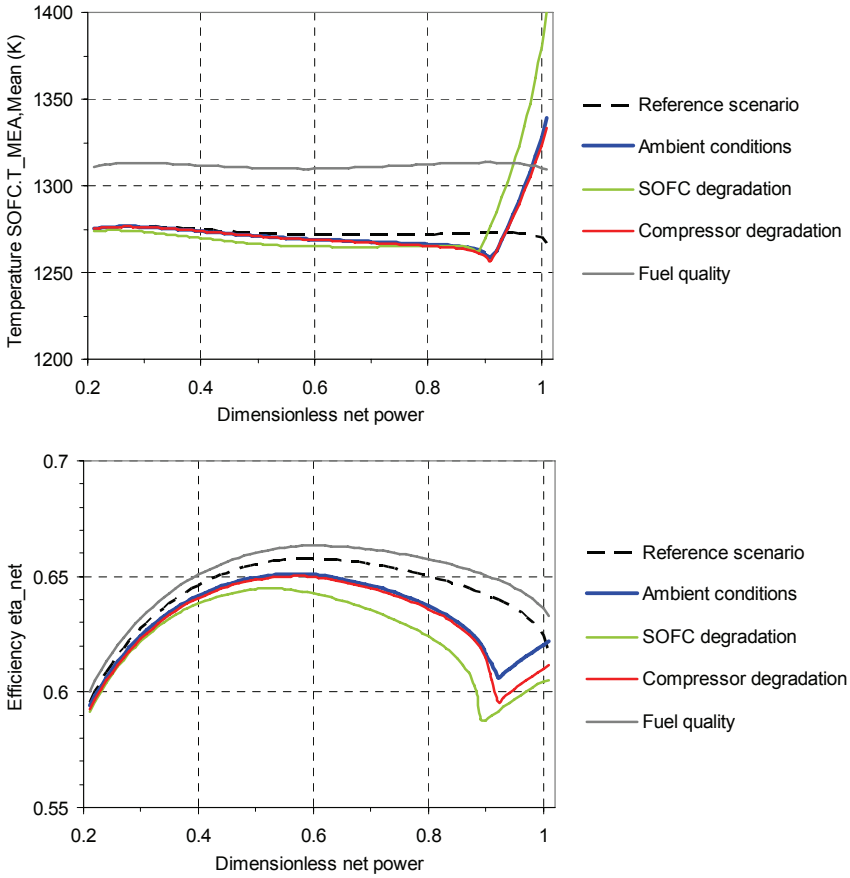

Figure 6-28: Steady-state mean MEA temperature and net efficiency for the different scenarios

Another way to decrease the temperature when the GT is at maximum speed is to open a bypass around the recuperative heat exchanger (see Figure 6-31). Thereby, more heat is extracted from the system, which causes a temperature decrease but obviously also an efficiency penalty. This approach is further discussed in Chapter 6.5.3.

The fuel quality scenario shows a constant deviation of temperature along the whole load range of app. 80 K above the design value. The reason for this is that the relationship between the controlled SOFC fuel outlet temperature and the mean MEA

temperature depends on the true fuel utilisation. It must be mentioned that the system is able to cope with different fuel qualities without any noticeable effect, as long as the molar hydrogen yield number γ_{H2} used for calculation of the fuel utilisation is correct. This implies that the fuel quality must be known to the operator.

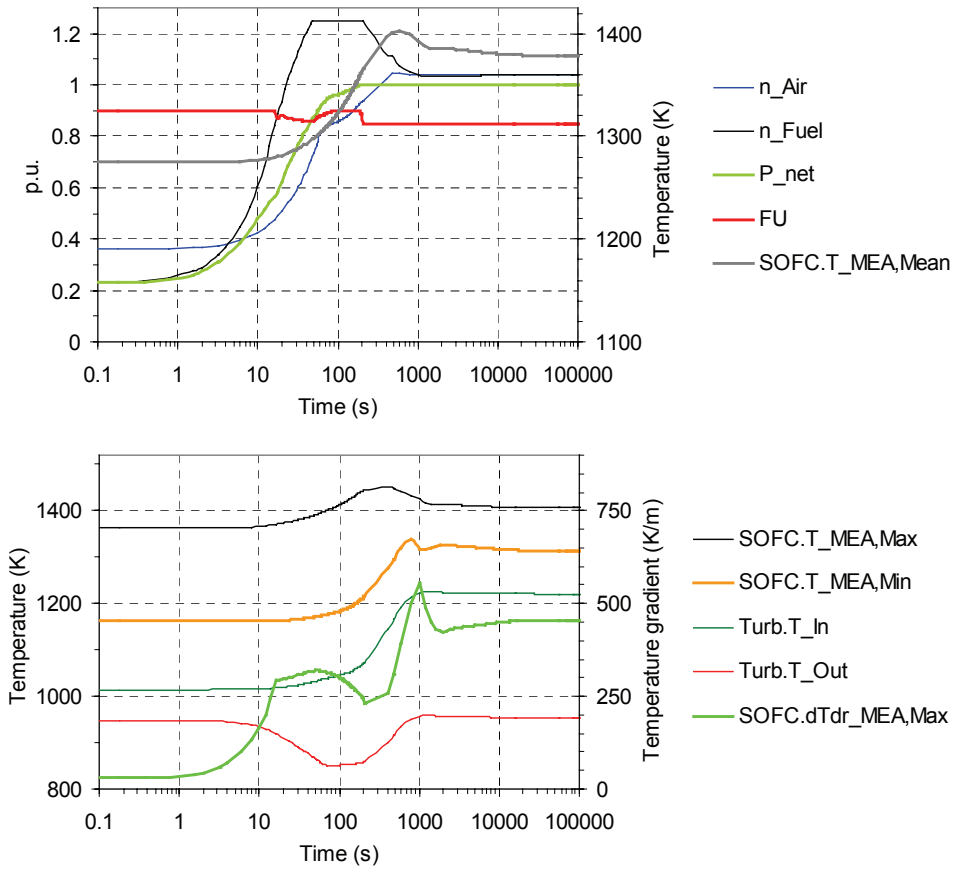

Figure 6-29: Response to large load increase at degraded SOFC (-0.05V at design current)

The net efficiency lines are similar for the different scenarios as long as the GT shaft speed is not at its maximum. The efficiency increases with the fuel cell temperature, which can be seen at the fuel quality scenario, and furthermore it depends on the operation line of the GT performance maps, which can be seen for the other scenarios.

The system response to large load decreases of the different scenarios is very similar to the scenario at reference conditions in Figure 6-22 and thus not shown here. It must be mentioned that the turbine outlet temperature reaches slightly higher peak values of 1055, 1040 and 1035 K for fuel cell degradation, compressor degradation

and changed ambient conditions, respectively. For the fuel quality scenario, it is with only 998 K lower than the reference value, despite the elevated SOFC temperature. This is because the higher true fuel utilisation in the SOFC causes less heat production in the burner and hence a lower turbine inlet and outlet temperature.

As for the system response to large load increases, particularly the SOFC degradation scenario is interesting, which is depicted in Figure 6-29. It can be seen that unlike the reference case (see Figure 6-23), the maximum radial temperature gradient in the MEA reaches a peak at 1000 s and decreases afterwards to a steady value which is 44% below the reference scenario. At the same time, the minimum MEA temperature increases and is significantly closer to the maximum MEA temperature than in the reference scenario.

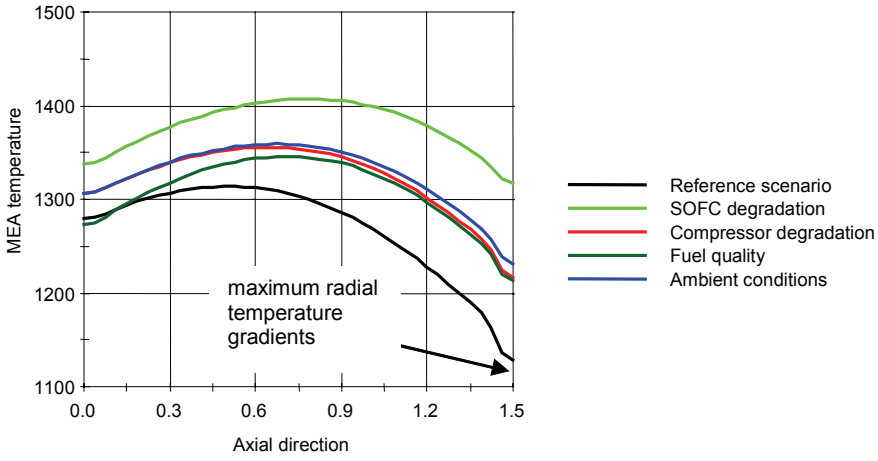

Figure 6-30: Temperature profiles along the SOFC tube (left: top, right: bottom) for the scenarios at full load

Figure 6-30 shows the axial temperature distributions along the SOFC tube for the different scenarios. The maximum radial temperature gradient occurs at the very bottom of the tube where air and fuel "meet" with different temperatures at either side of the MEA. The figure shows that the temperature profiles are quite different, which is mainly caused by the varying heat production in the cell. All other scenarios have slightly lower maximum radial temperature gradients than the reference scenario, even though the temperature difference between fuel and air is not lower. This may be a consequence of differing reaction ratios at the cell entrance.

6.3.5 Conclusions

The proposed control strategy seems to assure safe and efficient operation at the conditions it was designed for. Small load changes can be tackled without any safety

critical issues. During large load changes, problems could be caused by the temporarily temperature peak in the SOFC during load increase or the low steam to carbon ratio during load decrease which might lead to carbon deposition in the reformers. The extreme values are mitigated for load profiles with frequently changing load. Temporary peaking above the nominal power is connected to a sharp increase in the maximum radial temperature gradient in the MEA and may result in SOFC degradation.

For conditions deviating from the reference, especially such that lead to decreased air supply by the GT (decreased air density, compressor degradation) or increased heat production (SOFC degradation), the SOFC temperature may increase at high load. As a consequence, the GT should be capable of supplying significantly more air than the design value, or other measures to control the temperature, such as recuperator bypassing, should be implemented. An error in the fuel measurement or fuel supply quality leads to high temperature deviations. Such errors must hence be avoided through assured fuel quality and safe (redundant) measurements.

6.4 Startup and Shutdown

This subchapter is dedicated to incidents that can occur during shutdown and startup. Extra equipment required to control these incidents is introduced. Sequences for shutdown and startup are proposed and the system response to the execution of these is highlighted.

6.4.1 Introduction

During shutdown and startup trips of the hybrid system, its components must be protected from the critical incidents defined in Chapter 5.3.2. The shutdown trip must take the system to a state where it can be left alone without risk. Especially exposure of the anode to oxygen must be prevented until a temperature level is reached where no reactions occur. The cell cooling must be sufficiently smooth and slow to minimise the thermal load. During startup, the SOFC must be heated up smoothly and slowly to a temperature high enough for introducing fuel and starting the SOFC operation (in the following called SOFC *ignition*). During the SOFC ignition phase, the risk of carbon deposition due to insufficient steam must be mitigated. A further task for the shutdown and startup procedures is to minimise the amount of extra auxiliaries and other efforts.

In open literature, little information on shutdown and startup of hybrid systems is available. Veyo et al [2002] describe a startup strategy where air can be bypassed around the SOFC system in order to allow for startup of the turbine before the SOFC. A fired air heater allows for gradual heating up of the SOFC system to the required startup temperature. Chan et al. [2003a] propose a similar system where part of the compressed air is bypassed around the recuperator and the stack and directly fed to the gas turbine burner. At 973 K, the fuel is gradually channelled from the burner to

the SOFC. Hildebrand et al. [2005] state that the large volume of the SOFC can run the system to unstable conditions during shutdown, resulting in risk for the turbomachinery by surge and for the SOFC by pressure differences.

6.4.2 Proposed Approaches and Required Extra Auxiliaries

Suitable shutdown and startup strategies should facilitate quick, safe shutdown and startup with few extra auxiliaries. Furthermore, no external power shall be required for driving the turbomachinery during the trips, except for the inevitable startup to the minimum operation shaft speed. The following section discusses issues which appear only during startup and shutdown and proposes equipment to address these issues:

- To avoid oxidation of the anode while the SOFC is not active, it must be exposed to a reducing or inert atmosphere.
  - ⇨ Flushing the anode with nitrogen ensures an inert atmosphere. This implies the availability of a nitrogen mixing unit and a sufficient amount of bottled nitrogen for shutdown and startup.
- At **ignition of the SOFC**, carbon deposition due to insufficient steam must be omitted.
  - ⇨ This problem could be addressed by introducing externally generated steam. In this case an external steam generator is required. Further, the introduction of methane fuel will in the beginning cool down the cell due to the endothermic steam reforming reaction. It is hence chosen to use hydrogen as fuel instead of methane for the ignition. This implies the availability of a mixing unit and a relatively small amount of bottled hydrogen for the startup, but a steam generator can be omitted.
- In the **early phase of shutdown**, the GT system will deliver a net power output due to the heat stored in the SOFC system. It is assumed that no load is available after shutdown, hence this power must be dissipated.
  - ⇨ An electric dissipator would be a possible solution to this. However, it is chosen to introduce a variable throttle into the turbine exhaust stream, because it can also be used during startup (see below). Through throttling the exhaust gas, the pressure reduction in the turbine is decreased and hence the net power can be controlled to zero by manipulating the throttle opening.
- In order to drive the GT without extra power during **late shutdown** and during **startup**, and furthermore to heat up the system, firing of an auxiliary burner is required.
  - ⇨ A burner upstream the turbine is chosen, because it facilitates controlling the shaft speed and accordingly air flow due to the GT system's quick response to the turbine inlet temperature. During the shutdown and startup sequences

described below, the burner must supply a maximum heat duty of app. 124 kW.

- In the **late phase of shutdown**, the recuperation of turbine exhaust heat to the compressed air must be omitted in order to cool down the cell to a temperature of app. 400 K.
  - ⇨ A bypass of turbine exhaust gas around the heat exchanger is used to facilitate low SOFC air inlet temperatures. Control valves for high temperature gases are known to be expensive and delicate, and the existence of an adequate valve is somewhat unsure. An alternative is to bypass the compressed air instead of the exhaust gas; this results in a smaller valve with less temperature requirement (compressor outlet temperature). The drawback is, however, that the normally colder parts of the heat exchanger would heat up strongly when compressed air is bypassed while all exhaust gas flows through it. Furthermore, slow control of the bypass valve would be required in order to avoid a thermal shock of the fuel cell caused by the thermal capacity of the hot heat exchanger.
- In the **late phase of startup,** before the SOFC is ignited, the recuperator hot inlet temperature must be high enough to reach a sufficient SOFC temperature.
  - ⇨ This issue could be addressed by an additional burner between the turbine and recuperator. Another option is the exhaust throttle introduced above. A lower pressure drop in the turbine provokes a smaller difference between inlet and outlet temperature and therewith the throttle can be manipulated to control the recuperator hot inlet temperature. Simultaneously solving two issues, the exhaust throttle was preferred to the combination of an electric power dissipator and an additional burner behind the turbine.

The resulting layout of the system including the auxiliary burner and ducting for startup and shutdown is sketched in Figure 6-31. Additional ducts are painted in black colour and additional components/models in dark blue (compare Figure 5-1).

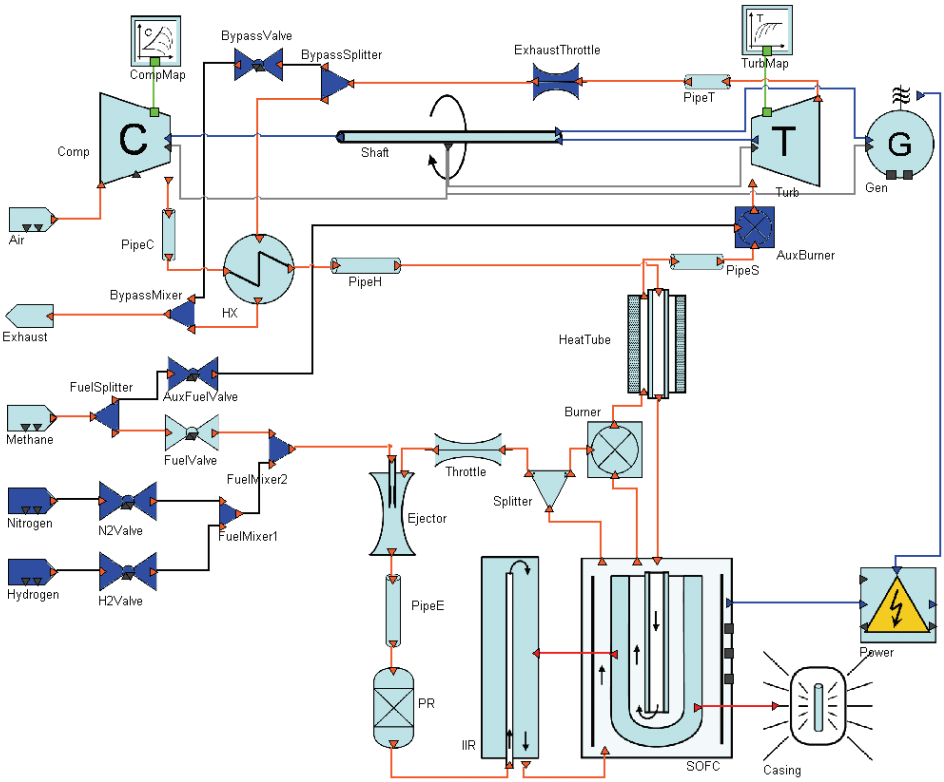

Figure 6-31: Directly integrated SOFC cycle with ducting for startup and shutdown

6.4.3 Shutdown Strategy and Simulation Results

The following section explains the proposed and simulated shutdown sequence step by step. It is assumed that the system is in normal operation at any valid load when the shutdown sequence is initiated.

1. At the initiation of the shutdown sequence, the following controllers are bumplessly switched (see control design in Figure 6-16):

   - The air flow loop is decoupled from the temperature loop. A manual air flow setpoint is dictated by switching the *rate limiter* model *Air_flow_smooth* from *automatic* to *manual mode* and specifying the manual signal $Air\_flow\_smooth.S_{In,man}$.
   - The temperature controller *C_temp* is not used anymore and thus switched to *manual mode* for omitting integral windup.
   - The FU controller *C_FU* is switched to *manual mode* for dictating a manual fuel flow setpoint $C\_FU.S^{m}_{Out}$.

- The power controller *C_power* is switched to manual voltage mode *(manualV)*. The voltage will from now on be manipulated by the parameter $C\_power.V_{man}$.

2. The manual air flow setpoint is reset to 80% of the design air flow. The *Air_flow_smooth* unit will smoothly approximate the setpoint.
3. Within 10 seconds, the following changes are applied by linear ramping:
   - *FuelValve* is closed.
   - *N2Valve* is opened to achieve a nitrogen flow of 0.44 mol s^{-1}, which equals the fuel flow at design point.
4. The cell voltage is decreased linearly by 0.01 V per second until it reaches 0.5 V. Due to the nitrogen flushing, the combustible hydrogen at the anode is depleted and thus the reversible potential decreases. The voltage must thus be lowered at this point in order to omit the local reversion of the electrochemical reaction in the cell and exposure of the anode to oxygen.
5. Due to the remaining heat of the SOFC, net power is produced in the turbine even with zero combustible fuel input. The air flow controller *C_Air* is now switched to *manual mode* and a manual generator power of 5359 W is imposed. This value equals the assumed power required to supply the control system. The exhaust throttle closure is now manipulated to control the airflow by an indirect proportional controller. As soon as all combustible fuel in the SOFC is consumed, the system net power output reaches zero. This operation is continued until the exhaust throttle is fully open again.
6. At this time, the SOFC temperature is exactly sufficient to drive the unthrottled GT at the desired air flow. From this point on, auxiliary firing will be required to maintain the air flow. Thus, instead of the exhaust throttle closure, the fuel flow to the auxiliary burner is now manipulated by an indirect p-control. To further cool down the cell, the exhaust bypass is slowly opened within 1000 s by a ramp function.
7. When the exhaust bypass is fully open and the recuperative heat exchanger is cooled, the SOFC system receives compressor air of approximately 400 K and cools down further. It is assumed that below the measured fuel recycle temperature of 573 K, the anode is not sensitive to oxygen anymore and the procedure can be stopped. The terminal temperature is critical in terms of SOFC safety and fuel consumption by the auxiliary burner.

Figure 6-32 depicts the described shutdown sequence and the response of the system in terms of power and temperatures. As initial condition, steady-state full load operation is assumed. The topmost diagram shows the first 30 s after the load change where the steps 1-4 of the above sequence are executed and step 5 is initiated.

The temperature of the SOFC decreases slowly without sharp breaks or high thermal gradients. The slight peak of the radial thermal gradient after app. 4500 s is due to the exhaust bypass opening and the consequent decrease in the SOFC air inlet temperature. If experiments or detailed thermal stress simulations reveal this as critical, it can be mitigated by adjusting the time period for the exhaust bypass opening.

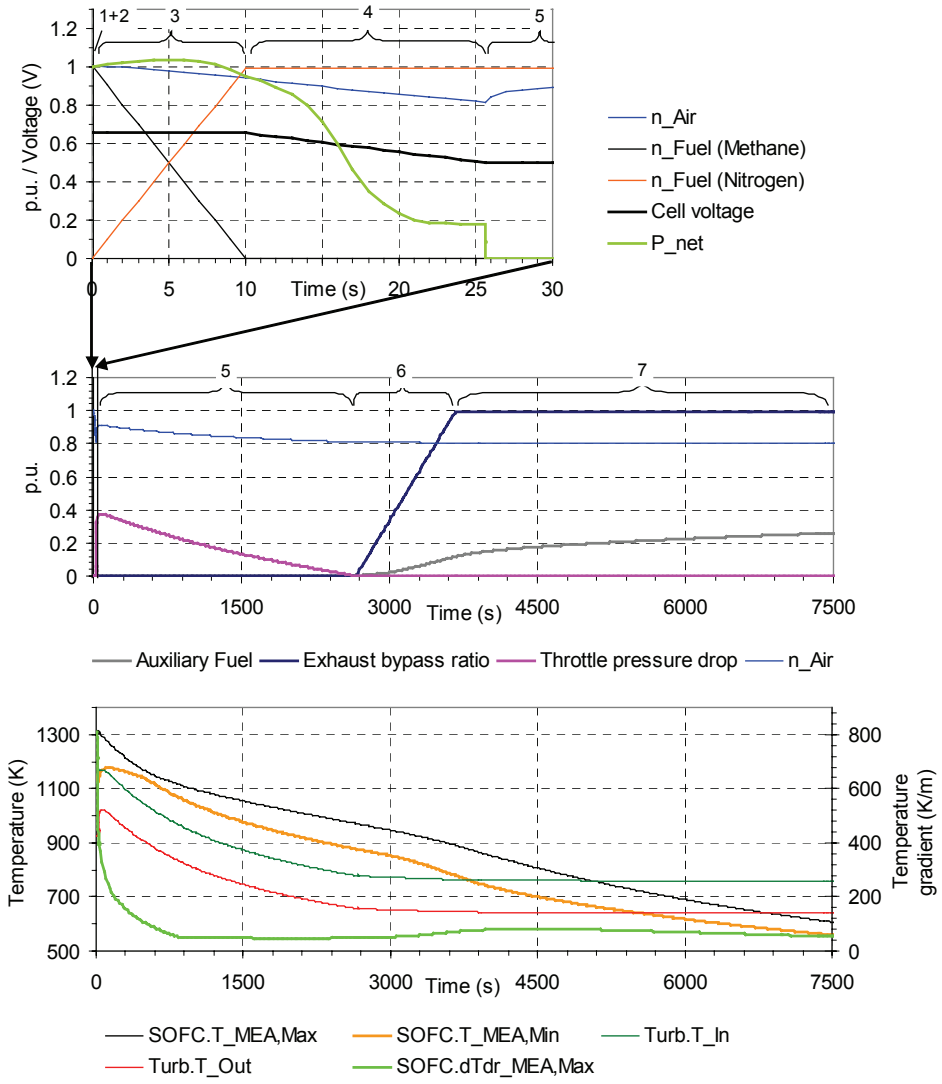

Figure 6-32: Shutdown sequence and system response

The surge margin (not displayed) decreases during the first phase from the original value of 32% to reach an minimum of 17% after app. 80 seconds. Afterwards, it increases slowly to a steady value of app. 52%. The minimum value does not represent a safety risk for the current system.

The system net power reaches zero after approximately 25 s. During this period, app. 3900 kJ electric work is produced. This value is similar to the excess work accumulating at a maximum step load decrease. This energy must be ingested by either a temporary storage device or an electric dissipator. If the latter is required, the exhaust throttle is still effective in reducing the cooling requirement and thus size of the component: In a similar strategy without exhaust throttling, approximately the eightfold electric energy would be produced during shutdown. The ability to stop the power output immediately and shutdown the system safely is required for practical power plants due to the danger of a grid breakdown and hence a load drop.

After approximately 2 hours, the temperature has reached an uncritical regime and the system can be switched off. For the whole shutdown sequence, the consumed amount of methane would correspond to app. 13 minutes of full load operation, or a LHV-based energy input of 79 kWh for the current system. The required amount of nitrogen is 461 kg, or 369 Nm^3. If bottled nitrogen is to be used, this corresponds to 30 standard 50 l-bottles with 300 bar. It is on the other hand assumed that the nitrogen flow for protecting the anode from oxygen can be much lower than in the current simulation. However, the current model does not include gas diffusion in the flow channels and is therefore not suited for such estimation. The nitrogen flow rate does not significantly influence the system thermal response shown above. Furthermore, thermal cycling is believed to strongly reduce the lifetime of the SOFC and the latter is therefore generally not suited for frequent shutdown and startup.

6.4.4 Startup Strategy and Simulation Results

The following section explains the proposed and simulated startup sequence step by step. The initial state is defined as follows:

- The SOFC system is at a homogenous temperature of 400 K when the startup sequence is initiated. Assuming room temperature will not imply any significant change in the startup behaviour but caused stability problems in the simulation.
- The gas turbine is rotating at app. 80% of the design speed. The startup of the gas turbine cannot be simulated because the characteristics are only known for a certain minimum shaft speed.
- The fuel to the auxiliary burner is manipulated by an indirect p-controller to control the air flow to 80%. The required fuel flow is app. 35% of the design value.
- All operational controllers are in *manual mode*.
- A manual generator power of 5359 W is imposed in order to supply the auxiliaries. Therewith, zero net power is produced.
- The fuel channel is flushed with nitrogen at a flow rate of 100% of the design fuel flow.

- The cell voltage is 0.5 V.

This state is equal to the steady-state which is reached if the shutdown sequence is run infinitely. The following steps take the system to full load operation:

1. After the startup sequence is initiated, the exhaust splitter is completely closed within 100 s by a linear ramp function. At the same time, the p-control manipulation of the fuel flow to the auxiliary burner is deactivated and the flow is decreased from its current value by 0.000225%-points per second (equals 4.5%-points in 20,000 s). The exhaust throttle closure is now manipulated to control the airflow by an indirect proportional controller. Therewith, the exhaust throttle will close slowly with the increased turbine inlet temperature caused by the warming up SOFC. This operation is continued until the measured fuel recycle temperature reaches 900 K.
2. At this point the SOFC is warm enough to be ignited. The following actions are taken:
   - The air flow controller *C_Air* is activated bumplessly by switching it to *cascade mode*.
   - The nitrogen valve closes and the hydrogen valve opens to achieve design fuel flow during a ramp of 10 s. The SOFC will begin to produce power as soon as hydrogen reaches the active surface.
   - The fuel flow to the auxiliary burner is ramped down to zero within 500 s.
   - The manual air flow setpoint at the *Air flow smooth* unit is ramped down to 48% within 500 s. This omits too strong cell cooling in the following phase where the auxiliary burner is not fired anymore. Further it provokes the exhaust throttle to fully open.
3. After 500 s, the auxiliary firing is switched off and the air flow is at 48%. The exhaust throttle is now manually set to full opening. With the hydrogen reaction, the SOFC heats up internally, increasing the reaction rate and fuel utilisation (FU). This operation is continued until the current corresponding to a total FU of 75% is reached. Note that for hydrogen fuel, the molar hydrogen yield is $\gamma_{H2} = 1$.
4. When the FU has reached 75%, the hydrogen valve is closed during a slow ramp with 2500 s duration. During the same period, the main fuel (methane) valve is opened to 45% of the design fuel flow. The slow ramp is necessary because a faster transition would imply too strong cooling of the cell by the initiating reforming reaction. According to steady state part-load behaviour, a fuel flow of 35% is required to match the air flow of 48% (see e.g. Figure 6-7). However, since the temperature has not yet achieved the steady value, more fuel is required.
5. When the fuel shift is completed, the FU controller and the temperature controller are bumplessly switched to *cascade mode*. The *Air_flow_smooth* unit is switched to *automatic mode*, forwarding the air flow setpoint from the temperature

controller to the air flow controller. The net power setpoint is reset to the power of 35%, which is correlating to the steady-state power value for the airflow of 45% (see Figure 6-7). At this time, the system is back to normal operation and can follow a load profile. However, it is not yet able to produce nominal power output, as the SOFC temperature is still low and the required fuel flow would exceed its maximum bound. In the simulation, the power setpoint is slowly ramped up to nominal power within 2 hours.

Figure 6-33 depicts the described startup sequence and the response of the system in terms of power and temperatures. The topmost diagrams zoom into some details.

The SOFC is heating up slowly until the reactions are started with hydrogen after app. 4.5 hours. At this point, the maximum MEA temperature is increasing rather steep. If necessary, this can be mitigated by slowing down the shift from nitrogen to hydrogen.

The turbine outlet temperature reaches a maximum of 1040 K app. 4.5 hours after the startup initiation, because the throttling provokes only a small temperature decrease in the turbine. If this is critical for the heat exchanger used in practice, the SOFC ignition (point 2) and hence cessation of auxiliary fuel and exhaust throttling may be advanced to an earlier time and hence lower temperature.

During phase 1, the surge margin (not displayed) decreases to reach a transient minimum of app. 15% after 4.5 hours, caused by the relatively high turbine inlet temperature. This moderate value does not represent a safety risk for the current system. Electric power production starts app. 4.6 hours after the startup initiation. During the steps 3 and 4, it is slowly increasing to a value of 38% of the design power until the operation control is started and it can follow a load. Until this point, an electric energy of 142 MJ has been produced. This is far beyond the required capacity of a temporary storage device for normal operation. Therefore, a practical solution where only a small load must be covered during the early phase is ideal. Additionally, the gas turbine could be used to supply power already during the first phase of startup. The system would then be able to deliver about 20% of its design power immediately after startup initialisation, at the cost of a low efficiency. This would, however, imply a more complex control strategy for supplementary fuel, air flow and exhaust throttle during the startup sequence. It is therefore not investigated here.

The LHV of the methane fed to the auxiliary burner for heating the cell (not including the ordinary fuel flow in phase 5) is app. 550 kWh, which corresponds to the fuel needed for 93 minutes of full load operation. The required amount of nitrogen is 1041 kg or 833 Nm^3. This is more than double the amount required for shutdown. Again, it must be pointed out that a significantly lower nitrogen flow may in practice be sufficient for anode flushing, but this cannot be predicted with the current model because it does not consider gas diffusion. The amount of hydrogen consumed during the startup sequence is app. 1.7 kg, respectively 18 Nm^3 or 57 kWh. Therewith, approximately two 50 l bottles with hydrogen at 200 bars are required per startup. It

must be pointed out that the bottles can only be emptied partially, as the gases must be supplied to the ejector at high pressure for achieving the foreseen flow rate.

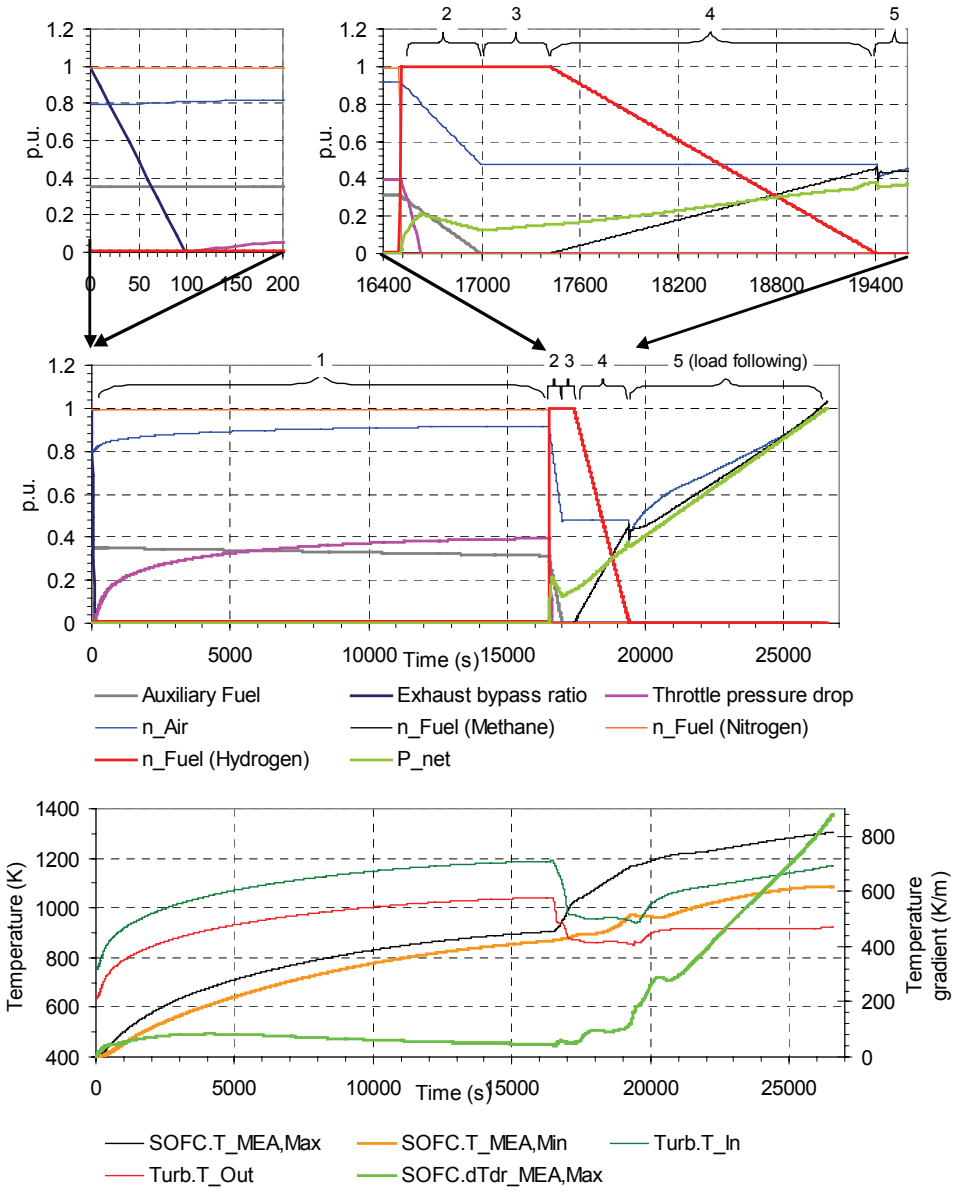

Figure 6-33: Startup sequence and system response

6.4.5 Conclusions

Shutdown and startup procedures are proposed based on the possibility to use the GT system for ventilation. Air flow and SOFC system inlet temperature are controlled by using auxiliary firing upstream the turbine, turbine exhaust gas throttling and a

variable bypass around the recuperative heat exchanger. The startup strategy utilises a relatively small amount of hydrogen for the ignition phase of the SOFC instead of supplying externally generated steam for the reforming reactions. A high nitrogen demand has been detected. However, it is uncertain how much nitrogen flow is required to safely protect the anode from oxygen exposure. Supposing the SOFC tolerates the thermal states it is exposed to during the processes, the shutdown takes app. 2 hours until the system can be switched off. Startup takes app. 4.5 hours until the system can be operated in load-following mode. Full load can, however, not be achieved at this time. A more flexible control could allow the system to follow a low load immediately after startup initiation. Due to the long time required and since thermal cycling reduces the SOFC lifetime, it may be concluded that such a system is not suited for frequent startup and shutdown.

6.5 Fuel Flexibility

This subchapter is dedicated to the fuel flexibility of a methane-designed DIC system. It discusses necessary modifications and presents the changed design objectives, part-load behaviour and control response when hydrogen or ethanol is used as fuel.

6.5.1 Introduction

In the current work, methane is the primary fuel for SOFC/GT hybrid systems. Methane is the main component of natural gas, which today is widely available in the world's densely populated areas. However, it is a fossil fuel with limited resources and cannot be produced from renewable sources in large scales once it is depleted. The importance of renewable and synthetic fuels is therefore expected to improve during the coming decades.

Another issue with natural gas is that it might be uneconomic to deliver gaseous fuels to sparsely populated, remote areas. Liquid fuels are advantageous for these applications due to their higher volumetric energy density which facilitates trailer distribution and on-site storage. Due to their scalability and efficiency, fuel cell power plants are considered an interesting option for power supply in such sparsely populated, remote areas.

Considering these points, the question arises whether a SOFC/GT hybrid system designed for methane fuel can easily be modified to other fuel sources once the focus turns from natural gas to other, novel fuels. With the DIC system design from Chapter 5.4/6.1 as starting point, this chapter discusses the required modifications, shows steady state performance and dynamic behaviour and discusses system particularities for two alternative fuels:

- Hydrogen, which is widely expected to become an important energy carrier in the future because it can be produced from almost any primary energy source with acceptable efficiency.

- Ethanol, which is a liquid fuel with high volumetric energy density and can be produced from biomass.

The most important properties of the two fuels compared to methane are listed in Table 6-5. The system designed for methane fuel shall be modified only slightly, i.e. no modifications to the SOFC and the turbomachinery will be done. The characteristics stored in the control system must, however, be adapted to match the new system behaviour.

Research on alternative fuels for SOFC is currently focussing on biogas [Proell 2004, Karl 2004, Norheim 2005]. A main issue within this topic is the risk of anode poisoning by hydrogen sulphide, which is a typical biogas component.

Table 6-5: Properties of the fuels

Fuel	Methane	Hydrogen	Ethanol
State at standard conditions	gaseous	gaseous	liquid
Molar hydrogen yield (steam reforming)	4	1	6
Required steam to carbon ratio for complete reforming	2	0	1.5
Heat consumption per yielded hydrogen (standard conditions)	41.26 kJ mol^{-1}	0	28.89 kJ mol^{-1}
Volumetric LHV (standard conditions)	35.8 MJ/Nm^3	10.8 MJ/Nm^3	21.2 MJ/l

6.5.2 Modifications of the Hybrid System

Hydrogen

Hydrogen is the electrochemically reacting species and therewith the primary fuel for most types of fuel cells. If hydrogen is used in the current system, there is no need for steam reforming. The reformers are thus not required, but do not represent a problem either. A difference to methane is that hydrogen due to its small molecules is very diffusive. This may cause hydrogen leakage in the fuel supply system if the sealing materials are not designed for hydrogen.

Because a mole of methane yields four moles of hydrogen by steam reaction, the hydrogen fuel flow must be fourfold the methane flow to produce a comparable electric current. Given a fixed critical cross-section in the ejector nozzle, a higher fuel supply pressure is required to accomplish this flow rate. This effect is partially mitigated by the significantly higher speed of sound of hydrogen (factor 2.82 for ideal gas) which facilitates a higher critical mass flow.

Other modifications required may be system safety measures, such as gas detectors and a ventilation system. This is depending on the differences in legal regulations between hydrogen and methane.

Ethanol

Ethanol with the chemical composition CH_3-CH_2-OH (simplified C_2H_6O) is liquid under ambient conditions. The boiling temperature under ambient pressure is app. 350 K; at elevated pressure of 30 bar, it increases to app. 480 K. The fuel must be vaporised before it enters the ejector. Therefore, a heater upstream the ejector is proposed which vaporises the ethanol and overheats it to 500 K. It is assumed that the heat can be supplied from the exhaust gas stream by a further recuperator downstream or parallel to the main recuperator, without influencing the latter thermally. Hence, no additional heat duty must be considered for the ethanol heating.

The sum reaction of the steam reforming is

$$C_2H_6O + 3H_2O \rightarrow 2CO_2 + 6H_2 \quad \Delta h_R = -173.31kJ$$

One mole of ethanol requires hence a total of three moles of steam for complete reforming, where six moles of hydrogen are yielded. The molar flow of ethanol must hence be two thirds of the methane value for achieving a certain SOFC current. Furthermore, the calculation of fuel utilisation (FU), steam to carbon ratio γ_{SC}, reforming degree γ_R, stoichiometric air ratio λ and heating value LHV (SOFC model) must be adapted to the new reaction. In equilibrium of ethanol-steam mixture, ethanol is completely decomposed to methane, carbon oxides and hydrogen [Assabumrungrat 2004]. It can hence be assumed that only species available in the model (i.e. CH_4, CO, CO_2, H_2, H_2O) leave the adiabatic pre-reformer, while no higher hydrocarbons remain. An uncertainty is, however, the stability of the current catalysts in the pre-reformer for reforming ethanol. Fierro et al. [2005] report that deactivation of nickel catalysts through carbon deposition can occur. Galvita et al. [2002] have achieved positive results for the performance of a SOFC fed by ethanol reforming products. The investigations with ethanol fuel are based on the availability of a suitable catalyst in the reformers.

6.5.3 Steady-State Performance

Design Objectives

To evaluate performance of the system with the new fuel, a new design point must be defined at first. However, it is assumed that the existing system design parameters should be kept. Hence, the design process is basically restricted to two degrees of freedom, as for example air flow and fuel flow, representing the axes on the performance maps shown in Chapter 6.2. For design air flow, the original value from the methane fuelled system is chosen, because the GT system is only slightly

influenced by the fuel choice. The fuel flow is designed with the objective to reach the same steady state mean SOFC temperature as with methane, i.e. 1273 K.

Table 6-6 lists the design objectives as they were decided for methane (see Chapter 6.1) and compares them with the two alternative fuels.

Table 6-6: Influence of fuel on system design objectives (for fixed design parameters)

Design Objective	Methane	Hydrogen	Ethanol
$\overline{\dot{n}}_{Fuel}$	1	2.56	0.57
$\overline{P}_{net}$	1	0.70	0.88
$SOFC.j_t$	3000 A m^{-2}	1922 A m^{-2}	2549 A m^{-2}
$Turb.T_{In}$	1173 K	1069 K	1132 K
$Turb.T_{Out}$	923 K	847 K	894 K
$SOFC.T_{MEA,mean}$	1273 K	1273 K	1273 K
$HX.\Delta T_{LM}$	50 K	43 K	47.4 K
$HX.u_{H,max}$	20 m s^{-1}	18.5 m s^{-1}	19.5 m s^{-1}
γ_{SC}	2.0	-	1.70
$Casing.\dot{q}_t$	10000 W	10001 W	10002 W
γ_R	0.8	-	0.97
$IIR.\Delta p_{rel}$	0.01	0.0044	0.0056
$PR.\Delta p_{rel}$	0.01	0.0049	0.0066
$Burn.\Delta p_{rel,Air}$	0.01	0.011	0.01
$Burn.\Delta p_{rel,Fu}$	0.01	0.0051	0.0096
$Ejec.p_{Ai}$	2.4·10^6 Pa	2.07·10^6 Pa	2.82·10^6 Pa
$Ejec.p_{An}$	1.1·10^6 Pa	0.98·10^6 Pa	1.26·10^6 Pa
$Ejec.u_{Im}$	100 m s^{-1}	137 m s^{-1}	130 m s^{-1}
$Ejec.u_{Mo}$	10 m s^{-1}	12.4 m s^{-1}	9.4 m s^{-1}
$Comp.\overline{\pi}$	1	0.95	0.99
$Turb.\overline{\dot{m}}$	1	0.99	1.01
$Turb.\overline{T}_{In}$	1	0.91	0.97
$Turb.\overline{p}_{In}$	1	0.95	0.99

$Turb.\bar{M}_{In}$	1	0.98	1.01
$Turb.\bar{\kappa}_{In}$	1	1.01	1

Hydrogen

The design calculation returns a fuel flow of 2.56 based on the design methane value, or 1.13 mol s^{-1}. Because one mole of methane yields 4 moles of hydrogen, this value corresponds to a SOFC current density of only app. 1900 A m^{-2}. The reason for the changed relationship between SOFC current and temperature lies in the lack of the cooling effect from steam reforming. To reach the original design current density of 3000 A m^{-2} at an acceptable temperature level, a higher air flow or less heat recuperation is required.

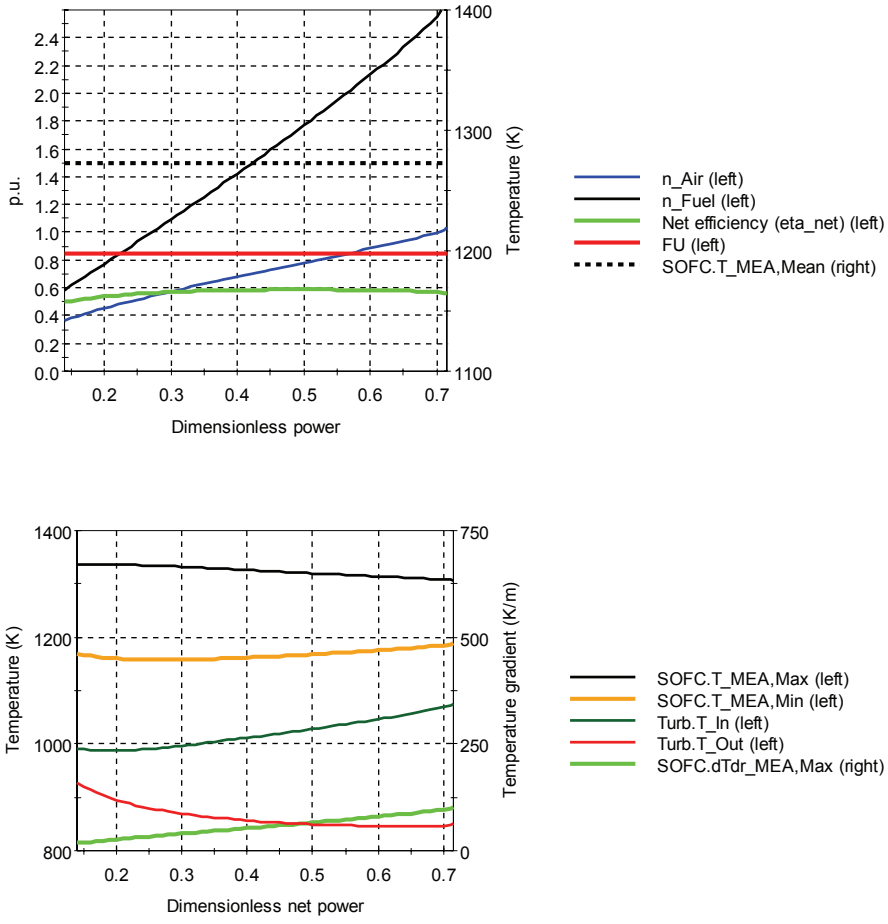

Figure 6-34: Steady-state parameters over power for the hydrogen fuelled system

The reduced current implies a reduction of design net power to 70% of the value reached with methane. The net efficiency is reduced to a value of 56.9%. The reason for the lower efficiency is the higher cooling air demand per power, and therewith the higher heat loss. The same effect has been observed by other researchers [Traverso 2005].

The steady-state operation lines of the hydrogen fuelled system are plotted in Figure 6-34. Comparison with the lines for the methane fuelled system in Figure 6-10 reveals that the strongest difference lies in the maximum radial temperature gradient, which for a certain power output is app. three times higher for the methane system. For both options the maximum radial gradient occurs at the cell bottom where air and fuel meet at either side of the MEA with different temperatures. Due to the absence of the endothermic reforming reaction, the temperature of the entering fuel is higher than if methane was used and the difference to the air is therewith lower. Another fact is that the turbine inlet temperature is lower with hydrogen fuel, both if points at equal power or air flow are compared. This causes the GT to operate on a different operation line which may reduce the efficiency of compressor and turbine.

Measures to Increase Power Output for Hydrogen Fuel

In order to increase the power output of the hydrogen fuelled system without changing the system configuration, the following measures were investigated in steady-state:

- **Change of fuel utilisation**: A lower fuel utilisation increases the voltage and thus decreases the internal heat production in the SOFC for a given current and could hence allow for higher current at constant SOFC temperature. A counter-effect is, however, the increased temperature boost in the burner and therewith enhanced heat recuperation. Simulations have shown that the two effects compensate each other and a different fuel utilisation is hence unable to increase power output significantly.
- **Firing the auxiliary burner**: As the turbine inlet temperature is below its target value, auxiliary firing upstream the turbine could increase the GT power output significantly. An attempt has been made by adding auxiliary fuel flow such that the relationship between turbine inlet temperature and air flow equals the methane fuel case. At design air flow, in order to lift the TIT to 1173 K, app. 15% of the fuel was directly fed to the auxiliary burner, while the total fuel flow was only slightly increased. However, burning fuel is generally increasing heat production and thus the SOFC current must be decreased in order to keep the temperature constant. The simulations show that with this method, the power cannot be increased significantly.
- **Exhaust gas bypassing around the recuperator**: In order to decrease heat recuperation, part of the exhaust gas can be bypassed around the recuperator by

using the bypass which is dedicated to shutdown and startup (see Chapter 6.4). The simulation shows that this method indeed can increase the power output at the design mean SOFC temperature to a value of e.g. 84% of the methane design net power if 70% of the exhaust gas is bypassed. Net efficiency decreases, however, to 48%, caused by the higher exhaust temperature. Also, the turbine inlet temperature decreases even further, which leads to less power contribution of the gas turbine.

- **Exhaust gas bypassing and firing the auxiliary burner**: If 70% of the exhaust gas is bypassed and at the same time the TIT is increased to its original design value of 1173 K with auxiliary firing, a net power output of approximately 94% of the methane design value can be achieved. Net efficiency, however, decreases to 45%.

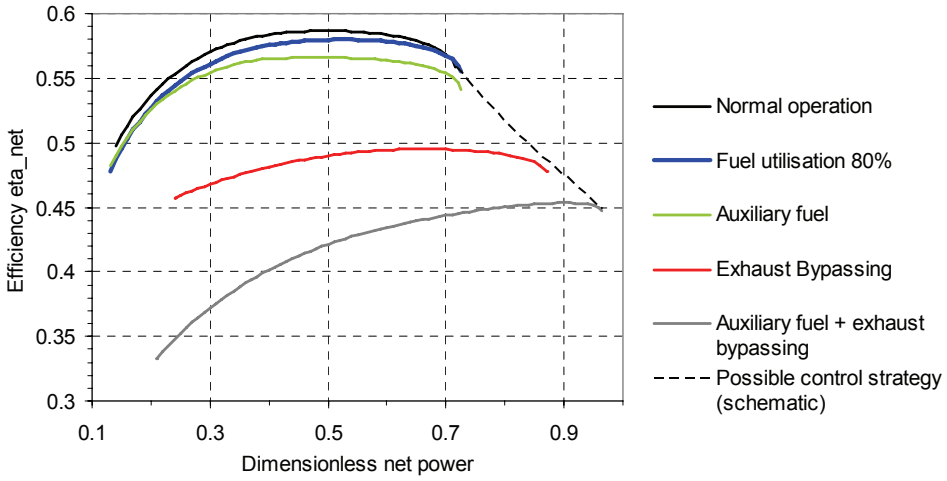

Figure 6-35: Enhancing power output for the hydrogen fuelled system

Figure 6-35 shows the minimum and maximum power and the efficiency curves of the discussed measures.

The last attempt has proven to be able to increase the power output almost to its original, methane-based value, although at the cost of a significantly lower efficiency. A promising control strategy for a system mainly operating at part-load would hence be to operate "normally" with closed bypass and without auxiliary firing up to a power of 70%, and for higher power gradually open the bypass and introduce fuel to the auxiliary burner (see dashed line in Figure 6-35) In order to implement this strategy, the exhaust gas bypass and the auxiliary fuel flow must be integrated into the operational control strategy. Assuming a digital control unit, this does not imply any hardware modifications.

Ethanol

The design calculation for ethanol fuel returns a relative fuel flow of 57% of the methane value, or 0.25 mol s^{-1}. With the higher molar hydrogen yield of ethanol, this value corresponds to a SOFC current density of app. 2550 A m^{-2}. Like for hydrogen, the reason for the changed relationship between SOFC temperature and current lies in the lower specific heat per mole of hydrogen required by the reforming reaction (see Table 6-5). In order to achieve the original current density and temperature, a higher air flow or less heat recuperation is required.

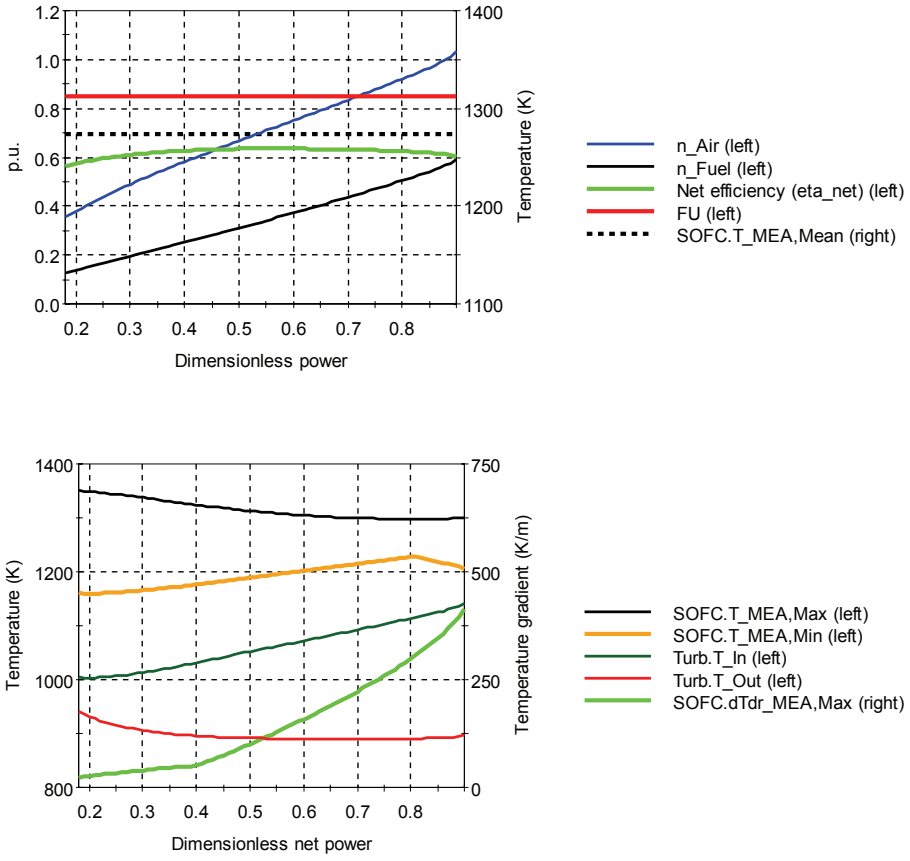

Figure 6-36: Steady-state parameters over power for the ethanol fuelled system

The reduced current implies a reduction of net power to 88% of the value reached with methane fuel, at a net efficiency of 61.2%. In comparison, the methane fuelled system achieves 64.4% net efficiency at 88% net power. The low efficiency decrease despite the higher exhaust flow per power for the ethanol system can be explained with the enhanced heat recuperation through fuel vaporisation. This result is based on the assumption that ethanol vaporisation is accomplished by exhaust gas heat. If an

electric heater was used for this purpose, the net power would reduce to 81% of the methane value and the net efficiency to 56%.

The steady-state operation lines of the ethanol fuelled system are depicted in Figure 6-36 (compare with Figure 6-10 for methane and Figure 6-34 for hydrogen).

It can be interpreted that the ethanol fuel slightly reduces the thermal load to the fuel cell, as the maximum local MEA temperature is lower and the minimum MEA temperature is higher than for the methane case. At 88% power, the maximum radial temperature gradient is furthermore app. 40% lower, which is a consequence of the lower heat consumption of the reforming reaction (see Table 6-5).

6.5.4 Dynamic Performance

Hydrogen

The dynamic performance of the hydrogen fuelled system is investigated by simulating step load changes between the new design power and a low load of 50 kW. Figure 6-37 shows the load increase.

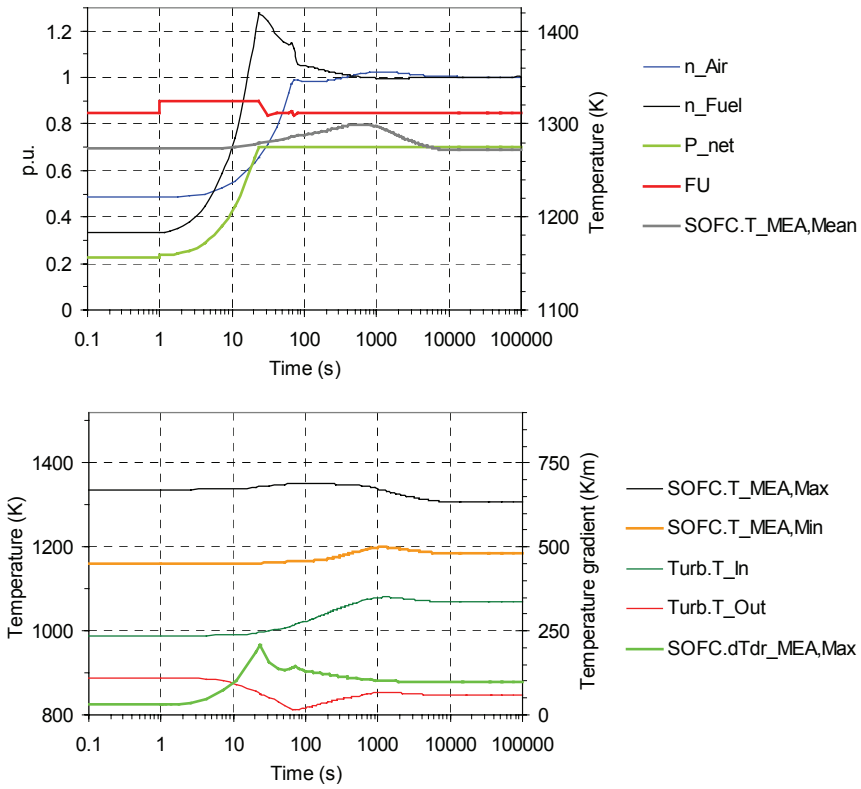

Figure 6-37: Response of the hydrogen fuelled system to large load increase (23% to 70%; fuel flow normalised)

It can be seen that the critical temperature peak which was observed during load increase of the methane fuelled system is mitigated to a lower level. The maximum mean temperature during load increase here is app. 1300 K (compared to 1374 K for methane). This confirms the assumption that the peaks are mainly caused by lack of cooling from the steam reforming due to heat stored in the IIR. On the other hand, it must be mentioned that the absolute load step is smaller than the one performed with the methane system.

Ethanol

The dynamic performance of the ethanol fuelled system is investigated by simulating step load changes between the new design power and a low load of 50 kW. The load increase is shown in Figure 6-38.

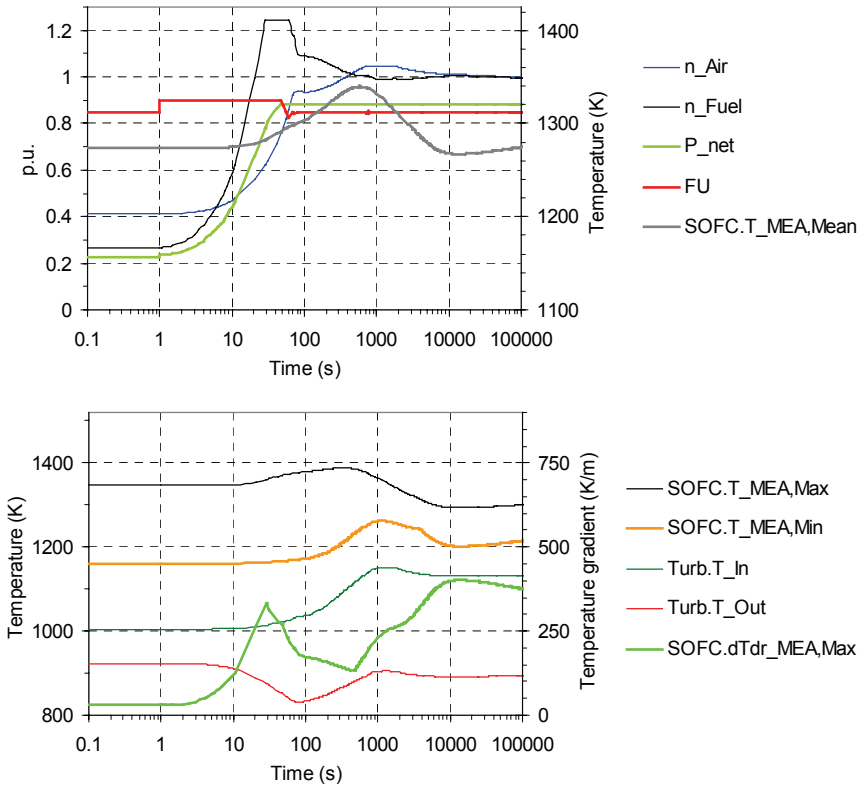

Figure 6-38: Response of the ethanol fuelled system to large load increase (23% to 88%; fuel flow normalised)

It can be seen that the critical temperature peak which was observed during load increase of the methane fuelled system is slightly mitigated to a lower level. The maximum mean temperature during load increase here is app. 1340 K (compared to

1374 K for methane at load increase from 22% to 100%). This can also be explained by the fact that the thermal impact of reforming is lower for ethanol than for methane because of the lower heat required per mole of hydrogen produced.

6.5.5 Conclusions

A system designed for methane fuel can in principle be operated with other suitable fuels without larger modifications.

Hydrogen

Under the given assumptions, a system designed for methane fuel can be operated with hydrogen fuel. A practical problem can be tightness of the fuel system due to the high diffusivity of hydrogen. Respecting legal regulations, additional safety measures might be required for a hydrogen fuelled system. Using the conventional control strategy with adapted characteristics, the net power output will decrease to app. 70% of the methane value due to lack of cooling by steam reforming. Design net efficiency will decrease to a value of app. 55%, caused by the increased relative exhaust heat loss per power output. Using an advanced control strategy which additionally manipulates a bypass of the exhaust gas around the recuperator and firing of a supplementary burner upstream the turbine, net power output can be increased to app. 94% of the original value, although at the cost of an even lower net efficiency of 45%.

Ethanol

To modify a system designed for methane to ethanol fuel, some adaptations in the fuel system are required, such as the installation of a vaporiser. With the conventional control strategy, the net power output will with a recuperatively heated vaporiser decrease to app. 88% of the methane value due to a lower cooling effect of steam reforming. The net efficiency remains with 61% at a high level due to the increased heat recuperation from exhaust gas. If an electric heater is used instead to vaporise the fuel, net power output will be app. 81% and efficiency app. 56%. An uncertainty in this investigation is the suitability of the present reformer material to be exposed to ethanol and its equilibrium product composition without deactivation due to carbon deposition.

7 Other Cycles

The chapter discusses two alternatives to the standard directly integrated SOFC cycle, namely the latter with two-shaft gas turbine and a cycle with indirect integration of the SOFC. Adaptations in system design for achieving comparable operation conditions are discussed. Steady-state part-load performance is investigated and compared to the standard cycle, and the differences in controllability are discussed.

7.1 Introduction

The directly integrated SOFC cycle (DIC) is the simplest and the most common hybrid cycle. The previous chapter has shown that it features efficient part-load operation and it is controllable in a reliable way. However, other cycle options have a potential to further facilitate safe operation and control. Common cycle alternatives are the DIC with two-shaft gas turbine (DIC-2T, see Figure 5-2) and the indirectly integrated SOFC cycle (IIC, see Figure 5-3). The former cycle has two independent shafts, where the first connects the first turbine and the compressor and is uncontrolled. The second shaft connects the *power turbine* to the generator and is controlled to rotate at constant speed. The fixed speed simplifies power conversion and therewith the primary control of the system. On the other hand, the air flow can no longer be controlled unless other control handles are introduced. This configuration has been investigated by other authors [Chan 2002, 2003a,b; Rao 2002]. In the IIC, the SOFC is situated downstream the turbine and hence operating on ambient pressure level, while the gas between compressor and turbine is heated indirectly by the SOFC exhaust gas. This increases the safety of the SOFC system in terms of pressure transients. Further, it reduces the pressurised volume and therewith simplifies safe GT operation. On the other hand, it reduces the electrochemical performance and moreover a more complex heat exchanger is required. This cycle option has been previously studied by Veyo et al. [2003].

7.2 System Design

The design cases for the alternative cycles should be as similar as possible to the standard cycle to facilitate a comparison. Hence, most of the design objectives will be equal. The following section discusses particularities of the cycles that must be respected when choosing the design cases and compares the resulting design parameters.

7.2.1 DIC-2T

Compared to the standard cycle, this cycle has a second turbine which must be designed. Thermodynamically, the systems do not differ strongly from each other in the design point, hence the operation parameters shown in Figure 7-1 are mostly equal to the ones in Figure 6-1. The only theoretical difference is the two-step expansion in

the two-shaft gas turbine. Even though isentropic efficiencies of both turbines are equal, the total end point of the expansion may differ from the single-turbine configuration (difference between isentropic and polytropic efficiency). As this difference is small, no adaptations in design objectives are required.

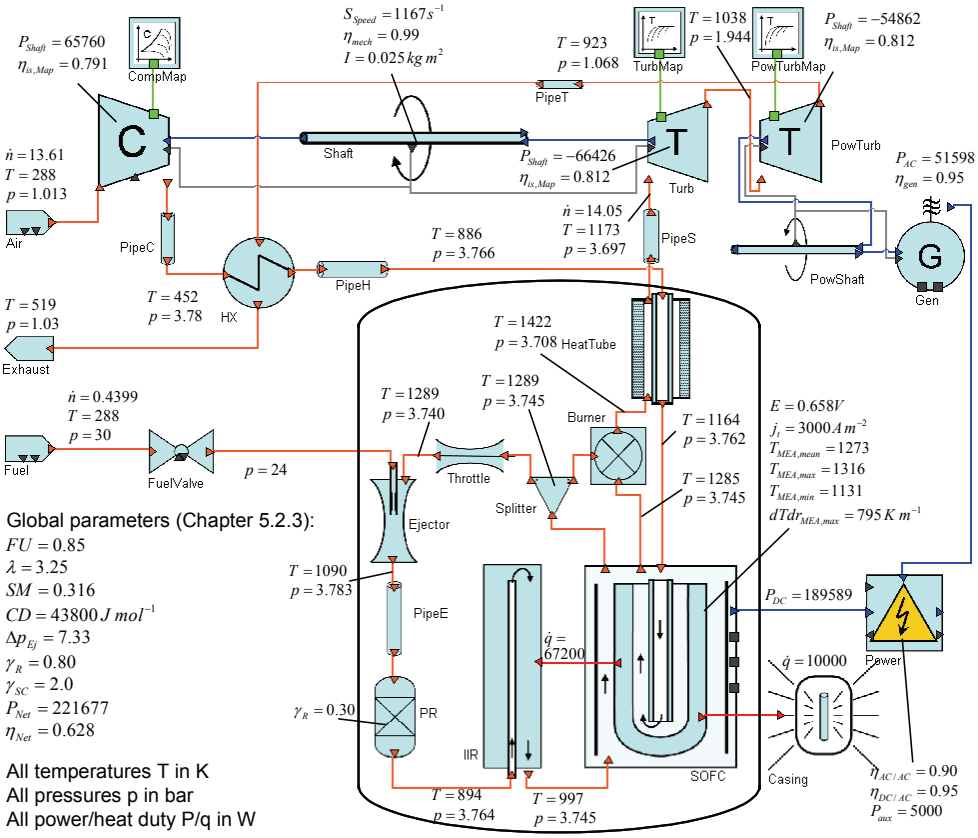

Figure 7-1: Main operation parameters of the DIC-2T process at design point

7.2.2 IIC

In the indirectly integrated cycle, the SOFC system exhaust gas is not fed directly into the turbine but heats up the turbine inlet gases through the recuperator. As a certain temperature difference is required for heat transfer, the turbine inlet temperature in the IIC will be lower than the SOFC system exhaust temperature. The SOFC system inlet temperature will on the other hand equal the turbine outlet temperature in the IIC, while it is lower in the DIC. However, in order to compare the DIC and the IIC performance, the thermal state of the SOFC system should be similar, and thus also their inlet and outlet temperatures. This means that the design objectives for turbine inlet and outlet temperature should be adapted. It is chosen to decrease these temperatures by the value of the mean logarithmic temperature difference in the

recuperative heat exchanger (i.e. 50 K). This does also lead to a lower maximum temperature in the latter and therewith mitigate the problems with overheating. However, the maximum temperature in the heat exchanger is still 200 K higher than for the DIC.

The other design objectives remain unchanged. Note that due to the higher volumetric flow, especially the components where a design pressure drop is chosen (i.e. IIR, pre-reformer, burner) must be redesigned in terms of flow coefficients. Assuming the same flow coefficients than in the DIC (pressurised) case, the ejector would not manage to recycle sufficient anode exhaust gas. This might also be the consequence of an overestimation of pressure losses for the pressurised case. The SOFC tube and the preheating tube are, however, not affected; their design is fixed and the pressure drops are calculated based on flow paths. Furthermore, the pipe radii downstream the SOFC system *PipeS* and the ejector *PipeE* (see Chapter 5.4.1) must be enlarged to 0.17 m resp. 0.09 m in order to maintain the assumed flow velocities inside. This has no influence on steady state behaviour.

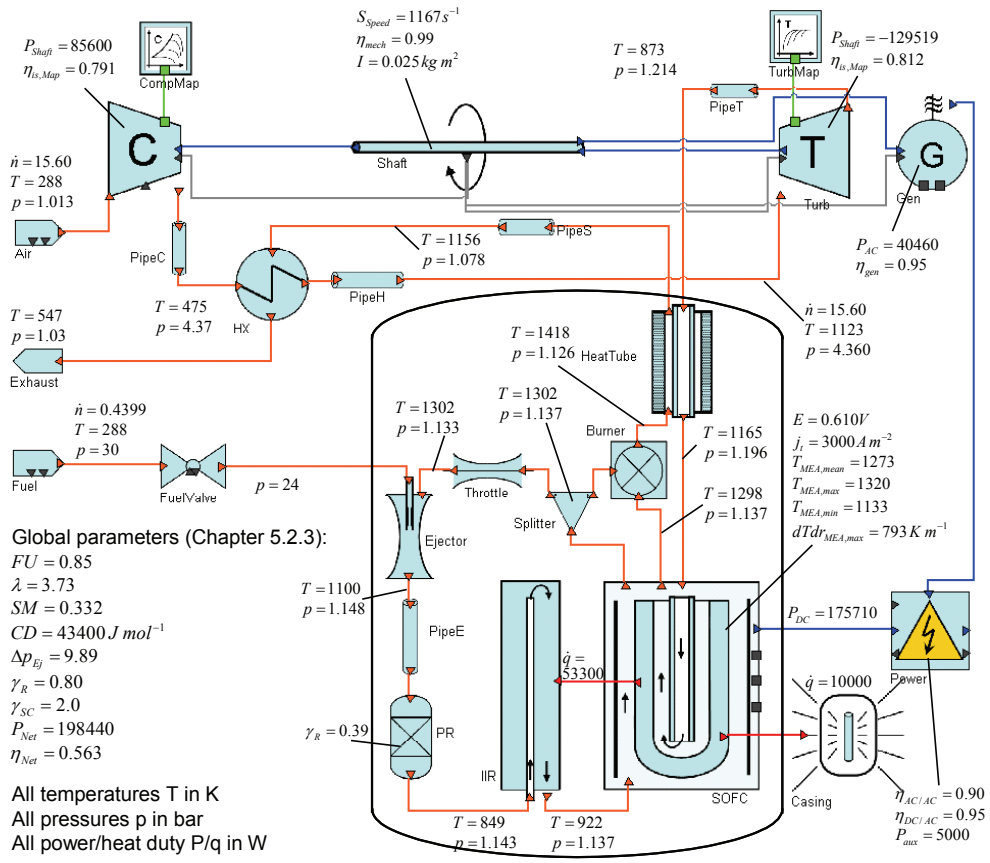

Figure 7-2: Main operation parameters of the IIC process at design point

The new process parameters at design point are depicted in Figure 7-2. Compared with the DIC (see Figure 6-1), it can be seen that the cell operating voltage is significantly lower, which is a consequence of the reduced partial pressure of the reactants. As this leads to higher heat production, more air flow and hence larger turbomachinery is required to achieve an equal mean MEA temperature. Furthermore the transferred heat in the recuperative heat exchanger, and therewith the component's exergy loss, is increased by app. 50%. Due to the improved exhaust heat loss, both net power output and efficiency decrease with app. 10%.

Not only does the IIC process require a larger recuperative heat exchanger, but the increased maximum temperature in the latter is also problematic. A temperature of 1156 K is far beyond the acceptable range of any steel recuperator, hence ceramic materials must be used at least for the high temperature side.

7.2.3 Design Cases

Table 7-1 highlights the design parameters of the two alternative cycles. The standard cycle is given as a reference for comparison. Values which are identical in all cases are not shown.

Table 7-1: Design parameters of the cycles

Design Parameter	DIC-2T	IIC	(DIC)
$P_{net,0}$	221677 W	198440 W	221032 W
$PHT.l_T$	0.4788	0.5855	0.4776 m
$Turb.\pi_{0,Map}$	1.902	3.598	3.5433
$\dot{n}_{Air,0}$	13.61 mol s^{-1}	15.60 mol s^{-1}	13.60 mol s^{-1}
$HX.l$	1.864 m	2.278 m	1.849 m
$HX.A$	0.1139 m^2	0.1613 m^2	0.1139 m^2
$Thro.c$	150099	33091	149669
$SOFC.\ \tau_{Ref}$	0.0005742	0.0004072	0.0005780
$IIR.c$	466742	42420	486812
$PR.c$	513656	48434	535362
$Burn.c_{Air}$	27658	1892	28881.7
$Burn.c_{Fu}$	$3.20481 \cdot 10^6$	292723	$3.3419 \cdot 10^6$
$Ejec.A_m$	0.0005199 m^2	0.001734 m^2	0.0005089 m^2
$Ejec.A_o$	0.006599 m^2	0.021993 m^2	0.006460 m^2

$Comp.\pi_{0,Map}$	3.726	4.314	3.803
$Turb.\dot{m}_0$	0.399 kg s^{-1}	0.450 kg s^{-1}	0.399 kg s^{-1}
$Turb.T_{In,0}$	1173 K	1123 K	1173 K
$Turb.p_{In,0}$	3.697 bar	4.360 bar	3.775 bar
$Turb.M_{In,0}$	28.45 g mol^{-1}	28.85 g mol^{-1}	28.45 g mol^{-1}
$Turb.\kappa_{In,0}$	1.308	1.324	1.308
$PowTurb.\pi_{0,Map}$	1.820	-	-
$PowTurb.T_{In,0}$	1037 K	-	-
$PowTurb.p_{In,0}$	1.943 bar	-	-
$PowTurb.M_{In,0}$	28.45 g mol^{-1}	-	-
$PowTurb.\kappa_{In,0}$	1.318	-	-

7.3 Steady-State Part-Load Operation

7.3.1 DIC-2T

While for the standard DIC process, the shaft speed can be varied to control the air flow, the intention of the two-shaft gas turbine system is to maintain a constant speed of the power shaft in order to simplify the electric conversion. The first shaft rotates freely and the speed can thus not directly be controlled. A new handle for air flow manipulation is hence required if the SOFC temperature is to be controlled. Candidates therefore are a controllable air blow-off, compressor variable inlet guide vanes (VIGV), and a bypass of air around the SOFC system. The first two alternatives are thermodynamically very similar; the main difference is that for an air blow-off, the mass flow through the compressor will not remain at a higher level in part-load and hence the efficiency will decrease significantly. The third alternative provokes a change of the relationship between SOFC and turbine inlet temperature, depending on the air bypass ratio. For simplicity it is chosen to apply the VIGV ability of the compressor model and control the air flow with this option.

An important issue for the power turbine rotating at constant speed with very different air flow rates is the operation point on the map. The operation will be approximately along a line of constant reduced dimensionless speed. For a high value of the latter, the turbine will hence "fall off" the map for an only slightly reduced air flow. Figure 7-3 points up that a lower shaft speed is advantageous in achieving low reduced mass flow. Therefore, the turbine is rescaled and the new design point is chosen on the line of 60% reduced speed and in a way that the efficiency is equal to

the old design point. This implies that larger turbines are required which can only be operated at part-load.

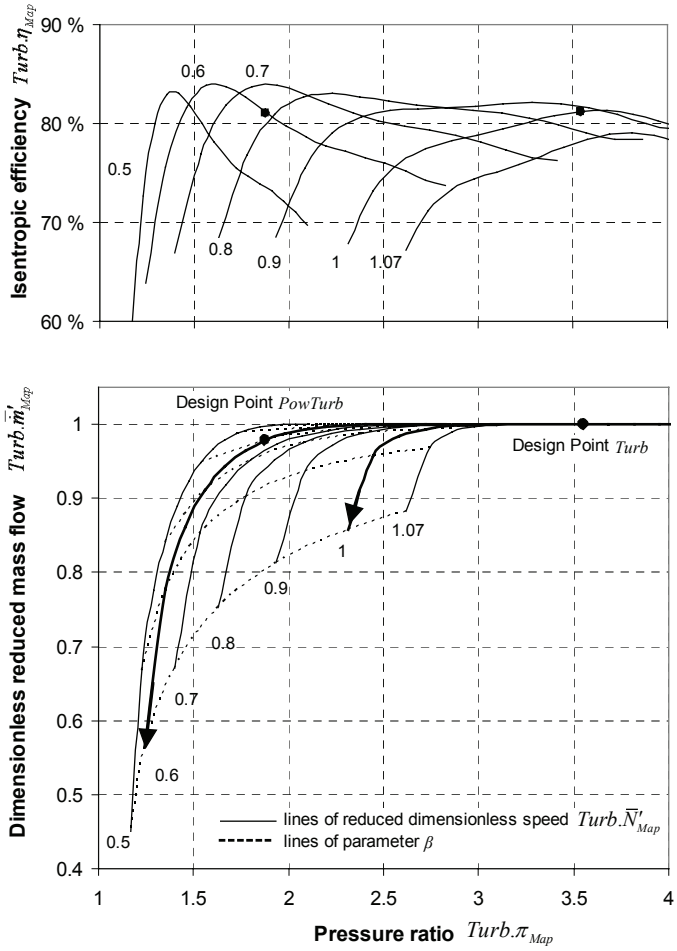

Figure 7-3: Choice of design point for the power turbine

The steady-state simulation of the operation line for constant mean MEA temperature reveals that a minimum part-load of 32% is possible. The system and thermal parameters in part-load are very similar to the DIC (see Figure 6-10). However, it is interesting to investigate the state of the gas turbine. Figure 7-4 reveals that the equilibrium speed of the free shaft decreases to 60% at low part load. The maximum closure of the VIGV is 20%, and the VIGV must be fully open again at low part load to maintain the constant mean SOFC temperature. This might add complexity to a control strategy. The β parameters of the compressor and free turbine are in safe ranges, while the power turbine β parameter approaches zero for low part load (lowest dotted line in Figure 7-3).

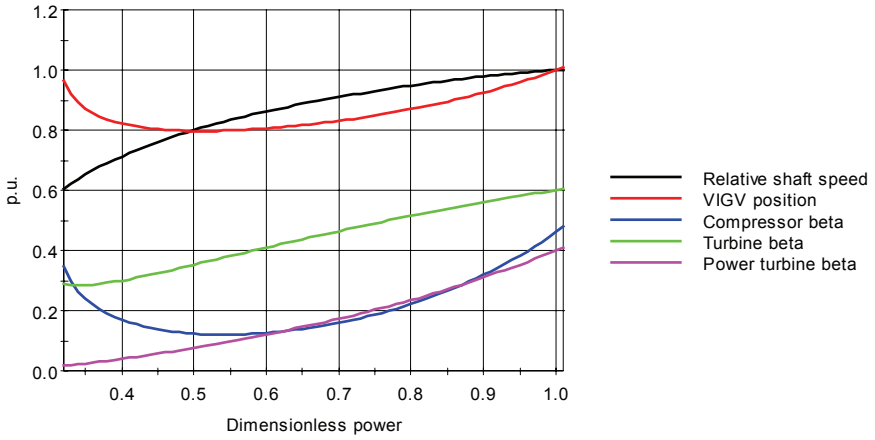

Figure 7-4: GT parameters for the DIC-2T process

7.3.2 IIC

For the indirectly integrated cycle, the air flow can be controlled as usual with the shaft speed. The system and thermal parameters along an operation line of constant mean MEA temperature are depicted in Figure 7-5. Comparing with Figure 6-10, it can be seen that the part-load performance is similar to the DIC system. The net efficiency has a maximum of app. 62% at intermediate part load (DIC: 65.8%). This difference is lower than the design point efficiency difference of 6.1% points between DIC and IIC because the temperature difference between hot and cold medium in the recuperator and therewith the exergy loss decreases in part load. The thermal load of the IIC and DIC configurations are similar.

7.4 Control System Considerations

7.4.1 DIC-2T

The control layout that has been introduced and tested for the DIC configuration (see Figure 6-12) can basically be transferred to the DIC-2T configuration. The air flow loop, however, must be modified to manipulate the VIGV position instead of the generator power. The latter must be manipulated to maintain a constant speed of the power shaft. High inertia of the power shaft may help to stabilise the speed during load changes and apply an energy buffer for quick load following.

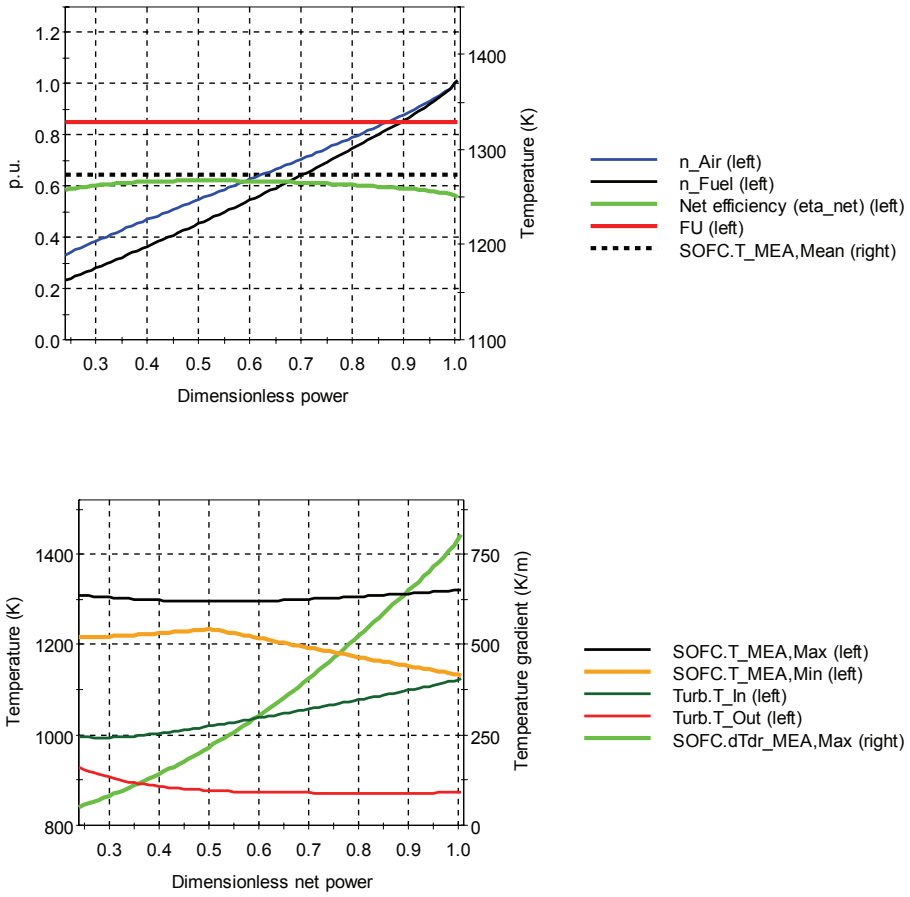

Figure 7-5: System and thermal parameters for the IIC

Supposed a reliable control of the air flow can be provided, the resulting control system is expected to be robust, because there is no direct interaction between the air flow controller output and the power controller input as this is the case for the DIC (see Figure 6-12). Therewith the temperature/air flow loops are practically uncoupled from the power/FU loops.

7.4.2 IIC

The IIC can basically be controlled with the same layout as the DIC configuration. A simplification is that the ejector pressure difference will not be a constraint to the FU control here, as the pressure level in the SOFC system is almost constant at ambient level (the constraint applies in the DIC when the fuel flow is decreased faster than the system pressure; see Figure 6-22). Furthermore, the atmospheric SOFC is not exposed

to pressure transients and the pressurised volume between the compressor and turbine is significantly smaller than for the DIC. Therewith, the gas turbine respectively air flow can be controlled faster without risk of SOFC destruction and surge. The indirectly integrated SOFC cycle can hence be expected to respond quickly to large load changes.

7.5 Conclusions

Two alternative hybrid cycles, namely a directly integrated one with two-shaft gas turbine and an indirectly integrated one, were investigated with respect to design point and steady-state part-load. Particularities for suitable control systems were derived.

The directly integrated cycle with two turbines (DIC-2T) is thermodynamically very similar to the single turbine cycle. The steady-state part-load behaviour does not vary significantly from the standard DIC. However, the two-shaft gas turbine system cannot produce as low part-load as the DIC while maintaining constant mean SOFC temperature, and furthermore the efficiency at low part-load is lower. This is due to the less favourable operation lines on the compressor and turbine map which confine the minimum air flow and furthermore decrease turbomachinery efficiency. A control strategy must have an extra handle such as variable compressor inlet guide vanes to control the air flow. Advantages of a two-shaft gas turbine system are the easier generator and power electronics due to the constant speed as well as the expected higher stability of the control system. A main disadvantage is the higher turbomachinery complexity.

The indirectly integrated cycle (IIC) has, compared to the DIC, a different relationship between turbine and SOFC temperatures. Lower turbine inlet and outlet temperatures are hence required to achieve comparable conditions in the SOFC system. Design calculations revealed that the pressure loss coefficients must be reduced in order to achieve sufficient recirculation. Net electric efficiency and design power output are significantly lower due to higher recuperator exergy losses and lower voltage of the unpressurised SOFC. The DIC control strategy can be directly transferred to the IIC system. An advantage of this option is the enhanced system safety due to the ambient pressure SOFC and the smaller pressurised volume which may allow for quick large load changes. Disadvantages are, however, the lower efficiency and power output as well as higher investment costs for the recuperator.

Altogether, the standard DIC seems to be the most advantageous cycle, as it combines satisfying performance (high efficiency; low part-load ability) with a simple system configuration (no ceramic recuperator, only one turbine). The controllability of this cycle has been demonstrated. Its weak points should rather be mitigated by auxiliary equipment than by choosing an alternative cycle option.

8 Conclusions and Further Work

8.1 Conclusions

This thesis investigates design, operation and control of solid oxide fuel cell (SOFC) and gas turbine (GT) hybrid systems on the basis of modelling.

A complex set of component models has been developed and used for the evaluations. Most relevant are tubular SOFC, indirect internal reformer and heat exchangers, and spatially discretised models are used therefore. For the turbomachinery, map-based steady-state behaviour is modelled. Gas residence times and pressure drops are accounted for in all relevant components.

Safety critical issues that must be prevented or minimised during operation are cell cracking, compressor surge, carbon deposition, anode oxidation, overheating, thermal fatigue and ejector malfunction.

The simplest hybrid cycle option with a pressurised, directly integrated SOFC is chosen for the main investigation. The system is based on the Siemens-Westinghouse SOFC and hybrid cycle concept and shall deliver an electric power output of app. 220 kW. Variation of the GT shaft speed provides control of the air flow.

To ensure safe operation during transient operation, a complex control design is applied which controls power output, fuel utilisation and fuel cell temperature, beside several constraints. The mentioned variables are controlled with the SOFC electric power, fuel flow and air flow respectively. Air flow variation is achieved through GT shaft speed. The generator power is manipulated to vary and stabilise the latter.

Steady-State Part-Load

Assuming constant fuel utilisation, the main degrees of freedom for operating the system are fuel and air flow. A "window" where steady-state operation is safe can be plotted and is confined by overheating, compressor and turbine map bounds, ejector malfunction and low voltage. Within the operation window, a part-load strategy where the mean MEA temperature is constant at 1273 K throughout the whole load range seems most promising in terms of safety, lifetime and performance. The ability for low part-load mainly depends on the ability of the GT system to reduce the air flow. With the current system, a minimum part-load of 21% can be achieved at app. 35% of the design air flow. The LHV-based net electric efficiency is between 59.6 and 65.8% throughout the whole load range.

Transient Operation

As an overall conclusion, it has been proven on a model basis that efficient and safe control of a SOFC/GT hybrid system in dynamic operation and load following is principally possible. Small step load changes (4.5%) can be followed quickly (<4 s),

while large load changes (78%) take longer (57-73 s). The deficit/excess between demand and supply of electrical work is 7-11 kWs for small load changes and app. 3200 kWs for large load changes. If required, these gaps can be filled with an additional power source/sink.

Transient deviations in SOFC temperature are high if large and quick load changes must be performed. This is mainly due to thermal capacities in the indirect internal reformer and cannot be mitigated satisfactorily by modifying the air flow. Smooth load profiles are therefore preferable for a long system lifetime and furthermore to prevent overheating. During load decrease, there is risk for carbon deposition due to a transient minimum of the steam-to-carbon ratio, and the compressor surge margin has a transient minimum due to the large pressurised volume between compressor and turbine.

The transient deviations in temperature are to some extent mitigated for load profiles with frequently changing load. Temporary peaking above the nominal power is connected to a sharp increase in the maximum radial temperature gradient in the MEA and may result in SOFC degradation.

For conditions deviating from the reference, especially such that lead to decreased air supply by the GT (decreased air density, compressor degradation) or increased heat production (SOFC degradation), the SOFC temperature may increase at high load. As a consequence, the GT should be capable of supplying significantly more air than the design value, or other measures to control the temperature, such as recuperator bypassing, should be implemented. An error in the fuel measurement or fuel supply quality leads to high temperature deviations. Such errors must hence be avoided through assured fuel quality and safe (redundant) measurements.

Shutdown and Startup

Shutdown and startup procedures are developed based on the possibility to use the GT system for ventilation. Air flow and SOFC system inlet temperature are controlled by using auxiliary firing upstream the turbine, turbine exhaust gas throttling and a variable bypass around the recuperative heat exchanger. The startup strategy utilises a relatively small amount of hydrogen for the ignition phase of the SOFC instead of supplying externally generated steam for the reforming reactions. A high nitrogen demand has been detected. However, it is uncertain how much nitrogen flow is required to safely protect the anode from oxygen exposure. Supposing the SOFC tolerates the thermal states it is exposed to during the processes, the shutdown takes app. 2 hours until the system can be switched off. Startup takes app. 4.5 hours until the system can be operated in load-following mode. Full load can, however, not be achieved at this time. A more flexible control could allow the system to follow a low load immediately after startup initiation. Due to the long time required and since thermal cycling reduces the SOFC lifetime, it may be concluded that such a system is not suited for frequent startup and shutdown.

Fuel Flexibility

A system designed for methane fuel can in principle be operated with other suitable fuels such as hydrogen or ethanol without larger modifications.

A practical problem for operation with hydrogen can be tightness of the fuel system due to the high diffusivity of the gas. Respecting legal regulations, more safety measures might be required for a hydrogen fuelled system. Using the conventional control strategy with adapted characteristics, the net power output will decrease to app. 70% of the methane value due to lack of cooling by steam reforming. Design net efficiency will decrease to a value of app. 55%, caused by the increased relative exhaust heat loss per power output. Using an advanced control strategy which additionally manipulates a bypass of the exhaust gas around the recuperator and firing of a supplementary burner upstream the turbine, net power output with hydrogen can be increased to app. 94% of the original value, although at the cost of an even lower net efficiency of 45%.

For modifying a system designed for methane to ethanol fuel, some adaptations in the fuel system are required, such as the installation of a vaporiser. With the conventional control strategy, the net power output will with a recuperatively heated vaporiser decrease to app. 88% of the methane value due to a lower cooling effect of steam reforming. The net efficiency remains with 61% at a high level due to the increased heat recuperation from exhaust gas. If an electric heater is used instead to vaporise the fuel, net power output will be app. 81% and efficiency app. 56%. An uncertainty in this investigation is the suitability of the present reformer material to be exposed to ethanol and its equilibrium product composition without deactivation due to carbon deposition.

Cycle Options

Two alternative hybrid cycles, namely a directly integrated one with two-shaft gas turbine and an indirectly integrated one, were investigated with respect to design point and steady-state part-load. Particularities for suitable control systems were derived.

The directly integrated cycle with two turbines (DIC-2T) is thermodynamically very similar to the single turbine cycle. The steady-state part-load behaviour does not vary significantly from the standard DIC. However, the two-shaft gas turbine system cannot produce as low part-load as the DIC while maintaining constant mean SOFC temperature, and furthermore the efficiency at low part-load is lower. This is due to the less favourable operation lines on the compressor and turbine map which confine the minimum air flow and furthermore decrease turbomachinery efficiency. A control strategy must have an extra handle such as variable compressor inlet guide vanes to control the air flow. Advantages of a two-shaft gas turbine system are the easier generator and power electronics due to the constant speed as well as the expected higher stability of the control system. A main disadvantage is the higher turbomachinery complexity.

The indirectly integrated cycle (IIC) has, compared to the DIC, a different relationship between turbine and SOFC temperatures. Lower turbine inlet and outlet temperatures are hence required to achieve comparable conditions in the SOFC system. Design calculations revealed that the pressure loss coefficients must be reduced in order to achieve sufficient recirculation. Net electric efficiency and design power output are significantly lower due to higher recuperator exergy losses and lower voltage of the unpressurised SOFC. The DIC control strategy can be directly transferred to the IIC system. An advantage of this option is the enhanced system safety due to the ambient pressure SOFC and the smaller pressurised volume which may allow for quick large load changes. Disadvantages are, however, the lower efficiency and power output as well as higher investment costs for the recuperator.

Altogether, the standard DIC seems to be the most advantageous cycle, as it combines satisfying performance (high efficiency; low part-load ability) with a simple system configuration (no ceramic recuperator, only one turbine). The controllability of this cycle has been demonstrated. Its weak points should rather be mitigated by auxiliary equipment than by choosing an alternative cycle option.

8.2 Recommendations for Further Work

The presented hybrid system model comprises a high level of detail and comprehensiveness, concerning spatial distribution of the components, flexibility of posing problems and the ability for control modelling. Further refinement which could be worthwhile is the modelling of a bundle of individual SOFC tubes and the heat transfer between them. This would enhance the understanding of stacking effects and lead to a more exact estimation of the temperature range appearing in the stack.

The components of the model toolbox can be used to set up and study other power cycles, be it steady state or dynamic analyses. The extension of the toolbox through further models based on the same platform, for example for steam cycle equipment or membrane burners, will allow studying advanced power cycles including combined cycles and CO_2 management.

For the studied hybrid cycles, it is the author's overall attitude that further going into detailed modelling without experimental validation is not target-oriented in terms of hybrid cycle evolution. It has been shown that for the current models, solutions to all operational challenges are available. Due to lacking possibility of model validation, it is uncertain to what extent these results can be transferred to a real system. The obligatory next step must thus be the experimental validation and calibration of the components and hybrid cycle models. Once a reliable matching between model prediction and experimental result is achieved, steps must be taken to implement the theoretical control strategies to the real system. There, despite positive modelling results, high caution is required when it comes to omitting critical incidents such as compressor surge, as these can instantaneously damage the system and cause high financial loss.

References

[Abis 2005] Web site of Abis GmbH, http://www.abis-gmbh.com/keramikfaserplatten.html (visited June 2005).

[Achenbach 1994] Achenbach, E., Riensche, E., "Methane/steam reforming kinetics for solid oxide fuel cells", Journal of Power Sources 52 (1994) 283-288.

[Achenbach 1995] Achenbach, E., "Response of a solid oxide fuel cell to load change", Journal of Power Sources 57 (1995) 105-109.

[Agnew 2003] Agnew, G., Moritz, R., Berns, C., Spangler, A., Tarnowski, O., Bozzolo, M., "A unique solution to low cost SOFC hybrid power plant", ASME Turbo Expo 2003.

[Aguiar 2005a] Aguiar, P., Adjiman, C.S., Brandon, N.P., "Anode-supported intermediate temperature direct internal reforming solid oxide fuel cell. I: model-based steady-state performance", Journal of Power Sources 138(2004), 120-136.

[Aguiar 2005b] Aguiar, P., Adjiman, C.S., Brandon, N.P., "Anode-supported intermediate-temperature direct internal reforming solid oxide fuel cell: II. Model-based dynamic performance and control", Journal of Power Sources 2005, in press.

[Anderson 2003] Anderson, H.U., Tietz, F., "Chapter 7: Interconnects", in Singhal, S.C., Kendall, K., "High Temperature Solid Oxide Fuel Cells: Fundamentals, Design and Applications" (pp. 173-195, Elsevier, Oxford, UK, 2003.

[Aspo 2005] Web site of ASPO (Association for the study of peak oil and gas), www.peakoil.net (visited June 2005).

[Assambumrungrat 2005] Assabumrungrat, S., Pavarajarn, V., Charojrochkul, S., Laosiripojana, N., "Thermodynamic analysis for a solid oxide fuel cell with direct internal reforming fueled by ethanol", Chemical Engineering Science 59 (2004) 6015 – 6020

[Autissier 2004] Autissier, N., Larrain, D., Van Herle, J., Favrat, D., "CFD simulation tool for solid oxide fuel cells", Journal of Power Sources 131 (2004), 313-319.

[Bakke 2004] Personal communication with Knut Bakke, Shell Technology Norway, March 2004.

[Bellona 2002] Kruse, B., Grinna, S., Buch, C., "Hydrogen – Status and possibilities", Bellona Report 6:02, Bellona Foundation, Norway, 2002.

[Bharadwaj 2005a] Bharadwaj, A., Archer, D.H., Rubin, E.S., "Modeling the performance of a flattened tubular solid oxide fuel cell", ASME Journal of Fuel Cell Science and Technology, 2 (2005), 52-59.

[Bharadwaj 2005b] Bharadwaj, A., Archer, D.H., Rubin, E.S., "Modeling the performance of a tubular solid oxide fuel cell", ASME Journal of Fuel Cell Science and Technology, 2 (2005), 38-44.

[Bistolfi 1996] Bistolfi, M., Malandrino, A. and Mancini, N., 1996, "The use of different modeling approaches and tools to support research activities: an industrial example", Computers and Chem. Engng, 20, Suppl., S1487-S1491.

[Bossel 1992] Bossel, U., "Final report on SOFC Data Facts & Figures", Bern, April 1992.

[Bronkhorst 2005] Internet page of Bronkhorst Hightech B.V., http://www.bronkhorst.com/elflowcontrollers.htm (visited 20th May 2005)

[Campanari 2000] Campanari, S., "Full Load and Part-Load Performance Prediction for Integrated SOFC and Microturbine Systems", Journal of Engineering for Gas Turbines and Power, 122 (2000), 239-246.

[Campanari 2001] Camparani, S., "Thermodynamic model and parametric analysis of a tubular SOFC module", Journal of Power Sources 92 (2001), 26-34.

[Campanari 2004] Campanari S., Iora, P., "Definition and sensitivity analysis of a finite volume SOFC model for a tubular cell geometry", Journal of Power Sources 132 (2004), 113-126.

[Campbell 2002] Campbell, C.J., Liesenborghs, F., Schindler, J., Zittel, W., "Ölwechsel! Das Ende des Erdölzeitalters und die Weichenstellung für die Zukunft", Global Challenges Network, dtv, Munich, 2002.

[CFCL 2005] Web site of Ceramic Fuel Cells Limited, http://www.cfcl.com.au/ (visited June 2005).

[Chan 2002] Chan, S.H., Ho, H.K, Tian, Y., "Modelling of simple hybrid SOFC and Gas Turbine Power Plant", Journal of Power Sources 109 (2002), 111-120.

[Chan 2003a] Chan, S.H., Ho, H.K, Tian, Y., "Modelling for Part-load Operation of SOFC-Gas Turbine Hybrid Power Plant", Journal of Power Sources 114 (2003), 213-227.

[Chan 2003b] Chan, S.H., Ho, H.K, Tian, Y., "Multi-level modeling of SOFC–gas turbine hybrid system", International Journal of Hydrogen Energy 28 (2003) 889 – 900.

[Christiansen 2004] Christiansen, N., Kristensen, S., Holm-Larsen, H., Larsen, P.H., Mogensen, M., Hendriksen, P.V., Linderoth, S., "Status and Recent Advances in SOFC Development at Haldor Topsøe/Risø", Proceedings of the 6th European Solid Oxide Fuel Cell Forum, Lucerne, Switzerland, 2004.

[Costamagna 1998] Costamagna, P., Honegger, K., "Modelling of Solid Oxide Heat Exchanger Integrated Stacks and Simulation at High Fuel Utilisation", Journal of Electrochemical Society 145 11 (1998), 3995-4007.

[Costamagna 2004] Costamagna, P., Selimovic,A., Del Borghi, M., Agnew, G., "Electrochemical model of the integrated planar solid oxide fuel cell (IP-SOFC)", Chemical Engineering Journal 102 (2004), 61-69.

[Deffeyes 2005] Deffeyes, K.C., "Beyond oil: the view from Hubbert's peak", Hill and Wang, 2005.

[Energiekrise 2005] Web site about oil depletion, www.energiekrise.de (visited June 2005).

[EP 2005] European Parliament, Press release: "Ambitious targets for greater energy efficiency", 07 June 2005.

[Epcos 2005] Online product catalogue of Epcos AG, Munich, Germany, at website www.epcos.com (visited October 2005).

[Ferrari 2004] Ferrari, M.L., Traverso, A., Massardo, A.F., "Transient Analysis of SOFC Hybrids – Part B: Anode Recirculation Model", ASME Turbo Expo 2004

[Fierro 2005] Fierro, V., Akdim, O., Provendier, H., Mirodatos, C., "Ethanol oxidative steam reforming over Ni-based catalysts", Journal of Power Sources 145 (2005) 659–666

[Fontell 2004] Fontell, E., Kivisaari, T., Christiansen, N., Hansen, J.B., Pålsson, J., "Conceptual study of a 250 kW planar SOFC system for CHP application", JPS 131 (2004) 49-56.

[FÖS 2003] Förderverein Ökologische Steuerreform e.V., Ökosteuer-News 16, Munich, 2003.

[Fosse 2003] Fosse, I., "Heat exchangers and ejectors for the SOFC-GT system", Summer job report, EPT/NTNU, Trondheim, 2003-09-18.

[Galvita 2002] Galvita, V.V., Belyaev, V.D., Frumin, A.V., Demin, A.K., Tsiakaras, P.E., Sobyanin, V.A., "Performance of a SOFC fed by ethanol reforming products", Solid State Ionics 152– 153 (2002) 551– 554

[Godø 2003] Godø, H., Nerdrum, L.,, Rapmund, A., Nygaard, S., "Innovations in fuel cells and related hydrogen technology in Norway – OECD Case Study in the Energy Sector", NIFU skriftserie no. 35/2003

[gPROMS 2004] Documentation of gPROMS, release 2.3 - June 2004, available on request at Process Systems Enterprise Limited

[Gravdahl 1998] Gravdal, J.T., "Modeling and Control of Surge and Rotating Stall in Compressors", Doctoral Thesis, Department of Engineering Cybernetics, NTNU, 1998.

[Hall 1999] Hall, D., "Transient Modelling and Simulation of a Tubular Solid Oxide Fuel Cell", IEEE Transactions on Energy Conversion, Vol. 14, No. 3, 1999.

[Halseid 2004] Halseid, R., "Ammonia as Hydrogen Carrier - Effects of Ammonia on Polymer Electrolyte Membrane Fuel Cells", NTNU, Doctoral Thesis, Trondheim, April 2004.

[Hermann, 2002] Hermann, F., Pålsson, J., Mauss, F., "Combustor esign Analysis for SOFC Off-gases", Proceedings of the 5th European Solid Oxide Fuel Cell Forum, Lucerne, Switzerland, 2002.

[Hildebrandt 2004] Hildebrandt, A., "Limitations of Turbomachinery in Gas Turbine Hybrid Systems Comprising Membrane and SOFC Technology", Licenciate Thesis, Lund Institute of Technology, Sweden, 2004.

[Hildebrandt 2005] Hildebrandt, A., Assadi, M., "Sensitivity Analysis of Transient Compressor Operation Behaviour in SOFC-GT Hybrid Systems", ASME Turbo Expo 2005

[Hydropole 2005] Web site of the swiss hydrogen association, http://www.hydropole.ch/Hydropole/Intro/H2EnergyCarrier.htm (visited 18 October 2005)

[Incropera 2002] Incropera, F.P., DeWitt, D.P., "Fundamentals of Heat and Mass Transfer", 5th edition, Wiley, 2002.

[Ishihara 2003] Ishihara, T., Sammes, N.M., Yamamoto, O., "Chapter 4: Electrolytes", in Singhal, S.C., Kendall, K., "High Temperature Solid Oxide Fuel Cells: Fundamentals, Design and Applications" (pp. 83-117, Elsevier, Oxford, UK, 2003.

[Ishino 1999] Ishino, M., Iwakiri, Y., Bessho, A., Uchida, H., "Effects of Variable Inlet Guide Vanes on Small Centrifugal Compressor Performance", ASME Turbo Expo 1999.

[Janssen 2003] Jansen, D., Dijkstra, J.W., "CO2 CAPTURE IN SOFC-GT SYSTEMS", Second Annual Conference on Carbon Sequestration, Hilton Alexandria Mark Centre, Alexandria, VA, USA, 5-8 May 2003.

[Johannesen 1951] Johannesen, N. H., "Ejector Theory and Experiments", Dissertation, Danish Academy of Technical Sciences, Copenhagen, Denmark, 1951.

[Kandepu 2005] Kandepu, R., Imsland, L., Foss, B.A., Stiller, C., Thorud, B., Bolland, O., "Control-relevant SOFC modelling and model evaluation", ECOS, Trondheim, Norway, June 20-22, 2005

[Karl 2004] Karl, J., Karellas, S., "Highly efficient SOFC systems with indirect gasification", Proceedings of the 6th European SOFC Forum, Lucerne, Switzerland, 28 June – 2 July 2004.

[Karoliussen 1992] Karoliussen, H., Nisancioglu, K., Solheim, A., Ødegård, R., "SOFC Stack modeling with internal reforming", 4th IEA Workshop on SOFC, Lausanne, Switzerland, August 1992.

[Kays 1984] Kays W. M., London A.L, "Compact Heat Exchangers", McGraw-Hill, 1984.

[Kemm 2004] Kemm, M., Hildebrand, A., Assadi, M., "Operation and Performance Limitations for Solid Oxide Fuel Cells and Gas Turbines in a Hybrid System", ASME Turbo Expo 2004.

[Kendall 2003] Kendall, K., Minh, N.Q., Singhal, S.C., "Chapter 8: Cell and Stack Designs", in Singhal, S.C., Kendall, K., "High Temperature Solid Oxide Fuel Cells: Fundamentals, Design and Applications" (pp. 197-228, Elsevier, Oxford, UK, 2003.

[Kimijima 2002] Kimijima, S., Kasagi, N., "Performance evaluation of gas turbine-fuel cell hybrid micro generation system", ASME Turbo Expo 2002.

[Kohl 1997] Kohl, A., Nielsen, R., "Gas purification", 5th edition, Gulf publishing company, Houston, Texas, 1997, pp. 1305-1307.

[Kuchonthara 2003] Kuchonthara, P., Bhattacharya, S., Tsutsumi, A., "Combinations of SOFC and several enhanced gas turbine cycles", Journal of Power Sources 124 (2003), 65-75.

[Kurzke 2004] Kurzke, J., "Compressor and turbine maps for gas turbine performance computer programs – Component Map Collection 2", Dachau, Germany, 2004.

[Larminie 2000] Larminie, J., Dicks, A., "Fuel Cell Systems Explained", John Wiley & Sons, Chichester, UK, 2000.

[Larrain 2004] Larrain, D., Van herle, J., Maréchal, F., Favrat, D., "Generalized model for planar SOFC repeat element for design optimization", Journal of Power Sources 131 (2004), 304-312.

[Lines 1999] Lines, J.R., "Understanding ejector system necessary to troubleshoot vacuum distillation", Oil & Gas Journal 97/7(1999) 40-45.

[Lockett 2004] Lockett, M., Simmons, M.J.H., Kendall, K., "CFD to predict temperature profile for scale up of micro-tubular SOFC stacks", Journal of Power Sources 131 (2004), 243-246.

[Lu 2005] Lu,Y., Schaefer, L., Li, P., "Numerical study of a flat-tube high power density solid oxide fuel cell Part I. Heat/mass transfer and fluid flow", Journal of Power Sources 140 (2005), 331–339.

[Luyben 1990] Luyben, W.L., "Process modelling, simulation, and control for chemical engineers", 2nd edition, McGraw-Hill, New York, 1990.

[Magistri 2004a] Magistri, L., Trasino, F., Costamagna, P., "Transient Analysis of Solid Oxide Fuel Cell Hybrids: Part A — Fuel Cell Models", ASME Turbo Expo 2004.

[Magistri 2004b] Magistri, L., Ferrari, M.L., Traverso, A., Costamagna, P., Massardo, A.F., "Transient Analysis of Solid Oxide Fuel Cell Hybrids: Part C — Whole-Cycle Model", ASME Turbo Expo 2004.

[Marsano 2004] Marsano, F., Magistri, L., Massardo, A., "Ejector performance influence on a SOFC anodic recirculation system", Journal of Power Sources 129 (2004), 216-228.

[McDonald 2003] McDonald, C.F., "Recuperator considerations for future higher efficiency microturbines", Applied Thermal Engineering 23 (2003) 1463–1487.

[McEvoy 2003] McEvoy, A., "Chapter 6: Anodes", in Singhal, S.C., Kendall, K., "High Temperature Solid Oxide Fuel Cells: Fundamentals, Design and Applications" (pp. 121-171, Elsevier, Oxford, UK, 2003.

[Möbius 2003] Möbius, H.-H., "Chapter 2: History", in Singhal, S.C., Kendall, K., "High Temperature Solid Oxide Fuel Cells: Fundamentals, Design and Applications" (pp. 23-52, Elsevier, Oxford, UK, 2003.

[Momma 2005] Momma, A., Kaga, Y., Takano, K., Nozaki, K., Negishi, A., Kato, K., Kato, T., Inagaki, T., Yoshida, H., Hoshino, K., Yamada, M., Akbay, T., Akikusa, J., "Experimental investigation of anodic gaseous concentration of a practical seal-less solid oxide fuel cell", Journal of Power Sources (2005), in press.

[Moran 2002] Moran, M.J., Shapiro, H.N., "Fundamentals of Engineering Thermodynamics", 5th ed., Wiley, 2004.

[Nakajo 2005] Nakajo, A., Stiller, C., Härkegård, G., Bolland, O., "Modeling of thermal stresses and probability of survival of tubular SOFC", Journal of Power Sources, in press.

[Nisancioglu 1989] Nisancioglu, Kemal, "Natural gas fuelled solid oxide fuel cells and systems - ohmic losses", International Energy Agency, Workshop on Mathematical Modelling, Charmey, Switzerland, July 2-6, 1989.

[Nisancioglu 1989] Nisancioglu, Kemal, "Natural gas fuelled solid oxide fuel cells and systems - ohmic losses", International Energy Agency, Workshop on Mathematical Modelling, Charmey, Switzerland, July 2-6, 1989.

[Norheim 2005] Norheim, A., "Experimental investigation of solid oxide fuel cells using biomass gasification producer gases", NTNU, Doctoral thesis 2005:188, Trondheim, September 2005.

[Ota 2003] Ota, T., Koyama, M., Wen, C., Yamada, K., Takahashi, H., "Object-based modeling of SOFC system: dynamic behaviour or micro-tube SOFC", Journal of Power Sources 118 (2003), 430-439.

[Pålsson 2002] Pålsson, J., "Thermodynamic Modeling and Performance of combined SOFC and GT systems", Doctoral Thesis, Lund University, Sweden, 2002

[Pangalis 2002] M.G. Pangalis, R.F. Martinez-Botas, N.P. Brandon, "Integration of solid oxide fuel cells into gas turbine power generation cycles. Part 1: Fuel cell thermodynamic modelling", Proc Instn Mech Engrs Vol 216 Part A: J Power and Energy (2002), 129-144.

[Proell 2004] Proell, T., Rauch, R., Aichernig, C., Hofbauer, H., "Coupling of biomass steam gasification and an SOFC-gas turbine hybrid system for highly efficient electricity generation", ASME Turbo Expo 2004, Vienna, Austria, GT2004-53900.

[PSE-online 2004] gPROMS product page on the web site of Process Systems Enterprise Limited, http://www.psenterprise.com/products_gproms.html (visited May 2005).

[Qi 2005] Qi, Y., Huang, B., Chuang, K.T., "Dynamic modeling of solid oxide fuel cell: The effect of diffusion and inherent impedance", Journal of Power Sources 150 (2005) 32-47.

[Rao 2001] Rao, A.D., Samuelsen, G.S., "A Thermodynamic Analysis of Tubular SOFC based Hybrid Systems", ASME Turbo Expo 2001.

[Rao 2002] Rao, A.D., Samuelsen, G.S., "Analysis Strategies for Tubular SOFC Based Hybrid Systems", J Eng for Gas Turb. and Pow., 124 (2002), 503-509.

[Rechenauer 1993] Rechenauer, C., "Dreidimensionale mathematische Modellierung des stationären und instationären Verhaltens oxidkeramischer Hochtemperatur-Brennstoffzellen", Doctoral Thesis, Forschungszentrum Jülich, Germany, 1993.

[Recknagle 2003] Recknagle, K.P., Williford, R. E.,. Chick, L. A, Rector, D. R.,. Khaleel, M. A, "Three-dimensional thermo-fluid electrochemical modeling of planar SOFC stacks", Journal of Power Sources 113 (2003), 109-114.

[Reid 1987] Reid, R.C., Prausnitz, J.M., Poling, B.E., "The properties of Gases and Liquids", McGraw-Hill, New York, 1987.

[Rohsenow 1998] Rohsenow, W.M., Hartnett, J.P., Cho, Y.I., "Handbook of Heat Transfer", third ed., McGraw-Hill, 1998.

[Rolls-Royce 2005] Fuel cell related web site of Rolls Royce, http://www.rolls-royce.com/energy/tech/fuelcells.jsp (visited June 2005).

[Romier 2004] Romier, A., "Small gas turbine technology", Applied Thermal Engineering 24 (2004) 1709–1723.

[Rothe 2005] Mechtild Rothe, Committee on Industry, Research and Energy, European Parliament, "Report on the proposal for a directive of the European Parliament and of the Council on energy end-use efficiency and energy services" (A6-0130/2005), 25 May 2005.

[Saravanamuttoo 2001] Saravanamuttoo, H.I.H., Rogers, G.F.C., Cohen, H., "Gas turbine theory", 5th edition, Pearson Education, Parson, England, 2001.

[Selimovic 2000] Selimovic, A, "SOFC Modelling for SOFC/GT Combined Cycle Simulations", Licentiate Thesis, Lund Institute of Technology, Sweden, 2000.

[Selimovic 2002a] Selimovic, A., Palsson, J., "Design and Off-Design Predictions of a Combined SOFC and Gas Turbine System", Journal of Power Sources 106 (2002), 76-82.

[Selimovic 2002b] Selimovic, A., "Modelling of SOFC Applied to the Analysis of Integrated Systems with Gas Turbines", Doctoral Thesis, Lund Institute of Technology, Sweden, 2002.

[S-W 2005] Fuel cell related web site of Siemens Westinghouse, http://www.siemenswestinghouse.com/en/fuelcells (visited Jund 2005)

[Singhal 2000] Singhal, S.C., "Advances in solid oxide fuel cell technology", Solid State Ionics 135 (2000) 305–313.

[Singhal 2003a] Singhal, S.C., Kendall, K., "High Temperature Solid Oxide Fuel Cells: Fundamentals, Design and Applications", Elsevier, Oxford, UK, 2003

[Singhal 2003b] Singhal, S.C., Kendall, K., "Chapter 1: Introduction to SOFCs", in Singhal, S.C., Kendall, K., "High Temperature Solid Oxide Fuel Cells: Fundamentals, Design and Applications" (pp. 1-22), Elsevier, Oxford, UK, 2003.

[Skogestad 2004] Skogestad, S., Postlethwaite, I., "Multivariable feedback control – Analysis and design", 2nd edition, John Wiley & Sons, 2005.

[Song 2004] Song, T.W., Sohn, J.L., Kim, J.H., Kim, T.S., Ro, S.T., Suzuki, K., "Parametric studies for a performance analysis of a SOFC/MGT hybrid power system based on a quasi-2D model", ASME Paper 2004-GT-53304.

[Song 2005] Song, T.W., Sohn, J.L., Kim, J.H., Kim, T.S., Ro, S.T., Suzuki, K., "Performance analysis of a tubular solid oxide fuel cell/micro gas turbine hybrid power system based on a quasi-two dimensional model", Journal of Power Sources, 142 (2005), 30-42

[Stephanopoulos 1984] Stephanopoulos, G., "Chemical Process Control – An Introduction to Theory and Practice", Prentice-Hall Inc., New Jersey, 1984.

[Stiller 2005] Stiller, C., Thorud, B., Seljebø, S., Mathisen, Ø., Karoliussen, H., Bolland, O., "Finite-volume modeling and hybrid-cycle performance of planar and tubular solid oxide fuel cells", Journal of Power Sources 141 (2005), 227–240.

[Tanaka 2000] Tanaka, K., Wen, C., Yamada, K., "Design and evaluation of combined cycle system with SOFC and gas turbine", Journal of Fuel 79 (2000) 1493-1507.

[Thorud 2005] Thorud, B., "Dynamic Modelling and Characterisation of a Solid Oxide Fuel Cell Integrated in a Gas Turbine Cycle", NTNU, Doctoral Thesis 2005:176, Trondheim, October 2005.

[Traverso 2005] Personal communication with Dr. Alberto Traverso, Thermochemical Power Group, University of Genoa, Italy, December 2005.

[Uechi 2001] Uechi, H., Kimijima S., Kasagi, N., "Cycle Analysis of Gas Turbine-Fuel Cell Hybrid Micro Generation System", ASME International Joint Power Generation Conference, New Orleans, Louisiana, June 4-7, 2001.

[Ulfsnes 2005] Ulfsnes, R., Doctoral Thesis, NTNU, Trondheim, to be published 2006

[Veyo 2002] Veyo, S., Shockling, L.A., Dederer, J.T., Gillett, J.E., Lundberg, W.L., "Tubular Solid Oxide Fuel Cell/Gas Turbine Hybrid Cycle Power Systems: Status", Journal of Engineering for Gas Turbines and Power 124 (2002) 845-849.

[Veyo 2003] Veyo, S,. Lundberg, W.L., Vora, S.D., Litzinger, K.P., "Tubular SOFC Hybrid Power System Status", ASME Turbo Expo 2003.

[White 2003] White, F.M., "Fluid Mechanics", 5th edition, McGraw-Hill, Boston, 2003.

[WHRC 2005] Web site of Woods Hole Research Center, http://www.whrc.org/resources/online_publications/warming_earth/scientific_evidence.htm (visited 18 October 2005)

[Yakabe 2002] Yakabe, H., Baba, Y, Sakurai, T., Satoh, M., Hirosawa, I., Yoda, Y., "Evaluation of residual stresses in a SOFC stack", Journal of Power Sources 131 (2004), 278-284.

[Yi 2003] Yi, Y., Smith, T.P., Brouwer, J., Rao, A.D., Samuelsen, G.S., "Simulation of a 220 kW Hybrid SOFC Gas Turbine System and Data Comparison", SOFC 8, Paris 2003, Electrochemical Society Proceedings, Volume 2003-07, 1442-1454.

[Yi 2004] Yi, Y., Rao, A.D., Brouwer, J, Samuelsen, G.S., "Analysis and optimization of a SOFC-ICGT intercooled GT hybrid cycle", Journal of Power Sources 132 (2004), 77-85.

[Yokokawa 2003] Yokokawa, H., Horita, T., "Chapter 5: Cathodes", in Singhal, S.C., Kendall, K., "High Temperature Solid Oxide Fuel Cells: Fundamentals, Design and Applications" (pp.119-147, Elsevier, Oxford, UK, 2003.

Paper I

Finite-volume modeling and hybrid-cycle performance of planar and tubular solid oxide fuel cells

Stiller, C., Thorud, B., Seljebø, S., Mathisen, Ø., Karoliussen, H., Bolland, O.

Journal of Power Sources 141 (2005) 227–240

Available online at www.sciencedirect.com
SCIENCE DIRECT®
Journal of Power Sources 141 (2005) 227–240
JOURNAL OF POWER SOURCES
www.elsevier.com/locate/jpowsour

Finite-volume modeling and hybrid-cycle performance of planar and tubular solid oxide fuel cells

Christoph Stiller*, Bjørn Thorud, Steinar Seljebø, Øistein Mathisen, Håvard Karoliussen, Olav Bolland

Department of Energy and Process Engineering, Norwegian University of Science and Technology, Kolbjorn Hejes vei 1B, Trondheim N-7491, Norway

Received 18 February 2004; received in revised form 14 July 2004; accepted 27 September 2004
Available online 23 November 2004

Abstract

The paper describes two 2D steady-state models for solid oxide fuel cells (SOFC) with planar and tubular geometries fuelled by methane. Following a description of the basic geometries and general premises the approaches, assumptions and simplifications for the calculation of ohmic resistance, convective, conductive and radiative heat transfer are given. The modeling approach of the chemical reactions and molar and thermal balances are depicted in detail with the intention to allow for reproduction of the models. The required boundary conditions and input parameters of the models are also discussed. Relying on models, a bottoming GT cycle is introduced and specified and a base case for operation defined. The influence of pressure ratio, air inlet temperature, air flow rate and anode gas recycling are investigated in a parameter study. For both designs air flow rate and pressure ratio are the most important parameters considering the system performance, but for the tubular system these parameters have less impact than for the planar design. Based on the parameter study, a near-optimum case is defined specifically for both systems and the conditions in the fuel cells are investigated. The cycle balance is different in both systems, as the tubular fuel cell requires a lower air inlet temperature. Both fuel cell systems achieve above 65% electric efficiency.

Keywords: SOFC; Tubular; Planar; Model; Hybrid

1. Introduction

Combined solid oxide fuel cells and gas turbine (SOFC)/GT cycles promise to achieve high electric efficiencies even for small-scale systems with power output below 10 MW and hence have a certain potential in decentralized power generation concepts. However, there is a lot of uncertainty about the best layout of the fuel cell and the hybrid cycle in terms of feasibility, performance, economics and controllability. This paper compares the performance of the two most common SOFC geometries, namely planar and tubular, in a gas turbine hybrid cycle. It describes the configuration of the fuel cells and gives a comprehensive and reproducible description of the approach, assumptions and methods used for the steady-state models of the different geometries. After a validation of the fuel cell models, their implementation into the gas turbine cycle simulation is described, and the performance of combined cycles with planar and tubular SOFCs are studied and compared. Departing from a base case, the sensitivities to certain process parameters are studied and discussed and operational options and constraints are derived. The maximum efficiency under near-optimum operation is estimated.

2. Fuel cell models

2.1. Fuel cell geometries and modeling premises

The investigated planar SOFC is a cross-flow, electrolyte-supported cell. A previously in-house developed repeat

Abbreviations: CV, control volume; FU, fuel utilization; GT, gas turbine; PEN, positive electrode–electrolyte–negative electrode; SOFC, solid oxide fuel cell; TIT, turbine inlet temperature

* Corresponding author. Tel.: +47 7359 3723; fax: +47 7359 8390.
E-mail address: Christoph.stiller@ntnu.no (C. Stiller).

0378-7753/$ – see front matter © 2004 Elsevier B.V. All rights reserved.
doi:10.1016/j.jpowsour.2004.09.019

Nomenclature

Symbols

A	area (m^2)
A_{act}	active cell area (m^2)
co	gas component
c_p	specific heat capacity ($J\,K^{-1}\,mole^{-1}$)
D_h	hydraulic diameter (m)
E^{rev}	reversible potential (V)
F	Faraday constant ($96485\,C\,mole^{-1}$)
I	total CV current (A)
J	lumped parameter
L	length (m)
n	molar flow ($mole\,s^{-1}$)
Nu	Nusselt number
p	pressure (Pa)
$\dot{Q}$	radiative heat flow (W)
R	universal gas constant ($8.314\,J\,K^{-1}\,mole^{-1}$)
r	radius (m)
$r_{...}$	reaction rate ($mole\,s^{-1}$)
$R_{1...}R_5$	heat resistivity of planar model building blocks (kW^{-1})
$R_{p,i}$; $R_{p,j}$	solid heat resistivity of planar model in i- and j-direction (kW^{-1})
$R_{t,ax}$	axial heat resistivity of tubular model (kW^{-1})
$R_{t1...}R_{t6}$	radial chain heat resistivity of tubular model (kW^{-1})
R_Ω	ohmic resistance (Ω)
T	temperature (K)
T_{black}	temperature of black body receiving radiation energy for the pre-reformer
U	cell voltage (V)

Greek letters

α	convective heat transfer coefficient ($W\,m^{-2}\,K^{-1}$)
δ	thickness (m)
ΔH	enthalpy change ($J\,mole^{-1}$)
ε	emissivity (0.8)
η	overpotential (V)
λ	heat conduction efficient ($W\,m^{-1}\,K^{-1}$)
ρ	specific resistance ($\Omega\,m$)
σ	Stefan–Boltzmann-constant ($5.67 \times 10^{-8}\,W\,m^{-2}\,K^{-4}$)

Indexes

a	anode
a_1	cathode air (tubular model)
a_2	injector air
air	air (planar)
c	cathode
co	gas component counter
e	electrolyte
electro	electrochemical reaction
f	fuel
i, j	counter for CV number in i- and j-direction
ic	interconnect
inj	injector
irrad	irradiation
p	planar
preref	pre-reformer
rad	radiation
ref	reforming reaction
s	solid (tube material)
shift	shift reaction
t	tubular

element geometry with a size of 3.8 mm × 3.8 mm [1] has been used as control volume. In order to scale the cell to the standard size of 100 mm × 100 mm, a matrix of 26 × 26 repeat elements is required. The resulting length of the cell is 98.8 mm. The tubular geometry is based on the current Siemens–Westinghouse technology [2], which is a cathode-supported, 1.5 m long and 22 mm diameter vertical tube. The air enters an inner tube (injector) from the top, is preheated while flowing downwards to the end of the tube where it turns and flows upwards between the cathode and the injector tube. The fuel is correspondingly fed from outside the tube and flows upwards. Fig. 1 shows the control volume of the planar and the tubular cell, together with the respective key dimensions and the materials. The tube interconnect that penetrates the anode and electrolyte is not shown here.

The following assumptions, simplifications and premises were chosen for the proposed models:

1. The fuel is partially pre-reformed methane.
2. Internal reforming at the anode. Kinetics of the reforming reaction are respected while the shift reaction is always at equilibrium.
3. A pre-reformer is thermally integrated by radiation from the edges of the cells for the planar design and radiation from the solid in the tubular design. The pre-reformer itself is not integrated in the SOFC model, but the required amount of heat is an input variable.
4. Single-cell setup is considered, i.e. adiabatic boundaries except the pre-reformer are assumed.
5. The electrochemical kinetics is limited to activation overpotential, i.e. no diffusion overpotential is calculated.
6. In the planar model, each CV has one temperature node respectively for solid, air and fuel temperature. The tubular model has additionally temperature nodes for the injector air and the injector tube.
7. Heat conduction is calculated in two dimensions in the planar model, neglecting heat flow in the stacking direction. The tubular model features heat conduction in axial direction as well as radiation between the concentric tubes.

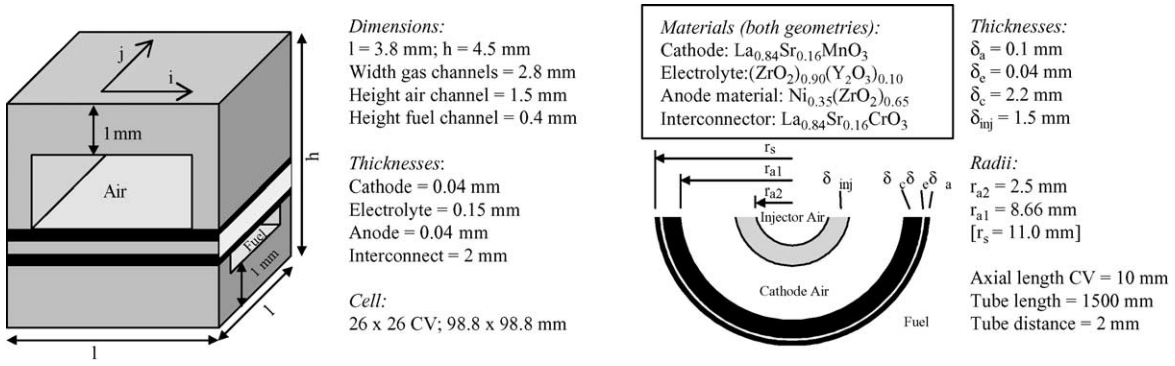

Fig. 1. Basic geometries of planar and tubular fuel cell control volume.

8. Radiation inside the planar cell is not included. In the tubular cell, radiation between the solid and the injector tube is modeled.

Similar work has been performed by Selimovic [3], Campanari [4] and some other SOFC researchers. The models present a common approach for finite-volume modeling of SOFC, detailed enough to give information about the internal behaviour of the cell and lean enough to be implemented into a hybrid system model and be solved within a reasonable calculation time.

2.2. Ohmic resistance

The ohmic resistance consists of the electronic current resistance in the interconnect and electrodes, and the ionic resistance in the electrolyte. The latter is the most dominating in both concepts.

In the planar model, the electronic resistance of anode, cathode and interconnect is low compared to the electrolyte resistance [5] and can be regarded as temperature independent within the given operating conditions. The material specific values for a temperature of 1173 K from Bossel [5] have been used to calculate the resistance of the layers. Conductivity and resistance for one CV as well as the temperature dependency of the electrolyte is listed in Table 1.

Even though in the tubular model, the same materials as for the flat plate model are applied, the properties given in literature are different due to unlike production techniques. Therefore, mostly temperature dependant resistances have been chosen for the tubular model. Also, the geometry is more complex than for the flat plate design. Although the tube is modeled in 2D, effects from current flowing in the 3rd direction (tangential) are accounted for by using the analytical expression for ohmic resistance of a control volume of the tube developed by Nisancioglu [6]. The expression is given in Eqs. (1)–(3), describing the so-called transmission line model. For further explanation, it is referred to the work of Niscanscioglu [6].

$$R_\Omega(\Omega) = L_{CV}\left(\frac{\left(\left(\frac{\rho_a}{\delta_a}\right)^2+\left(\frac{\rho_c}{\delta_c}\right)^2\right)\cosh(J_e)+\frac{\rho_a\rho_c}{\delta_a\delta_c}(2+J_e\sinh(J_e))}{2\left(\frac{1}{\rho_e\delta_e}\right)^{1/2}\left(\frac{\rho_a}{\delta_a}+\frac{\rho_c}{\delta_c}\right)^{3/2}\sinh(J_e)}+\frac{\sqrt{\rho_{ic}\delta_{ic}\left(\frac{\rho_c}{\delta_c}\right)}}{2\tanh(J_{ic})}\right) \quad (1)$$

where

$$J_e = \frac{L_e}{2}\sqrt{\frac{1}{\rho_e\delta_e}\left(\frac{\rho_a}{\delta_a}+\frac{\rho_c}{\delta_c}\right)} \quad (2)$$

and

$$J_{ic} = \frac{L_{ic}}{2}\sqrt{\frac{1}{\rho_{ic}\delta_{ic}}\frac{\rho_a}{\delta_a}} \quad (3)$$

with the terms $\rho_{ic}\delta_{ic} = 0.002\,\Omega\,cm^2$ (taken from Nisancioglu [6]); $\rho_e = 8.78\times10^{-3}\,e^{9165/T}\,\Omega\,cm$ (taken from Ota [7]); $\rho_a = 2.99\times10^{-3}\,e^{-1395/T}\,\Omega\,cm$ (taken from Ota [7]); $\rho_c = 7.99\times10^{-3}\,e^{601/T}\,\Omega\,cm$ (taken from Ota [7]); $L_{CV} = 1$ cm (axial length of CV); $L_e = 6.16$ cm (circumferential length of electrode); $L_{ic} = 0.6$ cm (circumferential length of interconnect) and the thickness δ to be taken from Fig. 1.

Table 1
Ohmic resistances for the planar model

Layer	Conductivity (S m^{-1})	CV resistance (Ω)
Anode	30.39×10^3	91.24×10^{-6}
Cathode	12.87×10^3	215.2×10^{-6}
Interconnect	3.11×10^3	44.53×10^{-3}
Electrolyte	$33.4\times10^3\,e^{(-10300/T)}$	$3.11\times10^{-4}\times e^{(10300/T)}$

Table 2
Nusselt numbers and hydraulic diameters

	Planar model		Tubular model			
	Air side	Fuel side	Inner air, injector	Outer air w.r.t. injector	Outer air w.r.t. cathode	Fuel, anode
Nu	4[a]	6.2[a]	4.36[b]	10[b]	7[b]	1.8[b]
D_h (mm)	1.953	0.7	5	9.328	9.328	11.3

[a] Taken from [10].
[b] Taken from [8].

2.3. Convective and conductive heat transfer

The heat transfer in the models is implemented by applying an electrical analogy, i.e. by calculation of thermal resistances.

The convective heat transfer coefficients α for all gas–solid interfaces are determined via the Nusselt number:

$$\alpha = \frac{Nu\lambda}{D_h} \tag{4}$$

The flow is assumed to be laminar and entrance effects have been neglected. Table 2 shows the Nusselt numbers *Nu* and hydraulic diameters D_h of the flow channels. Note that flow in annular ducts has different Nusselt numbers with respect to the inner and outer surface [8].

The heat conduction coefficients λ of the gases are calculated separately for the temperature and gas composition of each control volume using the polynomic formulae from Bossel [5] for each gas species.

Thermal conductivities of the solids are considered to be constant and their values are listed in Table 3.

The cells are assumed to operate under adiabatic conditions, thus heat conduction between adjacent cells is neglected. Only heat conduction between adjacent CVs, thus in *i*- and *j*-direction, is modeled. Due to its low thickness, the PEN structure is neglected in terms of heat conduction. For the heat transfer in *i*- and *j*-direction, the thermal resistance of a CV is calculated by dividing the interconnect into basic rectangular building blocks and calculating a total resistance of the circuit. The building block model, the resulting circuit in *i*-direction (*j* direction analogous) and the resulting total resistance equations are shown in Fig. 2.

In the tubular model, heat transfer in the radial direction is calculated by using an electrical analog circuit with conductive and convective resistances in series, shown in Fig. 3. The respective temperatures in the anode, electrolyte and cathode layer are regarded as uniform in each specific control volume. To calculate conduction into axial direction of the solid, the center temperature with respect to thermal resistance is chosen (i.e. the temperature at the radius where thermal resistance to inner and outer surface of the solid are equal). In

Table 3
Heat conduction coefficients

	Planar model	Tubular model			
	Interconnect	Anode	Electrolyte	Cathode	Injector
λ ($W m^{-1} K^{-1}$)	3.5[a]	3[a]	2[a]	3[a]	6.84[b]

[a] Taken from [5].
[b] Taken from [10].

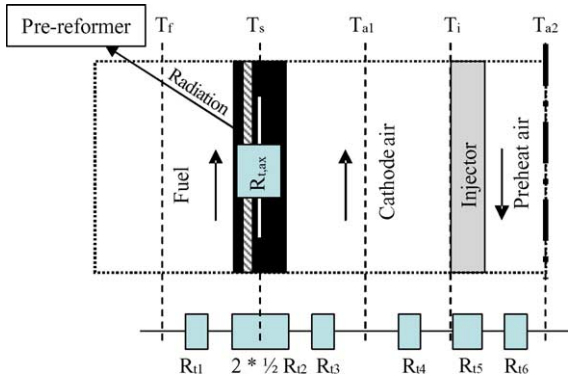

Fig. 3. Tubular radial heat conduction model.

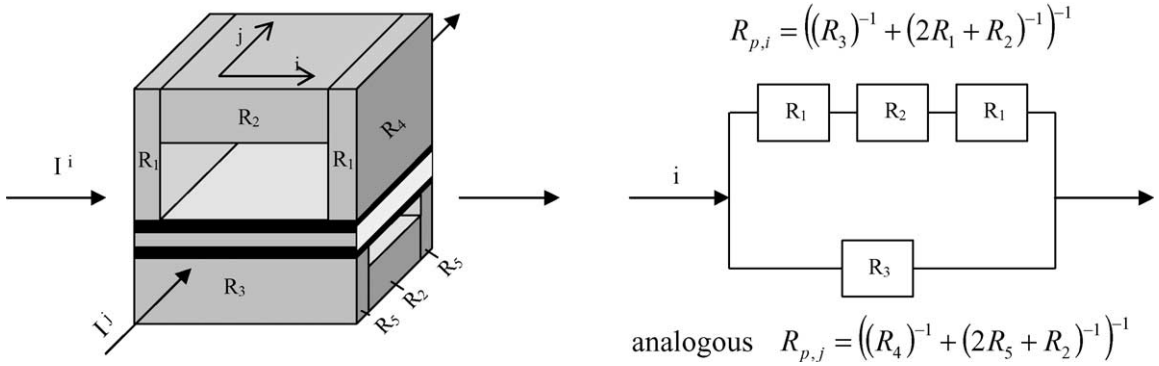

Fig. 2. Planar heat conduction model.

the injector tube, the outside temperature is used to calculate the radiation between injector and cathode. Axial heat conduction is only considered for the solid, not for the injector tube. The effect of interconnect and circumferential heat conduction is not considered.

2.4. Radiation

In order to reduce calculation time for the planar model, radiation between adjacent CVs was neglected. Even though the impact is lower than for the tubular model due to the small channel height, neglecting this phenomenon will according to Yakabe [9] lead to a steeper temperature profile and a shift of the maximum temperature upstream of the fuel flow. However, it is assumed that this effect does not seriously affect the key results, such as fuel utilization, efficiency and power output. Thus the model should still be able to produce reasonable results for use in combination with other processes, such as a gas turbine process. However, the energy demand of the pre-reformer is covered by radiation from the edges of the cell (i.e. the outermost CVs) towards a fictive black body with a uniform temperature. During the calculation, the black body temperature is adjusted iteratively until the radiative cell loss equals the pre-reformer duty. In order to be physically feasible, the black body temperature must be higher than or at least equal to the pre-reformer temperature.

The tubular geometry shows high temperature differences between the solid and the injector tube. Therefore, the tubular model includes radiation between the injector tube and the cathode. In this case, the control volumes of the tube represent a 10 mm high slice of the tube, and by pre-calculations it has been found that 95% of the radiative heat exchange occurs within the same CV and with the CVs lying above and underneath the CV in consideration. To reduce calculation time the remaining radiative heat exchange has been neglected. The implementation is shown in Fig. 1 with shape factors obtained from Incropera and Dewitt [10]. Note that the cathode has a shape factor of 34% to itself. Consequently only 66% of the radiation originating from the cathode occurs in the heat balance.

To reduce calculation time the pre-reformer heat duty is included as constant sink term in the tube solid heat balance, although this effect is of radiative character. Thus, all CVs deliver the same heat flow to the pre-reformer. To exclude a violation of the second law of thermodynamics, it is checked that the required temperature of the recipient for obtaining the required heat flow does not fall below the pre-reformer temperature.

2.5. Reactions and molar balances

Methane in the fuel is reformed at the entrance of the fuel cell in a reaction with steam, using nickel as catalyst:

$$CH_4 + H_2O \rightleftarrows CO + 3H_2 \tag{5}$$

The reaction rate of this reaction can, according to Rechenauer and Achenbach [11], be calculated by the following expression:

$$r_{CH_4}(\text{mole s}^{-1}) = 4274\,(\text{mole m}^{-2}\,\text{bar}^{-1}\,\text{s}^{-1})\,\text{e}^{-82\,(\text{kJ mole}^{-1})/RT}\,p_{CH_4}A_{\text{act}} \tag{6}$$

with the active area of $1.444 \times 10^{-5}\,\text{m}^2$ for the planar and $5.76 \times 10^{-4}\,\text{m}^2$ for the tubular CV. The carbon monoxide produced by methane reforming reacts with steam to form carbon dioxide and hydrogen:

$$CO + H_2O \rightleftarrows CO_2 + H_2 \tag{7}$$

At the SOFC operating temperature this reaction is very fast and assumed always to be in equilibrium. The equilibrium constant is determined with linear approaches for the Gibbs free energy found in standard literature. Due to a rather high steam to carbon ratio (~2–3) no carbon deposition is considered. A check whether this assumption is fair is however included.

Both carbon monoxide and hydrogen can theoretically participate in the electrochemical reactions, but for simplicity only the hydrogen reaction is considered.

$$H_2 + \tfrac{1}{2}O_2 \rightarrow H_2O \tag{8}$$

The reaction rate of the electrochemical reaction can be calculated by using the formulae (9)–(11):

$$U = E^{\text{rev}} - R_\Omega I - \eta \tag{9}$$

Table 4
Molar balance equations

Species	Planar model	Tubular model	Equation
CH_4	$n^{i,j}_{CH_4} = n^{i-1,j}_{CH_4} - r_{CH_4}$	$n^{i}_{CH_4} = n^{i-1}_{CH_4} - r_{CH_4}$	(26)
CO	$n^{i,j}_{CO} = n^{i-1,j}_{CO} + r_{CH_4} - r_{CO}$	$n^{i}_{CO} = n^{i-1}_{CO} + r_{CH_4} - r_{CO}$	(27)
CO_2	$n^{i,j}_{CO_2} = n^{i-1,j}_{CO_2} + r_{CO}$	$n^{i}_{CO_2} = n^{i-1}_{CO_2} + r_{CO}$	(28)
H_2	$n^{i,j}_{H_2} = n^{i-1,j}_{H_2} + 3r_{CH_4} - r_{H_2} + r_{CO}$	$n^{i}_{H_2} = n^{i-1}_{H_2} + 3r_{CH_4} - r_{H_2} + r_{CO}$	(29)
H_2O	$n^{i,j}_{H_2O} = n^{i-1,j}_{H_2O} - r_{CH_4} - r_{CO} + r_{H_2}$	$n^{i}_{H_2O} = n^{i-1}_{H_2O} - r_{CH_4} - r_{CO} + r_{H_2}$	(30)
O_2	$n^{i,j}_{O_2} = n^{i,j-1}_{O_2} - 0.5r_{H_2}$	$n^{i}_{O_2} = n^{i-1}_{O_2} - 0.5r_{H_2}$ (cathode air)	(31)
N_2	$n^{i,j}_{N_2} = n^{i,j-1}_{N_2}$	$n^{i}_{N_2} = n^{i-1}_{N_2}$ (cathode air)	(32)

$$\eta = 2.83 \times 10^{-4}\,(\Omega\,\mathrm{m}^2)\,\frac{I}{A_{\mathrm{act}}}\mathrm{e}^{8360\,(\mathrm{K})/T} \tag{10}$$

$$r_{\mathrm{H_2}} = \frac{I}{2F} \tag{11}$$

In Eq. (9) the current is calculated from a set operating voltage, open circuit potential, sum of the ohmic and ionic resistances and activation overpotential. The latter is approximated in Eq. (10), taken from Selimovic [3]. The reaction rate of H_2 can then be calculated by applying Faradays law as in Eq. (11). Being the most common approach for SOFC modeling, no diffusion overpotential has been regarded.

Applying these reactions and considering the gas flows into the CVs at anode and cathode side of the cell, the molar balance equations for all occurring species are determined as shown in Table 4.

2.6. Heat balances

In the planar model, heat balances are calculated for the air, fuel and solid (i.e. interconnect). Air flows in the *j*-direction, while fuel flows in the *i*-direction as depicted in Fig. 1.

Heat balance of the air is given by:

$$\alpha_{\mathrm{air}} A_{\mathrm{c}}(T_{\mathrm{air}}^{i,j} - T_{\mathrm{s}}^{i,j}) = \sum_{\mathrm{co}}^{\mathrm{co_{air}}}(c_{\mathrm{p,co}}(T_{\mathrm{air}}^{i,j-1})n_{\mathrm{co}}^{i,j-1}T_{\mathrm{air}}^{i,j-1} - c_{\mathrm{p,co}}(T_{\mathrm{air}}^{i,j})n_{\mathrm{co}}^{i,j}T_{\mathrm{air}}^{i,j}) \tag{12}$$

In words, the convective heat transport between air and solid material equals the sum of the heat capacity flows of all species into the CV minus the sum of the heat capacity flows of all species out of the CV.

The fuel heat balance is analogous; however, the fuel flows orthogonally to the air:

$$\alpha_{\mathrm{f}} A_{\mathrm{a}}(T_{\mathrm{f}}^{\mathrm{i,j}} - T_{\mathrm{s}}^{\mathrm{i,j}}) = \sum_{\mathrm{co}}^{\mathrm{co_f}}(c_{\mathrm{p,co}}(T_{\mathrm{f}}^{i-1,j})n_{\mathrm{co}}^{i-1,j}T_{\mathrm{f}}^{i-1,j} - c_{\mathrm{p,co}}(T_{\mathrm{f}}^{i,j})n_{\mathrm{co}}^{i,j}T_{\mathrm{f}}^{i,j}) \tag{13}$$

Due to the electrical analogy the heat balance in the solid is given by:

$$\begin{aligned}&\frac{2T_{\mathrm{s}}^{i,j} - T_{\mathrm{s}}^{i+1,j} - T_{\mathrm{s}}^{i-1,j}}{R_{\mathrm{p},i}} + \frac{2T_{\mathrm{s}}^{i,j} - T_{\mathrm{s}}^{i,j+1} - T_{\mathrm{s}}^{i,j-1}}{R_{\mathrm{p},j}} \\ &\quad + \alpha_{\mathrm{air}} A_{\mathrm{c}}(T_{\mathrm{s}}^{i,j} - T_{\mathrm{air}}^{i,j}) + \alpha_{\mathrm{f}} A_{\mathrm{c}}(T_{\mathrm{s}}^{i,j} - T_{\mathrm{f}}^{i,j}) \\ &= -r_{\mathrm{CH_4}}\Delta H_{\mathrm{ref}} - r_{\mathrm{CO}}\Delta H_{\mathrm{shift}} \\ &\quad - r_{\mathrm{H_2}}(\Delta H_{\mathrm{electro}} + 2UF) - \dot{Q}_{\mathrm{p,preref}}^{i,j}\end{aligned} \tag{14}$$

In words, the heat conduction in *i*- and *j*-direction plus the convection to air and fuel equals the heat conversion of reforming, shift and electrochemical reaction and the radiation to the pre-reformer. The latter is only different from zero at the edges of the cell (thus, $i = 1$, $i = 26$, $j = 1$ or $j = 26$) and where $T_{\mathrm{s}}^{i,j} > T_{\mathrm{black}}$ and is in these cases

$$\dot{Q}_{\mathrm{p,preref}}^{i,j} = \varepsilon\sigma A_{\mathrm{s}}((T_{\mathrm{s}}^{i,j})^4 - (T_{\mathrm{black}})^4) \tag{15}$$

with an emissivity of $\varepsilon = 0.8$. The tubular model is more complex, as it comprises three separate gas channels and furthermore includes radiation between the injector tube and the cathode.

The heat balance for the fuel is analogous to the planar model, however one-dimensional:

$$\frac{T_{\mathrm{f}}^{i} - T_{\mathrm{s}}^{i}}{R_{\mathrm{t1}}} = \sum_{\mathrm{co}}^{\mathrm{co_f}}(c_{\mathrm{p,co}}(T_{\mathrm{f}}^{i-1})n_{\mathrm{co}}^{i-1}T_{\mathrm{a}}^{i-1} - c_{\mathrm{p,co}}(T_{\mathrm{f}}^{i})n_{\mathrm{co}}^{i}T_{\mathrm{f}}^{i}) \tag{16}$$

The heat balance for the tube solid is extended by the radiation and irradiation terms and the pre-reformer duty:

$$\begin{aligned}&\frac{2T_{\mathrm{s}}^{i} - T_{\mathrm{s}}^{i+1} - T_{\mathrm{s}}^{i-1}}{R_{\mathrm{t,ax}}} + \frac{T_{\mathrm{s}}^{i} - T_{\mathrm{f}}^{i}}{R_{\mathrm{t1}} + \frac{1}{2}R_{\mathrm{t2}}} + \frac{T_{\mathrm{s}}^{i} - T_{\mathrm{a1}}^{i}}{R_{\mathrm{t3}} + \frac{1}{2}R_{\mathrm{t2}}} \\ &\quad + \dot{Q}_{\mathrm{s,rad}}^{i} - \dot{Q}_{\mathrm{s,irrad}}^{i} \\ &= -r_{\mathrm{CH_4}}\Delta H_{\mathrm{ref}} - r_{\mathrm{CO}}\Delta H_{\mathrm{shift}} - r_{\mathrm{H_2}}(\Delta H_{\mathrm{electro}} + 2UF) \\ &\quad - \dot{Q}_{\mathrm{t,preref}}\end{aligned} \tag{17}$$

where the radiative terms according to Fig. 4 can be expressed as:

$$\begin{aligned}\dot{Q}_{\mathrm{s,rad}}^{i} &= (0.3 + 2 \times 0.1 + 2 \times 0.08)\varepsilon\sigma A_{\mathrm{s}}(T_{\mathrm{s}}^{i})^4 \\ &= 0.64\varepsilon\sigma A_{\mathrm{s}}(T_{\mathrm{s}}^{i})^4\end{aligned} \tag{18}$$

and

$$\begin{aligned}&\dot{Q}_{\mathrm{s,irrad}}^{i} \\ &= \varepsilon\sigma[A_{\mathrm{inj}}(0.64(T_{\mathrm{inj}}^{i})^4 + 0.18(T_{\mathrm{inj}}^{i-1})^4 + 0.18(T_{\mathrm{inj}}^{i+1})^4) \\ &+ A_{\mathrm{s}}(0.1(T_{\mathrm{s}}^{i-1})^4 + 0.1(T_{\mathrm{s}}^{i+1})^4)]\end{aligned} \tag{19}$$

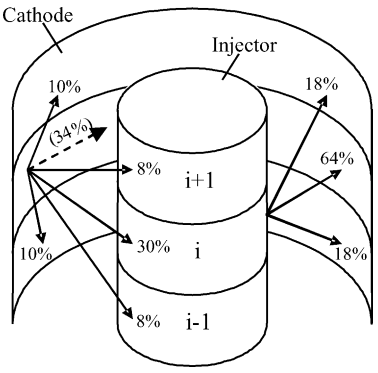

Fig. 4. Distribution of radiation energy between three adjacent control volumes in the tubular system.

with an emissivity of $\varepsilon = 0.8$. The pre-reformer duty $\dot{Q}_{\mathrm{t,preref}}$ is an input parameter, which must be determined externally to correspond with the pre-reformer inlet and outlet fuel composition enthalpies.

The heat balance for the cathode air between injector and cathode is:

$$\frac{T^i_{\mathrm{a1}} - T^i_{\mathrm{s}}}{R_{\mathrm{t3}} + \frac{1}{2}R_{\mathrm{t2}}} + \frac{T^i_{\mathrm{a1}} - T^i_{\mathrm{inj}}}{R_{\mathrm{t4}}} = \sum_{\mathrm{co}}^{\mathrm{co_{a1}}} (c_{\mathrm{p,co}}(T^{i-1}_{\mathrm{a1}}) n^{i-1}_{\mathrm{co}} T^{i-1}_{\mathrm{a1}} - c_{\mathrm{p,co}}(T^i_{\mathrm{a1}}) n^{\mathrm{i}}_{\mathrm{co}} T^i_{\mathrm{a1}}) \quad (20)$$

The heat balance for the injector tube is

$$\frac{T^i_{\mathrm{inj}} - T^i_{\mathrm{a1}}}{R_{\mathrm{t4}}} + \frac{T^i_{\mathrm{inj}} - T^i_{\mathrm{a2}}}{R_{\mathrm{t5}} + R_{\mathrm{t6}}} + \dot{Q}^i_{\mathrm{inj,rad}} - \dot{Q}^i_{\mathrm{inj,irrad}} = 0 \quad (21)$$

and again includes radiation and irradiation:

$$\dot{Q}^i_{\mathrm{inj,rad}} = (0.64 + 2 \times 0.18)\varepsilon\sigma A_{\mathrm{inj}} (T^i_{\mathrm{inj}})^4 = \varepsilon\sigma A_{\mathrm{inj}} (T^i_{\mathrm{inj}})^4 \quad (22)$$

and

$$\dot{Q}^i_{\mathrm{inj,irrad}} = \varepsilon\sigma A_{\mathrm{s}} (0.3(T^i_{\mathrm{s}})^4 + 0.08(T^{i-1}_{\mathrm{s}})^4 + 0.08(T^{i+1}_{\mathrm{s}})^4) \quad (23)$$

The gas composition in the injector is constant, as no reactions occur. Its heat balance is:

$$\frac{{T_{\mathrm{a2}}}^i - {T_{\mathrm{inj}}}^i}{R_{\mathrm{t5}} + R_{\mathrm{t6}}} = \sum_{\mathrm{co}}^{\mathrm{co_{a2}}} (c_{\mathrm{p,co}}({T_{\mathrm{a2}}}^{i+1}) n_{\mathrm{co}} {T_{\mathrm{a2}}}^{i+1} - c_{\mathrm{p,co}}({T_{\mathrm{a2}}}^i) n_{\mathrm{co}} {T_{\mathrm{a2}}}^i) \quad (24)$$

A check whether carbon deposition occurs can be included into the model by investigating the Gibbs energy of the reactions:

$$2\mathrm{CO} \rightleftarrows \mathrm{C} + \mathrm{CO_2} \text{ and } \mathrm{CH_4} \rightleftarrows \mathrm{C} + 2\mathrm{H_2} \quad (25)$$

If the Gibbs energy is less than or equal to zero, coking can theoretically occur. However, as the reactions are rather slow, small negative Gibbs energy values could possibly be tolerated. Nevertheless, Gibbs energy of zero was assumed to be the lower boundary for the carbon-deposition-free regime.

2.7. Boundary conditions and input parameters

The model requires temperature, pressure, composition and molar flow of the incoming gas streams as boundary conditions and therefore input parameters. The radiation heat from the cell edges to the pre-reformer is also a boundary condition which needs to be set according to the incoming (pre-reformed) fuel stream properties. This can be done by regarding the pre-reformer as a Gibbs reactor.

A further input parameter is the cell voltage, through which the current is determined by Eq. (9). The fuel utilization (FU), i.e. the fraction of fuel that is utilized by the fuel cell, is determined by evaluating Eq. (11) for each CV together with the solved heat balance equations.

In some cases it may be more desirable to define the fuel utilization instead of the operating voltage. This can be reached by a simple iteration routine, which modifies the voltage until the desired FU is reached. The electric current is a function of fuel flow, inlet concentration and fuel utilization and is thus also an implicit input parameter of the model.

In order to reduce calculation time both planar and tubular models do not consider special stacking particularities, i.e. except the specified heat exchange with the pre-reformer, the cell boundaries are adiabatic. This idealization means that indefinite stacks are modeled.

2.8. Numerical method and implementation

The implementation of the models results in a set of connected non-linear equations and some ancillary equations. The system is solved with the Newton–Raphson iteration procedure taken from Engeln-Muellges and Uhlig [12], which uses the partial derivatives of the equations to approach the solution.

The models have been implemented in Fortran 90, under the objective to integrate them into the flowsheet simulation software PRO/II by Simsci.

2.9. Type of results

The following results can be achieved with the SOFC models:

- Fuel utilization/voltage: depending on the running mode, one is an input parameter and the other one a result.
- Power output and global energy efficiency of the cell.
- Carbon deposition check: the CVs where carbon deposition is likely to occur.
- Black body temperature: the temperature an imaginary black body must have to receive the radiative heat flow that is required by the pre-reformer.
- Arrays of values for each CV (two-dimensional for the planar, one-dimensional for the tubular model)
  - Molar flow of all components.
  - Temperatures of air, fuel, solid (additional preheating air and injector for tubular model).
  - Temperature gradients in *i*- and *j*-direction of the planar and in axial direction of the tubular cell.
  - Electric current.
  - Molar amount of CO processed by the water gas shift reaction.

These results allow for a detailed study of the operation conditions of the fuel cells.

2.10. Model validation

The planar model has been validated against the models of Rechenauer [11] and Selimovic [3] using the input values of the IEA Benchmark Test [13]. The air and fuel flow rate were in both cases adjusted to the exact values selected by each compared model. The comparison in Table 5 shows that the planar model produces similar results in all shown parameters and a voltage deviation at identical fuel utilization and current density in the range of 2%.

The tubular model was validated using the experimental data and assumptions published by Campanari [4] for an atmospheric and a pressurized system. The input parameters and fuel utilization values of the experimental data have been simulated with the model, giving voltage and power as result. Input parameters and results are shown in Table 6. While the atmospheric case matches very well with a voltage deviation of only 0.8%, there is quite a high deviation in the pressurized case (13.3% in terms of voltage). However, the results are sensitive to the inlet temperature and fuel composition, which Campanari chose from a different work than the experimental results. If air and fuel inlet temperature for the model are increased by 90 K in case of the pressurized system, the voltage values match. As no complete set of input parameters and experimental results for tubular fuel cells was found in literature, we consider the exactness of the model as sufficient for the meanwhile. Once measurement data has been published, it is easy to calibrate the model to the data using parameter estimation.

Table 5
Validation of the planar model

	Rechenauer	Planar model	Selimovic	Planar model
Pressure (bar)	1	1	1	1
Fuel flow rate (mole s^{-1})	1.872×10^{-4}		1.784×10^{-4}	
Air flow rate (mole s^{-1})	3.047×10^{-3}		2.901×10^{-3}	
Inlet fuel and air temperature (K)	1173			
Fuel utilization (%)	85			
Inlet fuel composition (molar fraction)				
H_2	0.2626			
H_2O	0.4934			
CH_4	0.1710			
CO	0.0294			
CO_2	0.0436			
Voltage (V)	0.682	0.7	0.658	0.669
Voltage deviation (%)	2.64	2.64	1.67	1.67
Power (W)	20.46	21.12	19.74	19.02
Max. current density (A m^{-2})	4800	4570	6039	5798
Min. current density (A m^{-2})	1100	1260	804	1665
Max. solid temperature (°C)	1061	1036	1130	1063
Min. solid temperature (°C)	823	845	741	849
Max. temperature gradient (K mm^{-1})	7.09	8.95	n.a.	

Table 6
Validation of the tubular model

	Atmospheric (plant A)	Tubular model	Pressurized (plant B)	Tubular model
Pressure (bar)	1.05	1.05	3.5	3.5
Fuel flow per tube (mole s^{-1})	1.511×10^{-3}		2.287×10^{-3}	
Air flow per tube (mole s^{-1})	1.055×10^{-2}		1.290×10^{-2}	
Inlet fuel temperature (K)	823		860	
Inlet air temperature (K)	1104		1048	
Fuel utilization (%)	69		69	
Inlet fuel composition (molar fraction)				
H_2	0.258		0.226	
H_2O	0.284		0.334	
CH_4	0.11		0.131	
CO	0.057		0.057	
CO_2	0.228		0.241	
N_2	0.063		0.011	
Voltage (V)	0.69	0.695	0.639	0.564
Voltage deviation (%)	0.72	0.72	13.3	13.3
Power (W)	104.8	105.6	157.0	138.6

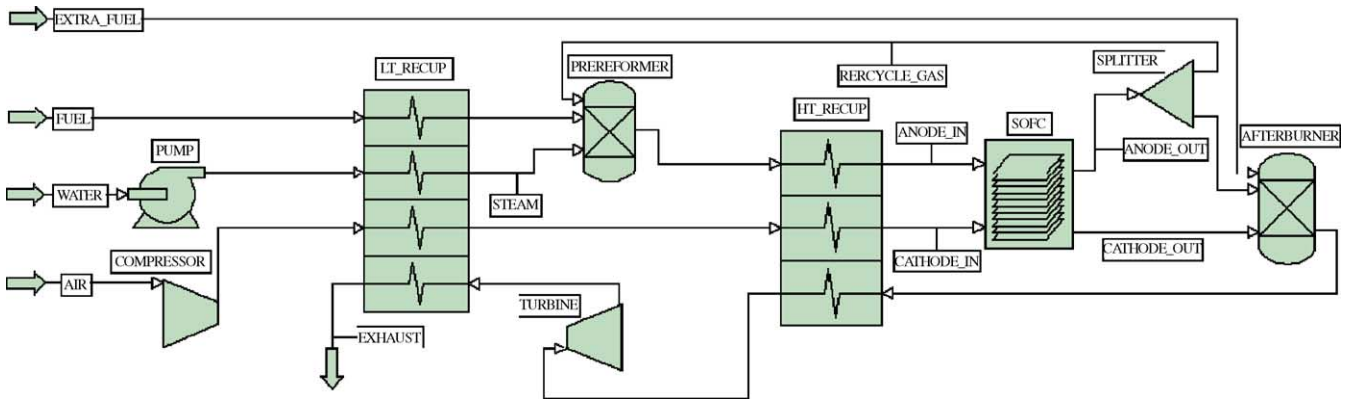

Fig. 5. Applied gas turbine cycle.

3. Hybrid cycle performance simulation

3.1. SOFC/GT cycle design and simulation premises

The modeled SOFC/GT cycle is illustrated in Fig. 5. The GT cycle and balance of plant equipment is implemented in PRO/II, where Fortran-based SOFC models are implemented as a user added subroutine in the flowsheet. The gas streams of the SOFC are defined by linking of the SOFC model in the flowsheet. The heat duty to the pre-reformer as well as voltage respectively fuel utilization of the SOFC models are entered via an entry form and can also be linked to process variables. Methane is partially reformed in a pre-reformer, which is modeled as a Gibbs reactor and thermally connected to the fuel cell. The operation temperature of the pre-reformer is controlled to equilibrium temperature of the desired pre-reforming level.

The cycle comprises two-stage cascaded heat recuperation, anode gas recycling and an afterburner for the unspent and possibly additional fuel. The pressure of the recycle gas is raised to the fresh fuel gas level by an ejector (not displayed). Losses in the ejector are not included in the energy balance of the system, as the fuel is assumed to be delivered directly from a high-pressure grid.

Table 7 summarizes the setup of the GT cycle. Most assumptions were taken from Pålsson [14]. The specifications that are most significant for the cycle or subject to changes during the parameter studies are shown below in Table 8.

The fuel cell input parameters, such as gas composition, pressure and temperature of the streams ANODE_IN and CATHODE_IN (Fig. 5) and the duty of the pre-reformer, are calculated in the PRO/II model and sent to the Fortran submodule. The solver operation mode and one further input parameter (operation voltage or fuel utilization level) must be specified in the SOFC module itself to be transferred to the Fortran routine.

The most important operational constraints for the planar SOFC are the maximum allowable temperature (T_{max}) of 1300 K [3] and the maximum temperature gradient in the area of 5 K mm^{-1} [11] to avoid thermal cracking of the cell. The tubular SOFC is less sensitive to this effect since the tubes can expand freely and the temperature is more uniform. Another issue is to avoid operational modes where coking can occur.

Table 7
GT cycle setup

Item (Fig. 5)	Specification
EXTRA_FUEL	100% Methane; 288 K/20 bar
AIR	288 K/1 bar
WATER	283 K/1 bar
COMPRESSOR	81% Adiabatic efficiency
TURBINE	84% Adiabatic efficiency; outlet pressure 1.1 bar
PRE-REFORMER	Gibbs reactor; pressure drop 2%; operating temperature 800–900 K (controlled to achieve desired pre-reforming degree); heat demand supplied by fuel cell
AFTERBURNER	Gibbs reactor; pressure drop 5%; complete combustion; coupled with HT_RECUP for heat transfer
SOFC	User added subroutine; pressure drop 2%; radiative heat loss is the PRE-REFORMER heat demand; specification of either operating voltage or fuel utilization
LT_RECUP	Pressure drop 2% for inlet air and exhaust (rest 0); cold products outlet 50 K below hot product inlet (1st and 2nd law check)
HT_RECUP	Pressure drop cold side 2% (hot side is coupled with AFTERBURNER), cold product temperature specified (fuel cell specifications)

Table 8
Base case parameters

Parameters	Planar	Tubular
Pressure (bar)	3	3
Steam to carbon ratio[a]	2.5	2.5
Fuel utilization (%)	85	85
Recirculation degree (%)	0	0
Fuel inlet temperature (K)	1123	1123
Air inlet temperature (K)	1123	923
Fuel flow per active cell area (mole m^{-2} s^{-1})	4.5×10^{-3}	3.8×10^{-3}
Air excess ratio, λ	6	4
Pre-reforming degree (%)	30	50

[a] Molar flow of steam divided by molar flow of methane in the fresh fuel entering the pre-reformer.

Table 9
Operational data at base case

System	Parameter	Planar system	Tubular system
Fuel cell	Efficiency (LHV, %)[a]	62.5	52.5
	Voltage[b] (V)	0.700	0.616
	Max. temperature (K)	1272	1130
GT cycle	TIT (K)	747	1185
	Spec. turbine power production[c] (%)	55	69
	Spec. compressor power consumption[c] (%)	48	37
SOFC/GT cycle	Total efficiency (LHV, %)	58.5	63.1

[a] Based on the fuel taking part in the electrochemical reaction.
[b] Voltage is a result of the model when a certain fuel utilization is determined.
[c] Ratio between power of compressor/turbine and fuel cell power.

3.2. Setup of a base case

As a starting point for parameter variations, a base case is defined. Table 8 shows the base case assumptions for the parameters that are of high importance for the cycle thermodynamics and fuel cell operation. The values represent typical values for SOFCs. A recirculation degree of zero has been chosen for calculation time reasons. Due to the nature of the different designs, some values differ for the planar and tubular model:

- The air inlet temperature of the tubular fuel cell lies well below the one of the planar SOFC in order to achieve the designated internal cooling effect of the preheating injector air.
- The fuel flow rate has been adapted geometry-specifically (i.e. fuel flow per m^2 s) in order to achieve comparable points in the operation ranges of the fuel cells. A value from Rechenauer [11] was chosen for the planar cell and a value from Yi [15] for the tubular cell.
- The tubular model is known to tolerate lower air excess ratios due to the ability of the tubes to tolerate higher thermal gradients by expanding freely. Therefore an air excess of 4 has been chosen for the tubular model.
- The pre-reforming degree of the tubular cell must be comparably high due to problems with the convergence of the model.

Table 9 shows main operational data of the fuel cell and the GT cycle for the base case. The listed fuel cell efficiency is based on the fuel taking part at the electrochemical reaction, i.e. without considering the fuel utilization. Power production and consumption by the gas turbine and compressor is given specifically as percentage of the fuel cell stack power. The power supplement of the GT cycle in relation to the fuel cell can thus be seen as the difference between specific turbine and compressor power. It is visible that in the planar system, the net power output from the GT cycle is very low and the system efficiency is below the fuel cell efficiency. This is mainly due to the low turbine inlet temperature. The tubular fuel cell has a lower efficiency due to the higher ohmic resistance, which leads to a higher heat production. The additional amount of heat is however spent on internal preheating of the incoming air flow. This in turn reduces the duty of the high temperature recuperator, which leads to a higher turbine inlet temperature (TIT) and therewith a higher output of the GT cycle.

3.3. Parameter study

A parameter study was performed by varying only one parameter at a time while keeping the others at their base case values. Figs. 6 and 7 shows the system efficiency for the planar design (left) and the tubular design (right) as a function of the varied parameters. The *y*-axis covers the same range

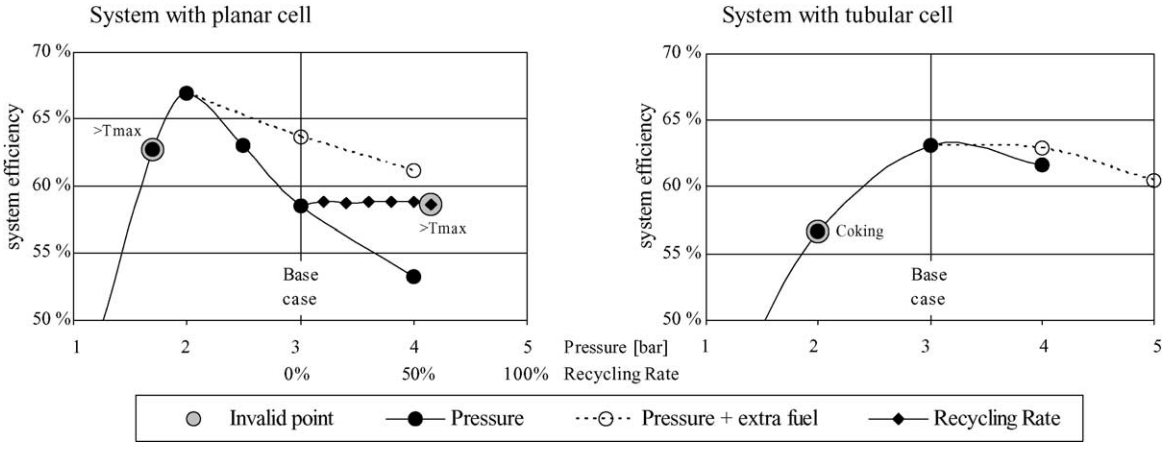

Fig. 6. Dependency of system efficiency on pressure and recycling rate.

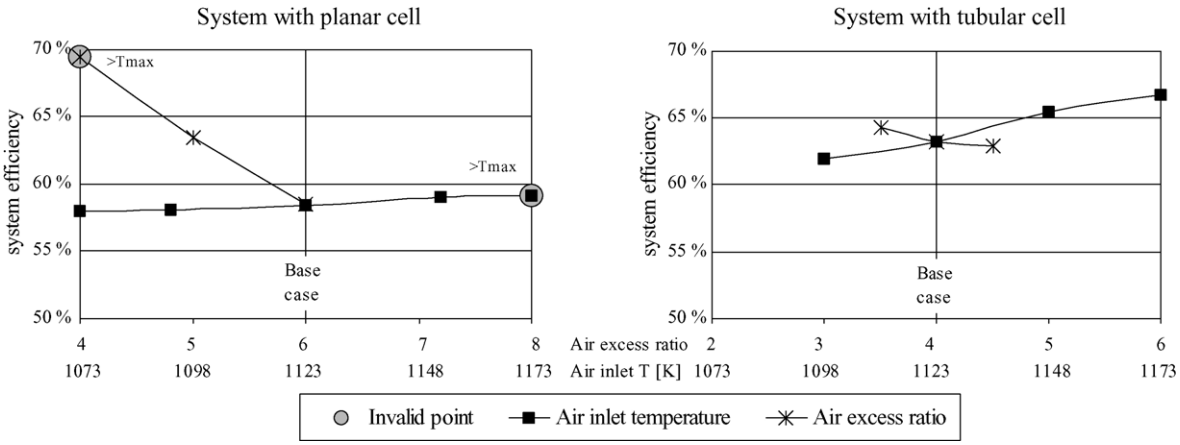

Fig. 7. Dependency of system efficiency on air inlet temperature and air excess ratio.

of values for all diagrams. The *x*-axis has been designed to show the base case value of each parameter and system in the middle, while the gradient is the same for each parameter. Figs. 8 and 9 show the gas turbine cycle power supplement to the fuel cell power in the same manner.

As can be seen from the bold line of Fig. 8, the turbine power output of the planar system decreases strongly at a pressure higher than 2 bar. That is because the TIT decreases due to a shift of the heat recovery duty towards the high-temperature recuperator. This can be countered by adding extra fuel to the afterburner. The dashed line in Figs. 6 and 8 shows the performance at a TIT controlled to 1173 K by this method. It can be seen that the power production of the planar system can be strongly increased at the cost of only a slight decrease in efficiency by adding extra fuel. For the tubular system, this effect is also present, however it is weaker. The system power output is furthermore increased slightly by the fuel cell efficiency increase at higher pressure.

Reducing the air flow rate would cause a high gain in efficiency of the planar system due to reduced heat and energy losses (see Fig. 6, left). However, the high excess air is required for cooling reasons, hence the maximum temperature is exceeded for an air excess ratio of 4. The tubular cell has better internal heat management and can thus be operated at a lower air excess ratio. This fact compensates for the lower efficiency of the tubular SOFC stack.

The air inlet temperature strongly influences the average temperature in the cell. Thus, a higher air inlet temperature has a positive influence on the reaction kinetics and results in higher fuel cell efficiency. This causes the tubular system efficiency to increase with increasing fuel cell air inlet temperature as can be seen in Fig. 7. In the planar system, this effect is partially compensated by the decreasing TIT caused by a higher heat transfer in the high-temperature recuperator. Regarding the internal temperature charts of the fuel cell, it turns out that the maximum local temperature of the SOFC can be effectively controlled by the air inlet temperature.

The influence of the recycling rate on the planar system efficiency is rather low. However it should be mentioned that anode gas recycling rate has practical advantages as it reduces the system complexity by providing steam and also decreases internal temperature gradients of the fuel cell. The recycling rate could not be checked in the tubular case due to solver stability reasons, but the same tendency could be expected.

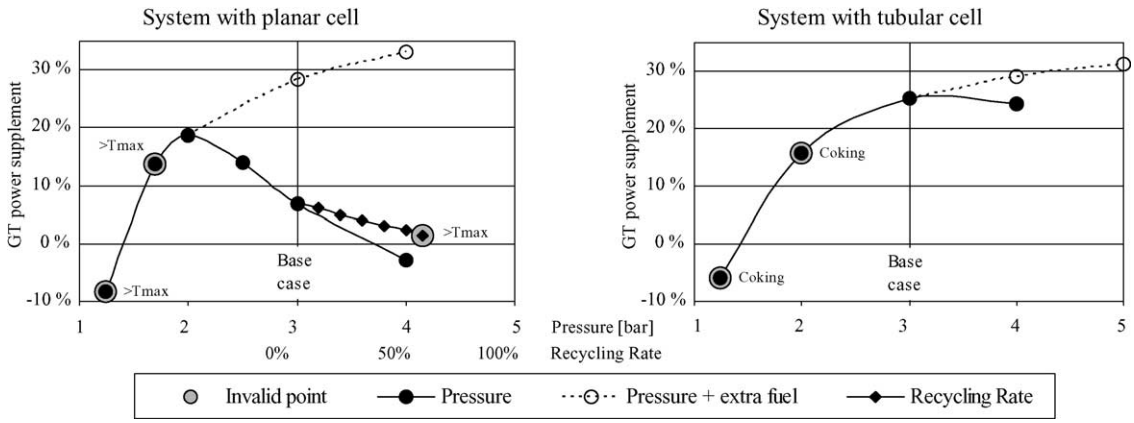

Fig. 8. Dependency of gas turbine power supplement on pressure and recycling rate.

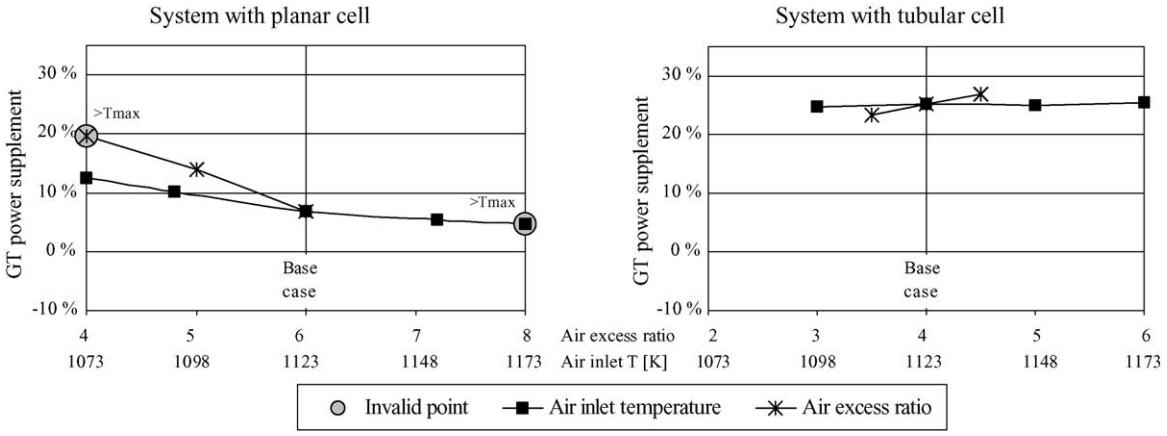

Fig. 9. Dependency of gas turbine power supplement on air inlet temperature and air excess ratio.

3.4. Near-optimum case

In accordance with preliminary studies, the pressure of the planar system has been reduced to 2 bar and the air inlet temperature of the tubular system is raised to 973 K in order to study a near-optimum case. Base case parameters have been assumed for the remaining values. For the planar system, the maximum local temperature in the cell is at its limit. Simulations with a combination of lower air inlet temperature and lower air excess ratio did not show significant efficiency improvements. Table 10 shows relevant operational data at the near-optimum point.

Fig. 10 displays charts for solid temperature, current density, hydrogen and methane of the planar fuel cell at near-optimum operation. The temperature distribution shows that the maximum local temperature occurs at the air outlet and near the fuel outlet. Close to the outlet of the fuel flow, temperature decreases due to decreasing electrochemical reaction

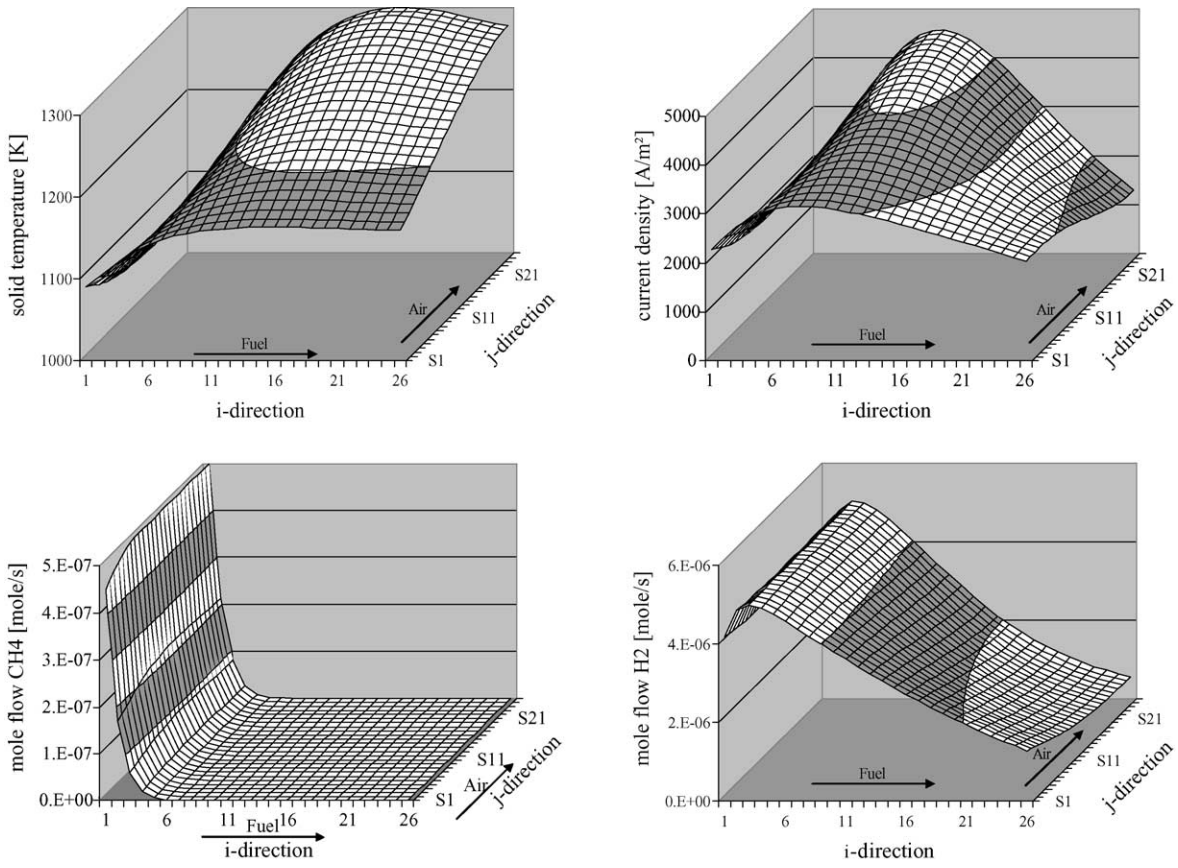

Fig. 10. Temperature, current density, H_2 and CH_4 molar flow fields for the planar cell at near-optimum case.

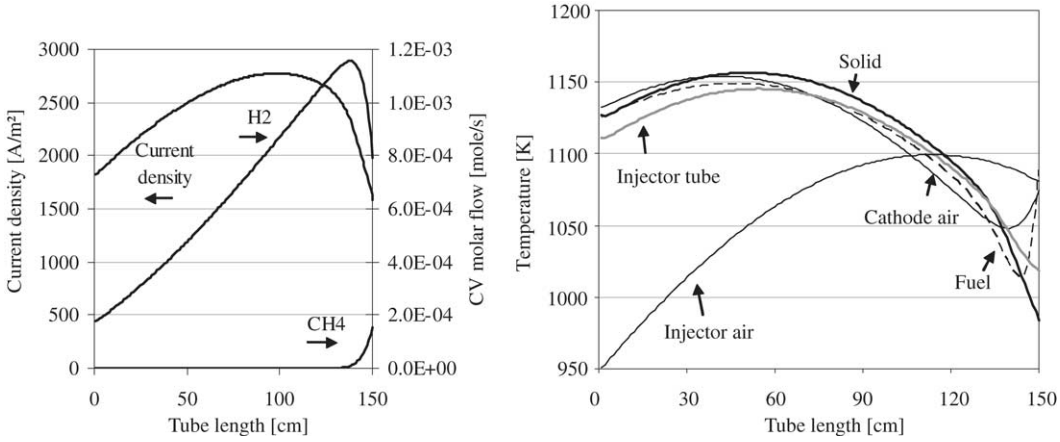

Fig. 11. Temperatures, current density, H_2 and CH_4 molar flow fields for the tubular cell at near-optimum case.

Table 10
Operational data at near-optimum case

System	Parameter	Planar system	Tubular system
Fuel cell	Efficiency (LHV, %)	62.5	54.7
	Voltage (V)	0.705	0.641
	Max. temperature (K)	1300	1175
GT cycle	TIT (K)	1191	1220
	Spec. turbine power[a] (%)	51	68
	Spec. compressor power[a] (%)	28	35
	Total efficiency (LHV, %)	66.9	66.7

[a] Ratio between power of compressor/turbine and fuel cell power.

rate, cooling by the air and the radiation to the pre-reformer. The figure also shows that most of the methane is reformed at the inlet. The hydrogen mole flow decreases steadily towards the fuel outlet. The current density as a measure for the electrochemical reaction is mainly influenced by the temperature (through the ohmic resistivity) and the amount of hydrogen (through the Nernst equation). Thus the maximum lies between the hydrogen and the temperature maximum.

Fig. 11 shows parameters in the tubular cell. The injector air flows to the right (downwards), while the reacting gases flow to the left (upwards) in these diagrams. It can be seen that the injector air is effectively cooling the cell in the upper section, while it provides some heat for the reforming reaction in the lower section. Hydrogen and methane mole flows and the current density behave similar to the planar model in *i*-direction.

4. Conclusions

The current paper describes two steady-state finite volume models for planar and tubular fuel cells. Although several simplifications and assumptions have been done during the development of the models, they provide reasonable results. This has been proven for the planar model by validation against the models from Selimovic [3] and Rechenauer [11]. A validation of the tubular model against Campanari [4] shows a certain divergence at high-pressure. However, no complete set of parameters from one source was found in literature, making a proper validation impossible.

It has been shown that hybrid systems can achieve efficiencies above 65% with the planar as well as the tubular geometry SOFC. The main difference between the planar and the tubular system for the gas turbine cycle is the internal pre-heating of the air in the tubular system, permitting a lower air inlet temperature. The thereby reduced amount of high-temperature heat in the pre-heating section allows for a higher-pressure ratio at acceptable turbine inlet temperatures. The tubular system's ability to be operated at lower air excess ratio lowers the exhaust gas losses and increases the afterburner temperature, improving the effectiveness of the GT cycle. These effects compensate for the lower efficiency of the tubular fuel cell stack, which is caused by its higher ohmic resistivity.

The introduction of additional fuel to the afterburner increases the turbine inlet temperature and therewith the GT cycle yield. The efficiency of both systems at higher pressures can be raised by this method. In case of the planar system, the power supplement of the GT cycle can be significantly increased. This effect could play a roll for the power output control of hybrid systems capable of pressure variation.

References

[1] H. Karoliussen, et al., SOFC stack modeling with internal reforming, in: Proceedings of the fourth IEA Workshop on SOFC, Lausanne, Switzerland, August, 1992.
[2] K. Hassmann, SOFC power plants, the Siemens–Westinghouse approach, Fuel Cells 1 (2001) 1.
[3] A. Selimovic, SOFC Modelling for SOFC/GT Combined Cycle Simulations, Licenciate Thesis, Lund University, Sweden, 2000.
[4] S. Campanari, P. Iora, Definition and sensitivity analysis of a finite volume SOFC model for a tubular cell geometry, J. Power Sources 132 (2004) 113–126.
[5] U.G. Bossel, Final Report on SOFC Data, Facts and Figures, Swiss Federal Office of Energy, Berne, 1992.

[6] K. Nisancioglu, Natural Gas Fuelled Solid Oxide Fuel Cells and Systems, Swiss Federal Office Of Energy, 1989, p. 96.
[7] T. Ota, M. Koyama, C. Wen, K. Yamada, H. Takahashi, Object-based modeling of SOFC system: dynamic behavior of micro-tube SOFC, J. Power Sources 5249 (2003) 1–10.
[8] W.M. Rohsenow, J.P. Hartnett, Y.I. Cho, Handbook of Heat Transfer, third ed., McGraw-Hill, 1998.
[9] H. Yakabe, et al., 3-D model calculation for planar SOFC, J. Power Sources 102 (2001) 144–154.
[10] F.P. Incropera, D.P. Dewitt, Fundamentals of Heat and Mass Transfer, fifth ed., Wiley and Sons Inc., 2002.
[11] C. Rechnenauer, E. Achenbach, Dreidimensionale mathematische Modellierung des stationären und instationären Verhaltens oxidkeramischer Hochtemperatur-Brennstoffzellen, Doctoral Thesis, Forschungszentrum Jülich, Germany, 1993.
[12] G. Engeln-Muellges, F. Uhlig, Numerical Algorithms with C, Springer-Verlag, 1996.
[13] E. Achenbach, International Energy Agency, Annex II, Modelling and Evaluation of Advanced SOFC, Subtask A: Numerical Modelling, Experimental Data Base and Validation, Activity A2: Stack Modelling, 1995.
[14] J. Pålsson, Thermodynamic Modelling and Performance of Combined SOFC and GT Systems, Doctoral Thesis, Lund University, Sweden, 2002.
[15] Y. Yi, T.P. Smith, J. Brouwer, A.D. Rao, G.S. Samuelsen, Simulation of a 220 kW hybrid SOFC gas turbine system and data comparison, in: Proceedings of the Electrochemical Society, vol. 7, 2003.

Paper II

Safe dynamic operation of a simple SOFC/GT hybrid system

Stiller, C., Thorud, B., Bolland, O.

ASME Turbo Expo 2005, Reno-Tahoe, USA, 6–9 June 2005, Paper 2005-GT-68481.

Accepted for publication in ASME Journal of Engineering for Gas Turbines and Power, anticipated April 2006.

Proceedings of GT2005
ASME Turbo Expo 2005: Power for Land, Sea and Air
June 6-9, 2005, Reno-Tahoe, Nevada, USA

GT2005-68481

SAFE DYNAMIC OPERATION OF A SIMPLE SOFC/GT HYBRID SYSTEM

Christoph Stiller
Tel. +47 735 937 23
Christoph.Stiller@ntnu.no

Bjørn Thorud
Tel. +47 735 939 34
Bjorn.Thorud@ntnu.no

Olav Bolland
Tel. +47 735 916 04
Olav.Bolland@ntnu.no

The Norwegian University of Science and Technology (NTNU)
Department of Energy and Process Engineering (EPT)
Kolbjørn Hejes vei 1B
N-7491 Trondheim, Norway

ABSTRACT

The current work shall prove the feasibility and show methods to safely operate a simple SOFC/GT hybrid system under part-load and load change. Dynamic and steady state studies on a detailed model of a SOFC/GT hybrid system have been performed. A design point is selected. Steady-state part-load behaviour is shown by means of performance maps. An operation line with fairly constant temperatures in the upper part-load regime and an almost constant efficiency down to app. 25% part-load is proposed and the dynamic behaviour of the system on rapid load changes is investigated. Strategies for the dynamic controlling of power by manipulating fuel flow are shown that might enable the system to adapt to a new setpoint power quite quickly.

Keywords: SOFC, Hybrid System, Dynamic Model, Part-load

INTRODUCTION

A large amount of modelling work [1-4] and a demonstration plant [5] have proven that a solid oxide fuel cell (SOFC) integrated with a gas turbine (GT) has a potential for high efficiency electricity production with low environmental emissions. However, these types of systems face many challenges when it comes to load change and part-load operation. A gas turbine alone has good dynamic properties compared to the SOFC, but part-load performance can be rather poor. In any operational point, compressor surge must be prevented. A SOFC is generally able to respond quickly to load changes [6], but it might be destroyed or seriously degraded either due to thermally induced stresses caused by different thermal expansion coefficients in the cell materials or from carbon deposition at the anode. Another phenomenon that may occur during load change is backflow of gas from the burner to the anode cycle. These incidents must not occur in any operation instance.

Results from part-load operation modelling have already been discussed by some authors. Costamagna et al. [7] investigated a hybrid system using a non-dimensional tubular SOFC model. In all simulations they assumed constant fuel utilisation (FU). If shaft speed was assumed constant, power output could only be controlled by varying the fuel flow. These simulations showed large variations in air utilisation (AU) and loss of efficiency for fixed shaft speed when operating at part-load. For variable shaft speed, however, AU and FU as well as SOFC inlet temperatures could remain fairly constant in part-load operation with only a small penalty on system efficiency. This effect was mainly due to increased recuperator efficiency owing to reduced air flow rate.

Campanari [8] also used a non-dimensional tubular SOFC model to investigate the hybrid system. Assuming constant FU of 80%, for constant shaft speed they suggested reducing AU and current density for part-load. This approach will reduce power output of the SOFC as well as the turbine inlet temperature (TIT) and consequently the power output of the GT. For variable shaft speed they suggested to reduce air flow rate and current density to maintain a constant AU. However, a reduction in air flow rate leads to pressure reduction and therewith higher turbine outlet temperature (TOT) and thus higher recuperator outlet temperatures. They concluded that for maintaining constant TIT, the current density has to be reduced further.

Chan et al. [3] also investigated a non-dimensional tubular SOFC-type in a hybrid system. In their system, power is reduced by shifting the load from the SOFC to the GT through introducing fuel to the combustor, which results in strong reduction of the system efficiency. This method also implies

that a SOFC bypass should be implemented for both fuel and air. Due to the low part-load efficiency, they state that this method is mainly for short term load reduction. The aim was to maintain a relatively high SOFC temperature.

Pålsson and Selimovic [9] used a 2-dimensional planar SOFC model for part-load studies. Design point was set where the compressor flow matched the cooling requirement of the SOFC. They introduced an air heater/cooler prior to the SOFC entry in order to meet the requirements for the air inlet temperatures at part-load operation. TIT was kept constant and shaft speed was varied. At part-load operation, increased FU and low GT part-load efficiency led to increased power contribution from the SOFC. Due to the problems associated with matching of the system components, they concluded that the load range for hybrid systems should be limited to 55 – 100%, corresponding to a load variation of the GT of 20 – 100%.

Kimijima and Kasagi [10] studied part-load of a 30 kW simple recuperated cycle using a non-dimensional SOFC model. Variable and fixed shaft speed operations are compared. FU is kept constant, even though it is mentioned that FU could be increased at part-load operation. They conclude that variable shaft speed operation is favourable in terms of part-load performance; however the higher TOT could cause problems.

All above mentioned authors have identified inlet and outlet gas temperatures as well as air and fuel utilisation of the SOFC as important parameters for part-load operation of hybrid systems. Maintaining a constant SOFC operation temperature is important to avoid thermal cracking, but this might be difficult to achieve at reduced pressure as the TOT increases and consequently the recuperator outlet temperatures.

We have recently investigated a SOFC system with recycle and pre-reformer to be fitted into a hybrid system [11]. Performance maps were introduced to illustrate the relationships between the most important SOFC parameters over air flow and either FU or AU, while keeping the other of the two latter parameters constant. Based on these maps, it was found out that strategies with fairly constant temperatures in the SOFC seem feasible. Due to the lack of a GT model, SOFC inlet temperature was assumed constant and the pressure was assumed proportional to the air flow. This was the main limitation of this work.

The current work presents a detailed dynamic model of a tubular SOFC system integrated into a simple recuperated GT cycle. It shall prove the feasibility and show methods to operate such a system in part-load and load change without any of the critical phenomena to occur. The system is designed for a certain nominal performance. The selection of the design point is discussed and vital parameters are highlighted. Furthermore, part-load behaviour as a function of the controllable parameters, i.e. fuel flow and shaft speed, is investigated. The dependency of crucial system parameters on the controllable parameters is displayed in steady state performance maps. From the maps, valid ranges of the controllable parameters and advantageous operation lines are derived. Applying the derived operation lines, transient behaviour of the crucial parameters during load-changes is investigated. Considering steady state and transient results, a strategy for safe operation of the investigated system is proposed. Finally, an overview on further opportunities is given.

NOMENCLATURE

Abbreviations

FU	- Fuel utilisation
GT	- Gas turbine
HEX	- Heat exchanger
RFF	- Fuel flow relative to design point
RP	- Net power relative to design point
RPM	- Rounds per minute
RSS	- Shaft speed relative to design point
SM	- Surge margin
SOFC	- Solid oxide fuel cell
TIT	- Turbine inlet temperature
TOT	- Turbine outlet temperature

SOFC AND GT-CYCLE MODEL

The investigated hybrid cycle is shown in Fig. 1. The ducts account for time delay of the flows under transient conditions. The SOFC system design (inside the vessel in Fig. 1) is similar to that of Siemens-Westinghouse. This type of design has been described by other authors [12, 13]. The model incorporates pre-reformer, afterburner and recirculation and mixing chamber, where part of the anode exhaust gas is admixed to the fresh fuel in an ejector in order to supply steam to the steam reforming and shift reaction. Required valves for start-up, shut-down and failure have not been included. The whole model is implemented in the equation based modelling tool gPROMS [14]. The sub-models comprise the following:

- The SOFC model is spatially discretised and fully dynamic in terms of gas transport and heat transfer, allowing the study of temperature distributions. Gas flows are treated as 1D plug flows, while the solid structures are modelled by a 2D discretisation scheme in axial and radial direction, neglecting effects in the circumferential direction. The model accounts for the effects of internal reforming, activation and concentration polarisation, ohmic resistance and pressure losses. A more detailed description of the model is given in Appendix 1.
- As the temperature distribution inside the pre-reformer is of minor interest, it is modelled as a non-dimensional Gibbs equilibrium reactor where reforming and water-gas shift reactions take place. It is thermally connected to the fuel cell tube. The consumed heat is supplied by radiation from the anode surface, adjusted by a shape factor to meet a certain pre-reforming degree at the design case. Gas residence time in the pre-reformer is accounted for by ducts up- and downstream the pre-reformer.
- The afterburner is non-dimensional and adiabatic and completely combusts the remaining anode exhaust gas together with the cathode air. By mixing cathode and anode exhaust streams, it causes pressure equalisation of these flows upstream.
- The afterburner exhaust is preheating the inlet air by a counter-flow tube-shell set-up, where the tube is the prolongation of the fuel cell air supply tube. The model accounts for thermal inertia, pressure loss and gas residence times. The approaches are equal to the SOFC model.

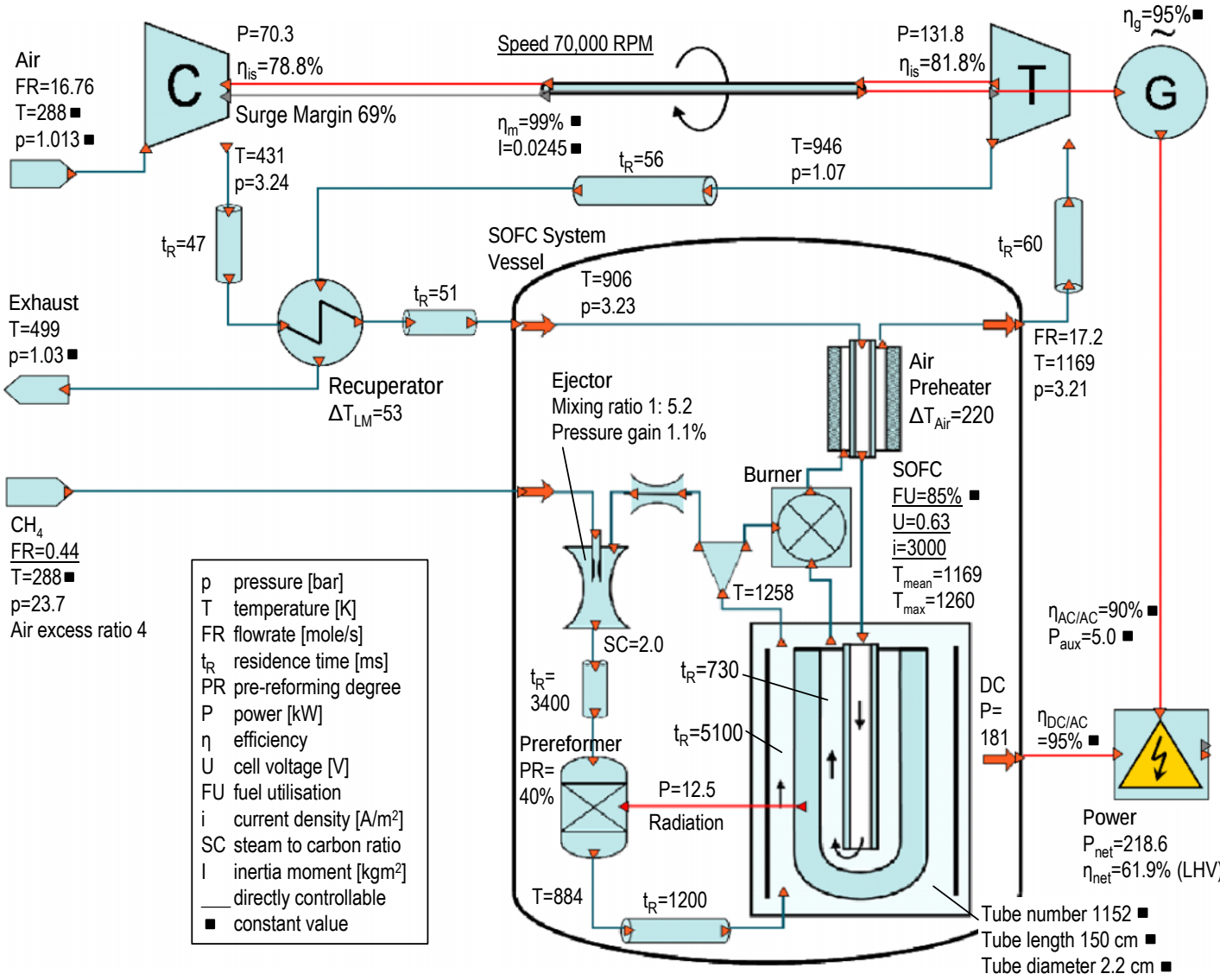

Figure 1: Cycle layout and design point values (square-marked values remain always constant).

- The pressure loss in the anode loop is overcome by an ejector. High induced (recycle) flow rates at low pressure differences are typically achieved by subsonic mixing ejectors. The actuating flow is accelerated to supersonic speed in a Laval nozzle before it enters the mixing chamber. The ejector model is based on section-wise momentum balances and has been validated against data from Marsano et al. [15]. Pressure losses are included by a fixed throttle valve.
- The ducts are adiabatic and frictionless. Their only purpose is to account for gas residence time.
- The HEX is a stack of counter-flow plate-fin type. A 2-dimensional distributed model is applied that accounts for thermal inertia, pressure loss and gas residence times. The approaches are equal to the SOFC model.
- Generator and power electronics account for transformation efficiencies which are assumed to be constant. A constant power sink accounts for power consumption of auxiliaries and transformation efficiency decrease at low load.
- The compressor is based on the performance map of a small centrifugal research compressor by the German Aerospace Centre [16]. The map is understood as a generic radial compressor map and therefore it has been scaled in terms of reduced mass flow, pressure ratio and shaft speed to fit the design case. The map has been modelled using polynomials of 4th and 5th order for reduced mass flow, pressure and efficiency as functions of reduced shaft speed and operation (β) line. A surge margin (SM) is calculated as follows:

$$SM = \frac{\pi_{surge}(\dot{m}) - \pi(\dot{m}, n)}{\pi(\dot{m}, n)} \quad (1)$$

where $\pi(\dot{m}, n)$ is the actual pressure ratio at the actual mass flow and reduced shaft speed and $\pi_{surge}(\dot{m})$ is the surge pressure ratio at the actual mass flow. An iso-line representation of the compressor characteristics is shown in Appendix 2.

- The turbine is based on the performance map of a small radial turbine [16] which is, similar to the compressor map, scaled to fit the design case. An ellipse approach has been used for the relationship between reduced mass flow, reduced shaft speed and operation (β) line. Pressure ratio and efficiency have been modelled through polynomials. An iso-line representation of the turbine characteristics is shown in Appendix 2.
- The shaft model includes acceleration/deceleration of the shaft through moment of inertia of the moving parts:

$$\frac{d\omega}{dt} = \frac{P_B}{I \cdot \omega} \quad (2)$$

Where ω is the angular shaft speed in [rad·s^{-1}], I is the moment of inertia in [kg·m^2], and P_B is the power balance

$$P_B = \eta_m P_{Turb} - P_{Comp} - P_{Gen} \text{ in [W]}. \quad (3)$$

The resulting whole model consists of approximately 9,000 algebraic and 2,000 state variables. The simulations were performed on a 2.5 GHz Intel Pentium-4 processor PC. Calculation time for a steady state point was approximately 5-10 seconds. The solver for dynamic calculations uses flexible time increments, thus calculation time depends on the momentary fluctuation rate of the variables. A calculation time of about 5 minutes was required for the dynamic performance studies shown below.

DESIGN POINT

Before part-load behaviour can be studied, a design point has to be defined. All relevant cycle data are displayed in Fig. 1. Most of the data are similar to recent literature on hybrid cycles [3,7,8,10] and public data from Siemens-Westinghouse. Values in the figure marked with a square are constant during all simulations. The design point and system dimensioning is furthermore based on the following assumptions:

- The system size is determined based on the Siemens-Westinghouse stack design which incorporates 1152 tubular cells [17].
- Pure methane is supplied as fuel.
- A length of 0.5 m was chosen for the air preheat tube, yielding a temperature increase of 220 K at design point.
- The ducts have a length of 1 m and are dimensioned for gas velocities around 20 m/s at design point. The residence times are calculated utilising the ideal gas law. Therefore they will vary slightly in other operation points. Residence times before and after the pre-reformer account for the actual pre-reformer residence time.
- The fuel utilisation (FU) is determined from current and fuel flow, as these parameters can be measured in a real system. Setting FU constant hence means maintaining a constant ratio of current to fuel flow. While this in steady state provokes a constant content of combustibles in the anode exhaust gas, the content may vary during dynamic operation due to pressure change and gas transport delay. Due to the variations of the heating value of the exhaust gas, this may cause severe oscillations in burner temperature during load change. The common fuel utilisation value of 85% has been chosen.
- The ejector has been dimensioned for supplying a steam to carbon ratio of 2 in the design point. The difference in static pressure of induced and actuating gas flow in the mixing zone is vital for the ejector performance. According to Johannesen [18], a lower actuating flow pressure than induced flow pressure, causes a strong reduction in induced flow rate, while a higher actuating flow pressure does not significantly increase induced fluid flow rate. For being able to reduce the fuel flow rate for part-load operation while maintaining a high recycle ratio, the inlet pressure of the actuating fluid at design point must be high. A value of 23.7 bar was chosen for design point.
- The recuperator is dimensioned in order to achieve a high amount of heat recuperation at tolerable size and pressure drop.
- The rotating parts of turbine, compressor, generator and shaft have together a moment of inertia of 0.025 kg·m^2. This is equivalent to a rotating mass of 20 kg and a mean radius of 5 cm. The moment of inertia influences the power output during shaft acceleration and deceleration.
- The generator is assumed to have a constant efficiency of 95%. The power electronics have constant efficiencies of 90% for AC/AC and 95% for DC/AC conversion. In order to account for power consumption of auxiliaries and the decreasing conversion efficiencies at load reduction, a constant sink term of 5 kW was applied.

STEADY-STATE PERFORMANCE

With the given design, three degrees of freedom remain for off-design operation:

1. Shaft speed variation
2. Fuel flow variation
3. Fuel utilisation/Current/Voltage variation.

Variation of the shaft speed can be controlled by the power electronics, i.e. generator power. Dependent on the power balance at the shaft, it runs steadily, accelerates or decelerates.

Fuel flow variation can be achieved by a control valve. For the dynamic simulations we assume that the flow rate can instantaneously be adjusted to a desired value.

Fuel utilisation and current are coupled via the fuel flow rate, while current and voltage are coupled via the fuel cell characteristics. However, large variations in FU are not recommendable, as low FU leads to low steam content in the anode recycle and high TIT, while high FU leads to steep internal temperature gradients in the fuel cell. Therefore, we chose to operate at constant FU by setting the current proportional to the fuel flow rate.

The remaining free parameters, shaft speed and fuel flow, may be varied independently from each other within certain limits. Each combination determines a certain operation point of the system. Thus, two-dimensional matrices of the interesting process parameter steady state values over the two free parameters can be produced and displayed in performance maps. We have previously introduced similar maps for a SOFC stack system [11]. In that work we used air utilisation and air flow rate as free parameters. Due to absence of a GT cycle model, in that work simplified assumptions for gas inlet temperature and operating pressure had to be made. These data

are in the present work being calculated by the GT cycle model, representing a more comprehensive study.

For easy reading, we give dimensionless values for shaft speed (RSS) and fuel flow (RFF), related to the design point values. RSS is varied between 65% and 105%, representing the valid range for the compressor and turbine map. RFF is varied between 15% and 110%.

Figure 2 and 3 show the steady-state behaviour of the parameters of interest as a function of RSS and RFF. For easier reading, each diagram shows only the fields of three parameters.

The blinded out area on the upper left (low shaft speed and high fuel flow) represents an area where no steady state exists. Transient experiments have shown that the temperature in this regime is steadily climbing far beyond the valid ranges and furthermore eventually causing compressor surge. This is because enhanced effectiveness of the heat recuperation loop and lower air excess ratio at lower airflow causes TIT to increase. Concurrently, the increased TIT causes decrease of airflow, originating from compressor and turbine characteristics.

In the lower right area (high shaft speed and low fuel flow), the cell is cooled down strongly and therefore the voltage is low. As it is not recommendable to operate in this regime, it is blinded out for cell voltages lower than 0.3 V.

A first result from the performance map is that reducing fuel flow at constant shaft speed (and therewith fairly constant air flow), i.e. going down a vertical line from design point, results in a strong reduction in temperatures and therewith efficiencies.

The figures also show that a load reduction by linearly reducing fuel flow and air flow will lead into the unstable region. Remaining in the stable regime therefore implies larger percentual reduction in fuel flow than air flow. This is a consequence of the lower pressure ratio at reduced shaft speed which results in an increased TOT. The same behaviour is also confirmed in a study by Costamagna et al. [7].

Surge margin and steam to carbon ratio do not reach any alarming values in the shown operation range.

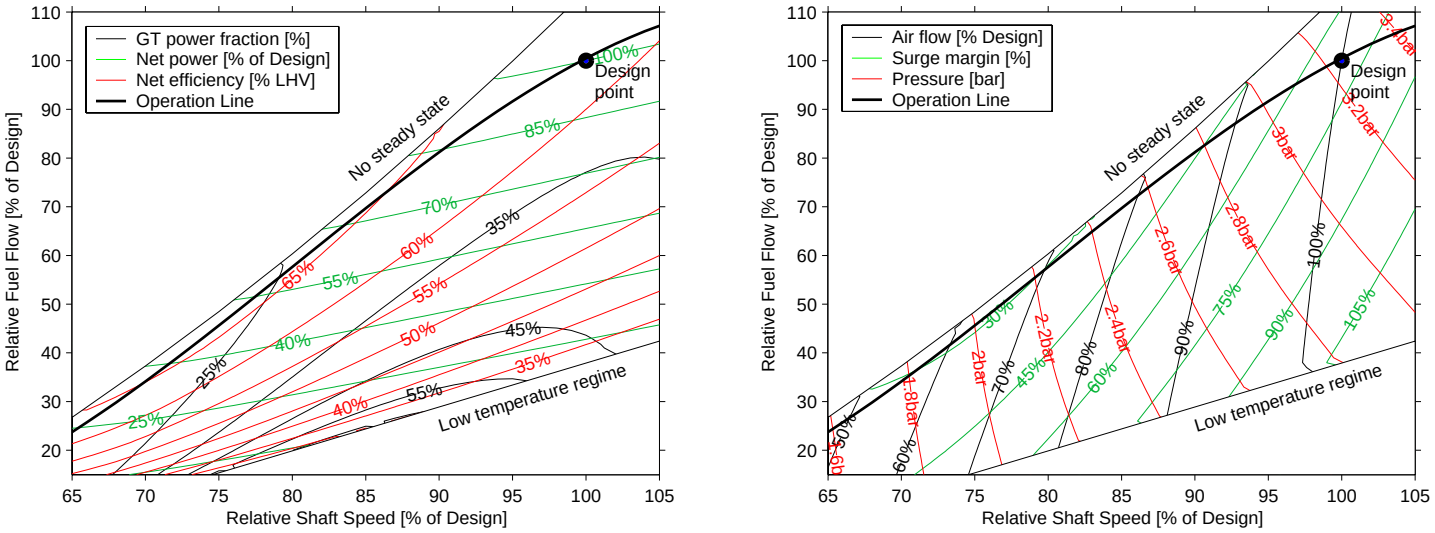

Figure 2: Power parameters (left) and turbomachinery parameters (right) in steady state.

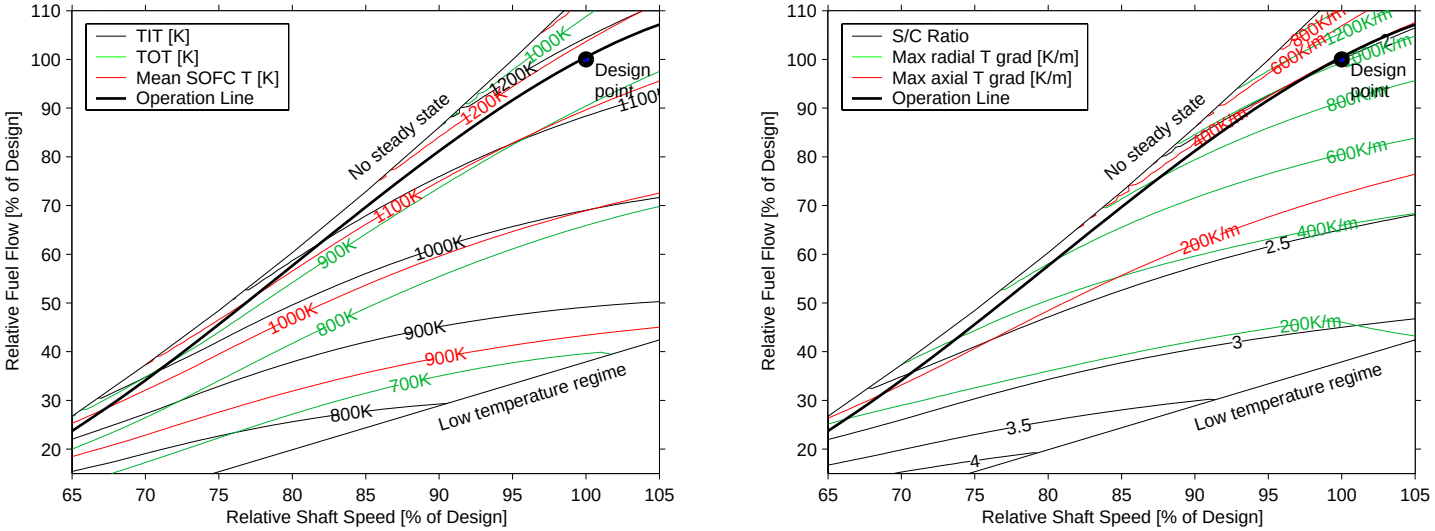

Figure 3: Significant temperatures (left) and steam to carbon ratio and SOFC temperature gradients (right) in steady state.

STEADY-STATE OPERATION LINE

The main parameter of interest for the power plant is simply the power output. Using the performance maps, we find lines of constant dimensionless net power in Fig. 2. For a certain desired power in steady state, each point of its line is basically a valid operation point. However, in order to decide which point is optimal, the following objectives need to be considered:

1. High efficiency
2. Safe operation: Distance from invalid regimes and alarming values for safety-relevant parameters.
3. Fairly constant SOFC temperature level

The latter point is the most restrictive requirement, as thermal cycling affects the lifetime of SOFCs. It is also the most important in terms of load following behaviour and thermal gradients in the fuel cell during dynamic operation.

From Fig. 3 can be seen that isolines of the most significant temperatures are almost parallel and linear in the area of interest.

At a given current, the mean SOFC temperature is strongly influencing voltage and thus power output of the SOFC. Due to high thermal inertia, the SOFC is quite slow in reaching a new steady temperature state after a load change, causing power to vary over a long time. The most favourable operation line in terms of quick load following would therefore be along a line of constant mean SOFC temperature. However, in Fig. 3 (left, red lines), it can be seen that reducing shaft speed at constant mean SOFC temperature results in approaching the regime where no steady state exists. We assume there is an indifferent regime close to the steady-state boundary, where the same values of air and fuel flow may cause different operation temperatures depending on the initial temperatures. However, if no reliable temperature feedback to the control system exists, the system cannot be operated safely in this regime. Hence the temperature *must* be decreased when strongly decreasing the load. The proposed operation line therefore follows a line of constant mean SOFC temperature for relative shaft speed between 90 and 100%. Below 90%, the operation line departs from the constant mean SOFC temperature line and instead pursues a parallel line to the steady-state border down to the minimum RSS of 65%. The resulting operation line can be developed as a 3nd order polynomial and is plotted in the maps. Its equation is

$$RFF = -7.21 \cdot RSS^3 + 17.31 \cdot RSS^2 - 11.45 \cdot RSS + 2.34 \quad (4)$$

With this strategy, a fairly constant mean SOFC temperature of app. 1170K can be maintained in a range of relative net power (RP) from 80% to 105%. The minimum part load operation at 65% RSS yields a relative power of 24% and a mean SOFC temperature of 970K. Knowing a desired output power (in steady state), the required shaft speed can be estimated through

$$RSS = 0.674 \cdot RP^3 - 1.08 \cdot RP^2 + 0.930 \cdot RP + 0.478 \quad (5)$$

The net LHV-based efficiency increases from 62% at design point to 66% at relative power of 50% and decreases again to 63% at minimum part load. TIT decreases from 1170K at design point slowly to app. 930K at minimum part load. This decrease helps in keeping the surge margin wide. Trends and values of all other parameters can be estimated from the performance maps. Including an air bypass around the SOFC system may facilitate constant mean SOFC temperature over the whole range. This will be studied further.

The shown behaviour certainly depends on the characteristics of all applied components and assumptions of the cycle. The displayed quantitative data represent only the current system. However, the trends are expected to be similar in a real system. Hence, the demonstrated methods can be applied on a real system, once an accurate model of its true behaviour is available.

DYNAMIC PERFORMANCE

In the following study, the control parameters of fuel flow and shaft speed are changed between several points and the behaviour of the crucial system parameters is investigated. There is no controller including a feedback loop of measured output parameters as normally found in control system designs. The purpose of this method is to show the straight, non-controlled behaviour of the system following a load change.

In order to study dynamic load changes, a strategy for changing shaft speed and fuel flow is required. Speed changes of the shaft are calculated by its inertia and power balance; see Eq. (2) and (3). In case of reduced generator load the shaft accelerates, and vice versa. We manipulate the shaft power balance in a way that the shaft acceleration/deceleration is either a constant value or zero:

$$\frac{P_B}{I \cdot \omega} = \frac{d\omega}{dt} = R \cdot \mathrm{sgn}\left(N_{Setpoint} - N\right) \quad (6)$$

where $N_{Setpoint}$ is the setpoint shaft speed in [s^{-1}] and R is the shaft speed change rate in [rad·s^{-2}]. The sgn function yields

1 if $N < N_{Setpoint}$;
0 if $N = N_{Setpoint}$;
-1 if $N > N_{Setpoint}$.

Therewith the shaft speed is either constant at setpoint or moving linearly towards a new setpoint. The value of 52.4 rad·s^{-2}, corresponding to a speed change rate of 500 RPM per second, is set for R. This approach only represents a theoretical investigation method; for practical speed control systems, additional requirements apply.

The relative fuel flow is coupled to the actual relative shaft speed via the operation line Eq. (4), i.e. a speed change will result in fuel flow following an approximate ramp function.

The time from initiation of a load change until the new steady state is reached, called relaxation time, is an important parameter in dynamic studies. Figure 4 shows relaxation behaviour for a quick load change between 100% and 24% RP (respectively 100% and 65% RSS). At time equals 1, the shaft speed setpoint is changed by a step.

As can be seen from Fig. 4, with the reset of the setpoint shaft speed at time equals 1, power performs an immediate step into the inverse direction due to the shaft deceleration/acceleration. It takes very long until the power reaches its steady value after the load changes, calling for a control strategy incorporating feedback loops for exact load following.

The surge margin has a minimum during load decrease and a maximum during increase. This behaviour is different from regular gas turbine cycles. It is caused by the fairly constant TIT during speed change, which is caused by thermal inertia of the air preheater inside the SOFC system.

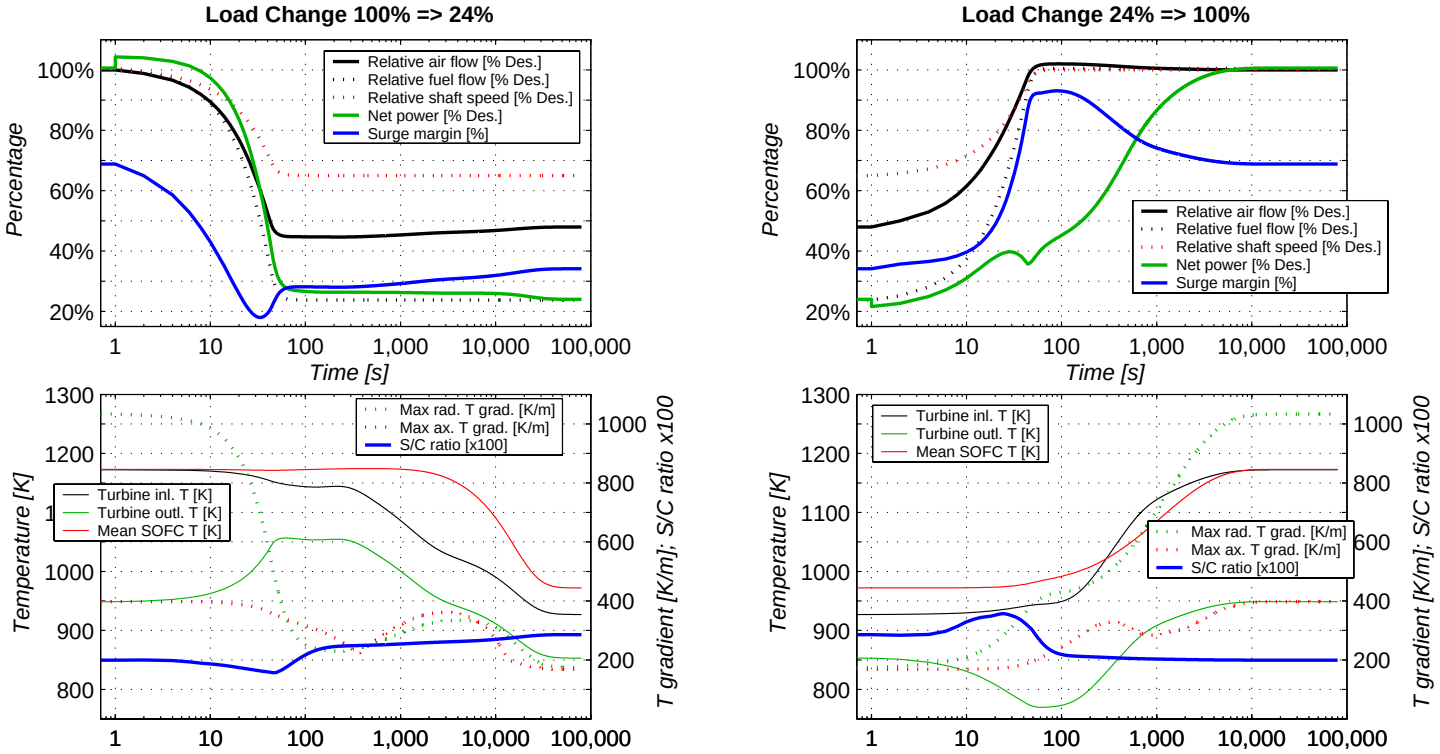

Figure 4: Load change between 24% and 100% (left: decrease; right: increase).

The maximum temperature gradients in the cell show unsteadiness along the relaxation time, indicating that the cell temperature profile is changing and the location of maximum gradients are moving. However, no global minima or maxima can be observed during the relaxation process.

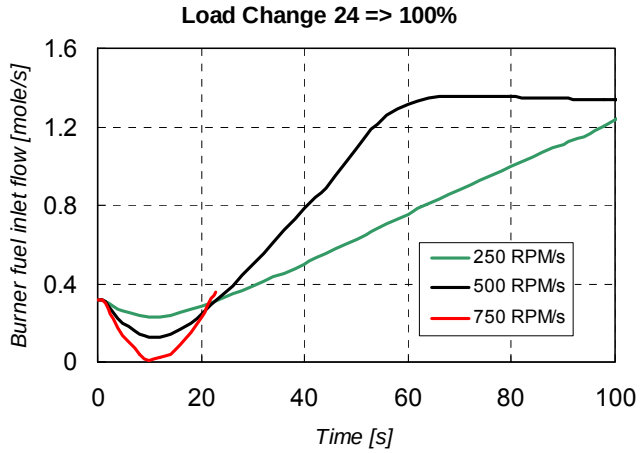

Figure 5: Burner fuel flow at different speed change rates

During load decrease, the steam to carbon ratio reaches a minimum of 1.8 after approximately 50 seconds, but this is not regarded as a critical value. During load increase, the anode exhaust gas recycle ratio increases temporarily to a very high value. This represents a danger, as it may cause backflow from the burner to the anode exhaust gas recycle loop. Thereby the anode may be exposed to oxygen. Figure 5 shows the fuel flow into the burner for a load increase at different speed change rates. The minima occur because during load change, the pressure is increasing and with it the gas mass in the fuel cell. Hence, less gas is leaving the cell than entering it during pressure increase. Furthermore, more fuel is being introduced, improving ejector performance. Anode backflow is hence restricting the maximum possible speed/pressure increase rate.

Another problem with quick pressure increase is the temporarily high depletion of the anode outlet gas due to the constant current to fuel flow ratio. In other words, the "true" fuel utilisation may temporarily come very close to 100% and the voltage must be decreased to very low values in order to keep the current to fuel flow ratio constant. The simulation with 750 RPM/s in Fig. 5 could not be finished due to numerical problems associated to this phenomenon. It may in practice lead to fuel cell degradation or burner extinguishing. However, it can be omitted by a more sophisticated current/voltage control (i.e. setting a minimum boundary for the voltage). The break in the power curve during load increase at a time of app. 50 seconds (see Fig. 4) is also a result of a temporarily too low voltage.

Table 1 lists the time required from the setpoint reset until the margin of ± 2% of the new steady state value of power and radial gradient has been reached for load change between three different points. The maximum radial thermal gradient is taken as a measure for the thermal steady state, simply because it shows the strongest variation of all temperature-related parameters. Steady power is always reached somewhat quicker.

It can be observed that between 80% and 100% relative net power, steady state is reached quicker. This is because of the fairly constant mean SOFC temperature in this regime, with the SOFC comprising the highest thermal inertia in the system. Beside the mean SOFC temperature, relaxation time is strongly influenced by the end point of the load change. Higher load end points cause quicker relaxation as a consequence of the higher gas and energy turnover. This has been reported previously by

Achenbach [6] and is the reason why load increases relax generally faster than load decreases.

Table 1: Relaxation times for load changes.

Relaxation time [s]		to 24%	to 80%	to 100%
From RP=24%	Power		5400	3800
	Radial Grad.		11000	6200
From RP=80%	Power	26000		360
	Radial Grad.	38000		2650
From RP=100%	Power	28000	40	
	Radial Grad.	40000	5300	

CONTROL STRATEGY

The dynamic performance study revealed slow relative power change and long time until power steady state is reached when moving along the proposed operation line. This might be sufficient for a power plant connected to the grid. However, a remote power plant without grid connection is required to follow load curves very quickly, thus load compensation units such as batteries or large capacitors would be required.

On the other hand, other methods of operating the hybrid cycle may be advantageous. At present, the fuel flow, which influences power output to great extent and which can be controlled quite quickly, is coupled to the rather slowly moving parameter of shaft speed via Eq. (4). Furthermore, during a load change, the system may be operated at any combination of RSS and RFF, as long as the end point is within the stable regime of the performance maps.

In an advanced control strategy, the setpoint shaft speed could be directly coupled to the setpoint power output via Eq. (5), ensuring that the system in steady state is always on the proposed operation line.

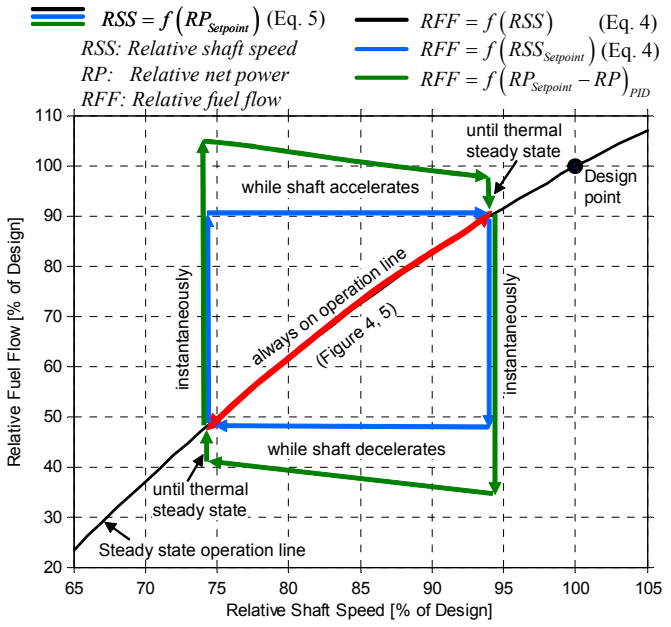

Figure 6: Control strategies for fuel flow.

The fuel flow could then be coupled to the setpoint shaft speed instead of the actual shaft speed in the same way as in Eq. (4), resulting in a much faster power change. The most efficient way though would be to control fuel flow by comparing the feedback measured actual power with the setpoint power.

Figure 6 shows the proposed strategies in a RFF-over-RSS diagram (same as Fig. 2 and 3). The red line indicates the movement of the parameters if fuel flow is coupled to actual shaft speed (strategy pursued for the above dynamic performance study). The blue lines indicate the movement of parameters if fuel flow is coupled to setpoint shaft speed, and the green lines sketch the possible behaviour if the power output is controlled a feedback loop. With the latter strategy, it should be possible to follow load curves with a very short delay between setpoint and actual power. However, the mentioned critical phenomena could be a restriction to very quick load variation with the proposed system.

Where quick load following is required, alternative systems with constant shaft speed and other means to control the air flow, such as variable inlet guide vanes or an air bypass, may be even more suitable, as these control means can be manipulated much quicker than the inertia-affected shaft speed. Another option would be introduction of an auxiliary burner in the current system directly upstream the turbine for quick TIT control.

CONCLUSIONS

A powerful full dynamic model of a simple hybrid system has been developed and the hybrid system performance has been characterised. The following main conclusions can be drawn:

1. The system power is mainly controlled by fuel flow, shaft speed and current.
2. Setting the ratio of current to fuel flow (and therewith fuel utilisation) constant, the part-load behaviour of the system shows the presence of unstable regimes (no steady state exists) at high fuel flow and low shaft speed, and regimes with very low SOFC temperatures at high shaft speed and low fuel flow.
3. In steady-state part-load, the air-to-fuel ratio must increase in order not to operate in an unstable regime.
4. Operation lines with constant mean SOFC temperature exist, but approximate the unstable regime. An operation line is proposed where the mean SOFC temperature is constant in a load range from 80% to 100%. Below 80% load, temperature must decrease if no temperature feedback controller is applied.
5. Load changes in the regime of constant mean SOFC temperature reach a new thermal steady state quite quick, while it takes much longer when the temperature is varied.
6. The effect of gas from the burner flowing back into the anode cycle restricts the pressure increase rate under load increase.
7. Quicker load changes may be performed when the fuel flow and SOFC current are varied quicker than the shaft speed.
8. With the present tool, a coherent design for control of the whole system may be developed.

The depicted quantitative data are only valid for the studied model. However, the qualitative trends are expected to be similar in a genuine system. Hence, the demonstrated

methods can be applied on a real system, given that relevant data of its behaviour are available.

ACKNOWLEDGMENTS

We thank the Norwegian Research Council, Shell Technology Norway and Statkraft for their financial support.

REFERENCES

[1] Stiller, C., Thorud, B., Seljebø, S., Mathisen, Ø., Karoliussen, H., Bolland, O., 2004, "Finite-volume modeling and hybrid-cycle performance of planar and tubular solid oxide fuel cells", accepted for publication in Journal of Power Sources

[2] Rao, D., Samuelsen, G. S., 2001, "A thermodynamic analysis of tubular SOFC based hybrid systems", ASME Paper 2001-GT-0522.

[3] Chan, S. H., Ho, H. K., Tian, Y., 2003, "Modeling for part-load operation of solid oxide fuel cell-gas turbine hybrid power plant", Journal of Power Sources **114** 213-227.

[4] Pålsson, J., Selimovic, A., Sjunnesson, L., 2000, "Combined solid oxide fuel cell and gas turbine systems for efficient power and heat generation", Journal of Power Sources **86** 442-448.

[5] Veyo, S.E., Lundberg, W.L. Vora, S.D., Litzinger, K.P., 2003, "Tubular SOFC hybrid power system status", ASME Paper 2003-GT-38943.

[6] Achenbach, E., 1995, "Response of a solid oxide fuel cell to load change", Journal of Power Sources **57** 105-109.

[7] Costamagna, P., Magistri, L., Massardo, A.F., 2001, "Design and part-load performance of a hybrid system based on a solid oxide fuel cell reactor and a micro gas turbine", Journal of Power Sources **96** 352-368.

[8] Campanari, S., 2000, "Full load and part load performance prediction for integrated SOFC and microturbine systems", Journal of Engineering for Gas Turbines and Power **122** 239-246.

[9] Pålsson, J., Selimovic, A., 2001, "Design and off-design predictions of a combined SOFC and gas turbine system", ASME Paper 2001-GT-0379.

[10] Kimijima, S., Kasagi, N., 2002, "Performance evaluation of gas turbine-fuel cell hybrid micro generation system", ASME Paper 2002-GT-30111.

[11] Thorud, B., Stiller, C., Weydahl, T., Bolland, O., Karoliussen, H., 2004, "Part-load and load-change simulation of tubular SOFC systems", 6th European Solid Oxide Fuel Cell Forum, Lucerne, Switzerland.

[12] Rao, A.D., Samuelsen, G.S., 2002, "Analysis strategies for tubular solid oxide fuel cell based hybrid systems", Journal of Engineering for Gas Turbines and Power **124** 503-509.

[13] Song, T.W., Sohn, J.L., Kim, J.H., Kim, T.S., Ro, S.T., Suzuki, K., 2004, "Parametric studies for a performance analysis of a SOFC/MGT hybrid power system based on a quasi-2D model", ASME Paper 2004-GT-53304.

[14] gPROMS (General Process Modelling and Simulation Tool), v.2.3.3, Process Systems Enterprise Ltd., London, http://www.psenterprise.com/

[15] Marsano, F., Magistri, L., Massardo, A.F., "Ejector performance on a solid oxide fuel cell anodic recirculation system", Journal of Power Sources **129** 216-228.

[16] Kurzke, J., 2004, "Compressor and turbine maps for gas turbine performance computer programs – Component Map Collection 2", Joachim Kurzke, Dachau, Germany

[17] Yi, Y., Smith, T.P., Brouwer, J., Rao, A.D., Samuelsen, G.S., 2003, "Simulation of a 220 kW hybrid SOFC gas turbine system and data comparison", Electrochemical Society Proceedings **2003-7** 1442-1454.

[18] Johannesen, N. H., 1951, "Ejector Theory and Experiments", Dissertation, Danish Academy of Technical Sciences, Copenhagen, Denmark.

[19] Achenbach, E., Riensche, E., 1994, "Methane/steam reforming kinetics for solid oxide fuel cells", Journal of Power Sources **52** 283-288.

[20] Karoliussen, H., Nisancioglu, K., Solheim, A., Ødegård, R., 1992, "SOFC stack modeling with internal reforming", 4th IEA Workshop on SOFC, Lausanne, Switzerland.

[21] Nisancioglu, K, 1989, "Ohmic losses", Natural gas fuelled solid oxide fuel cells and systems, IEA Workshop on Mathematical Modelling, Charmey, Switzerland.

[22] Reid, R.C., Prausnitz, J.M., Poling, B.E., 1987, *The properties of gases and liquids*, McGraw-Hill, New York.

[23] Mills, A.F., 1995, *Heat and Mass Transfer*, Irwin, Chicago.

APPENDIX 1 – SOFC MODEL

Table 2: Equations for heat transfer in the SOFC tube.

Ref. no in Fig. 7	Equation	Comment
1	$\frac{\partial\left(T_{air}c_p\rho_{air}\right)}{\partial t}+v_{air}\frac{\partial\left(T_{air}c_p\rho_{air}\right)}{\partial z}=\frac{2\alpha}{r_{AST,i}}\left(T_{AST}-T_{air}\right)$	Heat transfer between air supply tube and air within the tube
2	$\frac{dT}{dt}=\frac{k}{c\cdot\rho}\nabla^2\cdot T$	Heat conduction in solid structures (Air supply tube and SOFC membrane)
3	$\frac{\partial\left(T_{air}\rho_{air}c_{p,air}\right)}{\partial t}+v_{air}\frac{\partial\left(T_{air}\rho_{air}c_{p,air}\right)}{\partial z}=$ $\frac{2r_{AST,o}\alpha_{AST,o}}{\left(r_{c,i}^2-r_{AST,o}^2\right)}\left(T_{AST,o}-T_{air}\right)+\frac{2r_{c,i}\alpha_{c,i}}{\left(r_{c,i}^2-r_{AST,o}^2\right)}\left(T_{c,i}-T_{air}\right)$	Heat transfer between air supply tube, cathode air and cathode
4	$\frac{\partial\left(T_{fuel}\rho_{fuel}c_{p,fuel}\right)}{\partial t}+v_{fuel}\frac{\partial\left(T_{fuel}\rho_{fuel}c_{p,fuel}\right)}{\partial z}$ $=\frac{2\alpha_{fuel}r_{a,o}}{\left(\left(r_{a,o}+\Delta r\right)^2-r_{a,o}^2\right)}\left(T_{a,o}-T_{fuel}\right)$	Heat transfer between anode surface and fuel

Nomenclature	T	Temperature [K]	k	Thermal conductivity [W/mK]
	c/c_p	Heat capacity [J/kgK]	α	Convective heat transfer coeff. [W/m^{2}K]
	ρ	Density [kg/m^3]	Δr	Thickness of fuel plenum [m]
	v	Gas velocity [m/s]	r	Radius [m]
	t	Time [s]	z	Axis direction [m]
Subscripts	AST	Air Supply Tube	c	Cathode
	a	Anode	i	Inner radius
	o	Outer radius		

Figure 7 shows a break-down of the cell geometry. The numbers refer to the equations for the thermal model which are listed in Table 2. The following features are included:

- Heat transfer between the fuel cell tube walls and the fluids are calculated using Newton's law of cooling. Heat transfer coefficients are calculated from Nusselt numbers for laminar flow and for constant heat flux.
- Thermal radiation is incorporated between the air supply tube and the cathode surface by using a shape factor for radiation between two tubes, neglecting axial spreading effects and absorption in the gas.
- To reduce calculation time, the solid structure of the anode, electrolyte and the cathode is treated as one single material with weighted mean values for the thermal and electrical properties.
- As the total thickness of anode and electrolyte (0.14 mm) is very small compared to the cathode (2.2 mm), heat sources and sinks related to the electrochemical and methane reforming kinetics are located at the anode surface.
- For steam reforming kinetics, Achenbach's approach is used [19], while the water-gas shift reaction is assumed to be always in equilibrium.
- The local electrical potential is calculated by the Nernst equation, an approach for polarisation losses by Karoliussen et al. [20], an analytical expression for the ohmic resistance developed by Nisancioglu [21] and diffusion losses. For the latter, Knudsen-diffusion is applied using diffusion coefficients determined from the Fuller method [22] and correction factors for multi-component diffusion coefficient calculation. Electrochemical oxidation of CO is neglected.
- Friction losses in the air delivery tube, cathode and anode channels are accounted for by the Reynolds number approach and under the assumption of laminar flow [23].

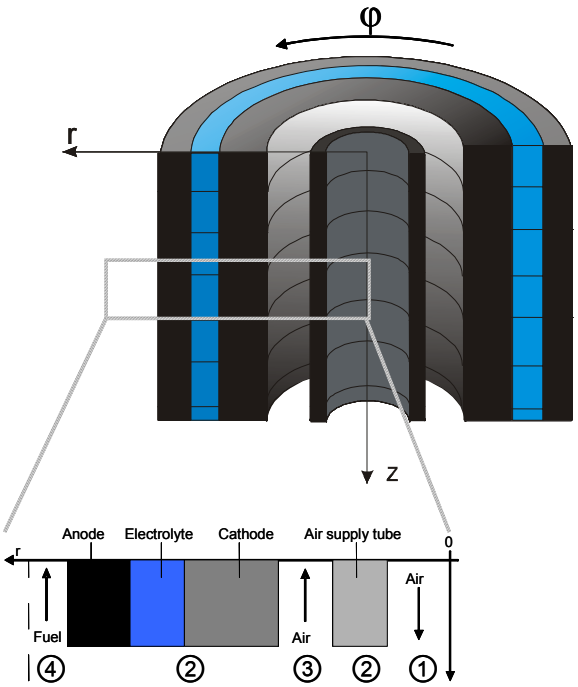

Figure 7: Break down of the cell geometry.

APPENDIX 2 – COMPRESSOR AND TURBINE MAP

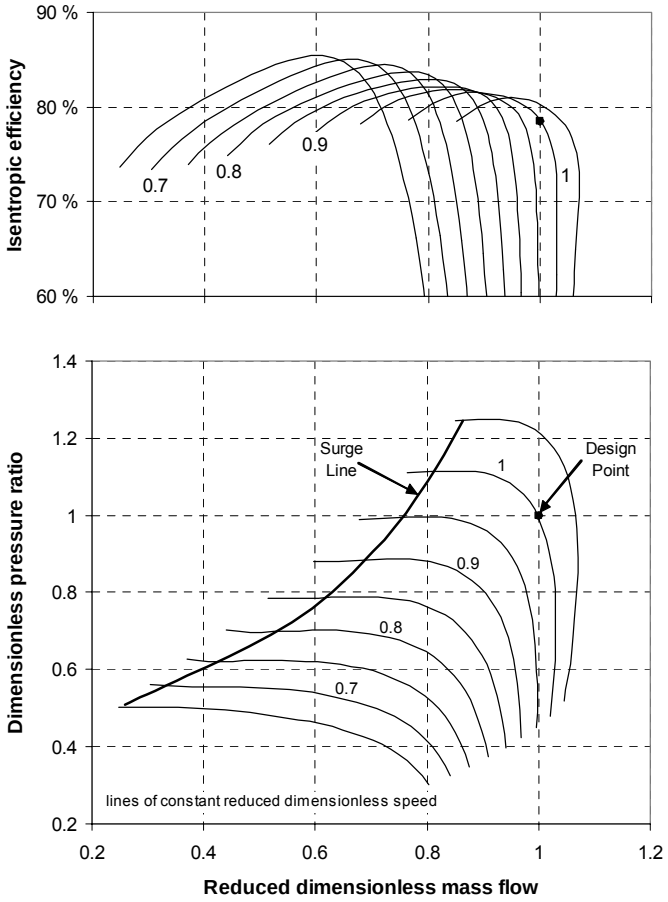

Figure 8: Normalized compressor map.

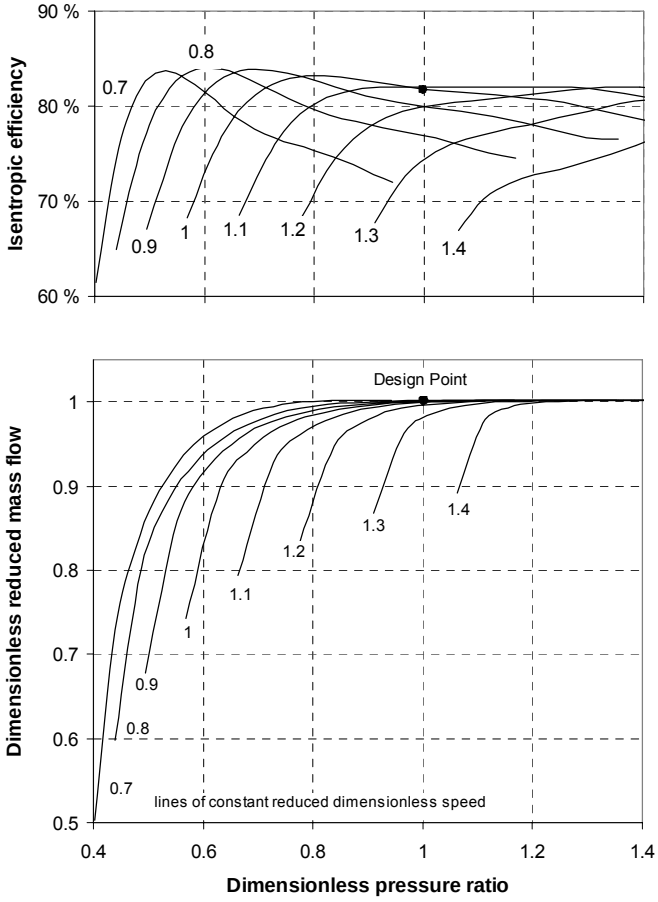

Figure 9: Normalized turbine map.

Paper III

Control strategy for a solid oxide fuel cell and gas turbine hybrid system

Stiller, C., Thorud, B., Bolland, O., Kandepu, R., Imsland, L.

Journal of Power Sources, in press (available online).

Available online at www.sciencedirect.com
SCIENCE DIRECT®
Journal of Power Sources xxx (2005) xxx–xxx
JOURNAL OF POWER SOURCES
www.elsevier.com/locate/jpowsour

Control strategy for a solid oxide fuel cell and gas turbine hybrid system

Christoph Stiller [a,*], Bjørn Thorud [a], Olav Bolland [a], Rambabu Kandepu [b], Lars Imsland [b]

[a] *Department of Energy and Process Engineering, Norwegian University of Science and Technology, Kolbjorn Hejes vei 1B, NO-7491 Trondheim, Norway*
[b] *Department of Engineering Cybernetics, Norwegian University of Science and Technology, NO-7491 Trondheim, Norway*

Received 8 April 2005; received in revised form 27 August 2005; accepted 6 September 2005

Abstract

This paper presents a multi-loop control strategy for a SOFC/GT hybrid system. A detailed dynamic model of the system is presented and its part-load performance is studied. The control objectives are discussed, with the main issue being a fairly constant fuel cell temperature under all conditions. Based on the system configuration and part-load performance, input and output variables of the control system are detected. Control cycles are introduced and their design is discussed. The responses of the resulting system on load changes, external disturbances as well as malfunction and degradation incidents are investigated. The system is stable under all incidents. An error in fuel flow measurement or assumed fuel quality provokes a steady-state fuel cell temperature offset. For a degraded system, it may be advisable to readjust the control system to the new characteristics.

Keywords: SOFC; Hybrid cycle; Modelling; Part-load; Control

1. Introduction

A large amount of modelling work [1–4] and a demonstration plant [5] have proven that a solid oxide fuel cell (SOFC) integrated with a gas turbine (GT) has a potential for high efficiency electricity production with low environmental emissions. The good scalability of such systems makes them especially advantageous for distributed generation. Provided that quick load-following is feasible, stand alone power generation is a possible application.

However, SOFC/GT hybrid systems face many challenges when it comes to load change and part-load operation. A gas turbine alone has good dynamic properties, but part-load performance can be rather poor. At any operation point, compressor surge must be prevented. A SOFC is generally able to respond quickly to load changes [6], but it might be destroyed or seriously degraded either due to thermally induced stresses caused by different thermal expansion coefficients in the cell materials or from carbon deposition at the anode. Another phenomenon that may occur during load change is backflow of gas from the burner to the anode cycle, exposing the anode to oxygen. These incidents must not occur in any operation instance. Furthermore, for high efficiency and low degradation of the fuel cell due to thermal cycling, the fuel cell temperature should remain fairly constant during operation. The fulfilment of the mentioned tasks requires a comprehensive control strategy.

Results from part-load operation modelling have already been discussed by some authors. Costamagna et al. [7] investigated a hybrid system using a non-dimensional tubular SOFC model. In all simulations they assumed constant fuel utilisation (FU). If shaft speed was assumed constant, power output could only be controlled by varying the fuel flow. These simulations showed large variations in air utilisation (AU) and loss of efficiency for fixed shaft speed when operating at part-load. For variable shaft speed, however, AU and FU as well as SOFC inlet temperatures could remain fairly constant in part-load operation with only a small penalty on system efficiency. This effect was mainly due to increased recuperator efficiency owing to reduced air flow rate.

Campanari [8] also used a non-dimensional tubular SOFC model to investigate the hybrid system. Assuming constant FU of 80%, for constant shaft speed he suggested reducing AU and

Abbreviations: SOFC, solid oxide fuel cell; GT, gas turbine; FU, fuel utilisation; AU, air utilisation; TIT, turbine inlet temperature; TOT, turbine outlet temperature; IIR, indirect internal reforming

* Corresponding author. Tel.: +47 735 93723; fax: +47 735 98390.
E-mail addresses: christoph.stiller@ntnu.no (C. Stiller), bjorn.thorud@ntnu.no (B. Thorud), olav.bolland@ntnu.no (O. Bolland), rambabu.kandepu@ntnu.no (R. Kandepu), lars.imsland@ntnu.no (L. Imsland).

0378-7753/$ – see front matter © 2005 Elsevier B.V. All rights reserved.
doi:10.1016/j.jpowsour.2005.09.010

Nomenclature

Symbols

AF	air flow (relative to design value)
c	concentration (mol m^{-3})
c_p	heat capacity at constant pressure (J kg^{-1})
c_s	heat capacity of cell solid (J kg^{-1})
FF	fuel flow (relative to design value)
GP	generator power (relative to design value)
h	heat transfer coefficient (W m^{-2} K^{-1})
I	moment of inertia (kg m^2)
k	thermal conductivity (W m^{-1} K^{-1})
$\dot{m}$	reduced mass flow
n	reduced shaft speed
P	power (relative to design value)
P_b	shaft power balance (W)
r_{ij}	turnover of species i in reaction j (mol m^{-3} s^{-1})
r_s	radius of cell solid wall (m)
SM	surge margin
t	time (s)
T	temperature (K)
TF	temperature of fuel leaving the cell (relative to design value)
v	gas velocity (m s^{-1})
z	axial direction (m)

Greek letters

η_m	mechanical efficiency
π	pressure ratio
ρ	density (kg m^{-3})
ω	angular shaft speed (rad s^{-1})

Indexes

∞	ambient
comp	compressor
g	gas
gen	generator
i	species
s	cell solid
setp	setpoint
surge	surge condition
turb	turbine

current density for part-load. This approach will reduce power output of the SOFC as well as the turbine inlet temperature (TIT) and consequently the power output of the GT. For variable shaft speed he suggested to reduce air flow rate and current density to maintain a constant AU. However, a reduction in air flow rate leads to pressure reduction and therewith higher turbine outlet temperature (TOT) and thus higher recuperator outlet temperatures. Campanari concluded that for maintaining constant TIT, the current density has to be reduced further.

Chan et al. [3] also investigated a non-dimensional tubular SOFC-type in a hybrid system. In their system, power is reduced by shifting the load from the SOFC to the GT through introducing fuel to the combustor, which results in strong reduction of the system efficiency. This method also implies that a SOFC bypass should be implemented for both fuel and air. Due to the low part-load efficiency, they state that this method is mainly for short term load reduction. The aim was to maintain a relatively high SOFC temperature.

Pålsson and Selimovic [9] used a two-dimensional planar SOFC model for part-load studies. Design point was set where the compressor flow matched the cooling requirement of the SOFC. They introduced an air heater/cooler prior to the SOFC entry in order to meet the requirements for the air inlet temperatures at part-load operation. TIT was kept constant and shaft speed was varied. At part-load operation, increased FU and low GT part-load efficiency led to increased power contribution from the SOFC. Due to the problems associated with matching of the system components, they concluded that the load range for hybrid systems should be limited to 55–100%, corresponding to a load variation of the GT of 20–100%.

Kimijima and Kasagi [10] studied part-load of a 30 kW simple recuperated cycle using a non-dimensional SOFC model and compared variable and fixed shaft speed operation. FU was kept constant, even though it is mentioned that FU could be increased at part-load operation. They conclude that variable shaft speed operation is favourable in terms of part-load performance; however the higher TOT could cause problems.

Some of the authors of the present work have recently presented a complex model of a SOFC/GT system [11]. Performance maps were introduced to illustrate the variations of the most important parameters over the two degrees of freedom, namely shaft speed and fuel flow. Based on these maps, it was found that strategies with fairly constant temperatures in the SOFC seem feasible but require a feedback control system for safe operation. Responses of the non-controlled system on variations of shaft speed and fuel flow were briefly studied.

All above-mentioned authors have identified inlet and outlet gas temperatures as well as air and fuel utilisations of the SOFC as important parameters for part-load operation of hybrid systems. Maintaining a constant SOFC operation temperature is important to avoid thermal cracking, but this might be difficult to achieve at reduced pressure as the TOT and consequently the recuperator outlet temperature increases.

A few studies on control layout and load-following of high temperature fuel cell systems and hybrid systems have been published so far. Zhu and Tomsovic [12] have studied the load-following of microturbine and fuel cell system models, however not as a hybrid system but as separate systems coupled together in a power network. Response time of approximately 10 and 30 s were observed for load increase in the microturbine and SOFC system, respectively. The slow SOFC response was mainly due to the slow dynamics of the fuel processor. It was concluded that load-following in a network is to be provided mainly by microturbine systems. Jurado [13] designed a control system for a molten carbonate fuel cell indirectly integrated into a gas turbine. Controllers for the gas turbine and fuel cell are introduced; however no coupling between these is established. Both references do not regard the thermo- and gas-dynamical processes during and subsequent to load changes.

The aim of the current work is to present a comprehensive control layout for a hybrid system. A detailed dynamic model of a tubular SOFC system integrated into a simple recuperated GT cycle as the basis for the investigation is described. The steady-state behaviour of the system is displayed in performance maps. Next, control objectives and the nature of disturbances influencing the system are discussed. A combined feedback–feedforward control layout is introduced. From the performance maps, an appropriate operation line is selected and the feedforward section is tuned to it. Feedback controller tuning is discussed. As a result, the responses of the controlled system to certain load changes and disturbances are studied.

2. Hybrid cycle model

The investigated hybrid cycle is shown in Fig. 1. The SOFC system design (inside the vessel in Fig. 1) is similar to that of Siemens–Westinghouse [14,15]. The model incorporates indirect internal reformer (IIR), afterburner and recirculation and mixing chamber, where part of the anode exhaust gas is admixed to the fresh fuel in an ejector in order to supply steam to the steam reforming and shift reaction. Required valves for start-up, shutdown and failure have not been included.

Since the last study [11] with this hybrid cycle model, the reforming section has been improved. Furthermore, heat loss from the stack by radiation has been added and the activation and diffusion potential models have been refined. The models are described below.

2.1. SOFC

The SOFC model is spatially discretised and fully dynamic in terms of gas transport and heat transfer, allowing the study of temperature distributions. Gas flows are treated as 1D plug flows:

$$\frac{\partial c_i}{\partial t} + v_g \frac{\partial c_i}{\partial z} = \sum_j r_{i,j} \tag{1}$$

The solid structures are modelled by a 2D discretisation scheme in axial and radial direction, neglecting effects in the circumferential direction. Heat conduction in solid structures is calculated by

$$\frac{dT_s}{dt} = \frac{k_s}{c_s \rho_s} \nabla^2 T_s \tag{2}$$

Internal reforming is implemented using the kinetic approach of Achenbach [16] for steam-methane reforming, while the water-gas shift reaction is assumed to be always in equilibrium. The model calculates the local electrical potential balance, accounting for the effects of activation (Butler–Volmer) and diffusion

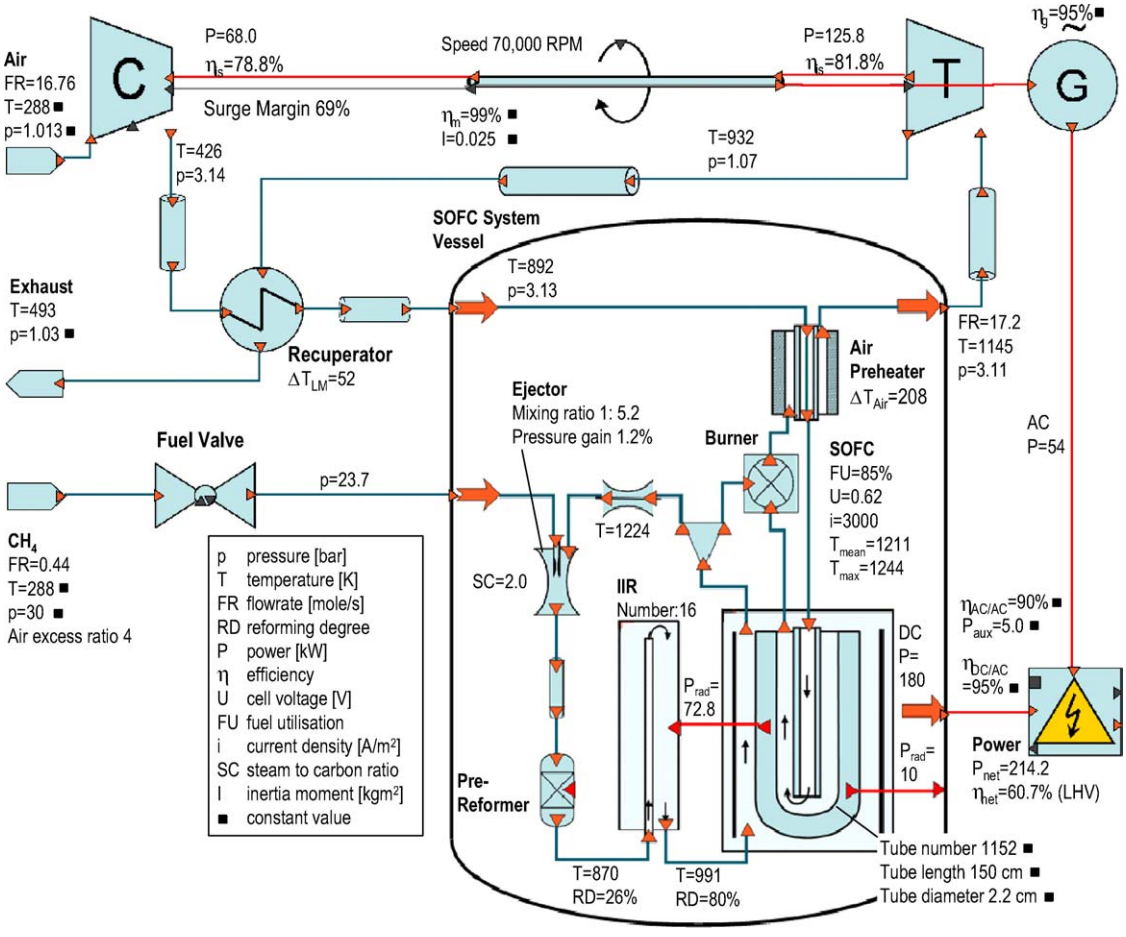

Fig. 1. Hybrid cycle layout and design point values (square marked values remain always constant).

potentials (Fick's law and Knudsen diffusion) and ohmic resistance. The constants used in the Butler–Volmer equation have been estimated based on measurement data from Singhal and Kendall [17]. For the heat transfer between the solids and the gases, Newton's law of cooling is applied in the following way:

$$\frac{\partial(T_g c_{p;g}\rho_g)}{\partial t} + v_g \frac{\partial(T_g c_{p;g}\rho_g)}{\partial z} = \frac{2h}{r_s}(T_s - T_g) \quad (3)$$

Spatially discretised radiation heat exchange is included between the cathode surface and the air supply tube. Furthermore, the anode radiates to the IIR to supply heat for the reforming reaction, and to the casing wall, leading to heat loss to the environment. Friction losses in the gas channels are accounted for by the Reynolds number approach.

2.2. Anode recirculation loop and reformers

In order to supply steam for the reforming process, a certain part of the anode exhaust gas must be recycled. The suction of the recycle stream and the mixing with the fresh fuel is performed by an ejector. High induced (recycle) flow rates at low pressure differences are typically achieved by subsonic mixing ejectors. The actuating flow is accelerated to supersonic speed in a Laval nozzle before it enters the mixing chamber. The ejector model is based on section-wise momentum balances and has been validated against data from Marsano et al. [18]. Pressure losses are included by a fixed throttle valve. Ejector behaviour is difficult to model without experimental validation and hence a practical ejector might differ from the model.

Before entering the anode, the gas leaving the ejector passes through two reformers: an adiabatic pre-reformer and an internal indirect reformer (IIR). The pre-reformer is modelled as a non-dimensional Gibbs equilibrium reactor where reforming and water-gas shift reactions take place. It is meant for cracking any higher hydrocarbons in the fuel gas and reform a part of the methane until equilibrium is reached. To account for reaction kinetics, a difference between the actual outlet temperature and the equilibrium temperature of 20 K is assumed.

The IIR is situated downstream the pre-reformer and it is based on Gibbs equilibrium. The gas is assumed to be reformed while flowing downwards rectangular ducts. The duct walls are coupled to the fuel cell anode by radiation. The latter is discretised in flow direction. A view factor is adjusted in the design calculation to meet the desired reforming degree. Gas residence time in the reformer is accounted analogously to the SOFC model (Eq. (1)). For accurately modelling reformer behaviour, its geometry and reaction kinetics must be regarded. For the present study, the modelling approach including thermal inertia of the reformer wall is however rated as sufficient.

2.3. Burner and recuperators

The burner is modelled non-dimensionally and adiabatically and completely combusts the remaining anode exhaust gas together with the cathode air. The mixing cathode and anode exhaust streams causes pressure equalisation of these flows upstream. In practice, difficulties may appear with reliably combusting highly depleted fuel.

The burner exhaust preheats the inlet air by a counter-flow tube-shell set-up, where the tube is the prolongation of the fuel cell air supply tube. The model accounts for thermal inertia, pressure loss and gas residence times, using the same approaches as in the SOFC model.

The recuperator heat exchanger is a stack of counter-flow plate-fin type. A two-dimensional distributed model is applied that accounts for thermal inertia, pressure loss and gas residence times. The recuperator model is based on data and relations from Kays and London [19].

2.4. Gas turbine

The gas turbine features map-based steady-state turbomachinery models, a shaft model accounting for rotating mass inertia, power electronics and ducts.

The compressor is based on the performance map of a small centrifugal research compressor by the German Aerospace Centre, found in a map collection from Kurzke [20]. The map is understood as a generic radial compressor map. Therefore it has been scaled in terms of reduced mass flow, pressure ratio and shaft speed to fit the design case. The map has been modelled using polynomials of fourth and fifth order for reduced mass flow, pressure and efficiency as functions of reduced shaft speed and operation (β) line. A surge margin (SM) is calculated as follows:

$$\mathrm{SM} = \frac{\pi_{\mathrm{surge}}(\dot{m}) - \pi(\dot{m}, n)}{\pi(\dot{m}, n)} \quad (4)$$

where $\pi(\dot{m}, n)$ is the actual pressure ratio at the actual reduced mass flow and reduced shaft speed and $\pi_{\mathrm{surge}}(\dot{m})$ the surge pressure ratio at the actual reduced mass flow.

The turbine is based on the performance map of a small radial turbine [20] which also is scaled to fit the design case. An ellipse approach has been used for the relationship between reduced mass flow, reduced shaft speed and operation (β) line. Pressure ratio and efficiency have been modelled by a polynomials approach.

Generator and power electronics account for transformation efficiencies which are assumed to be constant. A constant power sink accounts for power consumption of auxiliaries and transformation efficiency decrease at low load.

The shaft model includes acceleration/deceleration of the shaft through moment of inertia of the moving parts:

$$\frac{\mathrm{d}\omega}{\mathrm{d}t} = \frac{P_b}{I\omega} \quad (5)$$

where ω is the angular shaft speed in rad s^{-1}, I the moment of inertia in kg m^2, and P_b the power balance:

$$P_b = \eta_m P_{\mathrm{turb}} - P_{\mathrm{comp}} - P_{\mathrm{gen}} \text{ in W} \quad (6)$$

The ducts have the purpose to account for gas residence time in the piping. Heat and pressure losses and thermal inertia of the ducts and gas turbine components are neglected, as

they are considered to be minor compared to the SOFC system. This might lead to a slight overestimation of the system efficiency.

2.5. Complete model

The complete model is implemented in gPROMS [21], a process modelling tool based on an equation oriented solver. The strength of the equation oriented approach is that there is no fixed input–output structure. In fact, a certain number and combination of variables must be specified in order to achieve a valid equation system, but many degrees of freedom remain in choice of variables. As an example, either voltage or current of the fuel cell model may be specified.

The resulting system model consists of approximately 14,000 algebraic and 2300 state variables. The simulations were performed on a 2.5 GHz Intel Pentium-4 processor PC. Calculation time for a steady-state point was approximately 5–10 s. The solver used for dynamic calculations (SRADAU) varies time increments, thus calculation time depends on the occurrence of discontinuities and momentary fluctuation rate of the variables. A calculation time of about 5 min was required for the load change studies shown below, while the load profile simulation required about 20 h.

3. Design case and steady-state part-load behaviour

Before part-load behaviour can be studied, a design point must be defined. All relevant cycle data are displayed in Fig. 1. Most of the data are similar to recent literature on hybrid cycles [3,7,8,10] and public data from Siemens–Westinghouse. Values in the figure marked with a square are constant during all simulations. The design point and system dimensioning is furthermore based on the following assumptions:

- The system size is determined on the basis of the Siemens–Westinghouse stack design which incorporates 1152 tubular cells [22] and 16 indirect internal reformers.
- Pure methane is supplied as fuel.
- The view factor for the radiation from the anode surface to the IIR is equal for each cell and has been adjusted to achieve a reforming degree of 80%. High external reforming degrees cause flatter profiles of temperature and current density in the cell. Song et al. [15] report that the IIR exhaust gas includes only a small amount of unreformed methane at the Siemens–Westinghouse configuration.
- The view factor for the radiation from the anode surface to the stack casing has been adjusted in order to obtain a guessed heat loss at design point. A value of 10 kW is regarded as realistic and feasible.
- A length of 0.5 m was chosen for the air preheat tube, yielding a temperature increase of 208 K at design point. The length of the air preheat tube significantly influences the SOFC temperature.
- The ducts have a length of 1 m and are dimensioned for gas velocities of approximately 20 m s^{-1} at design point. The residence times are calculated utilising the ideal gas law. Residence times before and after the pre-reformer account for the actual pre-reformer residence time.
- The fuel utilisation (FU) is determined from current and fuel flow, as these parameters can be measured in a real system. Setting FU constant hence means maintaining a constant ratio of current to fuel flow. While this in steady-state provokes a constant content of combustibles in the anode exhaust gas, the content may vary during dynamic operation due to pressure change and gas transport delay. Due to the variations in heating value of the exhaust gas, severe oscillations in burner temperature may occur during load change. The common fuel utilisation value of 85% has been chosen.
- The ejector has been dimensioned for supplying a steam to carbon ratio of 2 in the design point. The difference in static pressure of induced and actuating gas flow in the mixing zone is vital for the ejector performance. According to Johannesen [23], a lower actuating flow pressure than induced flow pressure causes a strong reduction in induced flow rate. In contrast, a higher actuating flow pressure does not significantly increase induced fluid flow rate. For being able to reduce the fuel flow rate for part-load operation while maintaining a high recycle ratio, the inlet pressure of the actuating fluid at design point must be high. A value of 23.7 bar was chosen for design point. It is assumed that natural gas is available at high pressure, and hence there is no need for a fuel compressor.
- The recuperator is dimensioned in order to achieve a high amount of heat recuperation at tolerable size and pressure drop.
- The total moment of inertia for the rotating parts (turbine, compressor, generator and shaft) is assumed to be 0.025 kg m^2. This is equivalent to a rotating mass of 20 kg and a mean radius of 5 cm. The moment of inertia influences the power output during shaft acceleration and deceleration.
- The generator is assumed to have a constant efficiency of 95%. The power electronics have constant efficiencies of 90% for AC/AC and 95% for DC/AC conversion. As a comparison, von Spakovsky et al. [24] report values of 92–95% for DC/AC conversion for a 5 kW system. In order to account for power consumption of auxiliaries and the decreasing conversion efficiencies at load reduction, a constant power loss of 5 kW was applied.

With the given design and assuming a constant fuel utilisation in steady-state operation, two degrees of freedom remain for off-design operation, most pragmatically expressed by the parameters of fuel and air flow rate. Fuel flow can be controlled by a flow control valve. The air flow can be controlled through the gas turbine system in various ways; such as variable shaft speed, variable compressor inlet guide vanes or variable compressor bleed. Their effect on the system is very similar. Shaft speed variation is the option maintaining the highest efficiencies and the lowest pressure changes when reducing air flow. It was therefore selected here. The shaft speed is controllable through the power that is produced by the generator.

The free parameters air and fuel flow may be varied independently from each other within certain limits. Each

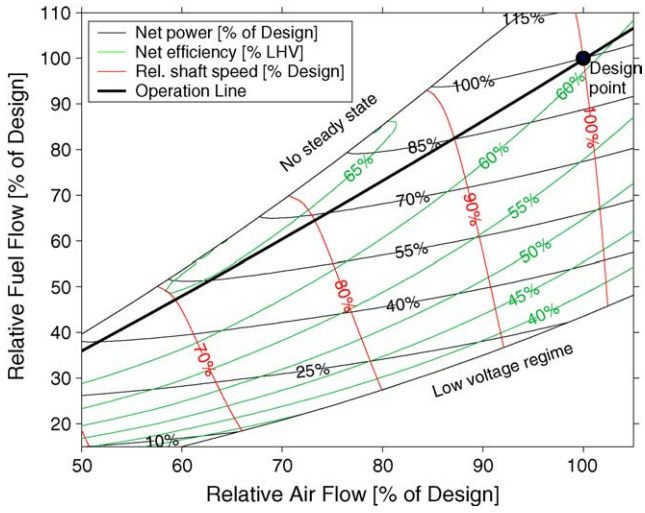

Fig. 2. Steady-state performance: power, efficiency and shaft speed.

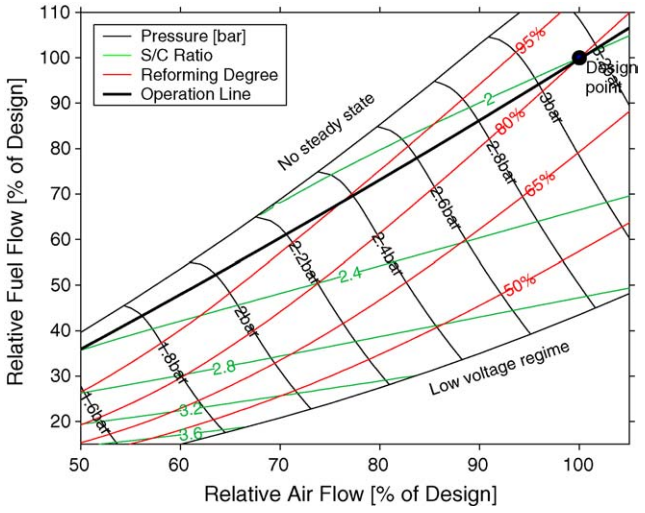

Fig. 4. Steady-state performance: pressure, steam-to-carbon ratio and reforming degree.

combination determines a certain operation point of the system. Figs. 2–4 show the steady-state behaviour of the parameters of interest as a function of fuel flow (FF) and air flow (AF) relative to their design values. Similar maps have been introduced for an SOFC stack system [25] and a full hybrid system [11].

In the blinded out regime on the upper left (low air and high fuel flow), no steady-state operation exists. Transient simulations have shown that the temperature in this regime is steadily climbing far beyond the valid ranges and eventually causing compressor surge. This is because enhanced effectiveness of the heat recuperation loop and lower air excess ratio at lower airflow causes TIT to increase.

In the lower right regime (high air and low fuel flow), the fuel cell is cooled down strongly and therefore the voltage is low. As it is not recommendable to operate in this regime, it is blinded out for cell voltages lower than 0.3 V.

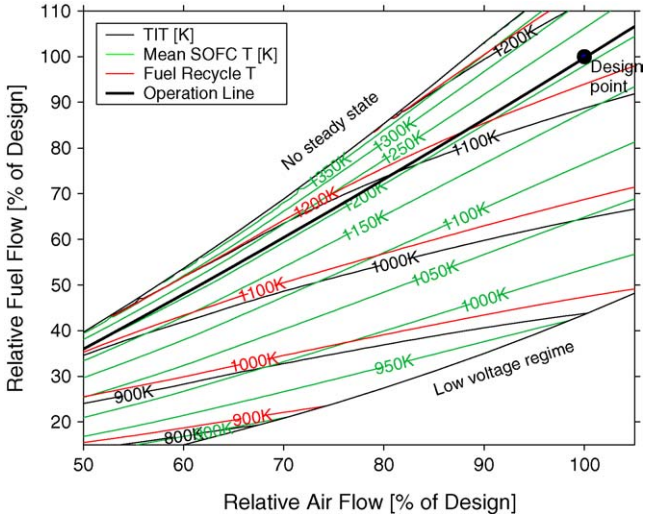

Fig. 3. Steady-state performance: TIT, mean SOFC and fuel recycle temperature.

A first result from the performance map is that reducing fuel flow at constant air flow, i.e. going down a vertical line from the design point, results in a strong reduction in temperatures and therewith efficiencies.

The figures also show that a load reduction by linearly reducing fuel flow and air flow will lead into the unstable region. Remaining in the stable regime therefore implies larger relative reduction in fuel flow than air flow. This is a consequence of the lower pressure ratio at lower shaft speed which results in an increased TOT. The same behaviour is also confirmed in a study by Costamagna et al. [7].

Surge margin and steam to carbon ratio do not reach any alarming values in the shown operation range.

4. Control design

4.1. Control objectives

A suitable control strategy for normal operation must meet the following objectives:

- *Safe operation of the system*: Incidents which may cause damage to the fuel cell or other components must be avoided. Such incidents are compressor surge or cell degradation due to thermal cracking or too high temperatures, carbon deposition and therewith blocking of the anode, and backflow of gas from the burner to the anode cycle, exposing the anode to oxygen. Compressor surge can occur in case of too high turbine inlet temperature. The occurrence of thermal cracking is coupled to the temperature and therewith stress profile in the cell. A model for thermal stress calculation in tubular SOFC has been developed recently at NTNU [26], however it is very computationally expensive and revealed a high degree of uncertainty and sensitivity to exact material properties. Carbon deposition occurs with too low temperatures and too low amount of steam at the cell inlet. Anode backflow has been observed with the

model used here during sharp pressure increases [11]. It is therewith restricting the maximum allowed pressure increase rate.

- *Quick load-following and high efficiency*: The selected control strategy should make it possible to follow a load profile quickly and accurately and furthermore maintain a high efficiency of the system in part-load operation.
- *Long lifetime of the fuel cell*: In addition to thermal cracking, the fuel cell may be degraded due to thermal fatigue and high local heat production rates [24]. The effect of thermal fatigue may be reduced by reducing the thermal cycling amplitude. Hence the mean cell temperature should be maintained as constant as possible throughout any part-load operation. Local heat production may be controlled by limiting the current drawn from the cell.
- *Governing external influences*: The system must react on external disturbances and adapt to changes in subcomponent performance, caused for example by fuel cell degradation or compressor fouling.

4.2. Analysis of the system

The hybrid cycle model is strongly non-linear and cannot be easily linearised due to its complexity. Therefore, most of the common controllability analysis techniques are not applicable [27]. However, having mapped the part-load behaviour, the system response is not so difficult to predict and thus the system is analysed manually.

The system has only one outer control variable, which is power. However, a certain operation strategy must be implemented, and thus also fuel utilisation, air flow and SOFC temperature have to be controlled. The manipulated variables are current, fuel flow and generator power.

There is strong interaction among the manipulated and controlled variables. However, as the required time scales are very different for the different control issues, a multi-loop control design may be applied without resulting in instabilities:

- Power is controlled by manipulating SOFC current due to its quick dynamics (magnitude of less than one second).
- Fuel utilisation must hence be controlled by manipulating the fuel flow (magnitude of few seconds).
- Air flow is controlled by manipulating the generator power and thus adjusting the shaft speed (magnitude of 1 min).
- Cell temperature is controlled by adjustment of the air flow setpoint (very slow).

The mentioned control loops are explained in detail in the following sections. The resulting control system is sketched in Fig. 5.

It must be pointed out that the control strategy presented here is adapted to the behaviour of the described system. Even though the shown parameters are only valid for this system, it is expected that the control strategy can be adapted to a real system once data of its true behaviour are available.

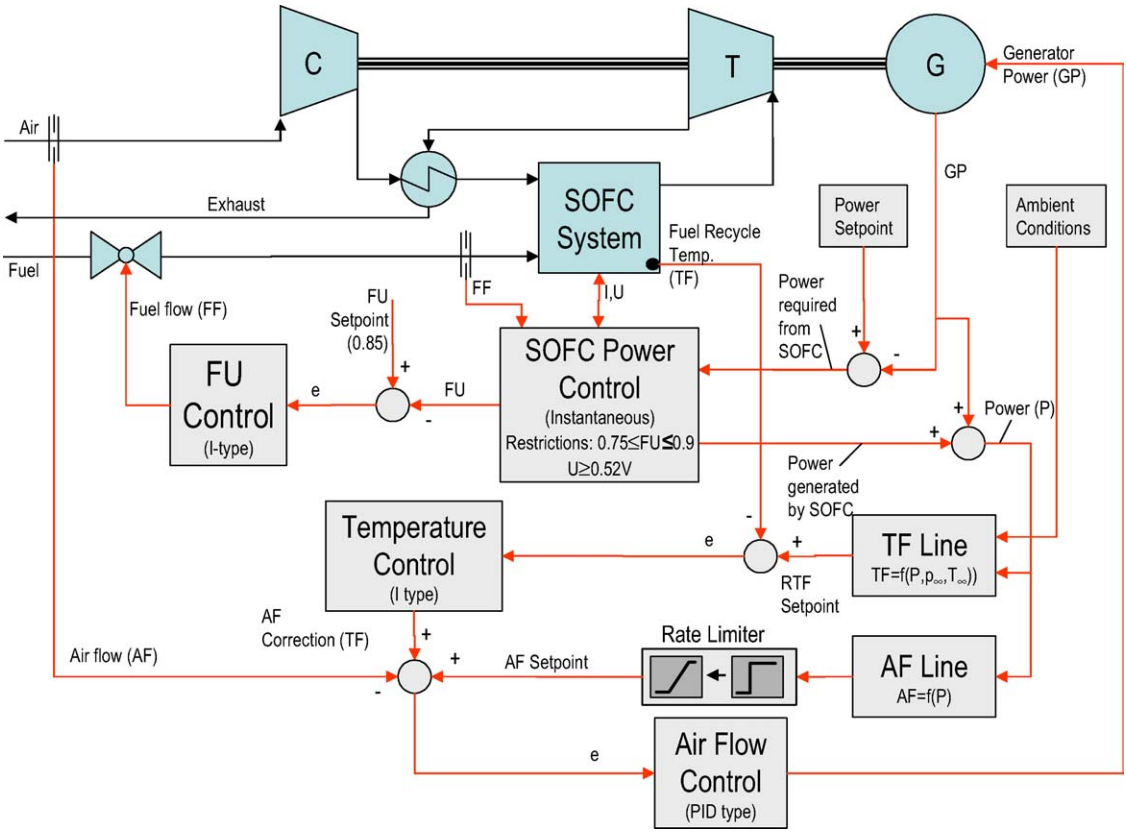

Fig. 5. Control system design.

4.3. SOFC power controller

The fuel cell can respond very quickly to load changes, as it is only limited by the electrochemical reaction restoring the charge which has been drained by the load [12]. Typically, time constants of below 1 s are assumed for a change in current [12,24]. For the primary control of power, it is therefore reasonable to manipulate the fuel cell current. It is assumed that this is done instantaneously by the power electronics subsystem which determines the operation point on the current–voltage line of the fuel cell. However, there are some limitations that prohibit the arbitrary movement on this line:

- The fuel utilisation must be kept within certain bounds. A too low FU leads to low steam content in the anode recycle and high TIT and therewith the risk of carbon deposition and compressor surge. A too high FU on the other hand leads to steep internal temperature gradients in the fuel cell and therewith advances thermal cracking. It is chosen to vary fuel utilisation in the range from 75 to 90%.
- The cell voltage must not drop under a certain level, as there is a maximum power output at an intermediate voltage (approximately 0.5–0.6 V, depending on the operation state). Lower voltage causes decreasing power in spite of increasing current and is unfavourable. A minimum voltage of 0.52 V is chosen.

The outcome is a multi-mode controller which switches between the modes of "*normal operation*", "*maximum FU*", "*minimum FU*" and "*minimum voltage*" to fulfil all above limitations. In "*normal operation*" mode, the current is manipulated so that the desired power of the whole system is produced. Small load steps in the range of some kilowatts can be followed instantaneously, while for larger steps, the controller switches to the mode "*maximum FU*" or "*minimum voltage*" in case a load increase and "*minimum FU*" in case of a decrease.

4.4. Fuel utilisation control

After a load change, the fuel utilisation must be reset to its static value of 85%. This is achieved simply by an indirect acting integral controller (integral time constant of 10 s), to which the fuel utilisation error serves as input and which manipulates the setpoint of the fuel flow valve. If the SOFC power controller is in "*normal operation*" mode, it will remain in this mode and the fuel utilisation will be reset to its static value. If it is in "*maximum FU*" mode, i.e. during a larger load increase, at first the error remains constant and the fuel utilisation controller will increase the fuel flow in a linear ramp function. At the point where the SOFC power controller can satisfy the power demand, it switches back to "*normal operation*", and the fuel flow ramp flattens to finally reach the new steady value. Zhu and Tomsovic [12] have previously shown a control strategy where fuel utilisation is reaching a high boundary during load increase.

4.5. Air flow control

The above-mentioned controllers fix the fuel flow. From the performance maps (Figs. 2–4) it can be seen that a fuel flow change should not be undertaken without a corresponding change in air flow, or the system will advance to unfavourable conditions. In Fig. 3 it can also be seen that a constant mean solid temperature is achievable over a load range from 40 to approximately 105%. Moreover, this operation line features a high efficiency in part-load. From the map data, a characteristic line for the air flow as a function of fuel flow or power can be developed which provides a setpoint to the air flow controller. However, the fuel flow will tend to overshoot the target values during load changes. This might cause instability in the system if fuel flow is taken as input to the air flow setpoint calculation. Hence, a controlled parameter is chosen, i.e. the produced power. The result is a characteristic function for the air flow setpoint (AF_{setp}) as a polynomial function of power (P) at constant mean solid temperature of the shape $AF_{setp} = f(P)$.

The setpoint together with the measured signal forms the error for the air flow feedback controller, which is an indirect acting proportional-integral-differential (PID) type. It manipulates the generator power (GP) through sending a power setpoint to the power electronics. We assume the power electronics to be able to instantaneously adjust the power drawn from the generator to this value.

With a given constant generator power, the system is at an unstable equilibrium. Departing from steady-state, for example, a step increase of the generator power will lead to deceleration of the shaft speed. No new equilibrium will be found within the valid bounds of shaft speed. By trial-and-error tuning, it has been found that a PID type controller with a high gain of ∼8, an integral time constant of ∼18 s and a differential time constant of ∼0.8 s is able to control the shaft speed and air flow reliably, stably and quickly. However, a too quick change of the air flow rate is not desirable, as this may lead to anode backflow, inverse reaction of system power due to high amplitudes in generator power and instability due to interference with the fuel utilisation control. In order to slow down the air flow change rate, the air flow setpoint signal is smoothened by a rate limiter.

Air flow and shaft speed are directly coupled. Nevertheless, for example a change in air density may lead to a higher required shaft speed for maintaining a certain air flow rate. Therefore the shaft speed must be monitored and overspeed protection must be provided.

4.6. Temperature control

Under ideal conditions, the above-mentioned strategy is able to follow a load line while maintaining safe operation and constant temperature. However, the strategy does not yet assure a stable cell temperature upon external disturbances as well as changes in system characteristics through degradation, or measurement errors. Especially in the low load regime, the cell temperature is very sensitive to the fuel flow. A small error of 1–2% points (caused by valve measurement error or varying fuel quality) may lead to steady-state temperature change of 50 K, even though it must be noted that the temperature advances very slowly to its new steady value (in the magnitude of hours to days). As the control strategy must also ensure temperature stability, an additional feedback loop is required.

An effective way to control the temperature by only influencing the power slightly is by manipulating the air flow (see almost horizontal power iso-lines in Fig. 2). An obstacle is that the mean cell temperature cannot be measured conveniently. However the related temperature of the fuel leaving the cell (TF) can be measured, for example in the recirculation plenum.

An implicit relationship between the two temperatures is established by once again determining a characteristic line. It has been detected that apart from the load, the relationship is dependent on the ambient air conditions. The setpoint of TF is hence calculated as a second order polynomial function of power, ambient pressure and ambient temperature; $TF_{setp} = f(P, p_\infty, T_\infty)$. The coefficients of this function have been fitted using the least squares method on simulation results with constant mean cell temperature.

The error from setpoint and measured fuel temperature is fed into a slow, direct acting integral controller (integral time constant of 20,000 s). A quicker controller would react too strongly on load change dynamics which provoke a temporary error in fuel temperature. The controller output signal is added to the air flow setpoint entering the air flow controller. This method of controlling a non-measurable variable indirectly by a measurable one is called inferential control [27].

5. System response results

5.1. Small load change

Small distributed networks supplying private households are assumed to have a maximum step change of power of about 10 kW (4.7% power). Figs. 6 and 7 show the system response to a load decrease, respectively, increase of this step size around design condition over a logarithmic time axis. At the power decrease, the setpoint power is reached after less than 1 s without the SOFC power controller reaching the "*minimum FU*" limit. At the load increase, the SOFC power controller switches to "*maximum FU*" for approximately 3 s before the setpoint power is reached. Air flow advances gently to the new point of the characteristics, while the fuel flow varies in order to keep the fuel utilisation at its setpoint value. The values are fairly steady after approximately 20 s. The cell temperature variation of approximately 2 K is due to the thermal inertia of the indirect internal reformer, which causes the reforming degree at the cell entrance to adapt slowly to the new steady-state. This affects the energy balance of the cell and therewith causes the temporary temperature variation. With greater time constants, the temperature resets to its design value.

5.2. Large load change

For industrial applications, larger load changes than the above may occur. In the following, the system response to a load change of 100 kW (from rated power down to 53%) is investigated and shown in Figs. 8 and 9. The setpoint power is reached after approximately 11 and 57 s at the load decrease and increase, respectively. The slower response at power increase is due to the lower deviation of fuel utilisation from its setpoint. It is furthermore technically required due to the risk of backflow from the burner into the anode recirculation system during pressure increase (this being not an issue at pressure decrease). A faster load increase may be achievable through higher gain of the fuel utilisation controller. Furthermore, the mean cell temperature reaches a minimum of 29 K below the design point approximately 1100 s after the load decrease and a maximum of 35 K above design point approximately 600 s after the load increase. This is again due to the IIR thermal inertia as mentioned above. The presented control strategy is hence able to stabilise the mean cell temperature in a bandwidth of 65 K under strong and quick load fluctuation.

5.3. Load profile

To demonstrate the stability of the cell temperature during load-following, the system is exposed to a randomly generated 24 h load profile. It implies average 24 random steps per hour

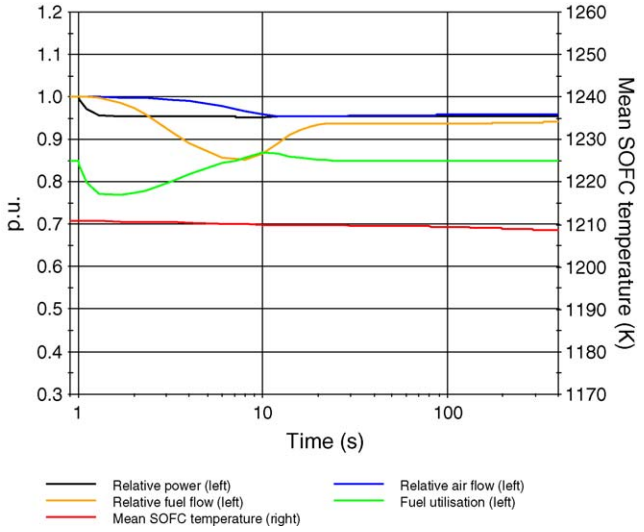

Fig. 6. Response to small load decrease (−4.7%).

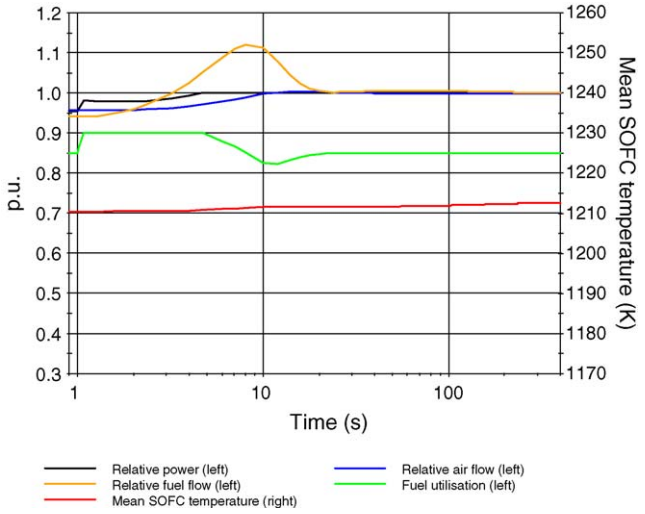

Fig. 7. Response to small load increase (+4.7%).

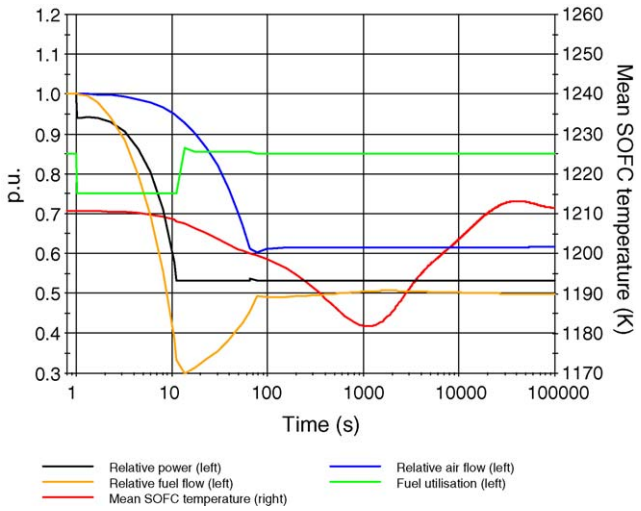

Fig. 8. Response to large load decrease (−47%).

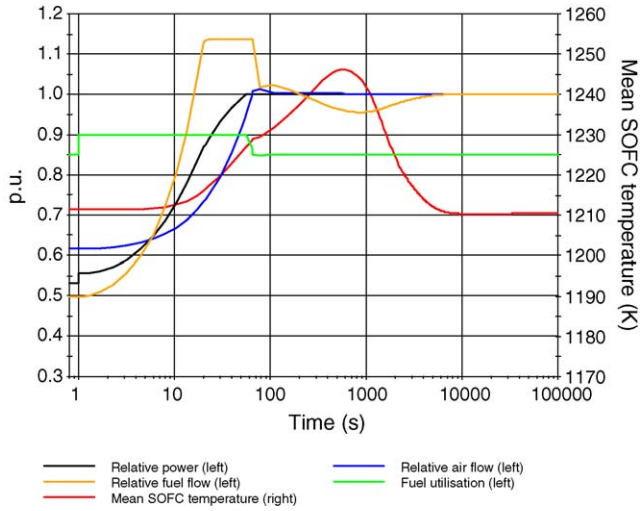

Fig. 9. Response to large load increase (+47%).

with a maximum size of 10 kW. Furthermore, a day–night variation covering the full load range of 40–105% is superposed. Fig. 10 shows the load line and the system parameters. Under these conditions, the observed bandwidth of the temperature is approximately 40 K. The strongest deviations result from steep load increase and decrease.

5.4. Ambient pressure and temperature change

In practice, the system is exposed to external disturbances, such as ambient pressure and temperature variation. These usually vary in the magnitude of hours. The response to a simultaneous temperature increase of 15 K and pressure decrease of 20 mbar over a time of 1 h, corresponding to a decrease of air density of 8%, has been studied.

In Fig. 11 it can be seen that after the change, the mean cell temperature increases about 7 K, as a higher air flow is required under these conditions. As the temperature control considers the measured ambient conditions, it is able to reset the cell temperature to the original value, however in a time scale of several days. It is therewith sufficient for compensating annual, but not daily fluctuations.

The effect of ambient air density could be compensated very quickly through a feedforward control which is providing an additional correction of the air flow setpoint. However, it has been shown that the cell temperature oscillations due to load cycling are higher than the ones caused by ambient conditions.

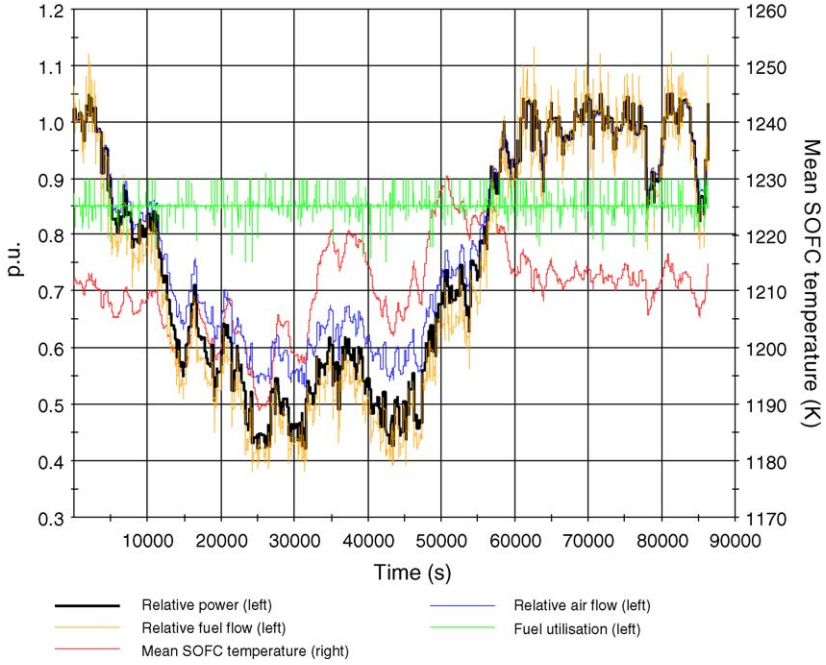

Fig. 10. Response to load profile.

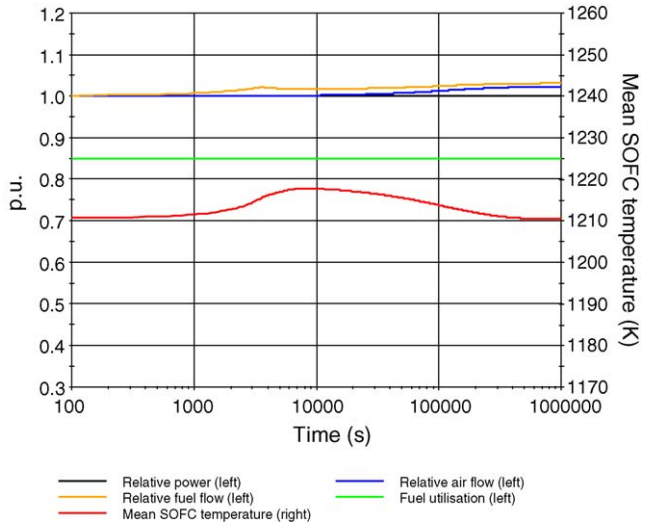

Fig. 11. Response to change in ambient conditions (+15 °C, −0.02 bar).

Hence, it is not considered as necessary under the given conditions.

5.5. Malfunction and degradation

The system characteristics shown in Figs. 2–4 are subject to changes during the system life due to degradation of the components. Furthermore, malfunction of the measuring may affect system stability. It is hence important to check the stability of the control system under these changed conditions.

In order to simulate fluctuation of load, we exposed the system to a sinusoidal oscillation between 53 and 100% of power with a period of 2000 s. Initially, the ordinarily working system is at steady-state. At time zero, the following incidents occur one at a time:

- *Fuel cell degradation*: An additional ohmic resistance is implied on the fuel cell, provoking a voltage loss of 50 mV at design current.
- *Compressor fouling and degradation*: Compressor design efficiency, flow rate and pressure ratio are decreased by 3%.
- *Fuel measurement malfunction*: Fuel flow is overestimated by 5%. This incident is similar to a change in the heating value of the fuel feed.
- *Air measurement malfunction*: Air flow is overestimated by 5%. Lower air flow leads to a higher mean SOFC temperature and is thus challenging the temperature control.

The resulting mean cell temperature responses are shown in Fig. 12. It can be seen that the temperature control system tackles all disturbances and the temperature always stays within an acceptable range. Nevertheless, steady-state deviations of the temperature occur in some cases. This is because the inferential control scheme is disturbed by a changed relationship between measured and controlled temperature. The effect is strongest for fuel measurement malfunction, as this leads to a falsified fuel utilisation, to which the system characteristics are very sensitive. Precise and possibly redundant measuring of the fuel flow and furthermore certainty of the fuel quality is thus recommended. The fuel cell degradation simulation shows a high peak of the temperature shortly after the incident. However, degradation effects usually occur gradually, and this peak will therewith not occur in practice. On the other hand, an increase in the temperature amplitude is also visible. This is due to mismatching of the real and assumed characteristics and may be eliminated by readjustment of the controller characteristics after a certain lifetime.

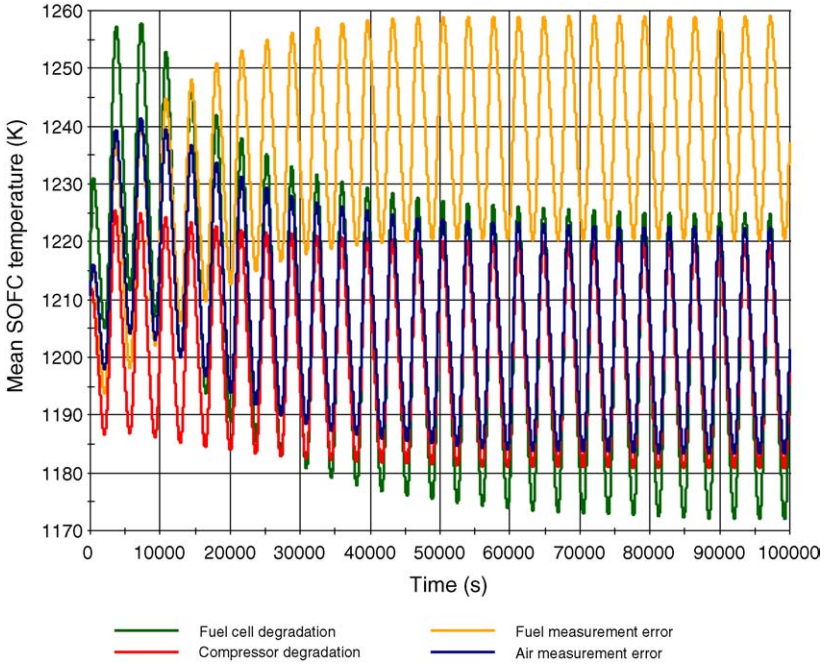

Fig. 12. Mean cell temperature response to malfunction and degradation effects.

Beside the mentioned malfunctions, several other and more severe malfunctions can occur, which the control system cannot tackle. A practical control system must therefore supervise further process parameters and if necessary run a safety shut-down routine to protect the hybrid system. This however exceeds the scope of this study.

6. Summary and conclusions

A powerful and flexible full dynamic model of a simple hybrid system has been developed that allows the characterisation of part-load performance and testing of control strategies. From the system configuration and part-load performance, the following control-relevant aspects have been detected:

- The degrees of freedom for the system are fuel flow and air flow. Furthermore fuel utilisation may be varied within certain limits during transients.
- The part-load behaviour of the system shows the presence of unstable regimes (no steady-state exists) at high fuel flow and low air flow, and regimes with very low SOFC temperatures at high air flow and low fuel flow.
- Operation with constant mean SOFC temperature is possible within a wide load range, but the temperature is very unstable in the low load regime. A feedback control of temperature is therefore required.
- Measurable, respectively, calculable inputs to the control system are power, air flow, fuel utilisation and temperature of the fuel leaving the cell.
- Manipulable variables are cell current, fuel flow and generator power.

Based on these aspects, a multi-loop feedback control scheme has been designed. Power is controlled by manipulating the SOFC current; fuel utilisation is controlled by manipulating the fuel flow; air flow is controlled by manipulating generator power; and the mean cell temperature is inferentially controlled by measuring the fuel cell exhaust fuel temperature and correcting the air flow setpoint. The interaction between the control loops does not lead to instability due to the strongly different controller time scales. The setpoints of the air flow and the measured temperature are calculated on the basis of steady-state characteristics of the hybrid system at constant fuel cell temperature operation.

The response of the system to load changes, load curve following, ambient air condition change and incidents of malfunction and degradation is tested. The system was stable during all the tests. The following conclusions on the system response may be drawn:

- Small load changes in the range of few kilowatts are followed in a time scale of below 1 s.
- Large load changes are followed in a time scale of 10–60 s.
- During normal operation, the mean SOFC temperature is stable within a band of 40–65 K around its design value.
- Ambient air conditions have only a small influence on system characteristics, provided their influence on the behaviour between measured and controlled temperature is accounted for.
- Fuel flow measurement errors or variations in fuel quality are severe, as they falsify the calculated control variable of fuel utilisation, which is an important parameter for the system performance. An overestimation of fuel flow by 5% may lead to a steady-state cell temperature offset of approximately 35 K above the design value.
- The temperature variation increases with increasing fuel cell degradation. It may therefore be advisable to readjust the control system characteristics after a certain system degradation.

The depicted quantitative data are only valid for the studied model. However, the qualitative trends are expected to be similar in a genuine system. Hence, the demonstrated methods can be applied on a real system, given that relevant data of its behaviour are available.

Acknowledgements

We thank the Norwegian Research Council, Shell Technology Norway and Statkraft for their financial support.

References

[1] C. Stiller, B. Thorud, S. Seljebø, Ø. Mathisen, H. Karoliussen, O. Bolland, Finite-volume modeling and hybrid-cycle performance of planar and tubular solid oxide fuel cells, J. Power Sources 141 (2005) 227–240.
[2] D. Rao, G.S. Samuelsen, A thermodynamic analysis of tubular SOFC based hybrid systems, ASME Paper 2001-GT-0522.
[3] S.H. Chan, H.K. Ho, Y. Tian, Modeling for part-load operation of solid oxide fuel cell-gas turbine hybrid power plant, J. Power Sources 114 (2003) 213–227.
[4] J. Pålsson, A. Selimovic, L. Sjunnesson, Combined solid oxide fuel cell and gas turbine systems for efficient power and heat generation, J. Power Sources 86 (2000) 442–448.
[5] S.E. Veyo, W.L. Lundberg, S.D. Vora, K.P. Litzinger, Tubular SOFC hybrid power system status, ASME Paper 2003-GT-38943.
[6] E. Achenbach, Response of a solid oxide fuel cell to load change, J. Power Sources 57 (1995) 105–109.
[7] P. Costamagna, L. Magistri, A.F. Massardo, Design and part-load performance of a hybrid system based on a solid oxide fuel cell reactor and a micro gas turbine, J. Power Sources 96 (2001) 352–368.
[8] S. Campanari, Full load and part load performance prediction for integrated SOFC and microturbine systems, J. Eng. Gas Turb. Power 122 (2000) 239–246.
[9] J. Pålsson, A. Selimovic, Design and off-design predictions of a combined SOFC and gas turbine system, ASME Paper 2001-GT-0379.
[10] S. Kimijima, N. Kasagi, Performance evaluation of gas turbine-fuel cell hybrid micro generation system, ASME Paper 2002-GT-30111.
[11] C. Stiller, B. Thorud, O. Bolland, Safe dynamic operation of a simple SOFC/GT hybrid system, ASME Paper 2005-GT-68481.
[12] Y. Zhu, K. Tomsovic, Development of models for analyzing the load-following performance of microturbines and fuel cells, Electric Power Syst. Res. 62 (2002) 1–11.
[13] F. Jurado, Study of molten carbonate fuel cell—microturbine hybrid power cycles, J. Power Sources 111 (2002) 121–129.
[14] A.D. Rao, G.S. Samuelsen, Analysis strategies for tubular solid oxide fuel cell based hybrid systems, J. Eng. Gas Turb. Power 124 (2002) 503–509.
[15] T.W. Song, J.L. Sohn, J.H. Kim, T.S. Kim, S.T. Ro, K. Suzuki, Parametric studies for a performance analysis of an SOFC/MGT hybrid power system based on a quasi-2D model, ASME Paper 2004-GT-53304.

[16] E. Achenbach, E. Riensche, Methane/steam reforming kinetics for solid oxide fuel cells, J. Power Sources 52 (1994) 283–288.
[17] S.C. Singhal, K. Kendall, High Temperature Solid Oxide Fuel Cells—Fundamentals, Design and Applications, Elsevier Ltd., 2003.
[18] F. Marsano, L. Magistri, A.F. Massardo, Ejector performance on a solid oxide fuel cell anodic recirculation system, J. Power Sources 129 (2004) 216–228.
[19] W.M. Kays, A.L. London, Compact Heat Exchangers, McGraw-Hill, 1984.
[20] J. Kurzke, Compressor and Turbine Maps for Gas Turbine Performance Computer Programs—Component Map Collection, vol. 2, Joachim Kurzke, Dachau, Germany, 2004.
[21] gPROMS (General Process Modelling and Simulation Tool), v.2.3.4, Process Systems Enterprise Ltd., London, http://www.psenterprise.com/.
[22] Y. Yi, T.P. Smith, J. Brouwer, A.D. Rao, G.S. Samuelsen, Simulation of a 220 kW hybrid SOFC gas turbine system and data comparison, Electrochem. Soc. Proc. 7 (2003) 1442–1454.
[23] N.H. Johannesen, Ejector Theory and Experiments, Dissertation, Danish Academy of Technical Sciences, Copenhagen, Denmark, 1951.
[24] M.R. Von Spakovsky, D. Rancruel, D. Nelson, S.K. Mazumder, R. Burra, K. Acharya, C. Haynes, R. Williams, R.S. Gemmen, Investigation of system and component performance and interaction issues for solid oxide fuel cell based auxiliary power units responding to changes in application load, in: IECON Proceedings (Industrial Electronics Conference), vol. 2, 2003, pp. 1574–1579.
[25] B. Thorud, C. Stiller, T. Weydahl, O. Bolland, H. Karoliussen, Part-load and load-change simulation of tubular SOFC systems, in: Sixth European Solid Oxide Fuel Cell Forum, Lucerne, Switzerland, 2004.
[26] A. Nakajo, C. Stiller, G. Härkegård, O. Bolland, Modeling of thermal stresses and probability of survival of tubular solid oxide fuel cells, J. Power Sources, doi:10.1016/j.jpowsour.2005.09.004.
[27] G. Stephanopoulos, Chemical Process Control—An Introduction to Theory and Practice, Prentice-Hall Inc., New Jersey, 1984.

Paper IV

Modeling of thermal stresses and probability of survival of tubular solid oxide fuel cells

Nakajo, A., Stiller, C., Härkegård, G., Bolland, O.

Journal of Power Sources, in press (available online).

Available online at www.sciencedirect.com
SCIENCE DIRECT®
Journal of Power Sources xxx (2005) xxx–xxx
JOURNAL OF POWER SOURCES
www.elsevier.com/locate/jpowsour

Modeling of thermal stresses and probability of survival of tubular SOFC

Arata Nakajo [a,*], Christoph Stiller [b], Gunnar Härkegård [c], Olav Bolland [b]

[a] *Laboratory for Industrial Energy Systems (LENI), Faculty of Engineering, Swiss Federal Institute of Technology, 1015 Lausanne, Switzerland*
[b] *Department of Energy and Process Engineering, Norwegian University of Science and Technology, Trondheim N-7491, Norway*
[c] *Department of Engineering Design and Materials, Norwegian University of Science and Technology, Trondheim N-7491, Norway*

Received 30 May 2005; received in revised form 16 August 2005; accepted 6 September 2005

Abstract

The temperature profile generated by a thermo-electro-chemical model was used to calculate the thermal stress distribution in a tubular solid oxide fuel cell (SOFC). The solid heat balances were calculated separately for each layer of the MEA (membrane electrode assembly) in order to detect the radial thermal gradients more precisely. It appeared that the electrolyte undergoes high tensile stresses at the ends of the cell in limited areas and that the anode is submitted to moderate tensile stresses. A simplified version of the widely used Weibull analysis was used to calculate the global probability of survival for the assessment of the risks related to both operating points and load changes. The cell at room temperature was considered and revealed as critical. As a general trend, the computed probabilities of survival were too low for the typical requirements for a commercial product. A sensitivity analysis showed a strong influence of the thermal expansion mismatch between the layers of the MEA on the probability of survival. The lack of knowledge on mechanical material properties as well as uncertainties about the phenomena occurring in the cell revealed itself as a limiting parameter for the simulation of thermal stresses.

Keywords: Solid oxide fuel cell; Tubular; Thermal stresses; Model

1. Introduction

The fossil fuel resources mainly used for power production are limited and cause environmentally harmful emissions. Furthermore, its use is suspected to cause global warming. Therefore, its judicious use appears important. The solid oxide fuel cell (SOFC) is a direct conversion process, which allows the production of electricity with high efficiency while maintaining pollutant emission at low level. Moreover, the SOFC technology is now far beyond the theoretical state. Indeed, prototypes have proven its ability to achieve the conversion of fuel into electricity with high efficiency, especially in the case of a SOFC and gas turbine hybrid system. The next step is commercialization, which may imply a drop of the specific cost and extended lifetime.

The major limitation to lifetime comes from the degradation of the materials, which is due to the aggressive environment related to operation conditions. A decrease of the performance of the cell is observed as well as structural failure. The knowledge of the stress field in the cell is therefore of main interest. The sintering phase during the manufacturing process, combined with the mismatch between the coefficients of thermal expansion (CTE) of the materials of the membrane electrode assembly (MEA) induces residual stresses in the cell. During operation, thermal gradients cause additional stresses and chemically induced stresses occur if interconnectors sensitive to oxygen activity gradient are used. The consequence of these phenomena is mainly delamination and thermal cracking in the critical layers of the MEA. Additional research is needed in order to quantify and predict the contribution of the thermal stresses to the failure of the cell. The operating condition of the cell can be adjusted by a suitable control strategy. The challenge is to maximize in particular the efficiency with respect to lifetime.

Two types of studies of thermal stresses in SOFC can be found in the literature. The first one focuses on the residual stresses in the cell at room temperature. Finite-element analysis is compared to experimental measurements in order to estimate its

* Corresponding author at: LENI-ISE-STI-EPFL, Bât. ME A2, Station 9, CH-1015 Lausanne. Tel.: +41 21 693 3505; fax: +41 21 693 3502.
E-mail addresses: arata.nakajo@epfl.ch (A. Nakajo), christoph.stiller@ntnu.no (C. Stiller), gunnar.harkegard@immtek.ntnu.no (G. Härkegård), olav.bolland@ntnu.no (O. Bolland).

0378-7753/$ – see front matter © 2005 Elsevier B.V. All rights reserved.
doi:10.1016/j.jpowsour.2005.09.004

Nomenclature

e	thickness (m)
E	Young's modulus (Pa)
m	Weibull modulus
P_s	probability of survival
P_f	probability of failure
r	radius (m)
u	displacement (m)
V_R	reference volume (m^3)

Greek letters

α	coefficient of thermal expansion, CTE (K^{-1})
λ	first Lamé coefficient
μ	second Lamé coefficient
ν	Poisson coefficient
σ_i	principal stresses, $i = 1, 2, 3$ (Pa)
σ_0	characteristic strength (Pa)
τ	temperature difference (K)
Ω	boundary

Indices

i	principal directions
j	radial, axial direction
r	radial direction
z	axial direction

suitability for stress simulation. Such studies were performed by Yakabe et al. [1], Atkinson and Selçuk [2] and Montross et al. [3]. The second situation of interest is operating conditions, which is known to cause the failure of the cell. For example, Yakabe et al. [4,5] and Selimovic et al. [6] have coupled their thermo-electro-chemical model with a finite-element tool in order to simulate the stresses in the cell during operation.

Little research has been conducted in thermal stresses in SOFC up to now, compared to the ones in thermo-electro-chemical modeling. Furthermore, there are many degrees of freedom in design, such as tubular or planar, anode or cathode supported. Therefore, no method to handle the problem has yet been clearly established which is generic, reliable and affordable in terms of modeling capabilities. Moreover, knowledge on the mechanical properties of the materials of the MEA is sparse. Other uncertainties remain in critical areas, such as the temperature at which no internal stresses occur or behavior of the bonds at the interfaces of the layers.

The purpose of the present work is to study the effects of the characteristics of the temperature profile on the stress field in a tubular cell during operation. The approach is to couple a thermo-electro-chemical model for the computation of the temperature profile with an additional module for the stress field. No feedback from the stress calculation to the thermo-electro-chemical model exists. Particular attention was paid to the values of the radial thermal gradients in the cell, which required separate calculation of the solid heat balances for the MEA. The Weibull analysis is a common way to estimate the failure probability of ceramic materials. Several authors [3,6] mentioned that the local maxima of computed stresses might exceed the yield strength of the materials if realistic probabilities of survival are targeted. In this work, a simplified Weibull analysis was applied, which allowed studying the evolution of the probability of survival for several cases including both steady state and dynamic operation. An analysis of the sensitivity of the stresses on the mismatch between the layers' coefficients of thermal expansion was performed in order to provide indication of the mechanical requirements on the choice of SOFC materials.

2. Modeling

2.1. Mechanical model and assumptions

The thermo-electro-chemical SOFC model, which provides the temperature profile in the cell, has been described by Stiller et al. [7]. The model was implemented in gPROMS, an equation oriented process modeling tool [8]. It was enhanced in order to detect the radial thermal gradients with higher accuracy. Thus, the MEA model is improved by calculating each layer separately. The steam reforming, water gas shift and electrochemical reactions are assumed to take place at the interface between the electrolyte and the anode. The model of the tubular cell geometry is simplified to an axisymmetric one, which implies neglecting circumferential temperature variations and the interconnect. Fig. 1 depicts the geometry and provides the actual dimensions.

The stress field model is based on the static uncoupled linear thermoelastic theory. The modeling has been performed with gPROMS in order have both the thermo-electro-chemical model and the stress model in the same computational tool. This approach is convenient, especially during dynamic operation. The drawback is the limitation of gPROMS in modeling complex geometries and its lack of advanced meshing possibilities.

The modeling assumptions to keep computing time reasonable are

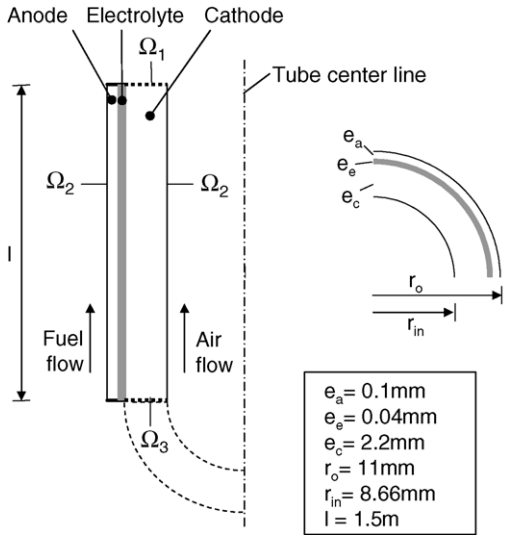

Fig. 1. Axisymmetric geometry of the cell used for modeling.

Table 1
Material properties of MEA components

	Young's modulus (GPa)	Poisson's coefficient	Coefficient of thermal expansion ($\times 10^{-6}$ K^{-1})	Characteristic strength (MPa)	Weibull modulus[a]
Cathode (LSM)	35 [20]	0.25 [20]	11.7 [17]	52 [12]	7 [12]
Electrolyte (YSZ)					
1073 K	183 [12]	0.313 [12]	10.8 [17]	256 [13]	5 [13]
298 K	212 [14]	0.32 [12]		332 [13]	5 [13]
Anode (Ni-YSZ)	57 [14]	0.28 [12]	12.2 [17]	115.2 [14]	6 [14]

[a] Only integer values could be implemented in gPROMS.

- The thermal expansion coefficients are constant over the considered range of temperature, e.g. values from the literature applicable over a range of 273–1300 K.
- The values of Young's modulus and Poisson's ratio at operating temperature are used when available, but their precise dependency on temperature is not modeled.
- The value of the zero stress temperature[1] is of the highest importance for the determination of the magnitude of the stresses. Major uncertainties remain in this area [1–3]. A uniform zero-stress temperature of 1400 K is used in the present work.
- The fixing of the cathode-supported cell is modeled by constraining the axial displacement at the boundary Ω_1 (Fig. 1). The boundary conditions at Ω_2 (Fig. 1) are determined by the pressure in the cell.
- The seal (Fig. 1) at the end is neglected due to meshing issues. The boundary Ω_3 (Fig. 1) is free.

The common Navier's equation is obtained by taking the displacement components u_j as the unknown of the fundamental equations of linear elastostatics. It is solved by the model under the previous assumptions. The resulting equation [9,10] is

$$\mu\nabla^2 u_j + (\lambda+\mu)u_{k,kj} - \frac{\alpha E}{1-2\upsilon}\tau_{,j} = 0 \quad (1)$$

The stress components are computed from the displacement fields. The three principal stresses,[2] σ_1, σ_2 and σ_3, are then determined with the principal invariants[3] method and used for a simplified version of the Weibull analysis [11]:

$$P_s = \prod_{i=1}^{3} \begin{cases} \exp\left(-\int_V \left(\frac{\sigma_i}{\sigma_0}\right)^m \frac{\mathrm{d}V}{V_\mathrm{R}}\right) & \sigma_i \geq 0 \\ 1 & \sigma_i < 0 \end{cases} \quad (2)$$

A simplification of the choice of the reference volume, V_R, was assumed. It considers the volume of the sample delimited by the outer ring of the so-called "ring on ring test", which was used in several sources on material properties [12–14]. Only few material configurations have been mechanically tested for the time being. They do not necessary correspond exactly to the materials used in tubular SOFC. The input data required for the whole process are listed in Table 1.

2.2. Verification against finite-element software (FEM)

gPROMS is not primarily designed to handle mechanical problems. Therefore its results were tested against those provided by a common FEM tool for stress computations, FEMLAB [15]. A typical temperature profile as it appears during operation was applied to a tube of 0.25 m length, made of layers of same diameter and thickness as the actual tubular cell. Fig. 2 depicts the comparison of the solution for the principal stresses of interest from gPROMS and FEMLAB. The agreement is considered as reasonable, especially when considering that the FEMLAB model uses more than 40 000 nodes, against only 738 for the gPROMS model.

2.3. Investigated cases

Both steady-state and dynamic operation of the SOFC were investigated. Several steady-state cases were chosen from a sequence of operating points designed in studies on part-load and load change with a model considering the SOFC and gas turbine hybrid system [7]. These operating points are characterized by the dimensionless shaft speed of the gas turbine (NDIM). High load is denoted by values around one. A particular feature of the pursued operation strategy is that it tries to keep the mean temperature of the SOFC at a fairly constant value over the range of NDIM 1.00 to NDIM 0.90. The fuel utilization[4] is close to 85% over the whole range. Furthermore, the stresses in the cell at room temperature were modeled by assuming a uniform temperature of 298 K in the cell.

The same model is used for dynamic simulation. Here, the input data, i.e. operating conditions, were assumed to vary linearly during a time interval of 60 s, since the model is limited to the SOFC and does not simulate the whole hybrid system. Only the SOFC conditions corresponding to the load cases were extracted from the hybrid system model. Two load changes were studied, NDIM 0.65 to NDIM 1.00 and NDIM 0.90 to NDIM 1.00. They represent changes of 75 and 15% of the rated power of the virtual hybrid system, respectively.

[1] *Zero stress temperature*: temperature at which no thermal stress act on the tube. In the SOFC, this coincides with the manufacturing temperature at which the layers are joined.
[2] *Principal stress*: stresses in the principal plane that is free of shear stresses.
[3] *Principal invariant*: coefficient in the eigenvalue problem required to establish the principal plane, the value of which is not altered by any rotation.
[4] *Fuel utilization*: fraction of the fuel which is oxidized in the fuel cell.

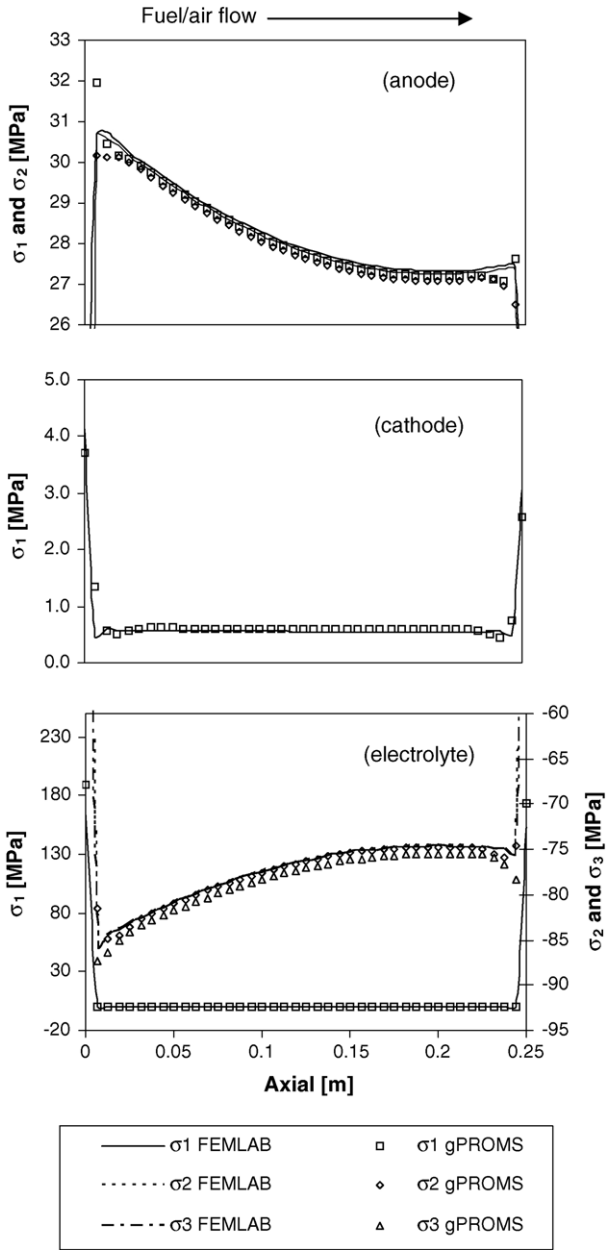

Fig. 2. Comparison of the thermal stresses in a tube computed by gPROMS and FEMLAB.

The sensitivity analysis considers a fixed value of the coefficient of thermal expansion of the anode, $12.2 \times 10^{-6}\,K^{-1}$, while those of the electrolyte and the cathode were allowed to vary in agreement with data found in the open literature. The large range of possible values is due to different doping methods. The Weibull modulus and strength, the Young's modulus and Poisson's coefficient were assumed to be constant. The analysis was performed at both high and low load, i.e. NDIM 1.00 and 0.65.

3. Results and discussion

3.1. Stress fields during operation

A comparison of the principal stresses at low and high load is depicted in Fig. 3. The stresses do not vary significantly in

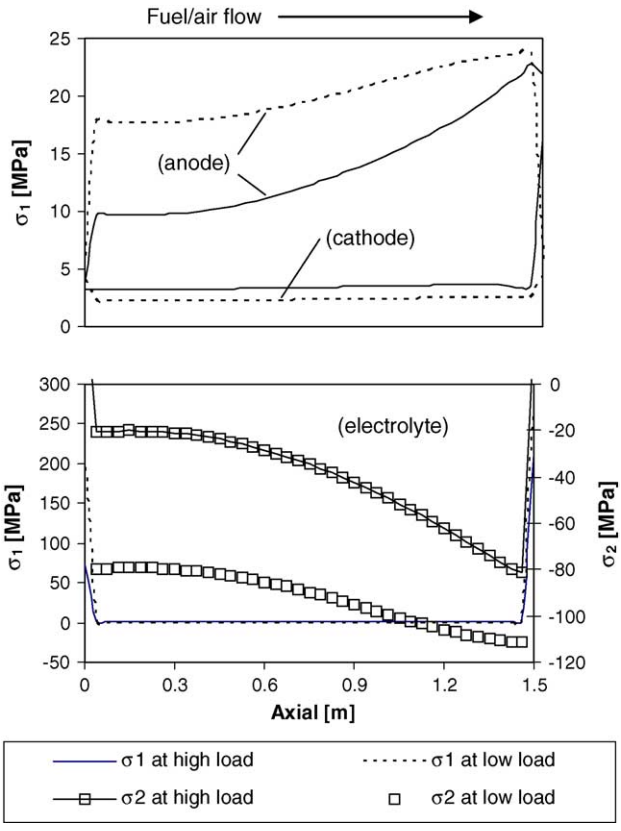

Fig. 3. Distribution of principal stresses at high and low load.

the radial direction. Two layers of the MEA undergo tensile stresses, the electrolyte and the anode. The variation of the shear stresses acting at the ends of the cell induces high tensile radial stresses in the electrolyte at the ends of the cell. They act in very small volume. The value exceeds 200 MPa, which is close to the characteristic strength of YSZ at the operating temperature. This behavior is opposite to that in the middle of the cell, where the smaller coefficient of thermal expansion of the electrolyte leads to compressive stresses. In the anode, both σ_1 and σ_2 are tensile, since the coefficient of thermal expansion of the Ni-YSZ cermet is the highest among the three layers. The stresses are highest at the fuel/air inlet, where the steam-reforming reaction induces a drop of the temperature.[5]

3.2. Steady-state cases

The observation of the specific values of the stress field cannot directly provide an indication of the risks associated with a particular operating point, since the failure of SOFC brittle materials are related to their defect structure. The probability of survival is a better criterion. Fig. 4 depicts its value for several operating points of the steady-state sequence. An optimum point for the global probability of survival occurs at intermediate load and is due to the opposite trends followed by the probabilities of survival in the layers. These are lower at low load in both

[5] In the fuel entering the cell, about 55% of the methane is reformed.

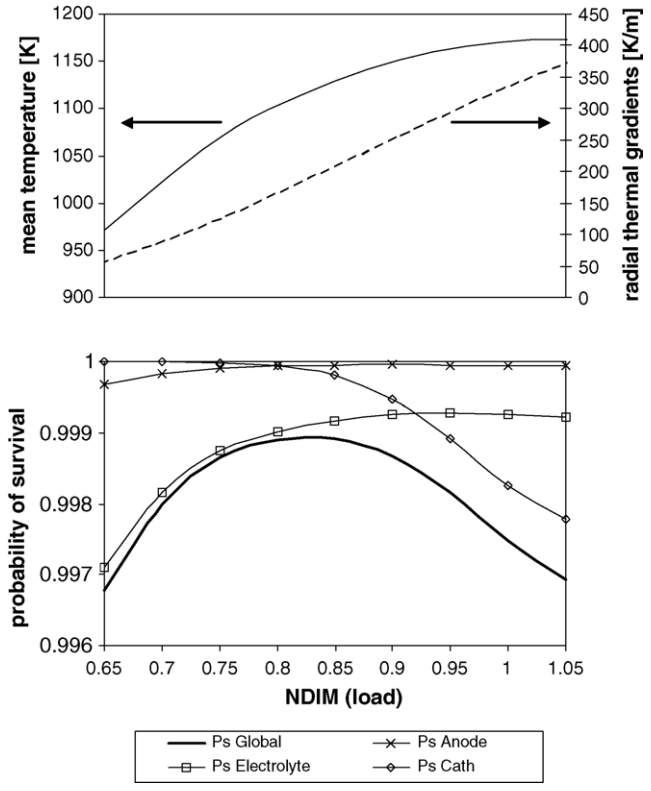

Fig. 4. Probabilities of survival as functions of the operating point during steady-state operation.

the electrolyte and the anode, due to the higher temperature difference τ induced by the low temperature in the cell. In the cathode, on the other hand, the probability of survival is lower at high load, when high radial thermal gradients act, which attain a local maximum at NDIM 1.0. Nevertheless, it must be noted that the results obtained here are restricted to a particular set of operating points and choice of material properties.

3.3. Dynamic simulations

The evolution of the probability of survival in the cell during both large and small load changes is depicted in Figs. 5 and 6, respectively. All load changes could be divided into a first phase with quickly changing probability of survival and a second phase where the probability of survival is slowly stabilizing.

From low load to high load, the increase of both mean temperature and temperature in the reforming area at the cell entrance induces an increase of the probability of survival during the first phase of the load change (Fig. 5). In the second phase, the probability of survival decreases due to the eventually increasing thermal gradients in the reforming area. At the transition point between both phases, the conditions are still close to the ones at low load, where the probability of survival in the cathode does not have a major contribution. Therefore, the trends are opposite during the reverse process: the quick decrease of the thermal gradients is during the first phase clearly effecting an increase of the probability of survival. The former is coupled to the increase of the temperature in the reforming area, which implies the same trend for the probability of survival of the electrolyte. In the second phase, the probabilities of survival of the anode and the electrolyte become dominant as they follow the decrease of the temperature.

At high load, the global probability of survival is dominated rather by the cathode than by the anode. Small load changes under these conditions are depicted in Fig. 6. The influence of the quick variations of the thermal gradients clearly appears on the evolution of the probability of survival, in both directions. The influence of the temperature acts through the same mechanisms

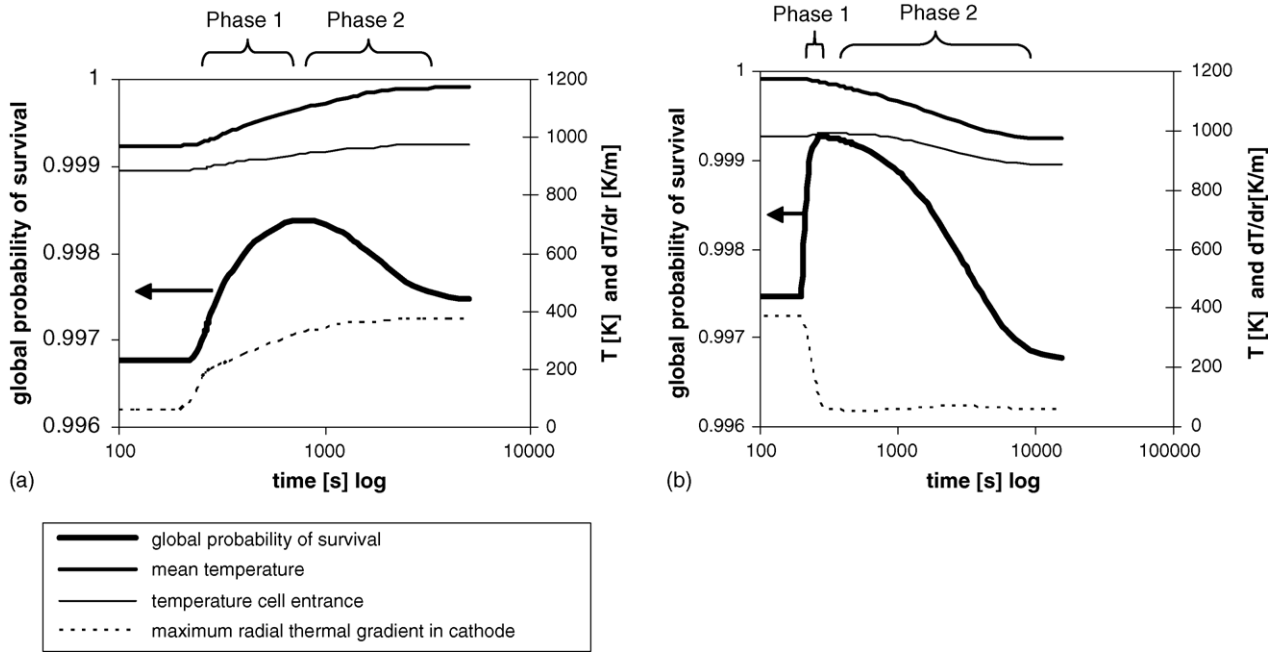

Fig. 5. Probabilities of survival, temperatures and gradients during load changes: (a) NIDIM 0.65 to NDIM 1.00; (b) NDIM 1.00 to 0.65.

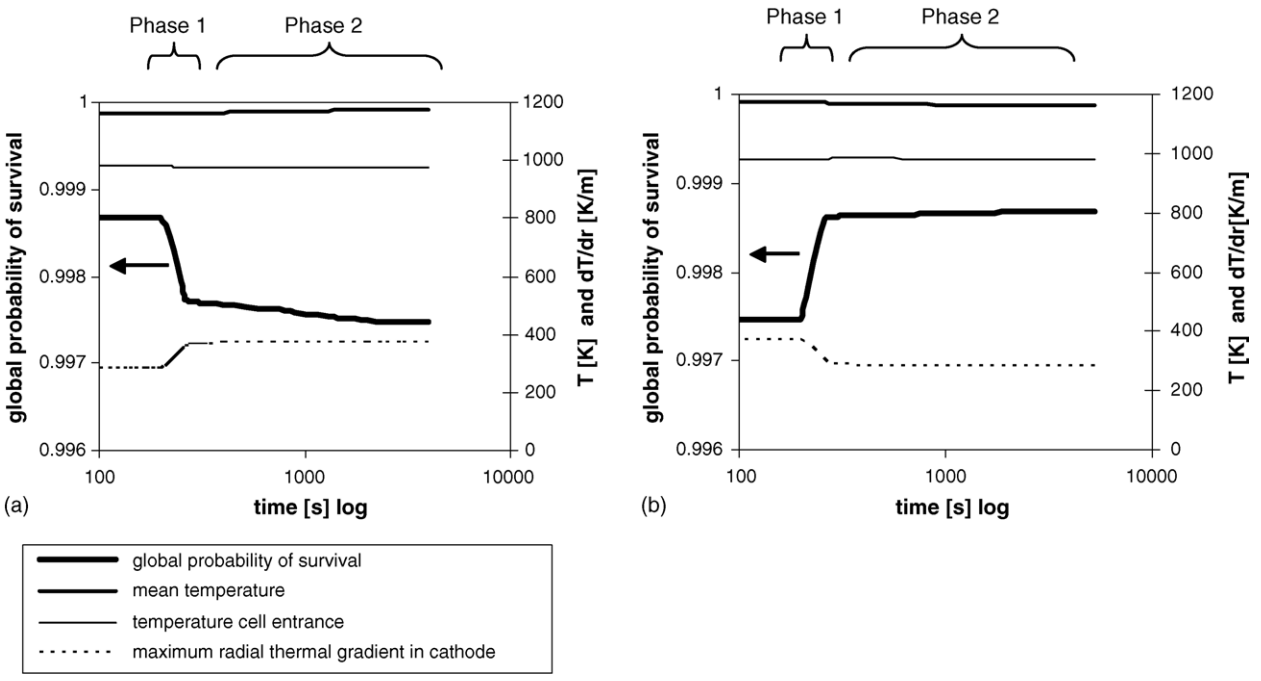

Fig. 6. Probabilities of survival, temperatures and gradients during load changes: (a) NIDIM 0.90 to NDIM 1.00; (b) NDIM 1.00 to 0.90.

as mentioned previously. From lower to higher load, the evolution of the probability of survival during the second phase is less dependent on the temperature. It is flatter during the decrease of temperature from NDIM 1.0 to NDIM 0.9. In contrast, the evolution of the radial thermal gradients is almost symmetric. The previous results do not show any intermediate drop of the global probability of survival during the investigated dynamic cases because of the combined effects of the temperature and the radial thermal gradients. This favorable combination may however not be generally true for all imaginable operation strategies of the system.

3.4. Sensitivity on mismatch between coefficients of thermal expansion

The differences between the layers' coefficient of thermal expansion mismatches are the primary cause of thermal stresses. High uncertainty exists about the CTE values. A multitude of values can be found in the literature, because of the wide possibilities in doping. In the present work, the range of coefficient of thermal expansion was found by literature review. In general, the CTE may be varied by modifying the material composition or other parameters, such as porosity [16]. Under these modifications, mechanical and electro-chemical properties of the materials would vary as well. This dependency was however not considered in the present sensitivity analysis; from Table 1 only the CTE is varied here. The CTE of the anode was kept constant at $12.2 \times 10^{-6}\,K^{-1}$ [17], while those of the electrolyte and the cathode were varied from $9.7 \times 10^{-6}\,K^{-1}$ [17] to $10.8 \times 10^{-6}\,K^{-1}$ [18] and from $11.3 \times 10^{-6}\,K^{-1}$ [16] to $12.8 \times 10^{-6}\,K^{-1}$ [17], respectively.

Fig. 7 depicts the results at both high and low load. The probability of survival is higher for high values of the coefficient of thermal expansion of the electrolyte, since the mismatch relative to both the cathode and the anode is reduced. The optimum set at low load differs slightly from the one at high load. Indeed, the cathode is the critical layer in the latter case and is prone to higher tensile stresses, if its coefficient of thermal expansion increases. In particular, the probability of survival is critical, when the coefficient of thermal expansion of the cathode exceeds that of the anode. This requirement is opposite to the one leading to the highest probabilities of survival in the anode. At low load, the contribution of the latter is larger and therefore induces a shift

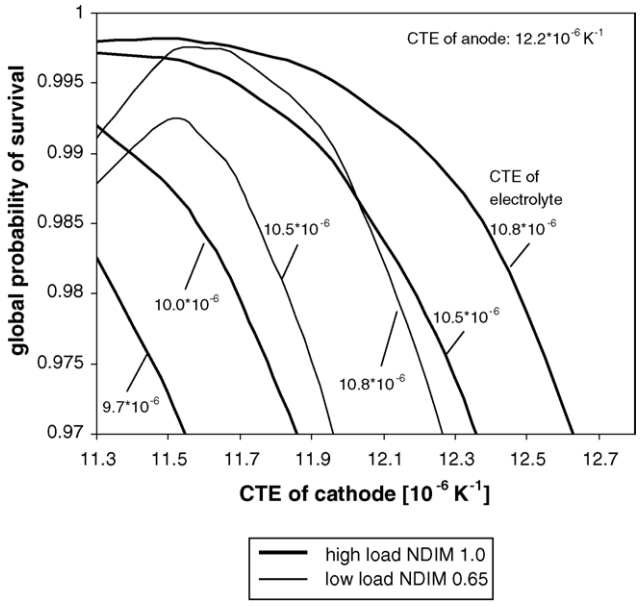

Fig. 7. Effect of cathode and electrolyte CTEs on the probability of survival at high and low load.

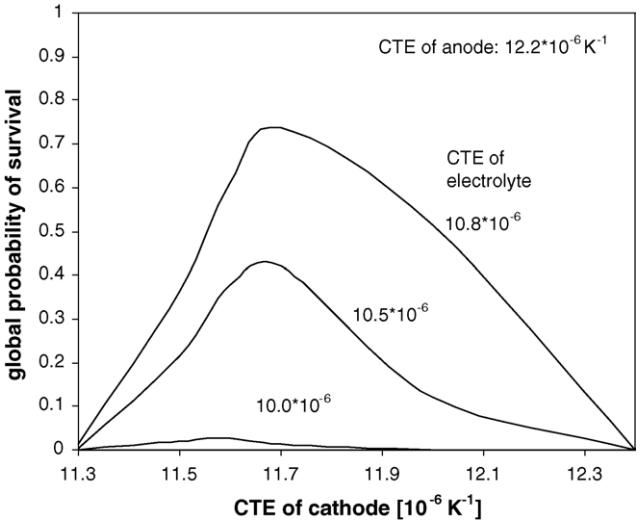

Fig. 8. Effect of cathode and electrolyte CTEs on the probability of survival at room temperature.

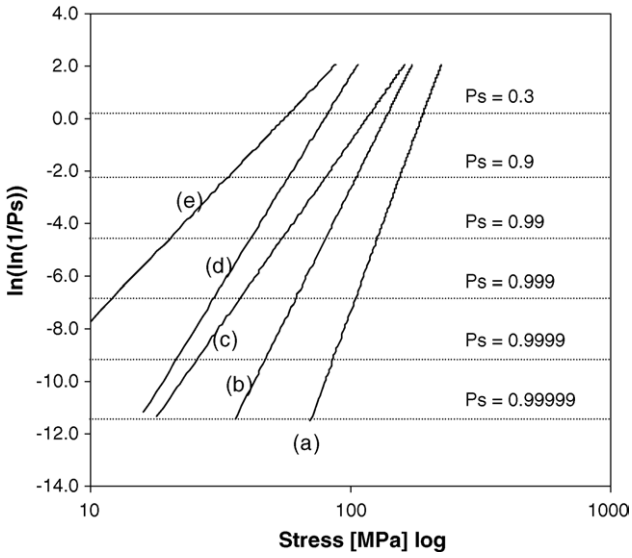

Fig. 9. Weibull plot of 75% Ni(O)-YSZ cermet (anode material) at room temperature: (a) unreduced [12]; (b) unreduced, porosity 0.06 [14]; (c) reduced, porosity 0.27 (used for the calculation in the present work) [14]; (d) reduced, porosity 0.36 [14]; (e) reduced, porosity 0.39 [14].

of the optimum point to higher cathode CTE compared with the case of high load. Furthermore, highest probabilities of survival can be achieved only for particular choices of CTE.

3.5. Room temperature case

The difference between the operating and the zero-stress temperature has been identified as a main driver of thermal stresses. From this point of view, room temperature appears as the most critical case. The shape of the stress fields shows the same global trend as during operation; that is high stresses at the ends of the cell in the electrolyte and tensile stresses in the whole anode.

Fig. 8 displays the result of a sensitivity analysis of the same kind as in Section 3.4. The optimum probability of survival over the considered CTE range is very low and located in a narrow regime.

3.6. Limitations

The comparison of the results presented in Sections 3.2–3.4 shows to some extent contradiction with the common observations, which indicate the failure of the cell during operation. However, the computation of stresses performed by Montross et al. [3] in the case of a planar cell at room temperature also indicates that probabilities of failure[6] as low as 10^{-5} cannot be achieved with the common SOFC materials. Nevertheless, this requirement is typical for applications targeted by the SOFC technology. Commercialization is obviously not possible under these conditions. Atkinson and Selçuk [12] pointed out the low values of the Weibull moduli as a limiting parameter. Ideally, these should be higher than 10.

Mechanical data for SOFC materials is still sparse. In particular, the dependency of the Young's modulus and the strength on temperature has not yet been precisely quantified. Its exploration is complicated by the wide possibilities in material composition, which mainly has to fulfill electro-chemical requirements. The manufacturing process also plays a major role; suitable sintering temperatures and processes are under investigation. The experimental data therefore depend on the supplier of the sample. The reduction of the anode material is another issue. Only few researchers [14] have consistently published its influence on the strength. This fact is visible in Fig. 9. It shows the probability of survival of 75% Ni(O)-YSZ over the stress at room temperature. The large discrepancies are partially due to different porosity and state, i.e. reduced and unreduced. However, in the most comparable case, the strength of the tested material differs significantly. For the preceding calculations, material (c) is used. The results presented in Sections 3.2–3.5 obviously change if material (a) or (b) was used. The dependency on porosity, which increases after reduction, amplifies the problem.

Other fundamental uncertainties remain. In particular, extended knowledge of the behavior of the bonds between the layers, as well as on the phenomena determining the value of the zero stress temperature are required. In the case of a tubular cell manufactured by electrochemical vapor deposition, the process requires the insertion of additional layers in order to prevent the growth of undesired phases [17]. A model assuming three layers joined to each other at a uniform temperature may not be refined enough to simulate the stresses in such tubular SOFC with satisfactory accuracy. The work of Li et al. [19] observed complex behavior of cell samples during their experiment for the analysis of crack density. In particular, reproducibility could not be achieved. The effect of the sintering temperature on the crack density was clearly observed. Unexpected behavior of the layers, such as compliance of the electrolyte is reported.

The experimentally observed mechanical failure of SOFC depends on the degradation of the materials due to the aggressive environment during operation. Studies on the evolution of

[6] Probability of failure: $P_f = 1 - P_s$.

the mechanical properties of the materials during the life of the SOFC are necessary to predict the SOFC life. Such phenomena have not been considered in the present study. The probability of survival, which has been used as test criterion, considers only the initial structure. Indeed, the current knowledge on the mechanical phenomena in SOFC does not allow modeling for the purpose of life assessment.

4. Conclusions

A model for calculating stresses was added to a thermo-electro-chemical model in order to simulate the thermal stresses in a tubular cell. For all studied cases, the stress fields display high tensile stresses in limited areas at the ends of the cell in the electrolyte and significant values in the whole anode. The latter is due to its high coefficient of thermal expansion. The magnitude of the stresses is higher at the fuel/air inlet, where the internal steam-reforming reaction induces a temperature drop. The comparison with FEMLAB, a suitable FEM tool, confirmed the ability of the modeling tool gPROMS to handle mechanical problems in particular cases, despite its limitation in meshing abilities, i.e. uniform, rectangular meshing and simple geometries.

The assessment of the risks related to particular operating points and load changes was performed through the probability of survival. The evolution of the latter is dependent on the temperature difference in both the anode and the electrolyte, whereas in the cathode, radial thermal gradients are most important. Therefore a maximum point for the value of the probability of survival of the cell is observed at intermediate load. Transient operation did not lead to any drop in the value of probability of survival. However, this favorable behavior may change when a different operation strategy is applied.

The greatest difference between the actual temperature and the sintering temperature occurs when the cell is at room temperature. The probability of survival calculated here reaches critical values, which might be acceptable for prototypes, but does not allow any commercialization. Significant improvement of the mechanical properties of the materials is required. This result is somewhat contradictory to the common observations, which rather indicate failure during operation. As a matter of fact, it shows the limitation of the thermal analysis alone and points out the importance of considering the degradation of the material during operation. Unfortunately, it appears that the published knowledge on material properties and complex phenomena occurring in the cell is not sufficient to allow any modeling for the purpose of lifetime assessment. Therefore, further studies should focus on the initiation and growth of cracks in SOFC and on improving the knowledge of material properties. An in-depth study of the influence of the choice of control strategy would also be of interest in order to find general criteria for stress-friendly operation.

Acknowledgement

We thank the Norwegian Research Council, Shell Technology Norway and Statkraft for their financial support.

References

[1] H. Yakabe, Y. Baba, T. Sakurai, Evaluation of residual stresses in a SOFC stack, J. Power Sources 131 (2004) 278–284.
[2] A. Atkinson, A. Selçuk, Residual stress and fracture of laminated ceramic membranes, Acta Mater. 47 (1999) 867–874.
[3] C.S. Montross, H. Yokokawa, M. Dokiya, Thermal stresses in planar solid oxide fuel cells due to thermal expansion differences, Br. Ceram. Trans. 101 (2002) 85–93.
[4] H. Yakabe, T. Ogiwara, M. Hishinuma, I. Yasuda, 3-D model calculation for planar SOFC, J. Power Sources 102 (2001) 144–154.
[5] H. Yakabe, I. Yasuda, Model analysis of expansion behavior of $LaCrO_3$ interconnector under solid oxide fuel cell operation, J. Electrochem. Soc. 150 (2003) A35–A45.
[6] A. Selimovic, M. Kemm, T. Torisson, M. Assadi, Steady state and transient thermal stress analysis in planar solid oxide fuel cells, J. Power Sources 145 (2005) 463–469.
[7] C. Stiller, B. Thorud, O. Bolland, Safe dynamic operation of a simple SOFC/GT hybrid system, ASME Turbo Expo, 2005-GT-68481.
[8] gPROMS (General Process Modelling and Simulation Tool), v.2.3.4, Process Systems Enterprise Ltd., London, http://www.psenterprise.com/.
[9] N. Noda, R.B. Hetnarski, Y. Tanigawa, Thermal Stresses, 2nd ed., Talyor & Francis, New York, 2002.
[10] S.P. Timoshenko, J.N. Goddier, Theory of Elasticity, 3rd ed., McGraw-Hill, Auckland, 1988.
[11] W. Weibull, A statistical theory of the strength of materials, Proc. Roy. Swed. Inst. Eng. Res. 151 (1939) 1–45.
[12] A. Atkinson, A. Selçuk, Mechanical behavior of ceramic oxygen ion-conducting membranes, Solid State Ionics 134 (2000) 59–66.
[13] F.L. Lowrie, R.D. Rawling, Room and high temperature failure mechanisms in solid oxide fuel cell electrolyte, J. Eur. Soc. 20 (2000) 751–760.
[14] M. Radovic, E. Lara-Curzio, Mechanical properties of tape cast nickel-based anode materials for solid oxide fuel cells before and after reduction in hydrogen, Acta Mater. 52 (2004) 5747–5756.
[15] FEMLAB Multiphysics modeling, v.3, COMSOL group, Sweden, http://www.femlab.com/in.
[16] M. Mori, Effect of B-site doping on thermal cycle shrinkage for $La_{0.8}Sr_{0.2}Mn_{1-x}O_{3+\delta}$ perovskites, Solid State Ionics 174 (2004) 1–8.
[17] N.Q. Minh, T. Takahashi, Science and Technology of Ceramic Fuel Cells, Elsevier, 1995.
[18] V.V. Kharton, F.M.B. Marques, A. Atkinson, Transport properties of solid oxide electrolyte ceramics: a brief review, Solid State Ionics 174 (2004) 135–149.
[19] W. Li, K. Hasinka, M. Seabaugh, S. Swartz, J. Lannutti, Curvature in solid oxide fuel cells, J. Power Sources 138 (2004) 145–155.
[20] N.M. Sammes, Yanhai Du, The mechanical properties of ceramic materials for solid oxide fuel cells, Electrochem. Proc. 97 (18) (2000) 671–679.